Communauté
UNIVERSITÉ Grenoble Alpes

THÈSE

Pour obtenir le grade de

DOCTEUR DE L'UNIVERSITÉ GRENOBLE ALPES

Spécialité : **Sciences de la Terre, de l'Univers et de l'Environnement**

Arrêté ministériel du 25 mai 2016

Préparée au sein de **Institut des Sciences de la Terre (ISTerre)**
et de l'école doctorale **Terre, Univers et Environnement**

Évolution des conditions d´écoulement du magma et du dégazage dans les conduits éruptifs des volcans andésitiques : apports de la modélisation numérique

Présentée par

Laure Chevalier

Thèse dirigée par **Virginie Pinel**
et codirigée par **Marielle Collombet**

Thèse soutenue publiquement le **9 Mai 2017**,
devant le jury composé de :

Mme, Alison Rust	Reader	University of Bristol, UK	Rapporteur
M, Antonio Costa	Researcher	INGV, Bologne, Italie	Rapporteur
M, Henri-Claude Nataf	DR1	CNRS, ISTerre	Président
M, Claude Jaupart	Professeur	Université Paris-Diderot, IPGP	Examinateur
M, François Beauducel	Physicien	IPGP	Invité
Mme, Virginie Pinel	CR1, HDR	IRD, ISTerre	Directrice de thèse
Mme, Marielle Collombet	MCF	USMB, ISTerre	Co-Directrice de thèse

Résumé

L'activité des volcans andésitiques, tels que le Mont St Helens (États-Unis), Montserrat (Antilles) ou encore le Merapi (Indonésie), alterne entre des périodes relativement calmes, avec coulées de lave et formation d'un dôme, et des événements explosifs parfois très violents. Prévoir les transitions entre ces deux régimes est essentiel pour assurer la sécurité des populations voisines, mais demeure actuellement un vrai défi. Or les données expérimentales et les observations de terrain montrent que l'explosivité du magma est étroitement liée à son contenu en gaz. L'objectif de cette thèse est d'améliorer notre compréhension de l'évolution de ce contenu en gaz et de son influence sur l'activité volcanique, en nous appuyant sur des simulations numériques, l'analyse de données expérimentales ainsi que sur l'interprétation de données de déformation enregistrées au Merapi.

Une part importante de ce travail réside dans le développement et l'amélioration de modèles d'écoulement en 2D pour prendre en compte le dégazage dans la partie supérieure du conduit, en régime transitoire. Nous présentons un modèle d'écoulement du gaz en temps qui tient compte des pertes en gaz aux bords du conduit et à sa sortie, selon les conditions présentes dans la roche encaissante et le dôme. Nous proposons également une adaptation des modèles de conduit permettant de coupler complètement l'écoulement du gaz avec celui du magma pour étudier l'évolution des conditions dans le conduit en régime transitoire. À partir de simulations de l'évolution du dégazage lors de l'emplacement d'un dôme, nous identifions les paramètres contrôlant les pertes en gaz. Nos résultats montrent que ces pertes sont extrêmement sensibles à l'évolution de la perméabilité du magma et des gradients de pression autour du conduit en réponse au poids du dôme. La perméabilité du dôme a quant à elle peu d'influence. Au cours de la croissance du dôme, les pertes en gaz diminuent en profondeur. En haut du conduit, la pression du gaz augmente de quelques dizaines de MPa. Ces effets sont associés à une augmentation de l'explosivité du magma et de l'aléa volcanique en cas d'effondrement du dôme.

Bien que la perméabilité du magma exerce un fort contrôle sur la perte de gaz, comme l'ont montré nos résultats, son évolution dans le conduit est peu contrainte. Les lois de perméabilité utilisées actuellement ne sont pas en accord avec l'ensemble des mesures réalisées sur des échantillons de magmas riches en silice. Dans le but d'améliorer notre compréhension du développement de la perméabilité dans le conduit, nous avons cherché à éclaircir le lien entre perméabilité, conditions d'écoulements, et caractéristiques géométriques du réseau de bulles connectées. Nous proposons une formulation du seuil de percolation, moment exact où le magma devient perméable compatible avec un grand nombre d'échantillons naturels et expérimentaux. Nous présentons aussi une nouvelle loi de perméabilité en accord avec la plupart des observations existantes, que nous avons intégrée à notre modèle 2D de dégazage. Nos résultats montrent qu'en fonction du nombre de bulles dans le magma et de la distribution de leurs tailles, l'importance des pertes en gaz et par conséquent les conditions d'écoulement dans le conduit varient d'effusives à explosives.

Enfin, afin d'évaluer l'utilité des données de déformation pour suivre l'évolution des conditions d'écoulement, nous utilisons des modèles d'écoulement simples couplés à de la déformation élastique en 3D pour retrouver la déformation observée au sommet du Merapi peu avant l'éruption de 2006. Bien que ces modèles permettent de mieux comprendre les déplacements observés, le peu de données, associé à la complexité géologique et rhéologique du sommet, ainsi qu'à celle des processus physiques intervenant dans le conduit font qu'il est difficile de contraindre les conditions d'écoulement grâce à la déformation dans ce cas précis.

Mots clefs

Volcan andésitique, Écoulement du magma, Dégazage, Perméabilité, Déformation de surface, Merapi, Modélisation numérique

Evolution of magma flow and degassing conditions in the upper conduit at andesitic volcanoes: insights from numerical modelling

Abstract

At silicic volcanoes, such as Mount St Helens (United States), Montserrat (British West Indies), or Merapi (Indonesia), periods of relative quiescence, with lava flows and dome emplacement, alternate with explosive, sometimes very violent events. Forecasting the effusive/explosive transitions, which is essential for the safety of nearby populations, remains currently a real challenge. However, experimental as well as field observations provide evidence that magma gas content is a major clue for understanding explosivity. This thesis, based on numerical simulations, experimental samples analysis, as well as on the interpretation of ground deformation data recorded at Merapi volcano, aims at improving our understanding of gas loss evolution, and its impact on the eruptive regime.

A major part of this work consisted in developing and improving 2D axisymmetric conduit flow models for integrating gas loss in transient conditions. We provide a time-dependent model for gas flow in the upper conduit, that accounts for gas loss both at the conduit walls and at its top, depending on conditions in the surrounding rock and dome. We also propose an adaptation of conduit flow models allowing for full coupling between magma and gas flow in 2D that should be used to further investigate flow conditions evolution during transient regimes. From time-dependent gas flow simulations in the case of an effusive dome emplacement, we identify controlling parameters for gas loss. Our results provide evidence that gas loss is extremely sensitive to the evolution of magma permeability and of pressure gradients around the conduit due to dome loading, whereas, contrary to the common idea, dome permeability has almost no influence. Along with dome growth, gas loss decreases at depth, thus causing an increase in the magma gas content. At the top of the conduit, this results in an increase in gas pressure by a few tens of MPa, thus increasing the likelihood of magma explosivity and hazard in the case of a rapid decompression due to dome collapse.

Although magma permeability plays a major role for gas extraction, as revealed by our results, its evolution within the conduit is poorly constrained. Currently used permeability laws fail in reassembling the whole dataset of permeability measurements from natural and experimental silicic samples. In order to improve our understanding of permeability development in the conduit, we worked on linking permeability and flow conditions with geometrical parameters that characterise the connected bubble network, based on experimental samples analysis. We propose an expression for the percolation threshold, i.e. the very moment when magma becomes permeable, that succeeds in classifying a wide dataset of natural and experimental samples. We also develop a new permeability law that reassembles most of the existing observations, and implement it within our gas flow 2D model. Results show that depending on the number of bubbles within the magma and on their size distribution, gas loss and then magma flow conditions evolve from effusive to explosive conditions.

Eventually, we evaluate the applicability of monitoring flow conditions from observed ground deformation by using simplified conduit flow models, coupled with elastic deformation in 3D, to interpret ground deformation recorded in the near field at Merapi a few days before the 2006 eruption. Although conduit flow models provide important clues for interpreting observed displacements, the sparsity of field observations together with the complexity of the volcano summit geology, rheology and processes happening in the conduit make it very complex to constrain flow conditions from observed deformation.

Key words

Andesitic volcano, Magma flow, Gas loss, Permeability, Ground deformation, Merapi, Numerical modelling

Remerciements / Acknowledgments

Ces quelques pages de mon manuscrit de thèse auront sans doute été les plus difficiles à rédiger. C'est sans doute parce que lorsque l'on souhaite remercier, les mots ne suffisent jamais.

First, I would like to thank Alison Rust and Antonio Costa, who both accepted to review this manuscript and to evaluate my research work. Thanks also to Claude Jaupart, Henri-Claude Nataf, and François Beauducel who accepted to be part of the Jury.

Je continue en français, pour plus de simplicité. Lorsque je suis arrivée au labo d'ISTerre à Chambéry pour commencer cette thèse, on m'a dit que j'avais la chance d'être encadrée par "les deux mamans du labo". C'est vrai, j'ai eu deux directrices de thèses formidables ! Je voudrais dire un très grand merci à Virginie Pinel et à Marielle Collombet, pour leur disponibilité, leurs conseils, leur soutien et leur aide pendant ces trois années et demie. Merci aussi pour la confiance que vous m'avez accordée, pour votre compréhensivité, et pour votre joie à l'annonce de mon mariage, puis à celle de ma grossesse. Je souhaiterais remercier Virginie en particulier pour m'avoir proposé ce sujet de thèse, qui s'est montré captivant et a su éveiller ma curiosité même lorsque j'avançais plus lentement que je ne l'aurais espéré. Merci aussi pour ton calme, particulièrement ces fois où je suis venue dans ton bureau en déclarant "j'ai fait un énorme bourde". Marielle, un merci particulier à toi pour ton soutien dans les galères comsol. Merci aussi pour ces heures de terrain partagées à encadrer les étudiants ... mes premières heures d'enseignement !, et pour tes conseils à ce sujet.

J'aimerais ensuite remercier Alain Burgisser, avec qui j'ai pu collaborer quelques semaines ... qui se sont transformées en quelques mois ! Quand la science passionne, on ne compte pas ! Merci pour ta bienveillance et ton enthousiasme. Merci aussi pour ta patience ! Au labo il existe un mythe, celui de "la fois où Alain s'est énervé" (je ne donnerai aucun nom). Merci aussi pour ton intérêt pour mon travail, et pour les discussions enrichissantes que nous avons partagées.

Un grand merci à François Beauducel, qui m'a guidée dans mon travail sur la déformation du Merapi. Merci pour ta disponibilité, malgré la distance, que ce soit lorsque tu étais à Paris ou maintenant en Indonésie. Merci aussi pour ton accueil à Yogyakarta et pour m'avoir fait découvrir les conditions réelles du terrain en Indonésie. Merci également à Yanti pour sa gentillesse !

Je voudrais aussi remercier David Cébron, pour son aide et son soutien dans mes bras de fer contre Comsol. Merci pour tes conseils, ainsi que pour ton intérêt pour nos modèles de volcanologues !

Un merci supplémentaire à vous cinq, ainsi qu'à Hélène Massol, qui avez accepté de faire partie de mon comité de thèse. Merci pour votre intérêt et pour vos retours sur mon travail, ainsi que pour les discussions enrichissantes qui s'en sont suivies. Merci en particulier pour avoir su me conseiller de me réorienter lorsque c'était nécessaire.

Merci à tout le groupe du projet DOMERAPI, qui m'a fait découvrir dans un cadre plus vaste les différentes facettes de la volcanologie et la richesse du travail d'équipe. Merci en particulier à ceux que j'ai eu l'occasion de croiser sur le terrain, et à ceux qui m'ont enrichie de leurs discussions.

J'aimerais aussi remercier celles et ceux qui m'ont fait découvrir et aimer la géologie puis la volcanologie, et qui ont su me conseiller pour cheminer dans cette voie. Merci en particulier à Nuria Paraire.

Une thèse, c'est loin de n'être qu'un projet scientifique. Merci à tous ceux que j'ai croisés au labo de Chambéry. Merci pour la convivialité presque familiale que vous avez su y installer. J'aimerais en particulier remercier toute l'équipe de géophysique des volcans, pour les conseils et les discussions si intéressantes. Merci aux doctorants et aux stagiaires (et à Fabien !), pour toutes ces discussions sans rapport avec la recherche, et tous ces moments partagés, entre balades en pédalo, dégustations de hervémisus, confection de jiaozi et de maki, soirées crêpes et ski ! Merci en particulier à mes co-bureau, ceux qui m'ont accueillie : Anaïs, Aurore et Thomas, et ceux qui leur ont succédé : Zhenlu, Alexandre, Abdullah et Yaping. Merci également à tous les membres du labo, et de l'administration, avec qui j'ai partagé discussions et repas en cafét'. Merci à Olivier pour le soutien informatique, et à Fabien pour son aide et sa patience pour tout ce qui concerne les questions administratives ! Merci enfin à ceux que j'ai rencontrés à ISTerre Grenoble, en particulier les délégués étudiants 2013-2015 !

Au delà de la vie au laboratoire, cette thèse représente pour moi aussi et surtout 3 ans et demi d'une vie bien remplie ! Je souhaiterais d'abord remercier mon mari, Augustin, pour son soutien sans faille. Merci d'avoir cru en moi quand je doutais, et d'avoir supporté mon stress et mes coups de blues sur la fin ! Merci aussi à notre bébé pour les coups de pieds d'encouragment me rappelant qu'il était temps d'y mettre un point final, à cette thèse ! Je voudrais ensuite remercier ma famille, pour leur présence pendant toutes ces années, et pour m'avoir accompagnée dans cette voie de la recherche. Merci également à ma belle-famille, pour sa joie et son accueil. Un grand merci aussi à tous mes amis, ceux de longue date, et ceux rencontrés ici grâce à qui quitter Chambéry ne sera pas facile ! Merci à Lucille, Antonin et Mathieu, qui ont accepté à la dernière minute de relire quelques pages, la qualité de ce manuscrit en a été enrichie ! Merci enfin à Celui sans qui tout cela n'aurait pas été possible.

Contents

Résumé français

Introduction

Les volcans à lave différenciée donc visqueuse, tels que le Merapi (Indonésie), le Mont St. Helens (États Unis) ou la Soufrière de Montserrat (Antilles), ont une activité qui alterne entre des phases effusives relativement calmes, lors desquelles le magma s'écoule et forme des coulées de lave ou un dôme, et des événements explosifs parfois très violents. Être capable de prévoir les transitions entre régime effusif et explosif est primordial pour pouvoir assurer la sécurité des populations voisines de ces volcans.

Aujourd'hui, les techniques utilisées pour quantifier les risques, et éventuellement décider de l'évacuation de la population, s'appuient sur des modèles empiriques basés sur l'observation de signaux précurseurs dans l'activité volcanique (sismicité, déformation, émissions de gaz). Ces modèles ne sont cependant pas totalement fiables et ne permettent pas de prévoir chaque éruption. Il est donc important de mieux comprendre les processus physiques qui conduisent à ces transitions dans l'activité volcanique.

Les observations de terrain, ainsi qu'un grand nombre d'études expérimentales, montrent que l'explosivité du magma est étroitement liée à son contenu en gaz. Or lorsque le magma remonte dans le conduit, une partie du gaz contenu dans le magma peut être perdu aux parois, ou à la sortie du conduit. Selon l'importance de ces pertes et leur évolution au cours d'une éruption, l'activité volcanique peut évoluer entre des régimes effusifs et explosifs.

L'objectif de cette thèse est d'améliorer notre compréhension de l'évolution de ces pertes de gaz au cours d'une éruption, et son influence sur l'activité volcanique. Dans le chapitres 1, nous développons des modèles numériques permettant de simuler l'écoulement du magma et les pertes en gaz dans le conduit au cours d'une éruption. Nous utilisons ensuite ces modèles dans le chapitre 2 pour quantifier l'évolution possible des pertes en gaz dans le conduit lors d'un épisode effusif avec formation de dôme. Les chapitres 3 et 4 s'intéressent ensuite aux liens entre ces modèles de conduit et les observations. Dans le chapitre 3, l'étude du développement de la perméabilité dans des échantillons de magma rhyolitique hydratés et soumis à une décompression permet de mieux contraindre la perméabilité du magma utilisée dans les modèles. Dans le chapitre 4, nous interprétons la déformation observée en champ proche à Merapi avant l'éruption de 2006 à partir de modèles d'écoulement du magma dans le conduit. Enfin, dans le chapitre 5 nous proposons une adaptation des modèles de conduit qui permette de coupler l'écoulement du magma avec les pertes en gaz en régime transitoire.

Modélisation numérique en 2D de l'écoulement du magma et du dégazage dans un conduit éruptif

Les modèles d'écoulement en 2D proposés par Massol et al. (2001, 2009), Collier et al. (2006), et Collombet (2009) ont récemment montré l'importance de considérer la variabilité des propriétés du magma en géométrie 2D axisymmétrique, pour modéliser l'écoulement d'un magma visqueux dans le conduit éruptif. Dans ce chapitre, nous présentons des modéles en axisymmétrie permettant d'étudier l'évolution des conditions d'écoulement du magma et du gaz dans le conduit, ainsi que la déformation associée à ces conditions d'écoulement.

Le modèle d'écoulement du magma utilisé dans cette thèse s'appuie sur l'hypothèse que les mouvements des bulles et des cristaux sont négligeables dans le magma, ce qui est valable pour des magmas très visqueux. Dans ce cas, le magma peut être assimilé à une phase unique, dont les propriétés (densité, viscosité dynamique et de volume, compressibilité) dépendent des proportions et des intéractions des phases liquide (melt), solide (cristaux) et gazeuse (bulles). Ces propriétés sont données par des lois empiriques déduites de l'étude expérimentale d'échantillons de magma ou de matériaux analogues. Nous comparons les solutions d'écoulement du magma obtenues avec ce modèle à celles de modèles précédents, et présentons également l'influence des principaux paramètres du modèle (fraction massique d'eau, quantité de cristaux, diamètre du conduit) sur cette solution.

Nous nous intéressons ensuite à la prise en compte de la déformation élastique du conduit associée à l'écoulement. Nous montrons que cette déformation reste limitée pour des caractéristiques élastiques de l'édifice volcanique réalistes. Par ailleurs, cette déformation a peu d'effet sur les conditions d'écoulement du magma dans le conduit.

Enfin, nous développons un modèle permettant de suivre l'évolution des conditions de dégazage dans le conduit pour des conditions éruptives qui évoluent dans le temps. Ce modèle résout une équation de conservation de la masse pour le gaz en chaque point du conduit, qui prend en compte l'écoulement perméable (Darcy) du gaz, l'advection par le magma des bulles de gaz, et les échanges de volatiles entre les phases liquide et gazeuse du magma. Ce modèle permet de suivre l'évolution des conditions de dégazage au cours d'une éruption, ce qui fait l'objet du chapitre 2.

Nous montrons également dans ce chapitre que l'utilisation couplée des modèles d'écoulement du magma et du gaz proposés ici ne présente pas de solution réaliste, et ne permet pas l'étude de l'évolution des conditions d'écoulement du magma en régime transitoire. Cet aspect est abordé plus particulièrement dans le chapitre 5, où une adaptation des modèles est proposée.

Effets de l'emplacement d'un dôme sur les conditions d'écoulement du magma et du dégazage

Le modèle d'écoulement pour le gaz présenté dans le chapitre 1 dépend de paramètres liés aux conditions d'écoulement du magma (porosité, pression et vitesse du magma) mais également de conditions aux limites du conduit (pression et vitesse aux bords, sortie, base) qui évoluent au cours d'une éruption. L'évolution de ces paramètres peut alors affecter les conditions d'écoulement pour le gaz, et donc l'importance des pertes en gaz. Dans ce chapitre, nous testons l'influence de différents effets liés à la formation d'un dôme sur l'écoulement et les pertes en gaz dans le conduit.

La présence d'un dôme peut en effet causer, du fait de son poids, une augmentation de la pression dans le conduit et dans la roche encaissante. Dans le conduit, cette augmentation de pression peut conduire à une évolution des conditions d'écoulement du magma, pouvant affecter la perméabilité du magma et ainsi les pertes en gaz. Dans la roche encaissante, l'augmentation de pression peut aussi conduire à la fermeture de fractures, diminuant ainsi la perméabilité dans la roche, ce qui peut affecter les pertes en gaz aux bords du conduit. Enfin, la présence du dôme en haut du conduit empêche le gaz de s'échapper directement dans l'atmosphère, et peut donc affecter les pertes en gaz dans la partie supérieure du conduit. À partir de conditions initiales réalistes d'écoulement effusif du magma (Collombet, 2009), nous considérons la construction progressive d'un dôme de lave, et testons chacun de ses effets possibles sur les pertes en gaz dans le conduit.

Nos résultats montrent que les pertes en gaz dans le conduit éruptif dépendent principalement de la perméabilité du magma, et des conditions de pression et de perméabilité dans la roche encaissante. La perméabilité du dôme a quant à elle très peu d'influence. Nous montrons également que, au cours de la formation du dôme, les pertes en gaz diminuent en profondeur. Les espèces volatiles (eau) restent donc plus longtemps dans le conduit, ce qui conduit à une augmentation du contenu en gaz et de la pression en gaz en haut du conduit. Cette évolution est associée à une augmentation de l'aléa volcanique.

Cette étude fait l'objet d'un article (Chevalier et al., 2017) publié dans le Journal of Volcanology and Geothermal Research.

Dévelopement et évolution de la perméabilité du magma dans le conduit

L'étude des effets de la formation d'un dôme sur les conditions de dégazage dans le conduit a mis en évidence l'importante influence de la perméabilité du magma sur les pertes en gaz. En effet, le gaz ne peut s'échapper du magma que si celui-ci est perméable. Il est alors important de bien contraindre la perméabilité du magma utilisée dans les modèles de conduit.

Dans les modèles présentés ici, nous avons utilisé une loi empirique reliant la perméabilité à la porosité du magma (Klug and Cashman, 1996), basée sur des mesures de perméabilité pour des échantillons de magma du volcans à lave visqueuse. Parmi les échantillons de magma provenant de volcans à laves visqueuses, on trouve cependant des relations entre perméabilité et porosité très dispersées, et qui ne suivent pas la même tendance que celle représentée par la loi que nous avons choisie. Ces mesures très dispersées ont donné lieu à une grande diversité de loi reliant perméabilité et porosité du magma. Choisir une de ces lois de perméabilité pour nos modèles revient à ne pas prendre en compte une part importante des données.

Afin de mieux comprendre cette diversité de relations perméabilité-porosité et de mieux contraindre la perméabilité du magma dans le conduit, nous étudions, dans le chapitre 3, le développement de la perméabilité dans un liquide rhyolitique en décompression. Nous utilisons pour cela des échantillons de composition rhyolitique réhydratés, qui ont été décompressés puis scannés par micro-tomographie aux rayons X. Nous avons alors accès à la perméabilité des échantillons et aux caractéristiques de leur réseau de bulles. Notre objectif est de mieux comprendre le développement de la perméabilité à partir de l'étude des caractéristiques de ce réseau de bulles. En effet, la perméabilité du magma se développe en grande partie par coalescence de bulles, processus qui est affecté par l'organisation du réseau de bulles.

Nous montrons d'une part que la percolation, c'est à dire le dévelopement d'une perméabilité dans le magma, peut-être déterminée à partir d'un paramètre qui dépend de la distance entre les bulles et de la dispersion de leur distribution de taille. Lorsque ce paramètre dépasse une valeur seuil, le magma devient perméable à l'écoulement du gaz. Nous proposons une valeur pour le seuil de percolation qui permet de classer correctement 88% d'un large panel d'échantillons.

En utilisant ce paramètre, ainsi que d'autres observations sur les liens entre les différentes charactéristiques du réseau de bulles connectées, nous proposons également une simplification de la loi de Degruyter (2010), qui peut être utilisée dans un modèle de conduit. La loi de perméabilité obtenue permet d'expliquer la diversité des relations entre perméabilité et porosité observées dans les échantillons naturels, et donc d'unifier les lois déjà existantes. Elle permet également de prédire correctement la perméabilité d'une grande variété d'échantillons. Cette loi prend également en compte la déformation des bulles, qui dans un écoulement de conduit est liée au nombre capillaire des bulles.

Nous intégrons ensuite cette loi de perméabilité dans deux modèles de conduit afin de tester son influence sur la modélisation du dégazage et des conditions d'écoulement dans le conduit. Pour chacun des deux modèle, nous varions les valeurs des paramètres de distance entre les bulles et de la dispersion de la taille de bulles. Cela affecte l'évolution de la perméabilité en fonction de la porosité en modifiant d'une part la valeur seuil de porosité à partir de laquelle le magma est perméable, mais aussi l'évolution de cette perméabilité avec la porosité.

Le premier modèle utilisé est le modèle 1D de Kozono et Koyaguchi (2009), modifié d'après Degruyter et al. (2012). Les résultats obtenus avec ce modèle montrent que les variations de perméabilité dans le conduit affectent peu le régime éruptif. Cependant, ce modèle considère uniquement l'écoulement vertical du gaz, or nous avons montré dans le chapitre 2 qu'une majeure partie du gaz perdu dans le conduit s'échappait horizontalement dans la roche encaissante.

Le deuxième modèle utilisé est le modèle d'écoulement du gaz présenté dans le chapitre 1 et utilisé dans le chapitre 2. Les résultats obtenus avec ce modèle montrent cette fois une influence importante des variations de perméabilité dans le conduit sur les pertes en gaz. En fonction de la distance entre les bulles et de leur dispersion de taille, le régime éruptif évolue entre des régimes effusifs et explosifs. Dans ce deuxième modèle, l'influence de la déformation des bulles est également testée. La déformation des bulles cause l'apparition d'une forte anisotropie dans la perméabilité du magma. Notre loi est cependant basée sur un faible nombre d'échantillons déformés, et d'autres études incluant la déformation des bulles seraient nécessaires pour valider ces résultats.

Interprétation de la déformation observée en champ proche à Merapi avant l'éruption de 2006

L'objectif de ce chapitre est d'estimer comment les informations obtenues grâce aux modèles de conduit permettent de mieux interpréter les observations de l'activité volcanique. Ce projet de thèse fait partie du projet ANR DOMERAPI, qui vise à améliorer l'instrumentation et la récupération de données à Merapi, pour mieux comprendre l'activité volcanique observée sur ce volcan. Dans le cadre de ce projet, nous nous sommes intéressés à la déformation observée en champ proche à Merapi, qui peut être affectée par l'évolution des conditions d'écoulement dans le conduit éruptif. Le but ici était de tester comment cette déformation observée permet de retrouver les conditions dans le conduit, pour permettre de surveiller l'évolution des conditions dans le conduit, et donc d'anticiper l'évolution du régime éruptif.

Nous utilisons ici des données de déformation GPS relevées peu avant l'éruption de 2006, en champ proche, que nous interprétons grâce à des modèles de conduit. Nous considèrons ici un écoulement simple de type plug : il s'agit de l'écoulement d'un magma incompressible et de densité constante, dont la viscosité augmente de façon importante dans une couche (quelques dizaines de mètres d'épaisseur) en haut du conduit. Cette couche visqueuse est appelée plug, et représente du magma dégazé et refroidit en haut du conduit. Connaissant les conditions de pression et de cisaillement aux bords du conduit associées à cet écoulement, nous appliquons ces contraintes à la roche encaissante, considérée comme élastique.

Nos résultats montrent que l'utilisation d'un modèle d'écoulement dans le conduit permet de retrouver et d'expliquer une grande partie de la déformation observée, avec des conditions dans le conduit qui sont réalistes, contrairement à ce que permet dans ce cas précis un modèle de Mogi. Une partie de la déformation reste cependant mal représentée par ce modèle de conduit. Le sommet de l'édifice du Merapi a une géologie et une rhéologie complexe, qui peuvent affecter de façon importante les observations de déformation. Pour tester l'influence de la prise en compte de cette rhéologie complexe, nous ajoutons au modèle une zone plus déformable dans l'édifice, qui correspond à une zone de faille observée sur le terrain. Les résultats en utilisant cette zone plus déformable se rapprochent de façon significative de la déformation observée.

Bien que les modèles de conduit permettent de mieux comprendre les déplacements observés, le peu de données, associé à la complexité géologique et rhéologique du sommet, ainsi qu'à celle des processus physiques intervenant dans le conduit font qu'il est difficile de contraindre les conditions d'écoulement grâce à la déformation dans ce cas précis. L'utilisation de la déformation en association avec d'autres observations devrait être envisagée à l'avenir pour mieux contraindre l'interprétation des données.

Modélisation couplée des écoulements du magma et du gaz en régime transitoire

Dans le chapitre 2, nous avons montré que la présence d'un dôme causait des variations significatives de la pression du gaz dans le conduit, et des pertes en gaz. Ces variations du contenu en gaz dans le conduit auront un impact sur les conditions d'écoulement global du magma. Afin de mieux étudier l'évolution des conditions dans le conduit au cours d'une éruption, il est alors important de pouvoir coupler complètement ces deux modèles.

Le couplage des modèles actuels ne permet pas d'étudier cette évolution dans le temps, comme montré dans le chapitre 1. Cela est dû aux hypothèses sur la pression du magma et du gaz utilisées dans ces deux modèles, qui ne sont pas compatibles. Dans ce dernier chapitre, nous proposons une adaptation des modèles, qui permet de prendre en compte la différence de pression entre le magma et le gaz dans le modèle d'écoulement du magma. Cette adaptation consiste à modifier, dans l'équation de conservation de la quantité de mouvement résolue pour le magma global, l'expression de la pression globale du magma. Plutôt que de faire l'hypothèse que cette pression est égale à celle de la phase incompressible, comme c'était le cas à présent, nous utilisons ici une moyenne pondérée par la porosité de la pression du gaz et de la pression dans la phase incompressible, semblable à celle utilisée dans les modèles diphasiques de Bercovici et al. (2001) et de Michaut et al. (2009).

Conclusion

Dans cette thèse nous avons montré que les pertes en gaz dans le conduit se font principalement aux bords du conduit, où le gaz s'échappe dans la roche encaissante. Nous montrons que l'importance de ces pertes dépend principalement des conditions de perméabilité et de pression dans la roche, mais également de la perméabilité du magma dans le conduit, ces paramètres contrôlant l'écoulement du gaz vers les bords du conduit puis vers la roche. Afin de pouvoir comprendre encore mieux l'évolution des conditions dans le conduit au cours d'une éruption, nous proposons une adaptation des modèles permettant d'étudier l'évolution de l'écoulement du magma en régime transitoire. Nous avons par ailleurs travaillé à mieux contraindre le développement de la perméabilité du magma dans le conduit, paramètre entrant du modèle, à partir d'observations expérimentales. Nous proposons une loi de perméabilité qui ré-unifie une part importante des observations pour les volcans à lave visqueuse, et qui est utilisable dans nos modèles. Nous montrons enfin que les modèles de conduit permettent de mieux comprendre la déformation observée en champ proche, bien que l'interprétation de ces signaux reste limitée par la complexité de l'édifice volcanique.

Introduction

Volcanic activity and hazard around the world

More than 600 active volcanoes have been identified over the world. Extending the list to volcanoes that have been active during the last 10 000 years, this number rises to more than 1500 (fig. 1), though remaining highly underestimated, considering that most of volcanoes are undersea. Although the major part of currently active volcanoes is located in distant areas and therefore has little impact on the population, a significant number of highly active volcanoes rises in densely populated areas and has caused millions of fatalities over the years. Hazard associated with volcanic activity can be classified into several groups:

- lava flows (e.g. Nyiragongo 1977 eruption, Democratic Republic of the Congo, Mt. Etna, Italy, Kilauea Volcano, Hawaii),
- volcanic bombs and ash fallouts (e.g. Vulcan and Tavurvur volcanoes 1944 eruption, New Guinea, Stromboli, Italy, ash clouds from the Eyjafjallajökull 2010 eruption, Iceland),
- gas emissions (e.g. Lake Nyos 1986 - 1700 fatalities, Cameroon),
- pyroclastic flows (e.g. Mount Vesuvius AD 79 - destruction of Pompei -, Italy, Montagne Pelée 1902 eruption - 30 000 fatalities -, Martinique, West Indies),
- lahars (Nevado del Ruiz 1984 - 24 000 fatalities -, Colombia),
- landslides (Mount St Helens 1980, United States, Merapi, Java, Indonesia),
- tsunamis (Santorini AD 1600, Greece, Mount Unzen 1792 - 15 000 fatalities -, Japan, Krakatau 1883 - 37 000 fatalities -, Java, Indonesia).

Despite important hazard, volcanoes have fascinated populations for centuries and sometimes were even at the origin of cultural mythology and beliefs. Millions

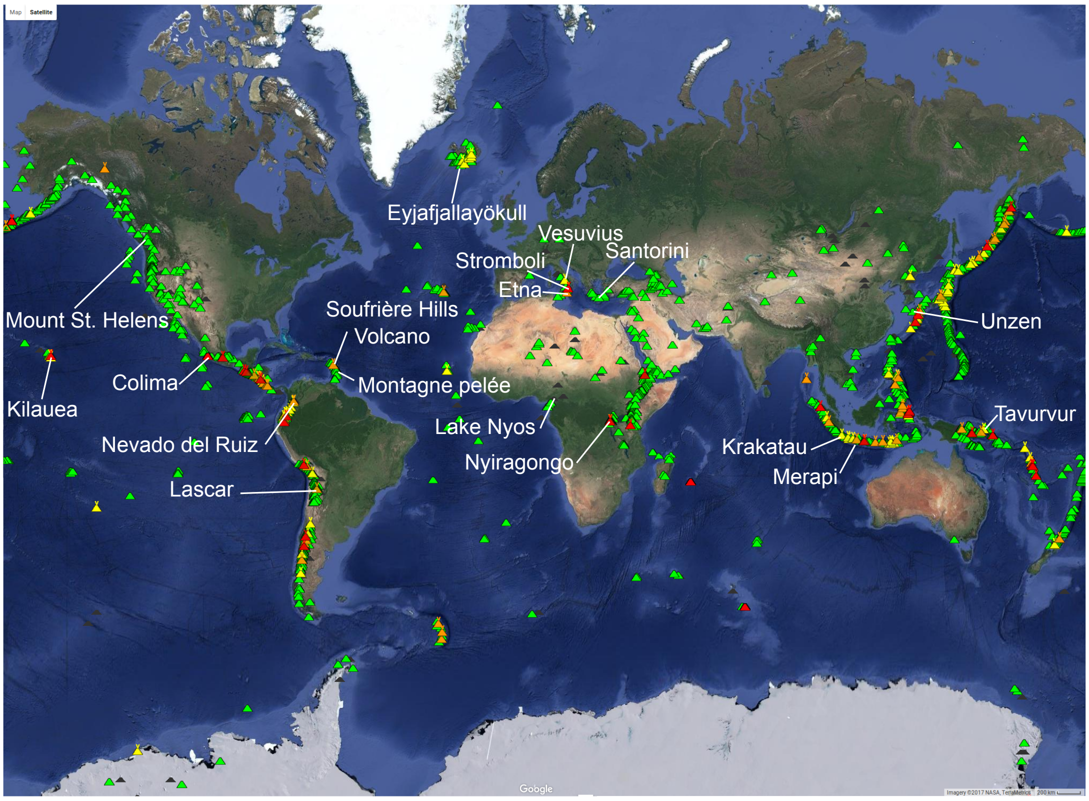

Figure 1: Active volcanoes in the world (from https://www.volcanodiscovery.com/volcano-map.html). Volcanoes that currently present volcanic activity are represented with yellow, orange and red triangles, corresponding to increasing activity intensity. Volcanoes currently quiescent are represented with green triangles.

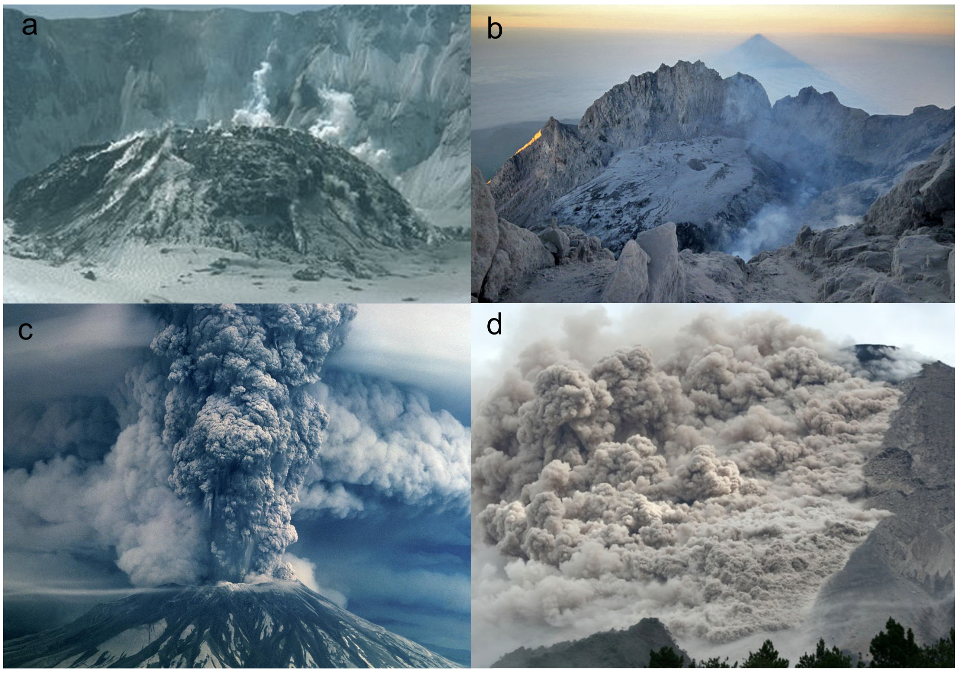

Figure 2: Examples of volcanic activity at silicic volcanoes. (a)Mount St Helens lava dome, 1983 (credit R. Symonds). (b) Merapi lava dome, 2012 (credit D. Berendes). (c) Plinian eruption of the Mount St Helens, 1980 (credit R. Bowen). (d) Pyroclastic flows triggered by dome collapse at Merapi, 2006 (credit BPPTK).

of people still live on their flanks today, and volcanoes continue attracting tourists and arousing scientist's curiosity. Aside from being of great scientific interest, better understanding the volcanic activity and being able to anticipate its evolution towards violent events is of first importance for ensuring the nearby populations safety.

Andesitic volcanoes activity

Silicic volcanoes (e.g. Merapi, Indonesia, Unzen, Japan, Montagne Pelée, Martinique, Kelud, Indonesia, Mount St Helens, United States, Soufrière Hills Volcano, British West Indies, Colima, Mexico) are characterised by a volcanic activity that alternates between periods of relative quiescence, with lava flows and dome emplacement (fig. 2a and b), and explosive episodes that can be extremely violent (fig. 2c). Transitions between these effusive and explosive regimes however remain almost impossible to forecast today. Moreover, even during effusive periods, dome destabilisation and collapse often trigger pyroclastic flows that can be devastating (fig. 2d).

Many of these volcanoes are located in densely populated areas (fig. 1). For the nearby populations safety, being able to anticipate the evolution of the eruptive regime is therefore of primary importance. The Merapi explosive eruption in 2010 lead to the evacuation of more than 350 000 people, in an area of 25km around the volcano. Pyroclastic flows generated during this eruption reached up to 17km from the volcano, and would have killed about 10 000 to 20 000 people if evacuation had not taken place (Surono et al., 2012). Similarly, the eruption of the Sinabung in 2013 forced about 30 000 people to evacuate, and about 100 000 were evacuated for the plinian explosion of the Kelud in 2014. Although field observations and geophysical signals show patterns that help preventing eruptions (Budi-Santoso et al., 2013; Kilburn, 2003) and deciding about evacuating people (Surono et al., 2012), empirical methods are not fully reliable (Arámbula-Mendoza et al., 2011; Boué et al., 2015), and lack of volcanic mechanisms comprehension. The evacuation during the Merapi 2010 explosive event was progressive, and based on the qualitative observation of a seismic activity by far more intense than that observed during previous eruptions (Surono et al., 2012; Budi-Santoso et al., 2013). Moreover, some explosive events at silicic volcanoes are not accompanied with clear precursors, such as phreatic explosions (e.g. Merapi 18 November 2013, Indonesia, Ontake 27 September 2014, Japan).

Being able to anticipate volcanic activity with reliability is not only important for forecasting explosions and evacuating people in time. It is also a condition for keeping populations trust and ensure that evacuation plans will be respected. Soundings after the 2010 Merapi eruption revealed that 50 to 70% of the displaced persons had return into the danger zone during the crisis (Mei et al., 2013). Improving anticipation of effusive to explosive transitions requires today to (1) better understand processes that happen in the volcanic system and how they evolve and may trigger explosive events, and (2) link these processes with geophysical signals that are recorded at volcanoes, in order to be enable monitoring of the volcanic activity evolution.

Conduit flow numerical modelling

During the last decades, numerical modelling has proven to be a powerful tool to get insights on processes that control volcanic activity. Although the first studies focused on conditions at the conduit's vent and their implication for the eruptive style (Walker et al., 1971; Wilson, 1976; Wilson et al., 1978), 1D conduit flow modelling rapidly appeared to be of first importance for understanding the eruptive conditions evolution (Wilson et al., 1980). First results highlighted the important role of the geometry of the conduit (Wilson et al., 1980), of the ascent rate (Woods and Koyaguchi, 1994), and of the magma gas content (Wilson et al., 1980; Jaupart and Allègre, 1991) for effusive/explosive transitions.

Conduit flow modelling then drew a lot of attention with the improving of instrumentation and data acquisition at volcanoes. The Soufrière Hills Volcano (Montserrat, British West Indies) current eruption, which started in 1995, has been the occasion of many observations, providing new information on shallow processes (Sparks and Young, 2002; Druitt and Kokelaar, 2002). In particular, data highlighted the importance of understanding conduit processes for interpreting geophysical signals, including shallow seismic activity (Voight et al., 2006; Neuberg, 2000), and the evolution of the volcanic activity (Voight et al., 1998; Sparks et al., 1998). A variety of 1D conduit flow models were then designed, exploring the role of microlite crystallisation (Sparks, 1997; Melnik and Sparks, 2005; Massol and Jaupart, 2009), overpressure build up (Sparks, 1997; Melnik et al., 2005), gas loss (Diller et al., 2006; Kozono and Koyaguchi, 2009), conduit deformation (Costa et al., 2009b; De' Michieli Vitturi et al., 2010), non-linear effects of magma rheology (Melnik and Sparks, 2005), and many other parameters. The increase in data collection and monitoring, especially at Soufrière Hills Volcano, Unzen (Japan), were a project of drilling through the volcanic conduit was carried on (Watanabe et al., 2008; Ikeda et al., 2008), and Mount St. Helens (United States), together with experimental studies brought new constraints on conditions in the conduit and on magma rheology, and models then gained in complexity and precision (Gonnermann and Manga, 2007). More recently, conduit flow models in 2D (Massol and Jaupart, 1999; Massol, 2001; Massol and Jaupart, 2009; Collier and Neuberg, 2006; Collombet, 2009) highlighted the importance of investigating 2D modelling for better capturing flow conditions evolution in the conduit, because of the complex magma rheology.

The role of gas, observations

In the meanwhile, data collected at andesitic volcanoes, together with experimental investigation, accumulated clues for the key role of gas in volcanic activity evolution. Gas emissions at several silicic volcanoes ((Sheldrake et al., 2016), Soufrière Hills Volcano (Watson et al., 2000; Edmonds et al., 2003), Santiaguito (Johnson et al., 2008), Galeras (Stix, 1993) and Lascar (Matthews et al., 1997)) were observed to be correlated with volcanic activity and geophysical signals. Anderson and Fink (1990) observed variations in the porosity of magma erupted during a dome forming event, at Mount St. Helens, correlated with extrusion rate variations. These observations provide evidence that the magma gas content, and gas loss conditions, are key for understanding volcanic activity at silicic volcanoes. The statistical observation of a correlation existing between explosions intensity and extrusion rate, which is thought to partly control degassing efficiency, corroborated this hypothesis. In addition, gas overpressure and degassing processes were invoked for interpreting pyroclastic flows importance (Sato et al., 1992; Sparks et al., 2002; Ritchie et al., 2002; Woods et al., 2002) and shallow seismicity source mechanisms (Voight et al., 2006; Neuberg, 2000), encouraging modelling of degassing processes in the upper conduit.

On another hand, experimental investigations on magma fragmentation provided evidence that magma explosivity is closely related to gas within the magma. Silicic magma indeed fragments when the strain rate to which it is submitted exceeds its tensile strength. At silicic volcanoes, this may occur when gas overpressure in bubbles, triggering bubble growth, becomes important, for example when the magma is submitted to rapid decompression. Experiments on fragmenting magma revealed that magma explosivity increases with increasing porosity (Spieler et al., 2004) and gas overpressure (Kueppers et al., 2006; Mueller et al., 2011), and decreases with increasing permeability, which allows gas to escape and accommodate overpressure (Spieler et al., 2004; Mueller et al., 2005, 2008). Understanding the evolution of the magma gas content in the conduit and during an eruption is therefore of first importance for understanding volcanic activity variations at silicic volcanoes.

Gas evolution at andesitic volcanoes

While ascending towards the surface, magmas undergo important decompression. Since the solubility of volatiles (water, carbon dioxide, sulfur, chlorine, fluorine) within the melt is pressure dependent, the magma becomes oversaturated, and bubbles nucleate (fig. 3). Bubbles then grow with further decompression, participating to the magma compressibility and highly non-linear rheology. The high viscosity of silicic magmas tends to inhibit this growth (Navon and Lyakhovsky, 1998; Lensky et al., 2002), possibly leading to gas overpressure build-up within the bubbles. In addition, gas exsolution triggers crystallisation of microlites, therefore increasing the magma incompressible phase (melt + crystals) viscosity (e.g. Szramek et al., 2006). At the top of the conduit, the highly porous and viscous magma, submitted to important decompression rates, may fragment in small particles, thus allowing gas expansion and magma explosive extrusion (fig. 3).

Effusive eruptions generally occur when magma has lost part of its gas before reaching the surface. The high viscosity of silicic magmas prevents the bubbles to rise through the melt. Gas therefore does not separate from the magma during its ascent towards the surface, unless a permeable network through the magma exist

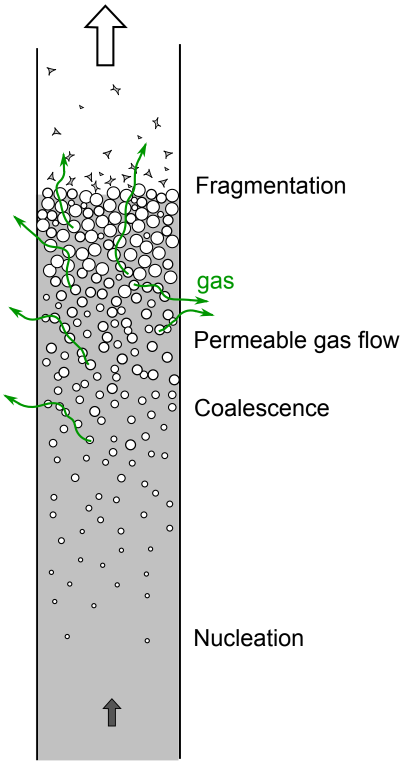

Figure 3: Sketch of the evolution of gas within the conduit.

and allows gas permeable flow. Such a permeable network can form due to bubble coalescence, as bubbles grow and interact with each other (Castro et al., 2012), or to magma fracturing at the conduit's margins (Holland et al., 2011; Lavallée et al., 2013). Gas then flows through this permeable network and may be lost at the conduit's margins, or at the top of the conduit, depending on surrounding conditions (fig. 3).

Modelling gas content variations in the conduit

Many conduit flow models aiming at understanding gas content variations in the erupting magma focused on the possibility for the gas to be lost during magma ascent. The main idea consists in assuming that incoming magma at the base of the conduit contains a constant amount of volatiles, and that the ability for this gas to be lost during magma ascent in the conduit controls the eruptive style. When conditions in the magma (permeability) and around the conduit (conditions in the country rock and at the top of the conduit) do not allow for gas loss, the system is said closed (fig. 4b), and magma erupts explosively. When gas loss is possible, the system is considered as open (fig. 4a) and depending on the importance of gas loss, magma might erupt effusively.

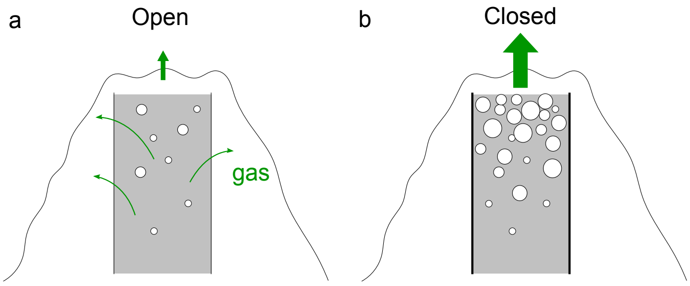

Figure 4: Sketch of (a) an open system, with possible gas loss at the conduit's edges and top, and (b) a closed system, in which gas cannot escape in the country rock.

The first conduit flow models that integrated gas loss in the conduit considered either vertical (e.g. Kozono and Koyaguchi, 2009) or horizontal gas loss (e.g. Jaupart and Allègre, 1991; Woods and Koyaguchi, 1994; Melnik and Sparks, 1999). They provided evidence that the eruptive style depends on the magma initial volatile content, but also on the magma extrusion rate and conduit's radius. Diller et al. (2006) considered both vertical and horizontal gas loss, and provided evidence that such magma degassing may account for the formation of a plug (gas depleted, viscous layer at the top of the conduit) and for the cyclic extrusion rate variations observed at the Soufrière Hills Volcano. More recently, Collombet (2009) modelled magma flow in 2D, accounting for gas loss in both vertical and horizontal directions. Results provide evidence for the formation, in steady-state effusive conditions, of gas depleted layers both at the top of the conduit and at its walls. The presence of these low porosity layers may prevent further degassing, and highlight the importance of 2D modelling for understanding degassing processes in the conduit.

Some other numerical models focused on the development of gas overpressure in the magma, including the role of magma stiffening due to microlite crystallisation (Sparks, 1997; Melnik and Sparks, 2005; Massol and Jaupart, 2009). More recently, Michaut et al. (2013) proposed a 1D numerical model that focuses on the interplay between bubble growth and gas segregation by magma compaction. Their results show that the competition between gas expansion and magma compaction causes the formation of periodic gas waves. These gas waves, rising through the conduit, may be another cause for the cyclic extrusion of magma at the top of the conduit, in agreement with observations at the Soufrière Hills Volcano.

The observation of important gas composition and emission variations associated with major explosive events also lead to consider some specific, deeper processes for magma gas content variations. These processes consider possible important variations in the volatile budget of magma ascending in the conduit. Major explosive events at Merapi, such as the 2010 eruption, were first explained by the possible assimilation, at depth, of large amounts of surrounding calcareous rocks, thus rising the magma CO_2 content (Deegan et al., 2010; Troll et al., 2013a; Borosiva et al., 2013). These large CO_2 amounts, together with the low solubility of carbon dioxide in silicic magmas, may have triggered transitions to explosive regime. Recent studies however tend to demonstrate that the specific event of 2010 may have rather been caused by hot, volatile–rich supply of basaltic magma in the storage system (Drignon et al., 2016). The interaction between this hot volatile–rich magma and the silicic stored magma may have triggered important gas exsolution and magma remobilisation, then leading to the explosive event (Huppert and Woods, 2002; Drignon et al., 2016). The role of basaltic volatile–rich magma supply in triggering transitions to explosive regimes had also been invoked for explaining major events at Montserrat (Murphy et al., 2000; Christopher et al., 2010). Based on the observation of high sulfur emissions variations at Montserrat, Christopher et al. (2015) recently proposed that magma and gas could decouple at depth, forming melt and gas layers in storage reservoirs. The destabilisation of these layers would be another mechanism for triggering explosive events, with variable proportions of melt and gas.

Objectives

In this thesis, we focus on gas variations caused by gas loss during magma ascent within the upper conduit. We develop a 2D conduit flow model for studying gas loss evolution during transient regimes, and its implications for magma flow conditions. We assume that magma can be considered as a single compressible phase, whose properties depend on the proportions and interactions of the liquid (melt), gas (bubbles) and solid (crystals) phases. For the model simplicity, and because we concentrate on controls on gas loss, we neglect microlite crystallisation, and assume that water is the only volatile present in the magma. Gas flow within the magma is then solved in the conduit, and takes into account gas permeable flow through the magma in both horizontal and vertical directions, bubble advection by the magma, and water exchanges between the melt and gas phases. We aim at identifying the processes that control gas flow, and to quantify their relative importance for gas loss evolution along with an eruption. We also study the translation of conduit flow conditions in terms of ground deformation, and evaluate their usefulness for eruption forecasting and monitoring.

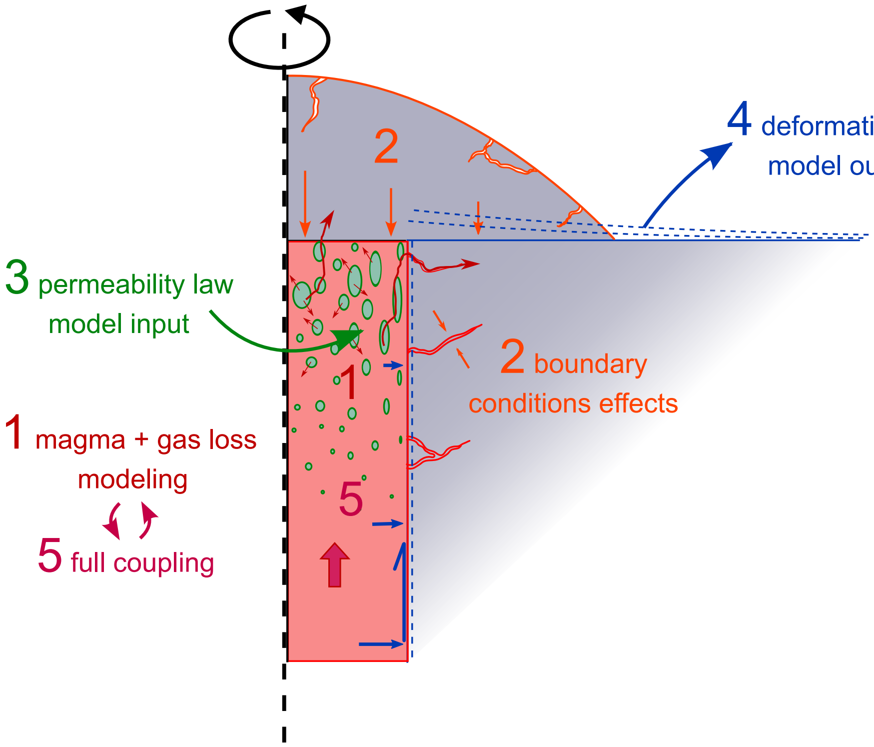

Figure 5: Synthetic sketch of the objectives and interactions of the different chapters. the 1-5 numbers correspond to the chapters' numbers.

Outline

Chapter 1 The steady-state effusive solution for magma flow in the conduit proposed by Collombet (2009), which takes into account gas flow in both horizontal and vertical directions, highlighted the importance of using 2D numerical modelling for studying degassing conditions in the conduit. Her results indeed provide evidence for the formation of low vesicularity layers both at the top of the conduit conduit and at its edges. The presence of such layers, which cannot be captured in 1D conduit flow models, may prevent for further degassing and play a significant role in degassing conditions evolution. Here, we therefore carry on using 2D numerical models. The model from Collombet (2009) is however not suitable for studying transient regimes, since it is built on steady-state resolution mechanisms. In the first chapter, we propose a time-dependent model for gas flow in the upper conduit that can be used for studying the evolution of degassing conditions along with an eruption (fig. 5). We also provide a full description of the numerical models we use for magma and gas flow modelling in 2D in the upper conduit.

Chapter 2 In the second chapter, we evaluate the sensitivity of gas flow to several parameters that may evolve along with an eruption, taking the example of a dome emplacement (fig. 5). Dome forming eruptions are common at andesitic volcanoes. Although relatively quiescent, they can precede much more explosive episodes. In addition, dome collapses, often triggered by gravitational instabilities, are associated with pyroclastic flows whose importance and hazard depend on the volume of the dome involved, but also on the gas pressurisation within the magma present in the dome and in the upper conduit. Modelling gas loss evolution during a dome emplacement and its consequences for the eruptive activity is therefore important for anticipating hazard evolution with dome formation. We test separately the influence on gas loss of several parameters (dome permeability, conditions in the conduit, country rock permeability, pressure in the country rock) that may evolve with dome growth, and quantify their relative importance for flow conditions and hazard evolution. This work was the object of an article (Chevalier et al., 2017), published in the Journal of Volcanology and Geothermal Research, that is attached to this chapter.

Chapter 3 In the third chapter, we study in greater details the development of permeability within the conduit, and its influence on gas loss. From the analysis of natural silicic samples, we develop a new permeability law for conduit flow modelling that unifies permeability observations on silicic experimental and natural samples, and accounts for bubble deformation in the conduit. We then integrate this new permeability law into conduit flow modelling (fig. 5), and show that depending on the characteristics of the bubble population in the conduit, gas loss, and then eruptive conditions may evolve from effusive to explosive conditions. This work was the object of an article (Burgisser et al., 2017), currently in revision for publication in Earth and Planetary Science Letters, that is attached to this chapter.

Chapter 4 In the fourth chapter, we evaluate the applicability of monitoring conduit flow conditions from ground deformation. We here use simple conduit flow models to interpret ground deformation observed in the near field at Merapi volcano before the 2006 eruption (fig. 5). The Merapi is an andesitic volcano that has been extremely active for the past three centuries and is actually considered as one of the 10 most dangerous volcanoes worldwide. After the 2010 eruption, that caused 367 fatalities and the evacuation of more than 350 000 people, the ANR project DOMERAPI has worked on improving instrumentation and data collection at Merapi. This project aims at better understanding processes happening at the volcano, in order to improve forecasting of future eruptions. As part of this project, we particularly aim at linking conduit flow conditions with available geophysical signal. Kinetic GNSS data collected at the Merapi summit before the 2006 eruption provide a unique opportunity for estimating the sensitivity of observed ground deformation to conduit conditions.

Chapter 5 The final chapter proposes an adaptation of magma and gas flow models so that magma and gas flow can be fully coupled (fig. 5). This new model aims at improving modelling of conduit flow conditions evolution during transient regimes.

Chapter 1

2D numerical modelling of magma flow and degassing in the upper conduit

Contents

1.1 Introduction

Andesitic magma is composed of a liquid (melt), a solid (crystals) and possibly a gas (bubbles) phase. These three phases interact with each other and result in a complex magma rheology. Because of the complexity of these interactions, and for flow modelling simplicity, magma flow conditions have generally been modelled using either a two–phase (gas + (liquid and crystals)), or a one–phase assumption. These assumptions are valid in andesitic magma because of the high magma viscosity. Two–phase models present the advantage of considering separately the gas and the compressible phase of the magma, which reveals useful when working on gas extraction issues (e.g. Michaut and Bercovici, 2009; Michaut et al., 2013). It has therefore been used in several 1D conduit flow models, however its application to 2D conduit flow modelling is very complex. Aiming at studying magma and gas flow in 2D, we here rather use a one–phase assumption for calculating bulk magma flow, and solve gas flow through the permeable magma in a second time.

A similar numerical model has been designed by Collombet (2009), for studying steady–state effusive flow conditions. This study provided evidence of the importance of 2D modelling for studying gas loss in the upper conduit. It is however not suitable for transient regimes, as magma and gas flow are always assumed to be at steady–state, and convergence is reached by iterative calculation. In order to study transient regimes, we need to integrate time–dependence into magma and gas flow modelling.

In this chapter, we also review some advances that have been made for modelling magma rheology and detail the magma and gas flow models we use in the following chapters. We quantify the influence of several parameters, such as magma composition and conduit geometry on magma flow conditions. We also propose a time–dependent model for gas flow in the upper conduit, that is suitable for studying gas loss evolution along with an eruption.

1.2 Magma composition

1.2.1 Chemical composition and texture

Andesitic composition was first defined after lavas erupting in the Andes. Many andesitic volcanoes are located in subduction arcs (e.g. Andes, Indonesia, Japan). Magmas of andesitic composition are formed by differentiation of more basaltic primary material. These differentiation processes involve differential crystallisation: part of the initial magma stored in magma reservoirs crystallises and separates from the remaining melt, and assimilation of crustal material. They are characterised by a weight fraction in silica (SiO_2) ranging from 52 to 63wt% (e.g. Matthews et al., 1999; Nakada and Motomura, 1999; Andreastuti et al., 2000; Savov et al., 2008; Blundy et al., 2008; Barclay et al., 2010; Coombs et al., 2013; Christopher et al., 2014; Sheldrake et al., 2016). They also are often water rich, with a water weight fraction in the melt of up to 7wt% (e.g. Matthews et al., 1994; Barclay et al., 1998; Martel et al., 2000; Blundy and Cashman, 2005; Scott et al., 2012; Erdmann et al., 2016), because of water supply from the subducted slab to the overlying melting mantle. Aside from silica and water, andesitic magmas mainly contain aluminium (Al_2O_3), iron (FeO), calcium (CaO), magnesium (MgO) and sodium (Na_2O) (table 1.1).

Andesitic magmas are composed of (1) a liquid phase, that includes dissolved volatiles, hereafter called melt, (2) a solid phase, made of crystals and (3) a gas phase, when specific conditions are reached. The proportions of these phases, described in the following sections, vary with magma composition and history.

	Bulk composition			Residual melt composition			
Volcano	Redoubt (1)	Colima (2)	Merapi (3)	Redoubt (1)	Colima(2)	Montagne Pelée (4)	Soufrière Hills (5)
SiO_2	57.50–62.45	59,10–60,89	51.83–55.84	66.57–79.57	72.48–74.26	70.98	78.66
TiO_2	0.58–0.65	0,60–0,62	0.79–0.83	0.12–0.69	0.59–0.67	0.24	0.39
Al_2O_3	17.86–18.99	17.45–17.93	18.43–19.20	10.92–15.79	12.89–13.21	16.19	11.2
FeO	4.92–6.78	5.72–6.13	(8.56–9.20)	0.27–4.21	2.14–2.86	2.28	1.93
MnO	0.13–0.15	0.1–0.11	0.18–0.20	0.01–0.15	0.04–0.05	0.11	0.1
MgO	1.94–3.06	2.82–4.04	2.95–3.63	0.03–1.33	0.24–0.44	0.41	0.3
CaO	6.10–7.79	5.81–6.62	8.46–9.30	0.20–3.73	1.69–1.81	4.45	1.48
Na_2O	3.82–4.17	4.52–4.76	3.31–3.70	3.18–4.78	4.45–5.03	4.07	3.57
K_2O	1.23–1.61	1.19–1.34	1.97–2.06	2.45–5.16	2.90–3.05	1.64	2.38
P_2O_5	0.14–0.23	0.19–0.20	0.28–0.30	0.01–0.26	0.08–0.31	–	

Table 1.1: Examples of bulk and melt compositions for andesitic magmas. Compositions are given as oxides weight fractions on the basis of a dry composition (water is not taken into account). (1) Coombs et al. (2013) (2) Kendrick et al. (2013) (3) Gertisser and Keller (2003) (the iron content indicated here was measured as Fe_2O_3) (4) Martel et al. (2000) (5) Burgisser et al. (2010)

1.2.2 Melt

The melt, i.e. the magma liquid phase, is composed of a solution of chemical species containing mainly silica, aluminium, iron, magnesium, calcium and sodium (table 1.1), and dissolved volatiles, such as water and CO_2. The melt composition and volume fraction evolve as the magma rises towards the surface and experiments crystallisation, degassing, and less frequent processes such as crustal assimilation. Because the first solid phases that crystallise have moderate silica contents, the melt composition evolves along with crystallisation from an andesitic initial composition to a more silicic composition (e.g. Rhyolite, dacite, trachyte) (Coombs et al., 2013; Kendrick et al., 2013) (table 1.1). Within the magma, the residual melt volume fraction φ_m depends on the gas and crystals volume fractions φ_g and φ_c, and is defined in our model as

$$\varphi_m = 1 - \varphi_g - \varphi_c \tag{1.1}$$

We consider a melt density of about 2300 kg.m^{-3} (Rivers and Carmichael, 1987; Barclay et al., 1998).

1.2.3 Crystallisation

1.2.3.1 Crystals in andesitic magma

As the magma ascends towards the surface, it undergoes cooling, thus getting closer to the melt liquidus (fig. 1.1). When crossing the liquidus curve conditions, the first crystals nucleate. As the magma temperature further decreases, those crystals grow and new crystals are created. At shallower depth, exsolution of volatiles from the melt can also promote crystallisation by changing the liquidus conditions (fig. 1.1) (Cashman and Blundy, 2000; Szramek et al., 2006). The chemical composition of

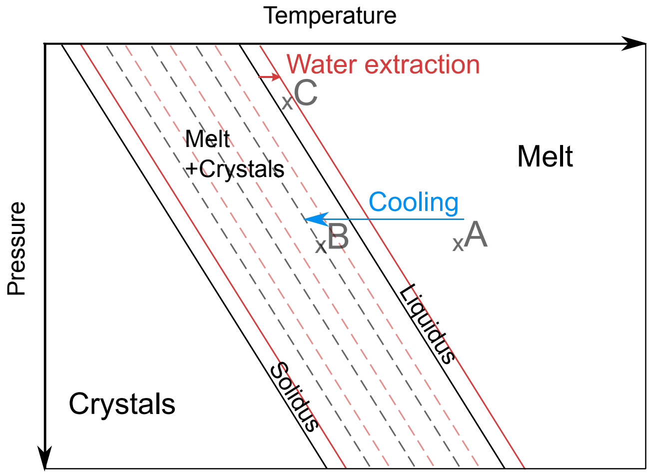

Figure 1.1: Sketch of liquidus and solidus curves for melt. In a volcanic system, crystallisation can occur due to magma cooling (moving from A to B) or volatile exsolution from the melt (staying in C).

the resulting crystals is highly dependent on temperature and pressure conditions, as well as on melt composition, and can be used to retrieve information on magma past evolution in the crust (e.g. Chadwick et al., 2013; Costa et al., 2013; Erdmann et al., 2016). Crystals present in andesitic magmas are mostly represented by plagioclase, with smaller portions of pyroxenes, and amphibole (Barclay et al., 1998; Burgisser et al., 2010; Lavallée et al., 2012; Scott et al., 2012).

A large amount of crystals forms in the magma storage reservoirs. Because of the relatively long residence time of the magma in these reservoirs (up to several thousands years), they have big sizes (up to a few mm), and are called phenocrysts (fig. 1.2). They sometimes include trapped batches of melt, that can be used, in erupted samples, to retrieve magma past composition and history. Besides, their progressive growth can record the melt chemical evolution, testifying of magma differentiation, supply of fresh magma, or crustal contamination processes that the magma has undergone (e.g. Chadwick et al., 2007; Borosiva et al., 2013). Phenocrysts account for 25 to 50vol% of the magma groundmass (magma without gas) (e.g. Martel, 1996; Barclay et al., 1998; Blundy and Cashman, 2005; Burgisser et al., 2010; Innocenti et al., 2013a; Kendrick et al., 2013; Coombs et al., 2013).

Microlites, on the other hand, generally form along with magma degassing, when magma ascends in the conduit, i.e. little time before magma extrusion and quenching (Szramek et al., 2006; Martel and Poussineau, 2007; Brugger and Hammer, 2010; Cichy et al., 2011). They can be used to retrieve information on magma ascent rate in the upper volcanic system. They are of small size, with an elevated aspect ratio (up to 19 (Clarke et al., 2007)). Microlites can account for up to 50 vol%

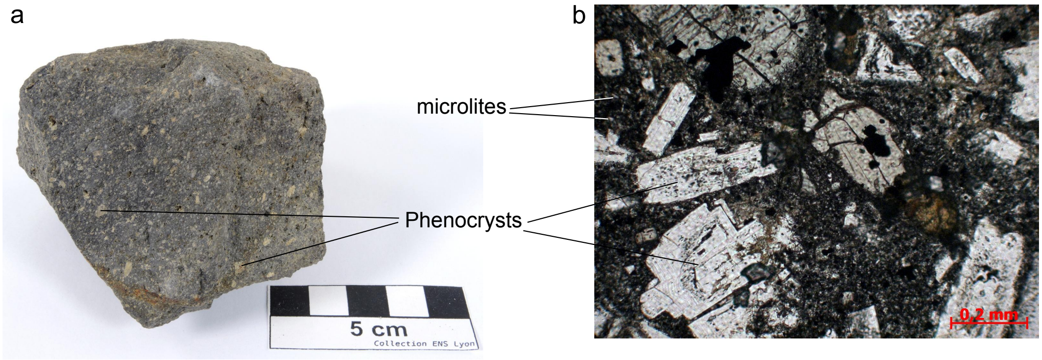

Figure 1.2: Phenocrysts and microlites in andesite lava collected at Santa Lucia Island (Lesser Antilles). (a) Macroscopic view of the sample. (b) Microscopic view of the sample, natural light. Sample PA80 from the ENS Lyon collection. credit: Damien Mollex

of the groundmass (Martel, 1996; Clarke et al., 2007; Burgisser et al., 2010; Kendrick et al., 2013) (fig. 1.2b). The crystallisation of microlites increases the concentration of water within the residual melt, therefore favouring further gas exsolution.

In the following sections and for numerical modelling, we neglect microlites crystallisation in the conduit. Although the presence of microlites can have a significant effect on magma viscosity and flow conditions (Sparks, 1997; Melnik et al., 2005; Massol and Jaupart, 2009), we here focus on gas loss issues, and use this simplifying assumption in order to limit the model complexity and facilitate results interpretation.

1.2.3.2 Crystals volume fraction

We assume an initial volume fraction of crystals $\varphi_{c,0}$ in the magma reservoir of 40%, which is representative of phenocrysts in andesitic magmas (Blundy and Cashman, 2005; Burgisser et al., 2010; Lavallée et al., 2012; Innocenti et al., 2013a) and remains in the range of viscosity for which magma can be considered as a Newtonian fluid. Along with degassing, and the increase of the gas phase volume fraction φ_g, the volume fraction of crystals φ_c evolves following (1.2).

$$\varphi_c = \varphi_{c,0} * (1 - \varphi_g) \tag{1.2}$$

We here neglect melt volume fraction decrease due to water exsolution.

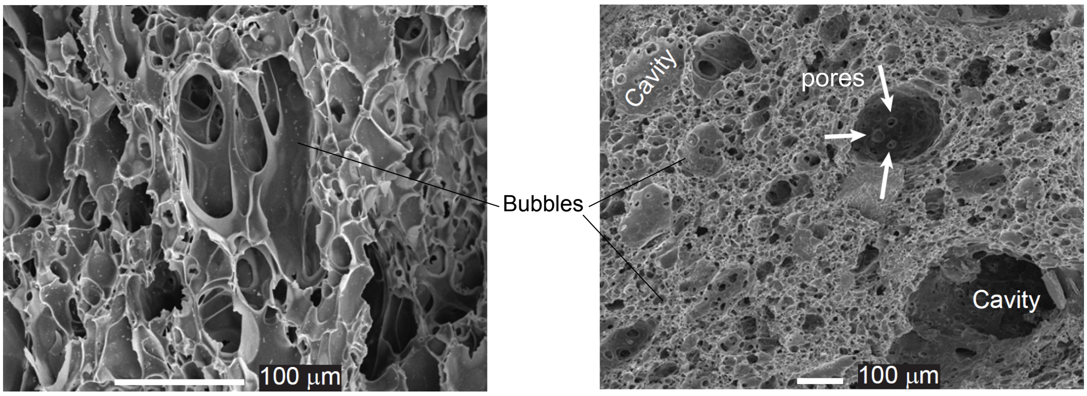

Figure 1.3: Scanning Electron Microscopy (SEM) images of bubbles in pumice samples from the Kos Plateau Tuff (Aegean Arc), from Bouvet de Maisonneuve et al. (2009).

1.2.4 Gas exsolution

Along with magma ascent towards the surface, the solubilities of volatile species present in the magma, which are pressure dependent, decrease. When magma pressure reaches a critical value, the magma becomes oversaturated with volatiles, and bubbles nucleate. Further decompression causes the bubbles to grow (fig. 1.3), and the gas volume fraction to increase. The main volatile species present in the magma are water, which is by far the most abundant (Wallace et al., 1995), carbon dioxide, sulfur, chlorine and fluorine (Wallace and Anderson, 1999). The magma gas content widely depends on the magma degassing history and eruption style, and porosity of erupted samples ranges from about 10vol% in dome rock samples to 85vol% in pumice erupted during plinian explosions (Klug and Cashman, 1994; Martel, 1996; Innocenti et al., 2013a). We assume that water is the only volatile present in the magma, as it is by far the most abundant (measurements in melt inclusions give: water vapor 2–7wt%, CO_2 a few hundred ppm, Sulfur 200–400ppm, Chlorine ≈1500ppm, fluorine ≈500ppm) (Wallace et al., 1995; Matthews et al., 1997; Wallace and Anderson, 1999). The presence of CO_2 can however influence degassing at volcanoes with magma enriched in CO_2, such as Merapi (Deegan et al., 2011; Troll et al., 2013a). Because of its lower solubility, CO_2 exsolves at greater depth than H_2O, and therefore impacts significantly the flow dynamics (Papale and Polacci, 1999). However, we here rather consider the case where CO_2 content is low, and water dominates degassing processes.

1.2.4.1 Water solubility

In the magma, water is present both within the liquid phase, as dissolved water, and in the gas phase, as water vapor. Water solubility in magmatic melts decreases

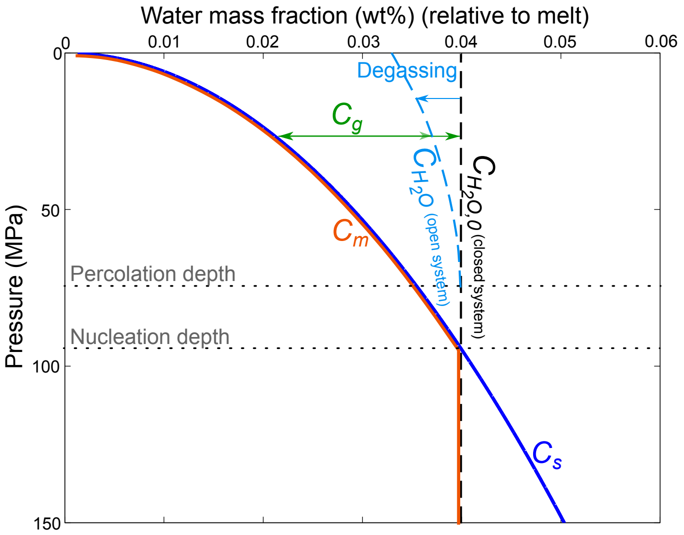

Figure 1.4: Evolution of the water mass fraction in the melt with pressure. C_s is the maximum weight fraction of water dissolved within the melt. $C_{H_2O,0}$ is the initial total weight fraction of water in the magma (vapor+dissolved), relative to melt. C_{H_2O} is the total weight fraction of water in the magma, relative to melt. C_m is the effective weight fraction of dissolved water in the melt. C_g is the weight fraction of water vapor in the magma, relative to melt. See (1.3)–(1.5)

with pressure. The maximum mass fraction of dissolved water within the melt C_s, follows Henry's law (Shaw, 1974):

$$C_s = K_h p^n \tag{1.3}$$

For andesitic magmas with melts of rhyolitic composition, $K_h = 4.11 \cdot 10^{-6}$ and $n = 1/2$ (Shaw, 1974). C_s is the theoretical mass fraction of dissolved water in a melt saturated with water. The initial amount of water present in the melt, $C_{H_2O,0}$, depends on the magma generation history (hosted rock, fusion degree, magma crystallisation, contamination). For andesitic magmas, $C_{H_2O,0}$ varies from 3 to 7wt%. If $C_{H_2O,0}<C_s$, which can occur at a few kilometers depth (5–10 km at most of andesitic volcanoes), in the magma reservoir, all the water present within the magma is dissolved in the melt (no gas phase is present), which is undersaturated. The mass fraction of dissolved water in the melt, C_m, then equates $C_{H_2O,0}$ (fig. 1.4).

Throughout its ascent towards the surface, magma undergoes decompression, and C_s decreases (fig. 1.4). When $C_{H_2O,0}>C_s$, the magma is oversaturated with water. Bubbles then nucleate, and a water gas phase is created from the excess of water. The remaining mass fraction of dissolved water in the melt C_m equates C_s (fig. 1.4).

As long as the magma behaves as a closed system, the total water mass fraction relative to the melt C_{H_2O} is $C_{H_2O,0}$. However, as the magma is further decompressed, bubbles grow and can coalesce, forming a connected network. Permeability then develops through the magma, and the gas can flow and separate from the magma. If conditions in the surrounding rock allow for it, gas can be lost at the conduit walls, and at its top. The magma gas content therefore varies. This is called open system. In this case, C_{H_2O} takes into account gas loss or gain, and is no more equal to $C_{H_2O,0}$ (fig. 1.4).

$$C_m = \min(C_{H_2O}, C_s) \tag{1.4}$$

Bubble nucleation generally occurs with a delay regarding magma saturation (Navon and Lyakhovsky, 1998). This is due to the fact that nucleation requires energy to balance for the surface tension of the new interface created between the melt and the gas. When the magma is oversaturated, the release of energy associated with gas exsolution balances this surface tension. Besides, gas exsolution is not instantaneous and depends on the gas and melt pressure, and on the volatile concentration gradient around the bubble (Navon et al., 1998). Here we consider that the time needed for reaching this equilibrium and the oversaturation delay are negligible, i.e. bubbles nucleate as soon as the magma becomes oversaturated, and equilibrium is instantaneously reached.

1.2.4.2 Gas volume fraction

The mass fraction of exsolved volatiles, i.e. gas, relative to melt C_g is

$$C_g = C_{H_2O} - C_m \tag{1.5}$$

We here consider that water vapor behaves as an ideal gas. The gas density therefore only depends on the gas pressure p_g:

$$\rho_g = \frac{M p_g}{RT} \tag{1.6}$$

with M, R and T the water molar mass, the ideal gas constant and the melt temperature, respectively. Assuming that each bubble present in the magma is associated with a small batch of liquid–solid magma S_0, that depends on the bubble density number N_m, we call S_b the volume of the gas bubble attached with this small batch of magma (fig. 1.5). S_b depends on S_0, C_g and ρ_g. and is related to the gas volume fraction φ_g as expressed in eq.

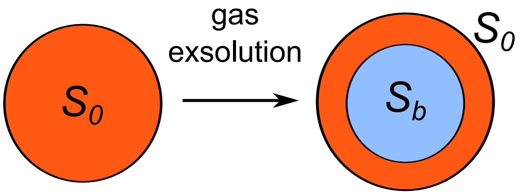

Figure 1.5: We assume that each bubble can be virtually attached to a small ammount of initial magma of volume S_0

$$S_b = C_g \varphi_m S_0 \frac{\rho_m}{\rho_g} \quad \text{with} \quad S_0 = \frac{1}{N_m} \tag{1.7}$$

The gas volume fraction φ_g is then easy to calculate:

$$\varphi_g = \frac{S_b}{S_b + S_0} \tag{1.8}$$

1.3 Equations for magma flow conditions

1.3.1 From the three–phase magma observation to one–phase, compressible magma modelling

1.3.1.1 One–phase assumption

Within the melt, crystals and bubbles in suspension are submitted to volume gravity forces, due to their weight and buoyancy, and to surface reaction forces from the liquid phase, that opposes to their movement (shearing, friction ...) (fig. 1.6). Crystals and bubbles can be modelled, at the first order, by spherical particles that fall into the melt. In this precise case, the particle velocity in the magma is given by Stoke's law at steady state (the sum of forces applied to the particle equates 0).

$$v_p = \frac{2}{9} \frac{(\rho_p - \rho_l)}{\mu_l} g R_p^2 \tag{1.9}$$

v_p, ρ_p and R_p are the particle velocity, density and radius. ρ_l and μ_l are the melt density and viscosity. For a melt viscosity ranging from 10^6 to 10^{12} Pa·s and a particle radius of 100 µm, and assuming crystal, melt and gas densities of respectively 2700, 2300 and 0 kg·m^{-3}, bubble velocity within the melt ranges from $5.01 \cdot 10^{-17}$ to $5.01 \cdot 10^{-11}$m·s^{-1}, while crystal velocity ranges from $8.72 \cdot 10^{-18}$ to $8.72 \cdot 10^{-12}$m·s^{-1}. In comparison, magma velocity in volcanic conduits ranges from 10^{-4}m·s^{-1} in effu-

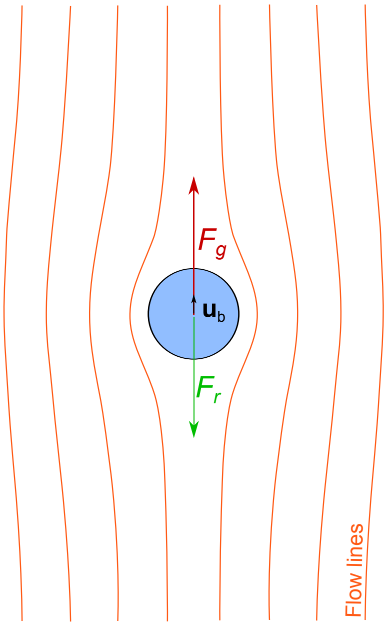

Figure 1.6: Bubble velocity within the magma depends on the relative importances of gravity forces (F_g) and liquid reaction forces (F_r). Due to its low density, a bubble tends to rise within the magma. Reaction forces oppose to this movement.

sive cases to supersonic velocities during Plinian explosions. Bubbles and crystals movements within the melt are therefore often neglected for silicic magma modelling.

Although a two–phase description of magma and gas flow has been used for studying degassing in 1D models (e.g. Kozono and Koyaguchi, 2009; Michaut and Bercovici, 2009; Michaut et al., 2013), the integration of two–phase equations to 2D modelling is very complex. Assuming that bubbles and crystals movements within the melt are negligible, magma can however be modelled as a single compressible phase, whose properties (density, viscosity) depend on the liquid, solid and gas phases volume fractions and interactions. We use this approximation in our models. The bulk properties expressions are detailed in the following sections. The one–phase assumption is often used for silicic magma modelling (Massol, 2001; Collier and Neuberg, 2006; Collombet, 2009), for calculation cost and numerical modelling simplicity reasons. It is valuable as long as the relative velocities between the different phases are negligible toward magma ascent velocity. In particular, when the magma is permeable to gas flow, gas velocities and interaction with magma have to be considered more specifically. This is detailed in section 1.6.

1.3.1.2 Mass and momentum conservation equations

Using the one phase assumption, we get steady–state magma flow conditions in the conduit by solving the Navier–Stokes mass and momentum conservation equations:

$$\nabla \cdot (\rho \mathbf{u}) = 0 \tag{1.10}$$

$$\rho(\mathbf{u} \cdot \nabla)\mathbf{u} = \nabla \cdot [-p\bar{\mathbf{I}} + \eta(\nabla \mathbf{u} + (\nabla \mathbf{u}^T)) + (\kappa - \frac{2}{3}\eta)(\nabla \cdot \mathbf{u})\bar{\mathbf{I}}] + \rho \mathbf{g} \tag{1.11}$$

with $\mathbf{u}$ and p the magma velocity and pressure. η, κ, and ρ, whose expressions are detailed in the following sections, are the magma bulk dynamic and volume viscosity, and bulk density, respectively. $\bar{\mathbf{I}}$ is the identity matrix and $\mathbf{g}$ is the gravitational acceleration (table parameters).

1.3.2 Magma bulk density

The magma bulk density depends on the crystals, melt, and gas densities and volume fractions, described in section 1.2:

$$\rho = \rho_m \varphi_m + \rho_c \varphi_c + \rho_g \varphi_g \tag{1.12}$$

1.3.3 Magma bulk dynamic viscosity

Although the rheology of two–phase magmas, either a crystal free bubble suspension or a bubble free crystal suspension, has been well studied and documented over the past decades (e.g. Llewellin et al., 2002a; Llewellin and Manga, 2005; Costa et al., 2009b; Mader et al., 2013), only a few models account for the presence of the three phases (melt, bubbles and crystals) simultaneously. Harris and Allen III (2008) assumed that the viscosity of a three–phase magma could reduce to a two–phase rheology, when one of the suspended phase (crystals or bubbles) is relatively smaller in size than the other. The bulk viscosity would then result from successive calculation of (i) the rheology of the melt and small–size suspension, to which is added (ii) the rheological influence of the suspension of larger size. When the two suspensions are of equivalent sizes, the bulk viscosity results from an intermediate expression. Truby et al. (2015); Truby (2016) used a similar assumption and considered that melt and suspended bubbles are a continuous medium in which crystals are suspended. In this case, however, the model was applied only to low capillary regimes, in which bubbles do not deform.

Pistone et al. (2016) considered the rheology of a three–phase silica rich melt containing deformable bubbles and a variable crystals volume fraction. They highlighted that, at low crystallinity (<44%), shearing caused outgassing, and therefore a shear–thickening; whereas at high crystallinity (>44%), bubbles did not connect and outgass, but regroup in shear bands, causing a shear–thinning. Their study, however, was restricted to low porosity (<12%), high pressure (>200 MPa), and near fracturing conditions, which are not representative of magma flow in the upper conduit.

We here estimate magma bulk viscosity following a similar calculation sequence to Harris and Allen III (2008). Bubbles in the upper conduit are deformable and their size and volume fraction can get important. Besides, we consider a constant crystals volume fraction in the magma. We therefore first calculate the influence of the presence of crystals on viscosity, and second calculate the influence of suspended bubbles. The magma bulk viscosity η therefore depends on the melt phase viscosity η_m, and on the influence of the presence of crystals and bubbles. A general form for the bulk magma viscosity can be written as follows :

$$\eta = \eta_m \eta_{rc} \eta_{rb} \tag{1.13}$$

where η_{rc} and η_{rb} are coefficients that depend respectively on the crystals and bubbles present in the melt and their interaction with the liquid phase. The expressions of η_m, η_{rc} and η_{rb} are detailed and discussed in the next paragraphs.

1.3.3.1 Melt viscosity

The viscosity of a silicate melt mainly depends on its composition, in particular its water mass fraction, and on temperature T. Pressure influence on melt viscosity is negligible compared with these two controlling parameters (Vetere et al., 2008).

The viscosity represents the ability for a fluid to adapt to new constraints by flowing. At the molecular scale, viscosity depends on the strength and number of weak chemical bonds (e.g. Hydrogen bonds, Van der Waals) that exist between the molecules composing the fluid, which is extremely dependent on the molecules nature and then on the fluid composition. Besides, these weak bonds ability to break up and form, i.e. their stability, is highly dependent on temperature. An increase in temperature generally leads to a decrease in viscosity, as weak bonds are less stable.

The first empirical models of silicate melt viscosity integrating water and temperature influence assumed an Arrhenian relationship between viscosity and temperature (e.g. Shaw, 1972) (1.14). Arrhenian relations are based on the fact that some energy is needed for the weak bounds between molecules to break, so that the fluid can deform and adapt to shear conditions. This activation energy E_η depends on temperature, as bounds are weaker at high temperatures, and on the water mass fraction.

$$\eta_m = Ae^{-E_\eta/RT} \tag{1.14}$$

where A is a function of the water mass fraction. These studies were however based on a few measurements realised at high temperature only. Subsequent viscosity measurements at lower temperatures evidenced the highly non–Arrhenian dependence of silicate melt viscosity on temperature (e.g. Dingwell et al., 1993; Richet and Bottinga, 1995). (Hess and Dingwell, 1996) were the firsts to propose a model for silicate melt viscosity based on the Vogel–Fulcher–Tamman (VFT) form (1.15). This new model gave reliable viscosity estimations for melt compositions ranging from rhyolite to leucogranite. Subsequent studies of melt viscosity further investigated viscosity laws in the VFT form, integrating more precise melt compositions and extending the model to a wider range of silicate melts (e.g. Vetere et al., 2006; Hui and Zhang, 2007; Giordano et al., 2008).

$$\log(\eta_m) = A + B/(T + C) \tag{1.15}$$

with A, B and C empirical functions of the temperature.

In the case of andesitic volcanoes, although the bulk magma composition is andesitic, it contains about 40% of crystals with a moderate silica content, and consequently the residual melt composition tends to be more rhyolitic (section 1.2.2). Although the viscosity model from Hess and Dingwell (1996) is less general than more recent models such as those from Giordano et al. (2008) or Hui and Zhang (2007), it gives more reliable estimates of viscosity for rhyolitic melts, and requires only two parameters (water mass fraction and temperature), compared with the 18 parameters from Giordano et al. (2008), and the 37 parameters in the model from Hui and Zhang (2007). It has therefore been widely used for silicic magma flow modelling (Massol, 2001; Diller et al., 2006; Collombet, 2009; De' Michieli Vitturi et al., 2013). In our modelling, we also estimate melt viscosity using the Hess and Dingwell (1996) model (1.16).

$$\log(\eta_m) = -3.545 + 0.833\ln(100C_m) + \frac{9601 - 2368\ln(100C_m)}{T - 195.7 - 32.25\ln(100C_m)} \tag{1.16}$$

Figure 1.7 presents η_m evolution with C_m, for different temperatures. Both have

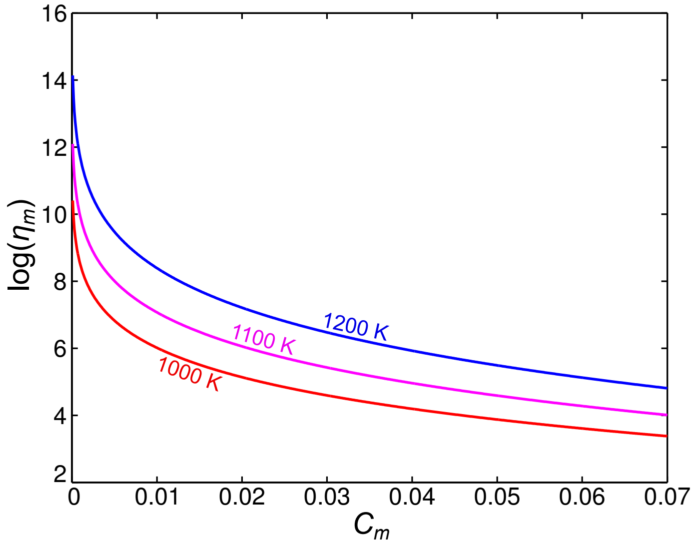

Figure 1.7: Melt viscosity as a function of C_m, for different temperatures. We here use the Hess and Dingwell (1996) permeability law (1.16).

a huge impact on η_m an must be taken into account while describing the magma rheology. Here we neglect temperature variations in the conduit, and T is 1100K. This assumption is valuable for volcanic systems such as the Soufrière Hills Volcano (Montserrat), or Merapi (Java, Indonesia), that have been active for a long time, causing heating of the surrounding rock.

1.3.3.2 Crystals influence on the magma viscosity

Although crystals can accommodate part of the bulk strain in the magma through solid–body rotation, their presence increases viscous dissipation by forcing the flow lines to deviate around them. Crystals influence on the magma viscosity mainly depends on their volume fraction and on their aspect ratio. At low volume fractions, crystals are distant from each other and affect the flow locally. Thus, their influence on the magma viscosity resides mostly in their volume fraction and as such was first described using Polynomial laws (e.g. Einstein, 1911; Guth and Gold, 1938) (fig. 1.8). However, as the crystals volume fraction increases, crystals interaction occurrences get more frequent and can affect the viscosity furthermore. As a result, Polynomial laws can no longer account for the observed viscosities.

The maximum packing fraction was defined as the maximum volume fraction of crystals that can geometrically fit in a volume of magma. This maximum packing fraction is highly dependent on the size distribution (e.g. Del Gaudio, 2014; Moitra and Gonnermann, 2015) and decreases with the aspect ratio of the crystals (e.g. Cimarelli et al., 2011; Mader et al., 2013; Moitra and Gonnermann, 2015), except for

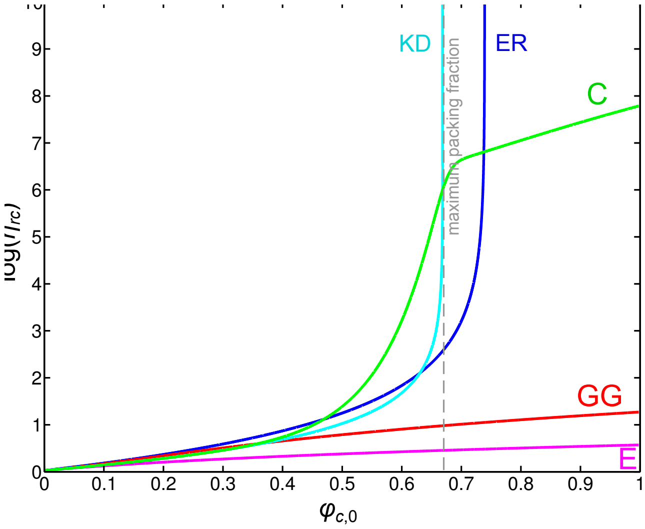

Figure 1.8: Relative viscosity due to the presence of crystals as a function of the crystals volume fraction, using viscosity laws from (E) Einstein (1911) (GG) Guth and Gold (1938) (ER) Einstein–Roscoe (Roscoe, 1952) (KD) Krieger and Dougherty (1959) and (C) Costa et al. (2009a)

specific conditions when important shear stress leads to crystals alignment. When the crystals volume fraction approaches this maximal packing fraction, the magma viscosity increases exponentially, and the magma rheology evolves from a Newtonian to a Bingham rheology, for which strain rate is no more proportional to the yield stress. Several viscosity laws have been proposed to describe viscosity evolution in function of φ_c, for several ranges of crystals volume fractions. The Einstein–Roscoe and the Krieger–Dougherty equations well describe viscosity evolution with φ_c for volume fractions that are smaller than the maximum packing (fig. 1.8). Costa et al. proposed a viscosity law for high crystals volume fraction, that describes the magma viscosity evolution around the maximum packing fraction (fig. 1.8). Their viscosity law is also in good agreement with granular flows, which would happen at very high crystals volume fractions.

Here we consider that crystals account for 40 vol% of the groundmass, and are phenocrysts (no microlites) of unimodal size with an aspect ratio of 1. We can therefore consider that the magma behaves as a Newtonian fluid (Mader et al., 2013), i.e. the strain rate is proportional to the yield stress. In our model, we use the Einstein–Roscoe (Roscoe, 1952) equation (1.17) for calculating the influence of crystals on the magma viscosity.

$$\eta_{rc} = (1 - 1.35\varphi_{c,0})^{-2.5} \tag{1.17}$$

In our model, $\eta_{rc} = 6.97$. We call $\eta_{mc} = \eta_m \eta_{rc}$ the viscosity of the magma incompressible phase (melt + crystals).

1.3.3.3 Bubble influence on magma viscosity

Observations of bubble influence on the magma viscosity proved that bubbles can either be responsible for an increase (e.g. Sibree, 1934; Eilers, 1943) or a decrease (e.g. Mackenzie, 1950; Bagdassarov and Dingwell, 1992) of viscosity. These apparently contradictory observations were brought back together when considering that they were made for bubble suspensions in fluids of very different viscosities. Further investigations evidenced that bubbles influence on viscosity depends on their ability to deform in response to shear (e.g. Manga et al., 1998; Llewellin et al., 2002a; Llewelling et al., 2002b; Rust and Manga, 2002b).

Capillary number Bubbles in the magma are made of compressible gas and are deformable. They can accommodate part of the viscous stresses and, unlike crystals, cause a decrease in magma bulk (apparent) viscosity. When bubbles in the magma are submitted to a steady shear stress, they deform until they reach a stable shape, that balances between deforming shear stresses ($\eta_{mc}\dot{\gamma}$) and the restoring action of surface tension (Γ/r_b). This balance between deforming and restoring forces is described by the Capillary number C_a (1.18).

$$\begin{aligned} C_a &= \frac{\eta_{mc} r_b \dot{\gamma}}{\Gamma} = \lambda\dot{\gamma} \qquad (1.18) \\ \text{with} \quad r_b &= \left(\frac{3S_b}{4\pi}\right)^{1/3} \end{aligned}$$

r_b, Γ and $\dot{\gamma}$ are the bubble radius, the bubble/melt interface tension and the shear strain rate, respectively. The Capillary number can also be described as the balance between the timescale of deformation in the magma, corresponding to $1/\dot{\gamma}$ and the bubble relaxation time $\lambda = \eta_{mc} r_b/\Gamma$, i.e. the time scale needed for a deformed bubble to retrieve a spherical shape. At low C_a (small bubbles, low shear rate, or low magma viscosity), bubbles are hardly deformable ($Ca << 1$), and tend to increase the magma bulk viscosity by forcing the flow lines to deviate around them. Conversely, at larger C_a ($Ca >> 1$), bubbles are highly deformable. When submitted to shear, they get an elongated shape: they oppose a smaller obstacle to the flow, and, in addition, they provide free slip surfaces that help accommodating shear stresses, and therefore tend to decrease the bulk viscosity.

Dynamic capillary number In the conduit, bubbles can be submitted to shear conditions that are far from steady. In such cases, they do not reach the equilibrium deformation shape. Llewellin et al. (2002a); Llewelling et al. (2002b); Llewellin and Manga (2005) adressed this problem and defined the dynamic capillary number, that compares the relaxation time with the time scale for describing the rate of change of the shear environment, $\dot{\gamma}/\ddot{\gamma}$.

$$C_d = \lambda \frac{\ddot{\gamma}}{\dot{\gamma}} \tag{1.19}$$

For a small C_d ($C_d << 1$), the flow approaches steady conditions and the bubble deformation is controlled by C_a. For large C_d ($C_d >> 1$), the flow is highly unsteady and C_a is therefore not defined. In this case, bubbles deform in response to rapid changes in the shear conditions, and cause a decrease in viscosity.

Relative viscosity for a suspension of bubbles The influence of bubbles on magma viscosity, represented by the ratio between the magma bulk viscosity and the groundmass viscosity $\eta_{rb} = \eta/\eta_{mc}$, depends on their ability to deform, through C_a and C_d, and on two factors, η_1 and η_2, that respectively correspond to the two end–member effects of bubbles in non–dilute suspensions (Llewellin and Manga, 2005):

$$\begin{aligned} \eta_1 &= (1-\varphi_g)^{-1} \qquad (Ca << 1) \\ \eta_2 &= (1-\varphi_g)^{5/3} \qquad (Ca >> 1) \end{aligned} \tag{1.20}$$

For high C_d, the relative viscosity equals η_2. For law C_d, the relative viscosity depends on C_a. It equals η_1 for law C_a, and η_2 for high C_a. Following Mader et al. (2013), we integrate these different effects in our model using a single equation for determining η_{rb}:

$$\eta_{rb} = \frac{\eta_1 + \eta_2 C_x^2}{1 + C_x^2} \tag{1.21}$$

With $C_x = \sqrt{C_a^2 + C_d^2}$. When $C_d << 1$ and $C_a << 1$, η_{rb} tends to η_1: the presence of bubbles tend to increase magma viscosity. For $C_d >> 1$ or $C_a >> 1$, η_{rb} tends to η_2: The presence of bubbles decreases magma viscosity (fig. 1.9).

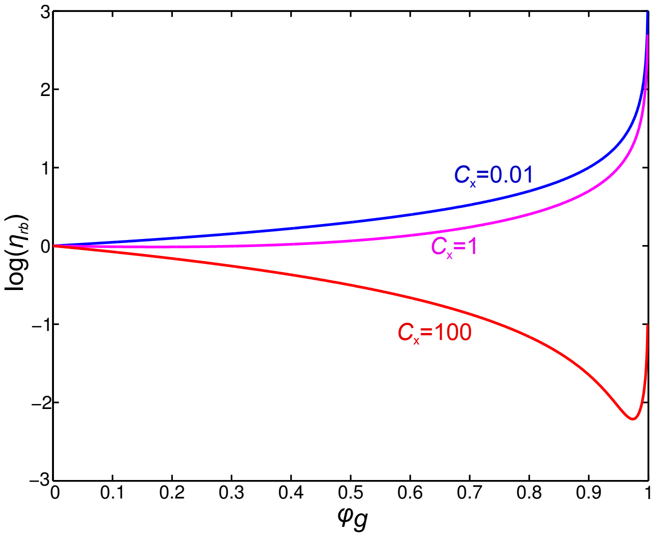

Figure 1.9: Relative viscosity due to the presence of bubbles as a function of φ_g. The three solutions presented here correspond to three values of C_x, and show the bubble influence on viscosity whether it is deformable ($C_x >> 1$) or not ($C_x << 1$)

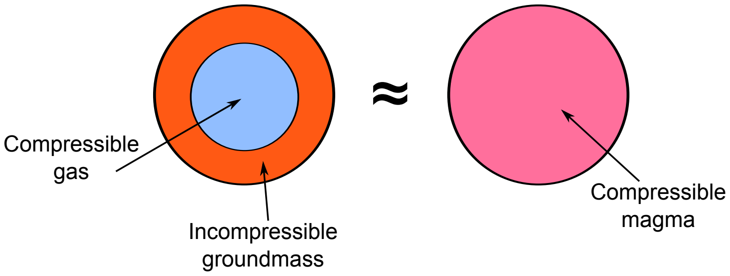

Figure 1.10: The bulk volume viscosity of the magma is retrieved by assuming that the bulk compressible magma has equivalent compressibility properties than a bubble suspension in melt.

1.3.4 Magma bulk volume viscosity

The volume viscosity κ, also known as "second viscosity", "dilatational viscosity", "expansion viscosity" and "bulk viscosity", accounts for viscous forces generated by compression and dilatation. It is required for solving problems involving a compressible fluid. For magmas, the volume viscosity was retrieved from the comparison of the expansion of a cell consisting of a spherical compressible bubble surrounded with a shell of incompressible fluid (fig. 1.10), with the expansion of an equivalent cell of compressible fluid (Prud'Homme and Bird, 1978). We here follow Prud'Homme and Bird (1978) and use equation (1.22) for calculating the magma volume viscosity.

$$\kappa = \frac{4}{3}\eta_c\frac{(1-\varphi_g)}{\varphi_g} \tag{1.22}$$

1.4 Modelling magma flow conditions in a closed system

A closed system, in the case of andesitic volcanoes, refers to a volcanic plumbing system (e.g. chamber, conduit) within which magma flows without exchanging material with the surrounding edifice. Here, we consider that gas cannot escape from the magma by permeable flow. This impermeable condition is not only set at the conduit edges and top, but also inside the magma: it is considered to be impermeable, and the gas remains trapped in the bubbles in which it exsolved at first. This closed system assumption can be used for modelling extreme conditions, though some degassing always occurs in a real system.

In such systems, where magma porosity can reach huge values, fragmentation is likely to occur. Fragmentation is the disruption of the magma foam that occurs when strain rate or bubble overpressure, in case of a rapid decompression, exceed the magma tensile strength (Alidibirov and Dingwell, 1996, 2000; Spieler et al., 2004). The fragmentation level then marks a transition in the flow dynamics from magma flow with a suspension of bubbles to gas flow with a suspension of particles. The transition from bubbly to gas and particles flow has been implemented in several 1D model, and used for studying variations of the fragmentation depth and transitions from effusive to explosive activity (e.g. Wilson et al., 1980; Kozono and Koyaguchi, 2009). In the model presented here, however, we consider that magma does not fragment, though porosity can reach up to 99%. The closed system solution is used here as an initial condition for studying magma flow conditions and degassing. It is a first step in identifying parameters that control flow conditions, and is simpler to implement than open system conditions, because gas exchanges are not taken into account. From this model, we evaluate the relative importance of the different parameters on pressure, viscosity, and porosity profiles in the conduit.

1.4.1 Conceptual model

We consider magma flowing from a pressurised shallow reservoir (at a depth of 5km) to the surface within a cylindrical conduit. More complex geometries for shallow system modelling have been used in the case of andesitic volcanoes, for example by Costa et al. (2009b); Hautmann et al. (2013); Melnik and Costa (2014). However the formation of domes with a sub rounded shape like those observed at Soufrière Hills Volcano, Merapi or Kelud, as well as the extrusion of cylindrical spines at Mount

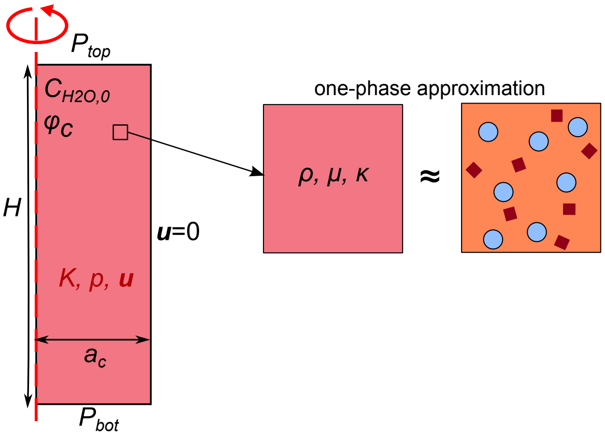

Figure 1.11: Sketch of the conduit flow model. Magma flow is solved in 2D axisymmetry, and depends on the conduit geometry, (H=5km, a_c=15m), on the magma composition (φ_c=0.4, $C_{H_2O,0}$=0.04), and on pressure conditions at the conduit top (atmospheric) and bottom (chamber pressure) see section 1.4.2. We use a one–phase approximation for the magma (zoom), whose bulk properties (ρ, η, κ) depend on the proportions and interactions of melt, bubbles and crystals (section 1.3.1).

St. Helens (Gaunt et al., 2014) suggest that the volcanic conduit is cylindrical, at list in its upper part.

At the top of the conduit, the magma extrudes effusively (we do not model fragmentation). We do not model the extruded magma. We use geometrical parameters for the plumbing system, as well as a magma water and crystals contents that are similar to flow conditions at Montserrat (Barclay et al., 1998; Sparks et al., 2000; Mastin et al., 2009). This volcano is representative of andesitic volcanoes, has a stable and repetitive activity, and has been intensely studied over the past years.

1.4.2 Numerical implementation

Magma flow conditions are solved in 2D axisymmetry using the Comsol Multiphysics software (version 4.4).

1.4.2.1 Model geometry and mesh

The conduit geometry consists in a cylinder of depth H = 5km (Barclay et al., 1998) and radius a_c = 15m (Voight et al., 2006) (fig. 1.11). We use a mesh made of elements of width 1m and length 5m, since flow conditions are likely to evolve at shorter scales in the radial direction than in the vertical direction. It is however refined in the top 100m of the conduit with a 1m by 1m mesh.

1.4.2.2 Boundary conditions

Boundary conditions are applied at the top of the conduit, bottom and edges (fig. 1.11). At the conduit center, conditions are set through axisymmetry. At the bottom of the conduit, we use a Comsol "boundary constraint" condition: magma flow is purely vertical ($\mathbf{u}.\mathbf{t} = 0$) at the bottom of the conduit. In addition, we set the pressure at the bottom of the conduit to magmastatic conditions (weight of a magma column with no gas) with an additional overpressure P_c of 10 MPa. This corresponds to the pressure in the magma reservoir (1.23).

$$P_{bot} = (\rho_c \varphi_{c,0} + \rho_m (1 - \varphi_{c,0})) g H + P_c \tag{1.23}$$

At the top of the conduit, we use a similar condition: magma flow is also purely vertical, and the pressure P_{top} is set to atmospheric. Purely vertical flow would correspond to extrusion conditions associated with a dome emplacement, for example. Another possibility would be to impose pressure added with a "no tangential shear" constraint, which would correspond to lava flow emplacement conditions (Massol, 2001). At the conduit edges, a no slip no exchange condition ($\mathbf{u} = 0$) is applied.

1.4.2.3 Solver options

Numerical simulations are solved using the Comsol Multiphysics finite element software (version 4.4), using cubic interpolation for velocity and quadratic interpolation for pressure. Equations are solved using the PARDISO direct solver, with a convergence criteria defined from tolerance (error tolerance=0.001).

Because the Comsol 4.4 version assumes $\kappa = -3/2\eta$ for every compressible fluid, we had to change its expression manually in every variables defined by comsol for the weak expression of equations. We check for its correct implementation by comparing results we obtained with results using the Comsol version 3.5, in which it can be modified by the user.

1.4.3 Results and discussion

The results we present here correspond to a closed system in which magma would never fragment. This is obviously unrealistic. However, it gives a first idea of the model results and of the governing parameters.

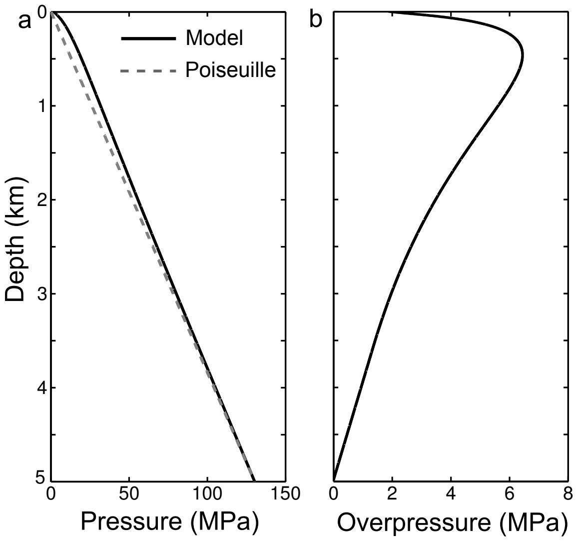

Figure 1.12: (a)Pressure at the conduit center (r=0m), compared with the pressure that would be present for an ideal Poiseuille flow (constant viscosity, incompressible fluid). The pressure difference between the conduit flow model and Poiseuille flow is represented in (b)

1.4.3.1 Results

Magma pressure The magma pressure in the conduit remains quite close to a Poiseuille flow pressure gradient (fig. 1.12). Comparing the pressure profile at the conduit center with a linear profile, we note, however, an overpressure that reaches about 6MPa a few hundred meters below the conduit vent. This overpressure increases from the bottom of the conduit to 500m below the conduit vent, where it reaches its maximum, and then drops to 2MPa. This overpressure trend results from important increase in magma viscosity at shallow depth, together with important bubble growth as magma is decompressed (Sparks, 1997).

Magma velocity The magma vertical velocity increases as the magma ascends towards the surface (fig. 1.13). This mainly results from the formation and growth of bubbles as the magma is decompressed. Magma velocity is $0.09 \mathrm{m \cdot s^{-1}}$ at the bottom of the conduit and reaches about $4 \mathrm{m \cdot s^{-1}}$ at the top of the conduit, at the conduit center.

Gas exsolution In this model, bubbles nucleate at a depth of approximately 3500m. This depth is called the nucleation depth Z_g. It is visible both on the dissolved water weight fraction and gas volume fraction profiles. (fig. 1.14). In closed conditions, the magma gas content then increases exponentially (fig. 1.14b), due to accelerated solubility decrease (fig. 1.14a) and decompression of the exsolved gas.

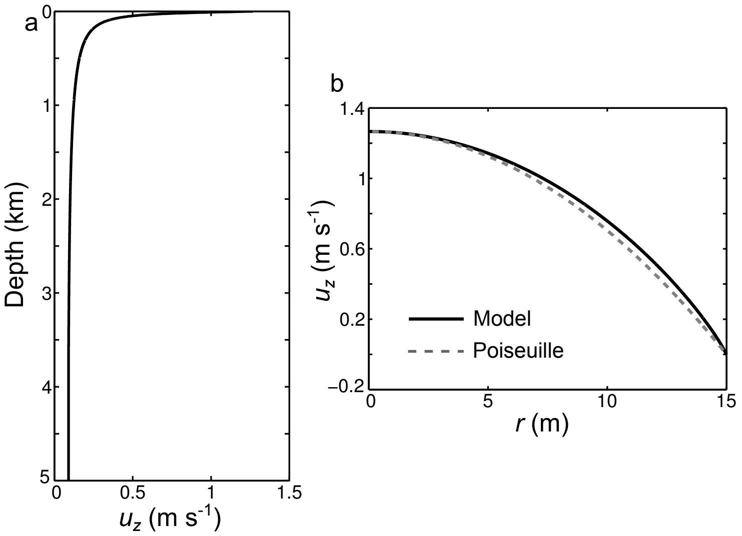

Figure 1.13: Magma velocity (a) at the conduit center and (b) at the top of the conduit, compared with a typical Poiseuille radial velocity profile.

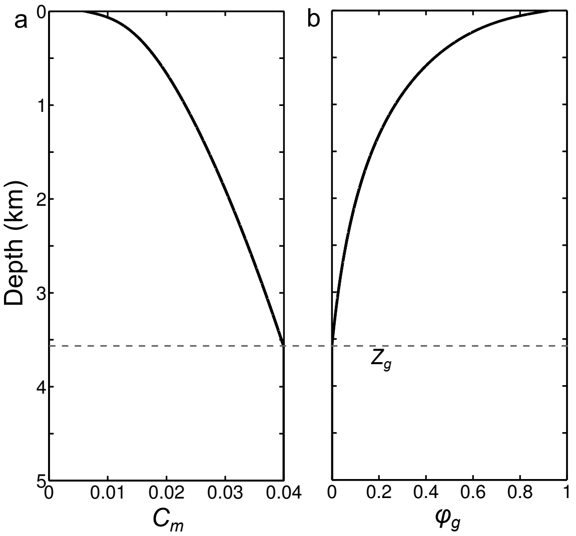

Figure 1.14: Evolution of the dissolved water mass fraction in melt (a) and gas volume fraction in the magma (b) at the conduit center, as a function of depth.

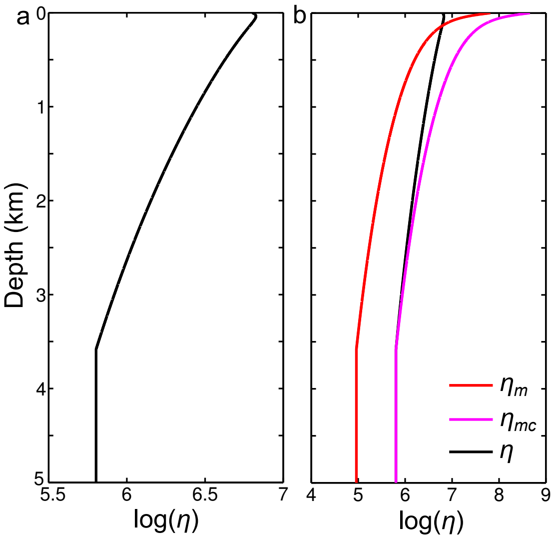

Figure 1.15: (a)Bulk dynamical viscosity at the conduit center (r=0m). (b) Comparison of the bulk viscosity η with the melt viscosity η_m, and the viscosity of the mush (melt+crystals) phase $\eta_m c = \eta_m \eta_{rc}$.

Bulk dynamical viscosity The bulk magma viscosity ranges from $10^{5.8}$ to $10^{6.8}$ Pa·s in closed conditions. It increases in the conduit until a depth of a few tens of meters below the vent, and then decreases (fig. 1.15). We observe the effect of bubbles that act to decrease viscous stresses, and the higher φ_g is, the more important the effect of bubbles on bulk dynamical viscosity.

1.4.3.2 Parameters influence

We here test the relative influence of several parameters on the model results.

Initial water fraction We change the initial dissolved water mass fraction in the melt $C_{H_2O,0}$ from 2 to 7wt% (original model 4wt%). Changing the initial dissolved water mass fraction in the melt has a huge impact on flow conditions (fig. 1.16). First, the volume fraction of gas changes a lot, leading to changes in the magma density and then in the pressure gradients and velocity field. It also causes changes in the viscosity, then further affecting magma flow by increasing shear stress and decreasing velocity.

Conduit radius Changing the conduit radius from 10 to 30m (original model 15m) causes few changes in flow conditions (fig. 1.17), except for magma velocity since it is controlled by shear stress and by the proximity of the boundary no–slip condition.

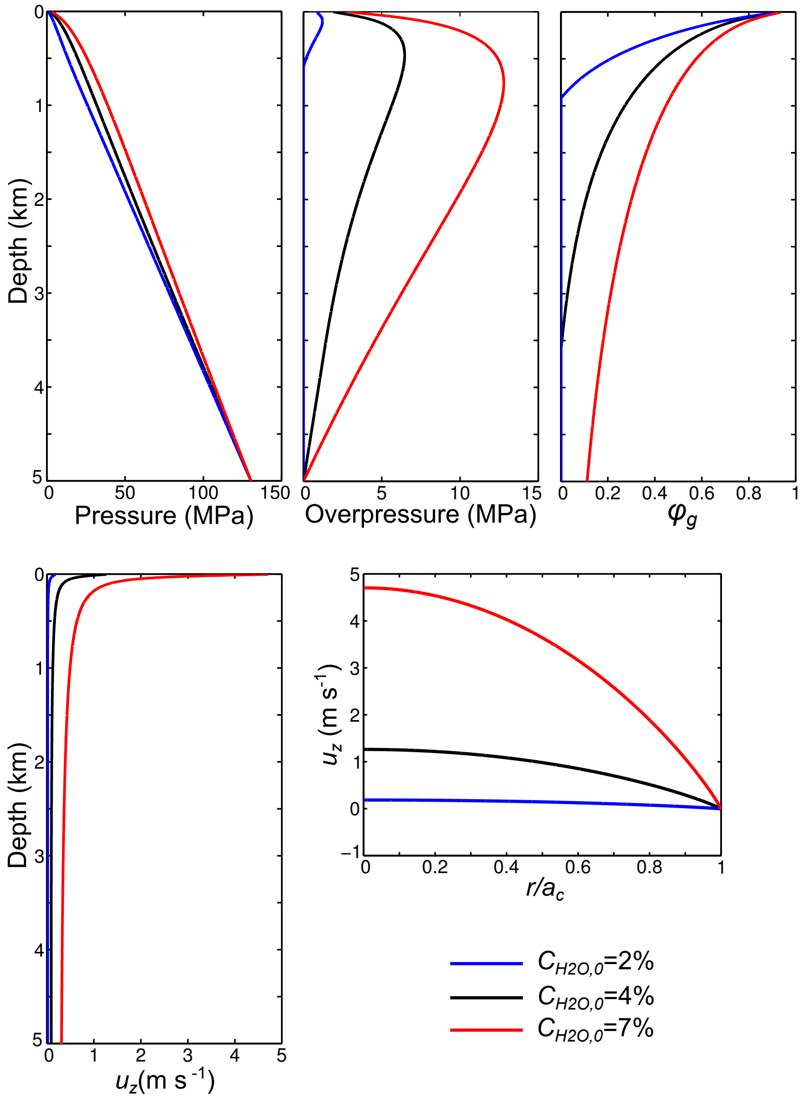

Figure 1.16: Influence of $C_{H_2O,0}$ on magma flow conditions in closed system for $C_{H_2O,0}$ of 2wt% (blue curves), 4wt% (black) and 7wt% (red). (a) Pressure at the conduit center (r=0). (b) Overpressure at the conduit center, compared with a Poiseuille flow pressure gradient. (c) Gas volume fraction at the conduit center. (d) Magma vertical velocity at the conduit center. (e) Magma vertical velocity at the conduit vent.

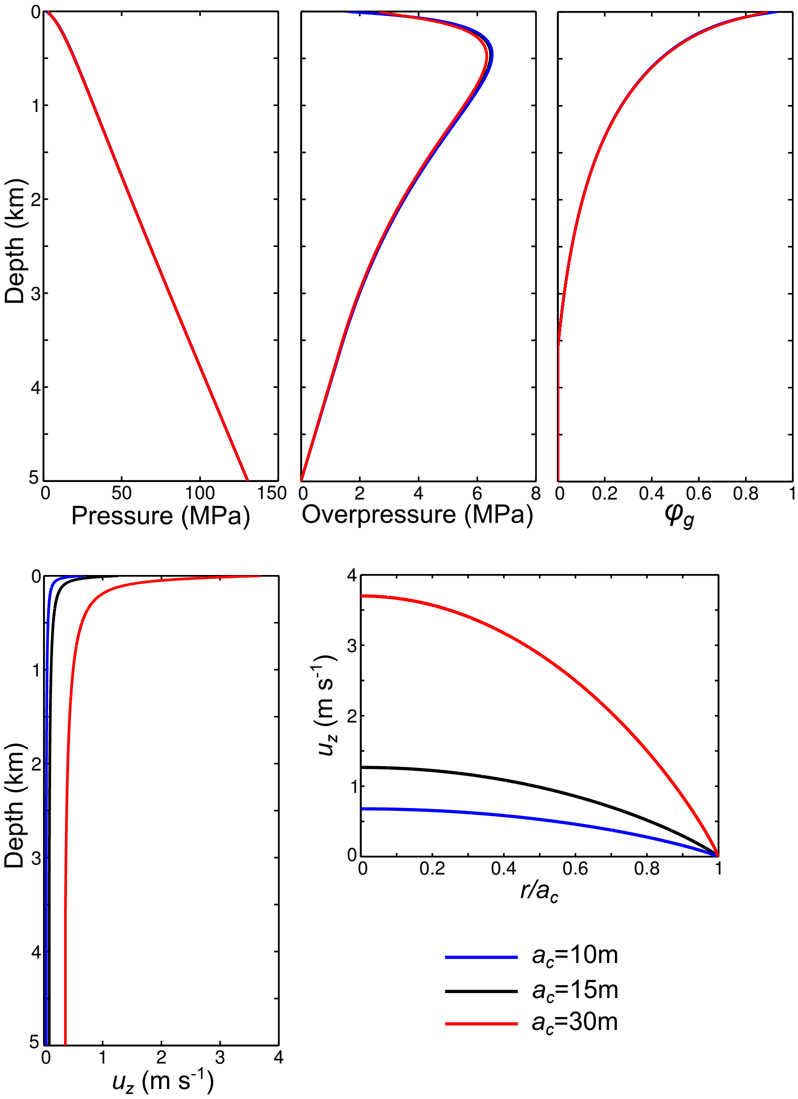

Figure 1.17: Influence of the conduit radius on magma flow conditions in closed system for a_c of 10m (blue curves), 15m (black) and 30m (red). (a) Pressure at the conduit center (r=0). (b) Overpressure at the conduit center, compared with a poiseuille flow pressure gradient. (c) Gas volume fraction at the conduit center. (d) Magma vertical velocity at the conduit center. (e) Magma vertical velocity at the conduit vent.

Crystals We varied the magma phenocrysts content from 30% to 50% of the groundmass (original model φ_c=40%). Increasing the crystal content by 10% causes an increase in the magma viscosity of about 0.6 orders of magnitude. These changes in viscosity cause important changes in the magma velocity. On the other hand, the presence of crystals has little influence on the pressure gradient, since the density difference between crystals and melt is relatively small (comparing with gas).

1.4.3.3 Benchmark

In this section, we compare our model with the one defined by Collier (2005), and used in Collier and Neuberg (2006) and in Collombet (2009).

The evolution of pressure in our conduit flow model follows a similar trend as in the model from Collier (2005) (fig. 1.19a and d). Differences are mainly due to some differences in the rheology we defined. Collier (2005) and Collombet (2009) indeed used a crystal content of 42% (fig.1.18). Besides, some advances in rheological laws have been made since these models were published, in particular for bubbles crystals influences of viscosity, that we integrated in our model and slightly differ from the laws used in these previous models.

The velocity in the conduit also differs between our model and the one from Collier (2005) (fig. 1.19c), which can be explained as a consequence of the higher viscosity in the model from Collier (2005), partly due to the higher crystals content they considered. However, the general trends of vertical and horizontal evolution of the vertical velocity are comparable, and deviate in a similar way from a Poiseuille flow (fig. 1.19d).

1.5 Potential influence of elastic deformation of the conduit.

Magma flow within the conduit exerts pressure and shear stress at the conduit walls, thus causing deformation of the surrounding rock, and then changes in the conduit geometry. Conduit deformation may in turn influence magma flow conditions.

The interaction between magma flow and rock deformation is of primary importance for the propagation of magma through dikes, which are planar structures that form when magma ascends through brittle rocks. In the case of diking, numerical as well as analogical modelling have proven that flow conditions in the dike

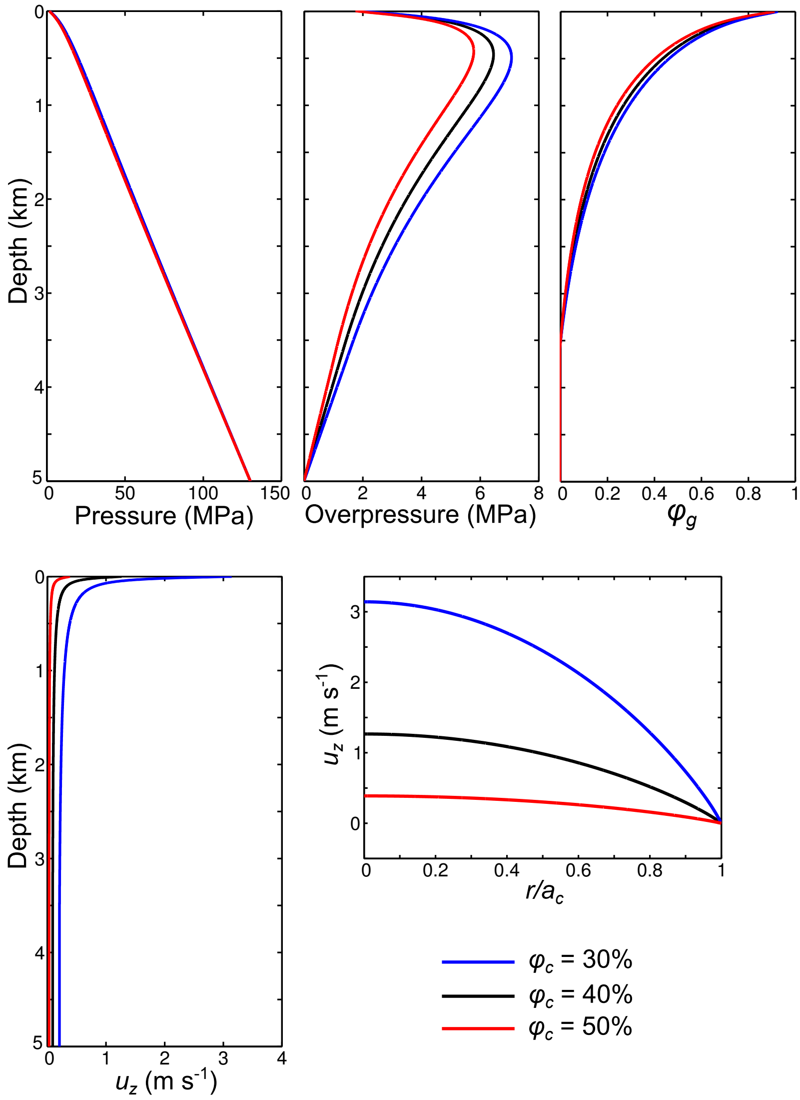

Figure 1.18: Influence of $\varphi_{c,0}$ on magma flow conditions in closed system for $\varphi_{c,0}$ of 30% (blue curves), 40% (black) and 50% (red). (a) Pressure at the conduit center (r=0). (b) Overpressure at the conduit center, compared with a Poiseuille flow pressure gradient. (c) Gas volume fraction at the conduit center. (d) Magma vertical velocity at the conduit center. (e) Magma vertical velocity at the conduit vent.

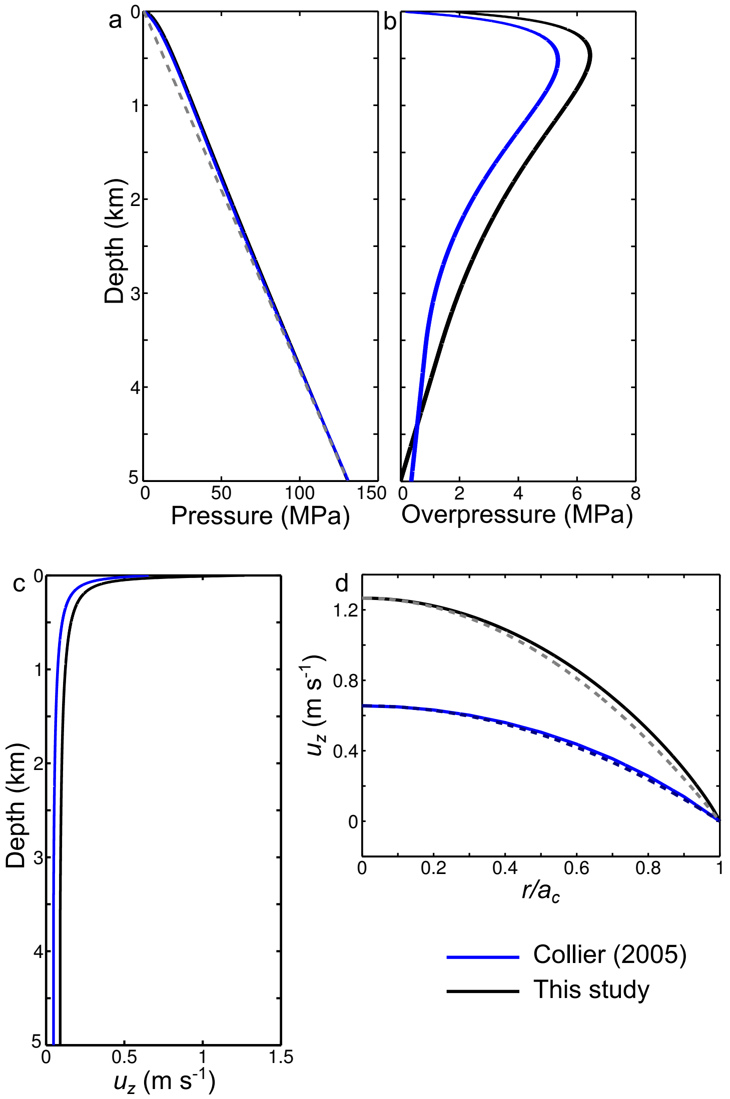

Figure 1.19: Comparison of flow conditions from our model (black curves) with the solution from the model of Collier (2005), in a closed system. (a) Pressure at the conduit center. (b) Overpressure at the conduit center (difference from Poiseuille pressure). (c) Vertical velocity at the conduit center. (d) Vertical velocity at the top of the conduit. Dashed curves in panel (a) and (d) represent equivalent Poiseuille flow conditions, for comparison.

and properties in the surrounding rock, such as stress field (e.g. Bonaccorso et al., 2010; Maccaferri et al., 2010, 2011, 2014; Menand et al., 2010) and rigidity (e.g. Maccaferri et al., 2010), were determinant for the dike propagation (Rivalta et al., 2015). The interplay between magma flow and rock deformation and fracturation controls the way the dike evolves.

Costa et al. (2009b, 2012) modelled magma ascent through a volcanic conduit composed of a dike turning into a cylindrical conduit at shallow depth (about 1km). They provided evidence that the interaction between pressure conditions in the magma and elastic deformation of the dike walls are responsible for cyclic magma extrusion, with cyclic storage and removal of the magma in the dike.

Although cylindrical conduits are less deformable than dikes, deformation of the conduit at shallow depth may also interact with magma flow and make flow conditions to evolve. In section 1.4.3.2, we observed that changes in the conduit radius were associated with little changes in the flow conditions, except for the magma ascent velocity. On another hand, numerical modelling of magma flow conditions at shallow depth in widening or tightening conduits provided evidence that variations in the conduit geometry at shallow depth are strongly coupled with magma ascent dynamics and conditions for the extruding magma (Massol, 2001; De' Michieli Vitturi et al., 2008, 2010).

In this section, we couple magma flow with elastic deformation of the surrounding rock, and quantify the influence of resulting conduit deformation on magma flow. The influence of plug flow in the conduit on deformation in the near field at andesitic volcanoes has been studied by Albino et al. (2011), in one way coupling. They discuss the influence of fully coupling flow conditions with deformation on ground deformation estimates (Albino et al., 2011) (Appendix A). They, in particular, evidence that the error introduced in ground deformation estimations when considering only one–way coupling depends on the ratio between conduit overpressure and surrounding rock Young's modulus. This error can be neglected for a Young's modulus higher than 1GPa when conduit overpressure is around 10MPa. This tends to prove that conduit elastic deformation, for a Young's modulus of 1GPa and more, does not cause huge changes in the flow conditions. We however quantify this effect here.

Although magma flow may cause detectable ground deformation in the near field at andesitic volcanoes (Beauducel and Cornet, 2000; Green et al., 2006; Nishimura, 2009; Albino et al., 2011), we here do not discuss this aspect and concentrate on implications for magma flow conditions only. The influence of flow conditions evolution along with an eruption on observed ground deformation are however discussed

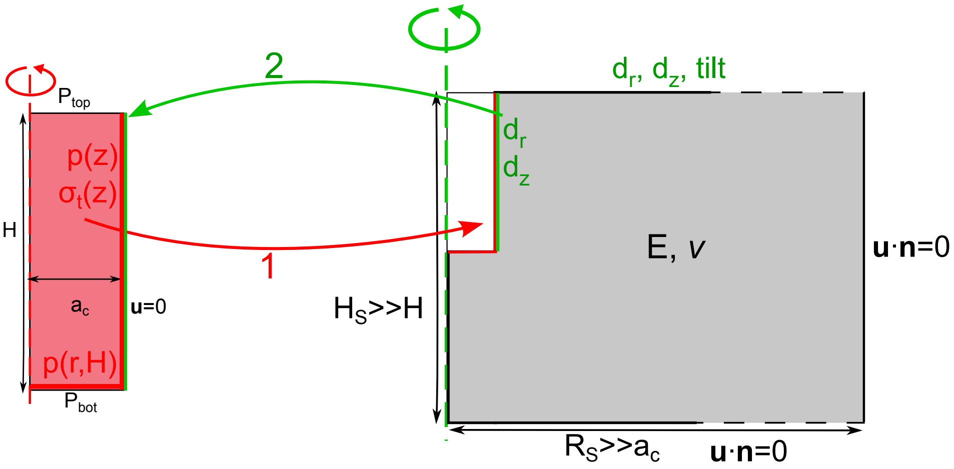

Figure 1.20: Sketch of the coupling model for conduit flow and edifice deformation. Flow conditions are solved using the conduit flow model (section 1.4) and are used as boundary conditions to calculate the edifice and conduit wall deformation (1). Flow conditions are then adapted to the new conduit geometry (2).

in Chevalier et al. (2017) (chap. 2) and in chap. 4.

1.5.1 Numerical modelling

1.5.1.1 Geometry

The volcanic conduit is surrounded with a cylinder of rock of radius $R_s >> a_c$ (R_s=20km) and depth $H_s >> H$ (H_s=10km), with a flat ground surface (fig. 3.3). Here we neglect the influence of the volcano topography. The mesh inside the rock is made of triangular elements. It is refined around the conduit and ground surface (maximum element sizes of respectively 5 and 10m), and larger in the rest of the domain (maximum size up to 700m). The volcanic edifice is characterised by its Young's Modulus E and Poisson's ratio ν and behaves elastically.

1.5.1.2 Boundary conditions

We impose roller conditions (displacement is only tangential), at the rock domain bottom and edges. The top surface is free. At the conduit walls and bottom, the normal and tangential stress perturbations associated with magma flow are applied to the rock. These applied perturbations correspond to the difference between calculated conduit flow conditions and a reference magmastatic state (constant pressure gradient, no shear, magma does not flow).

1.5.1.3 Calculation sequence

In order to couple magma flow conditions with the conduit deformation, we first solve magma flow conditions in a cylindrical conduit. We then apply the resulting normal and tangential stress at the conduit walls to the surrounding elastic media (1 in fig. 1.20). Edifice deformation is then solved, and we obtain a new geometry for the conduit, that is used to calculate new flow conditions (2 in fig. 3.3). This process is iterated until convergence. This coupling calculation sequence is valid for steady–state flow conditions. The adaptation of flow conditions to deformation in a transient regime may indeed require consideration of time–dependent flow evolution.

1.5.2 Results

We here observe the influence of taking conduit deformation into account for magma flow conditions calculation. The surrounding rock Young's modulus ranges from 0.1 to 10 GPa. These values correspond to bounding order of magnitude values for E in the case of volcanic edifices (Beauducel and Cornet, 2000; Voight et al., 2006; Widiwijayanti et al., 2005). We use a Poisson's ratio ν of 0.25. Flow conditions are calculated for a closed system, with a conduit overpressure of P_c=10MPa at the bottom of the conduit.

Fig. 1.22 presents the conduit initial and final geometry for $E = 0.1$GPa. The conduit deformation appears to be mainly radial. Although vertical deformation at the conduit edges occurs and can be of the same order of magnitude as the radial deformation, it is much smaller compared with the conduit dimensions, and has little influence on the conduit overall geometry. We can notice the important influence of flow overpressure on conduit deformation: The maximal change in the conduit geometry indeed occurs at the bottom of the conduit, where magma overpressure is the highest (fig. 1.12). It remains high until the few top hundred meters, where it drops, in agreement with overpressure evolution at the top of the conduit. In the case presented here ($E = 0.1$GPa), conduit widening associated with magma flow reaches up to 12.3% of the conduit initial radius. The smaller radial deformation at the base of the conduit is due to the conduit initial geometry used here: the conduit extends to a depth of 5km, and is not open deeper (see fig. 1.20).

Fig. 1.22 presents the evolution, for each value of E, of the maximal variation in the conduit radius, normalised with the initial radius (a_c=15m), between two successive conduit deformation calculation. The initial geometry is a cylindrical conduit of radius 15m. We observe a rapid decrease in the evolution of conduit

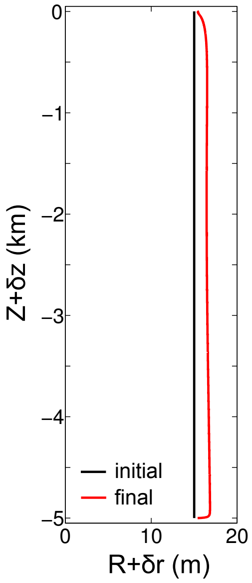

Figure 1.21: Evolution of the conduit geometry due to coupling between flow conditions and surrounding rock elastic deformation. Both the initial cylindrical geometry (black curve) and the final conduit geometry (red curve) are presented, for E=0.1GPa.

deformation. Besides, we observe that the conduit deformation is low (less than 1%), except for extremely small values of E, that exist at volcanoes only at the top of the edifice, where deposits, less consolidated, are very malleable. These results confirm observations from Albino et al. (2011).

Fig. 1.23 presents the evolution of flow conditions at the top of the conduit (magma pressure and velocity), between the initial and final conduit geometries. Except for a small Young's modulus, we observe little changes in the flow conditions. Even in the case where $E = 0.1$GPa, the evolution of flow conditions at the top of the conduit is relatively small compared with the influence of the parameters we tested in section 1.4.3.2.

To summarize, conduit deformation associated with magma flow in the conduit has little influence on flow conditions, and can be neglected in our calculations.

1.6 Magma degassing in open system

At andesitic volcanoes, the eruption style alternates between effusive and explosive regimes (Newhall et al., 2000; Ogburn et al., 2015; Sheldrake et al., 2016). A major difference between these two eruptive styles is the magma gas content. Magma extruding effusively (lava domes and flows) has a gas volume fraction of only 10% to 30% (Innocenti et al., 2013a; Kushnir et al., 2016; Kendrick et al., 2016), whereas

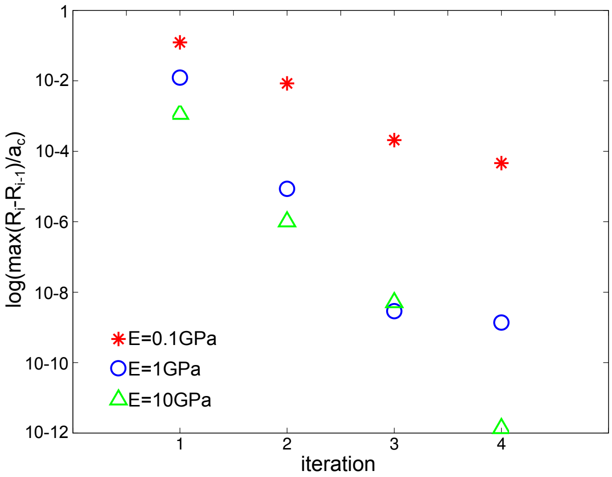

Figure 1.22: Evolution of the deformation with coupling iterations. The conduit maximal radius evolution (unit log), normalised with the initial radius, is represented for the first 4 iterations, for E ranging from 0.1 to 1GPa.

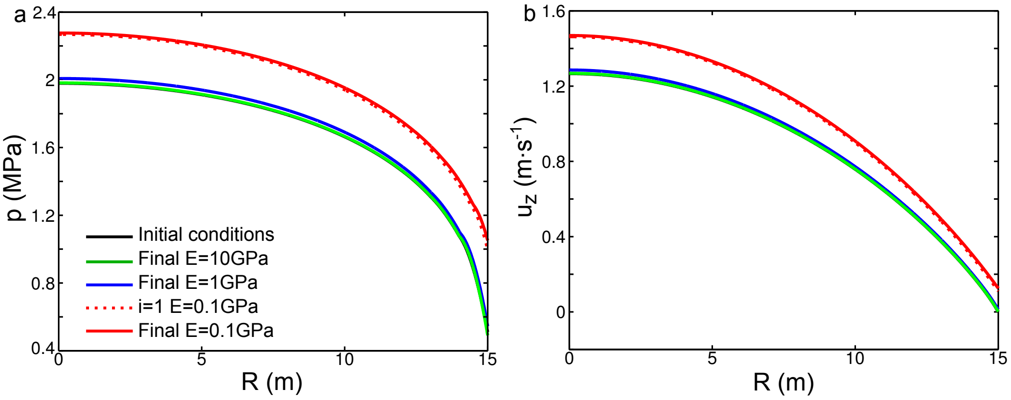

Figure 1.23: Evolution of flow conditions with conduit deformation, for E values ranging from 0.1 to 10 GPa. The initial (black curve) and final (plain coloured curves) conditions are both represented. For E=0.1GPa, a supplementary curve was added, representing flow conditions after the first calculation iteration. The black curve (initial state) is almost hidden by the green curve, in each panel. (a) Magma pressure at the top of the conduit (z=0m). (b) Magma vertical velocity at the top of the conduit.

fragmented magma erupted during Plinian eruptions has a porosity as high as 85% (Klug and Cashman, 1994; Martel, 1996). In addition, experiments on magma fragmentation conditions have provided evidence that the porosity and the gas pressure have a huge influence on magma explosivity (Spieler et al., 2004; Kueppers et al., 2006; Mueller et al., 2011). The magma gas content is therefore a controlling parameter for magma flow conditions and explosivity. In the case of andesitic volcanoes, variations in the magma gas content rarely come from variations in the composition of the magma supplying the reservoirs. It is rather associated with degassing processes that the magma undergoes while rising towards the surface. In this section, we therefore work on including degassing processes to magma flow modelling in the upper conduit.

1.6.1 Permeable gas flow

Bubbles movements through the andesitic magma are negligible because of the magma high viscosity (section 1.3.1). Gas can therefore extract from the magma only by flowing through a permeable network. Such a permeable network can form due to bubble coalescence (fig. 1.24) and, at the upper conduit edges, to magma fracturing. Gas then flows through this permeable network of connected bubbles and fractures, and escapes at the conduit walls and top.

1.6.1.1 Darcy flow

Gas permeable flow through the magma and edifice rocks depends on the pressure gradient and on permeability, and is described by the Forchheimer law (Rust and Cashman, 2004):

$$\nabla p_g = -\frac{\mu_g}{k_1} u_f - \frac{\rho_g}{k_2} u_f^2 \tag{1.24}$$

where k_1 (m^2) and k_2 (m) are the viscous and inertial permeability coefficients, ∇p_g is the gas pressure gradient and $\mu_g = 1.5 \cdot 10^{-5}$Pa.s is the gas dynamical viscosity. $\mathbf{u_f}$ is averaged on a small volume of magma. Note that $\mathbf{u_f}$ is not the gas absolute velocity due to permeable flow, which would be $\mathbf{u_f}/\varphi_g$, with φ_g the gas volume fraction. When permeable gas flow is laminar (high permeability, small pressure gradient), the inertial term of the Forchheimer equation drops down, and the Forchheimer equation reduces to a Darcy equation:

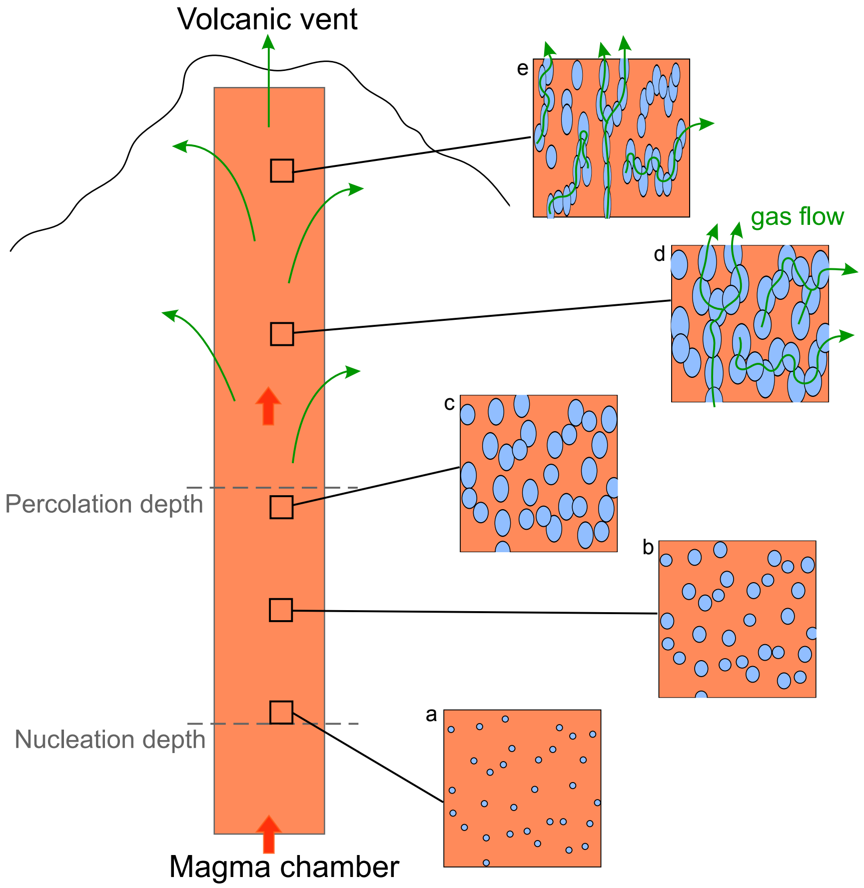

Figure 1.24: Sketch of the porosity and permeability evolution in the magma. (a) Bubbles nucleate when the melt is oversaturated with water. (b) As magma is further decompressed, bubbles grow due to decompression and further exsolution from the melt. (c) Growing bubbles get closer, interact and sometimes coalesce. (d) Further bubble coalescence leads to the formation of a permeable network in which gas flows. (e) High permeability may remain in the high–viscosity magma after gas extraction.

$$\mathbf{u_d} = -\frac{k_1 \nabla p_g}{\mu_g} \tag{1.25}$$

Whether gas flow is laminar or turbulent is determined from the Reynolds number *Re* for the gas, which is defined as the ratio between inertial and viscous forces (1.26).

$$Re = \frac{\rho_g u_d L}{\mu_g \varphi_g} \tag{1.26}$$

with L the characteristic length for gas flow, which corresponds here to the bubble diameter d_b. For low *Re*, gas flow is laminar. In our conduit flow models, *Re* is very low (<0.6). We thus consider that gas flow is laminar and is described by the Darcy equation (1.25).

1.6.1.2 Magma permeability

Permeability law from measurements A large amount of permeability measurements for andesitic pumice, pyroclasts, tephra, lava and dome rock samples exist (Klug and Cashman, 1996; Martel, 1996; Kushnir et al., 2016; Kendrick et al., 2016) and has been used to understand and describe the permeability development and evolution in andesitic magmas. Most of the permeability laws resulting from the interpretation of these measurements describe a power–law dependence of permeability on porosity (Klug and Cashman, 1996; Mueller et al., 2005; Gonnermann and Manga, 2007; Rust and Cashman, 2011) (1.27). Besides, permeability is thought to develop above a critical porosity value ϕ_{cr}, called the percolation threshold. This threshold would be consistent with the percolation theory, in which permeability should develop above a porosity of 30% (Lee, 1990; Sahimi, 1994; Blower, 2001). In the literature, however, permeability–porosity relationships retrieved from measurements are extremely variable, and invoke percolation thresholds varying from 0 to 60%, depending on the data considered (e.g. Eichelberger et al., 1986; Klug and Cashman, 1996; Saar and Manga, 1999; Mueller et al., 2005; Takeuchi et al., 2009; Rust and Cashman, 2011).

$$K = A(\phi_g - \phi_{cr})^n \tag{1.27}$$

with K the magma viscous permeability and $\phi_g = 100\varphi_g$. A and n are empirical coefficients. Rust and Cashman (2004) introduced the possibility of a hysteresis relation between permeability and porosity, as degassed magma can conserve a high permeability (fig. 1.24). Although they invoked this possibility to explain permeability measurements in low crystallinity obsidian samples, this hysteresis behaviour of the permeability could also be present in magmas of higher viscosity and crystal content. Thus would result in the conservation of a significant magma permeability at low porosity. We aim at studying magma flow and degassing conditions evolution during transitions from effusive to explosive regimes. Magma erupting effusively has likely experienced several degassing events, and may conserve a high permeability at low porosities. We choose to use the Klug and Cashman (1996) permeability–porosity relationship, which was deduced from permeability measurements in natural silicic pumice, and assumes that the percolation threshold is 0, in agreement with the hysteresis possibility.

$$K_V = 2 \cdot 10^{-19} \phi_g^{3.5} \tag{1.28}$$

Permeability measurements on samples with elongated bubbles show that permeability in the direction of elongation can be 0.5 to 3 orders of magnitude higher than orthogonal permeability (Wright et al., 2006; Klug et al., 2002; Degruyter et al., 2009; Rust and Cashman, 2004; Blower, 2001; Bouvet de Maisonneuve et al., 2009). In our models, the capillary number for bubbles Cx is higher than 1 in most of the conduit, where the gas phase is present. Bubbles can then deform and have an elongated shape. We therefore consider that, in the conduit, the horizontal permeability K_H is ten times smaller than the vertical permeability K_V (Collombet, 2009). This simple consideration of anisotropy could however be improved by linking K_H/K_V with flow conditions and with the bubble capillary number. This is discussed in chap. 3.

Mechanisms for permeability development Inside the magma, permeability develops due to bubble coalescence and possibly magma fracturing. Although several studies described observations of bubble coalescence stages (e.g. Castro et al., 2012), the mechanisms for bubble coalescence are still poorly understood. The geometrical characteristics of the bubble network (e.g. Degruyter et al., 2009), the magma viscosity, and the presence of crystals (Melnik and Sparks, 2002; Blower, 2001) have been proven to have a huge control on coalescence and permeability development. Such parameters may also explain the wide variability in permeability measurements on natural samples. We will further discuss permeability development due to coalescence in chapter 3.

Recent work on magma rheology evidenced that, at andesitic volcanoes, magma can experience shear fracturing, which would be responsible for the formation of a damage halo at the conduit margins (Holland et al., 2011; Lavallée et al., 2013). Magma permeability in this area would be increased by up to three orders of magnitude in the direction of fractures, such promoting efficient gas transport at the conduit edges. These rheological observations give relevant explanation for degassing observations at Santiaguito (Bluth and Rose, 2004; Holland et al., 2011). Besides, Gaunt et al. (2014) observed the presence of such a damage area around spines extruded at Mount St Helens, where the vertical permeability was up to four orders of magnitude greater than horizontal permeability. Magma fracturing may be of great importance for understanding magma permeability and degassing in the conduit uppermost part. However, brittle failure criteria for three–phase magmas does not exist for the pressure ranges we are interested in (Shields et al., 2014). In this study, we thus rely on permeability measurements for silicic lava samples (Klug and Cashman, 1996), and do not further take into account magma fracturing influence.

1.6.1.3 Surrounding rock permeability

Permeability in the volcanic edifice is badly constrained. It depends on the initial permeability of the rocks composing the edifice and on the presence of fractures. Edifice permeability can also vary with space and time due to deposits compaction, fracture closing, and the formation of mineral deposits in association with hydrothermal circulations of water and gas. Eventually, the transition of the rock rheology from brittle to ductile close to important heat sources (e.g. magma reservoirs) can cause a local decrease in the rock permeability. In the absence of any typical permeability profile estimation in andesitic volcanic edifices, we assume a constant and isotropic permeability value in the rocks surrounding the conduit. A permeability of $10^{-12}\mathrm{m}^2$ is in agreement with several permeability estimation and measurements for volcanic edifice rocks (Melnik and Sparks, 2002; Edmonds et al., 2003; Farquharson et al., 2015; Kushnir et al., 2016; Kendrick et al., 2016). The influence of the surrounding rock permeability is however discussed in Chevalier et al. (2017) (chap. 2).

1.6.2 Mass conservation for the gas

In the magma and surrounding rock, the magma gas content, at a given, fixed point, evolves due to (i) volatile exchanges between the melt and gas phases (dissolution or exsolution), (ii) magma flow that advects bubbles, and (iii) gas flow through the permeable magma and surrounding rock. In order to study the evolution with time of the gas content and of degassing conditions, we solve a mass conservation equation for the gas that takes into account these three terms. We calculate a time–dependent solution for the gas pressure p_g, which enables us to follow the evolution of gas pressure in the conduit and of gas flux at the conduit edges with time. Bubble advection due to magma flow can be equated with a gas flux having the following velocity $\mathbf{u_a}$:

$$\mathbf{u_a} = \mathbf{u}\varphi_g \tag{1.29}$$

We assume that gas flow does not affect magma flow conditions during the time considered for degassing (a few hours). This hypothesis can be considered as valid as long as the magma viscosity is high enough. The magma porosity and permeability are assumed to be constant with time along degassing calculation, as well as the magma pressure and velocity fields. As a consequence, the gas exsolution flux is constant, and accounts for magma decompression while rising through the conduit. The expression for the gas exsolution rate comes from mass conservation equations for dissolved volatiles in the bulk magma:

$$Q_{melt \rightarrow gas} = -\nabla \cdot (\mathbf{u}\varphi_m C_m \rho_m) \tag{1.30}$$

where $Q_{melt \rightarrow gas}$ is the volatile mass flux from the melt to the gas phase. φ_m and ρ_m are the melt volume fraction and density. Assuming a Darcian permeable gas flow with a gas velocity u_d, the final mass conservation equation for the gas is given in (1.31):

$$\frac{\partial m_g}{\partial t} = -\nabla \cdot ((\mathbf{u_d} + \mathbf{u}\varphi_g)\rho_g) - \nabla \cdot (\mathbf{u}\varphi_m C_m \rho_m) \tag{1.31}$$

Where m_g is the mass of gas in one unit volume of magma. Since magma porosity is constant during gas flow calculation, m_g is related to the gas pressure:

$$p_g = \frac{RTm_g}{M\varphi_g} \tag{1.32}$$

with $R = 8.314\text{J.mol}^{-1}.\text{K}^{-1}$ the universal gas constant, $M = 0.018\text{g}\cdot\text{mol}^{-1}$ the water molar mass, and T the gas temperature (T=1100K). Equation (1.31) can then be arranged in :

$$\varphi_g \frac{\partial p_g}{\partial t} + \nabla \cdot (\frac{-K}{\mu_g} p_g \nabla p_g + \mathbf{u}\varphi_g p_g) = -\frac{RT}{M}\nabla \cdot (\mathbf{u}\varphi_m C_m \rho_m) \tag{1.33}$$

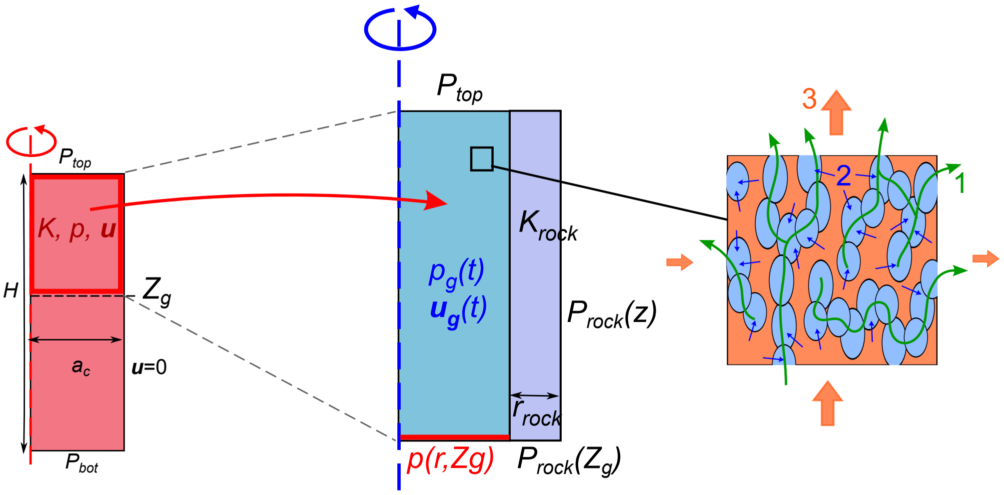

Figure 1.25: Gas flow time–dependent conditions are solved in the conduit and surrounding rock, taking into account (1) gas permeable flow, (2) gas exsolution from the magma and (3) bubble advection by the magma. Initial gas pressure, magma velocity and permeability are set using results from magma flow conditions calculation. The surrounding rock pressure conditions take into account the transition from hydrostatic to lithostatic pore pressure at depth, as well as a pressurisation effect from the conduit (section 1.7.2).

1.7 Numerical implementation of degassing

1.7.1 Geometry and mesh

The mass conservation equation for the gas is solved in the upper part of the conduit (2km) where most of gas exchanges occur, and in the surrounding rocks. The cylindrical conduit is surrounded with a shell of rock of width $r_{rock} = 5$m (fig. 1.25). We use a mesh of width 0.5m and length 5m in the rock surrounding the conduit.

1.7.2 Boundary conditions

1.7.2.1 Pressure at the top of the conduit

At the top of the conduit, we use a Dirichlet condition and impose an atmospheric gas pressure.

1.7.2.2 Pressure at the bottom of the conduit

At the bottom of the conduit, i.e. a depth of 2km, the gas pressure is assumed to be equal to the magma pressure, and is set again with a Dirichlet condition.

1.7.2.3 Pressure in the surrounding rock

At the rock shell edges, we impose a pressure condition P_{rock} that corresponds to the pore pressure in the volcanic edifice rocks and is detailed in the following paragraphs. We again use a Dirichlet condition.

The pore pressure, in volcanic edifices, depends on the circulation of fluids within the edifice rocks. It depends on the nature of these fluids, and on the rock permeability. When the rock is highly permeable, because of the host rock permeability and of the existence of a fracture network, fluid flow within the rock is easy, and a static state can be reached. The pore pressure then depends on the fluids nature. In dry meteorological conditions, for example, the top part of the volcanic edifice is likely filled with gas, and the pore pressure is close to atmospheric. In wet conditions, conversely, important water supply at the ground surface causes the edifice to be filled with water, and the pressure to be rather hydrostatic. At depth, however, the presence of magmatic intrusions causes heating of the rock, which leads locally to transitions of the rock behaviour from brittle to ductile that are associated with a drop in the rock permeability. In these area, the pore network is no more connected with the rest of the edifice, and the pressure is observed to be lithostatic, as it now depends on the surrounding rock confining pressure. Smaller changes in the rock permeability, due for example to alteration and mineral deposits, or the presence of important pore pressure sources, such as a hydrothermal system or the presence of the conduit, may lead to local changes in the pore pressure field.

We here tried to get the best compromise between realism and the model representativeness and simplicity. Because a large number of andesitic volcanoes are located in tropical regions (e.g. Soufrière Hills Volcano, Merapi, Santiaguito), under wet meteorological conditions with frequent water supply (Ball et al., 2015; Hurwitz et al., 2003), we assume that pore pressure in the upper part of the edifice is hydrostatic (fig. 1.26 and 1.27). We also assume that pore pressure evolves from hydrostatic to lithostatic at a depth Z_{lith}, set at 1500m (fig. 1.27). The depth of the brittle/ductile transition depends a lot on the volcanic activity and on the volcanic system. As it is badly constrained, we test the influence of varying Z_{lith} on degassing. The pore pressure in the rock surrounding the conduit P_{rock0} evolves with depth as described in equation (1.34), in which the density evolves from water density ρ_{H20} at the surface to crust density at depth and is described by the Comsol step function, f (with a transition zone width of 800m centered at $z = Z_{lith}$).

$$P_{rock0} = P_{atm} + P_d + gzf(\rho_{H20}, \rho_{rock}) \tag{1.34}$$

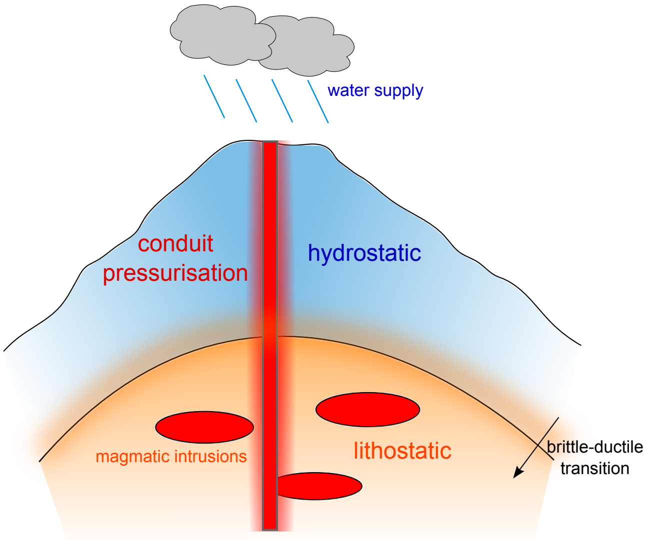

Figure 1.26: Simplified sketch of pore pressure conditions in the edifice. Frequent water supply because of rainfalls ensure the presence of a hydrostatic pore pressure in the top part of the edifice. At depth, rock heating due to volcanic activity and magmatic intrusions cause a transition from hydrostatic to lithostatic pressure. The high pressure in the conduit also causes a local increase in the surrounding rock pressure.

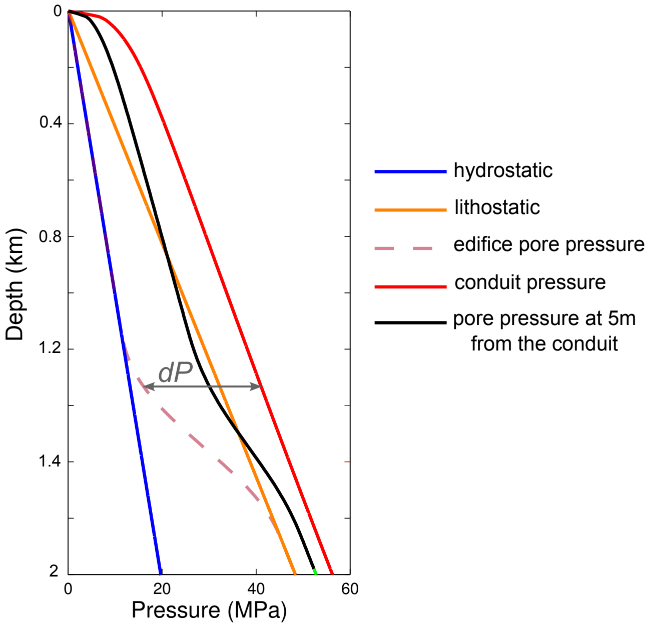

Figure 1.27: Pressure P_{rock} in the surrounding rock, at the distance r_{rock} ($r_{rock} = 5$m) (black curve), depends on surrounding rock pressure under loading far from the conduit P_{rock0} (purple curve) and on the conduit pressurizing effect. P_{rock0}, that is not influenced by the conduit, slightly evolves from hydrostatic (blue curve) to lithostatic (orange curve), with a Comsol smoothed step function (transition of width 800m centered at $Z_{lith} = 1500$m). Overpressure in the conduit has a pressurizing effect that depends on the difference dP between the conduit (red curve) and the surrounding rock P_{rock0} pressures, and on a radius–dependent coefficient c, that comes from elastic deformation equations: $c = a_c^2/(a_c + r_{rock})^2$ (≈ 0.56 at $r_{rock} = 5m$, for a conduit radius of 15m).

The high pressure in the conduit has a pressurising effect in the surrounding rock. This effect depends on the pressure difference between the conduit and rock pressures, and on the distance from the conduit. We take this pressurising effect into account to estimate pressure boundary conditions at the rock shell edges.

$$P_{rock} = P_{rock0} + \frac{r_{rock}^2}{(a_c + r_{rock})^2}(p_{r=ac} - P_{rock0}) \tag{1.35}$$

1.7.3 Initial conditions

The magma porosity, pressure, velocity and dissolved water content are set from the magma flow conditions solution. Besides, gas initial pressure in the conduit is equal to the magma pressure. In the surrounding rock, gas initial pressure evolves linearly from conduit pressure to the pressure boundary condition set at the rock edges.

1.7.4 Solver options

The time–dependent solution for gas pressure in the conduit and surrounding rock is calculated using the Comsol Multiphysics finite element software (version 4.4), using quadratic interpolation for gas pressure. Equations are solved using the MUMPS direct solver, with a convergence criteria defined from tolerance (error tolerance=0.001). We impose an initial time step of 10^{-7}s. Steady–state conditions for gas flow are reached in a few hours in most of the models.

In some models in which initial conditions for gas flow were defined from a solution for magma flow that had not been calculated using the Comsol 4.4 version, some oscillations could grow along with time–dependent calculation, that may be due to the evolution of discretisation methods, solvers, and tolerance criteria defined in this Comsol version. Following advices from the Comsol support, we added in this case some isotropic diffusion in the gas flow model. This added diffusion allows calculation without singularities growing up, and was limited to values sufficiently low so that the global solution for gas flow is not affected. We had to use this adaptation for models presented in chap. 2, for example, for which initial magma flow conditions were calculated using the Comsol version 3.5.

1.7.5 Benchmark

Here we compare our results for gas flow with results obtained using the gas flow model proposed by Collombet (2009). The model used in Collombet (2009) for

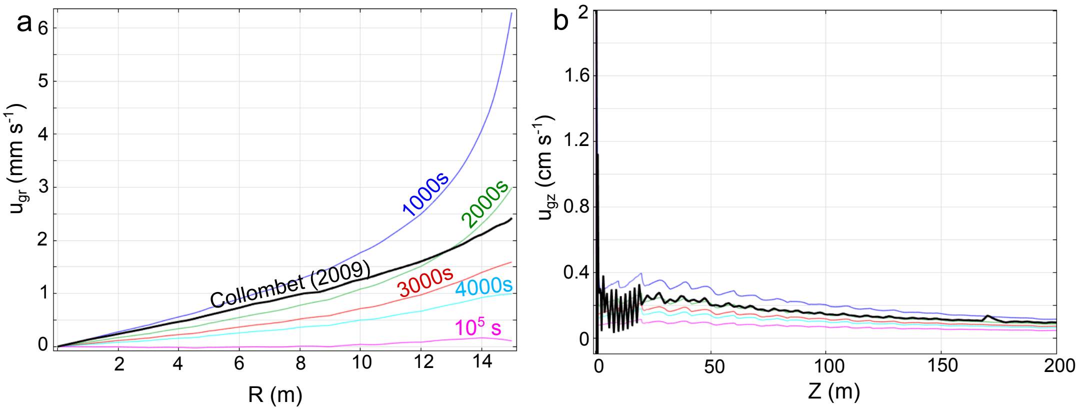

Figure 1.28: Evolution of gas vertical and horizontal velocity in the conduit. We here compare the solution from Collombet (2009) with our time–dependent solution, at different time steps. (a) Horizontal gas velocity, at a conduit depth z=100m. (b) Vertical velocity, at a conduit radius r=5m.

gas flow calculation is a steady–state solution that does not take into account gas exsolution from the melt. In order to compare our results with this solution, we here neglect gas exsolution during gas flow calculation. We also assume that pressure at the conduit walls is purely hydrostatic, as in Collombet (2009). Since we use the same initial calculations for both models (closed system), with the same boundary conditions, the steady–state solutions in both models should be similar. Fig. 1.28 presents gas velocities from the steady–state solution from Collombet (2009), and for several time–steps extracted from our time–dependent solution. We notice that solutions at steady state are not identical. The steady–state solution from Collombet (2009) is indeed closer to the solution we get for a calculation time of 2000s. This might be linked with the solver options used in Comsol Multiphysics. A relatively high tolerance for the determination of steady–state solution might explain such results.

1.7.6 Results

We here used the steady–state effusive flow conditions from Collombet (2009) as initial conditions (pressure, magma velocity, viscosity and porosity) for gas flow. Results for time–dependent gas flow from this initial conditions are presented in fig. 1.29. In most of the conduit, the gas pressure decreases (fig. 1.29) with time. At the top of the conduit, conversely, the gas pressure is increasing.

In the model from Collombet (2009), gas loss is calculated from gas fluxes at steady–state conditions for the gas. In addition, gas flow conditions do not take into account gas exsolution from the magma. Results from this model provide evidence for the formation of law vesicularity layers at the top of the conduit and at the conduit edges. Taking gas exsolution into account, as we do in our model, may however have led to different results. This may be a reason why we observe in our results an increase in gas pressure (fig. 1.29), and therefore a trend towards magma gas content increase at the top of the conduit, in contradiction with the important degassing observed there in Collombet (2009).

We also notice from our results that the gas pressure evolves quickly during the first hours, and stabilises at a time of about 20 hours. We see from fig. 1.29a, that the pore pressure in the rock tends to be constant with the distance from the conduit, while the pressure in the conduit evolves significantly with distance from the conduit center. This is due to the difference in horizontal permeability between the rock (K_{rock}=10^{-12}m^2) and the conduit (K_H=10^{-17}-10^{-13}m^2).

Gas permeable flow depends on permeability and on pressure conditions. Results may therefore evolve for varying permeability conditions in the conduit and in the rock, as well as with variations in the pressure conditions at the top of the conduit and in the surrounding rock. The influence of these different parameters on gas flow, as well as the possible consequences for gas loss evolution during an eruption are discussed in Chevalier et al. (2017) (see chap. 2).

1.7.7 Coupling with magma flow conditions

Because of degassing, flow conditions likely evolve with time, as gas depleted magma rises in the conduit. In order to be able to follow magma flow conditions evolution with gas loss and with variations in the degassing conditions, gas and magma flow conditions need to be coupled. Gas loss therefore has to be taken into account when calculating magma flow conditions.

1.7.7.1 Steady–state effusive conditions (Collombet, 2009)

A coupling model was proposed by Collombet (2009) for calculating steady–state effusive magma flow conditions. In this model, magma flow conditions are first calculated in the conduit, using a model similar to the one described here. The resulting magma pressure, porosity and velocity are then used to calculate a steady–state solution for gas flow. Based on these steady–state gas flow conditions, gas loss is calculated in the conduit. The resulting new amount of gas in the conduit $C_{H_2O,new}$ is then used for calculating new magma flow conditions, assuming that gas pressure equals the magma pressure.

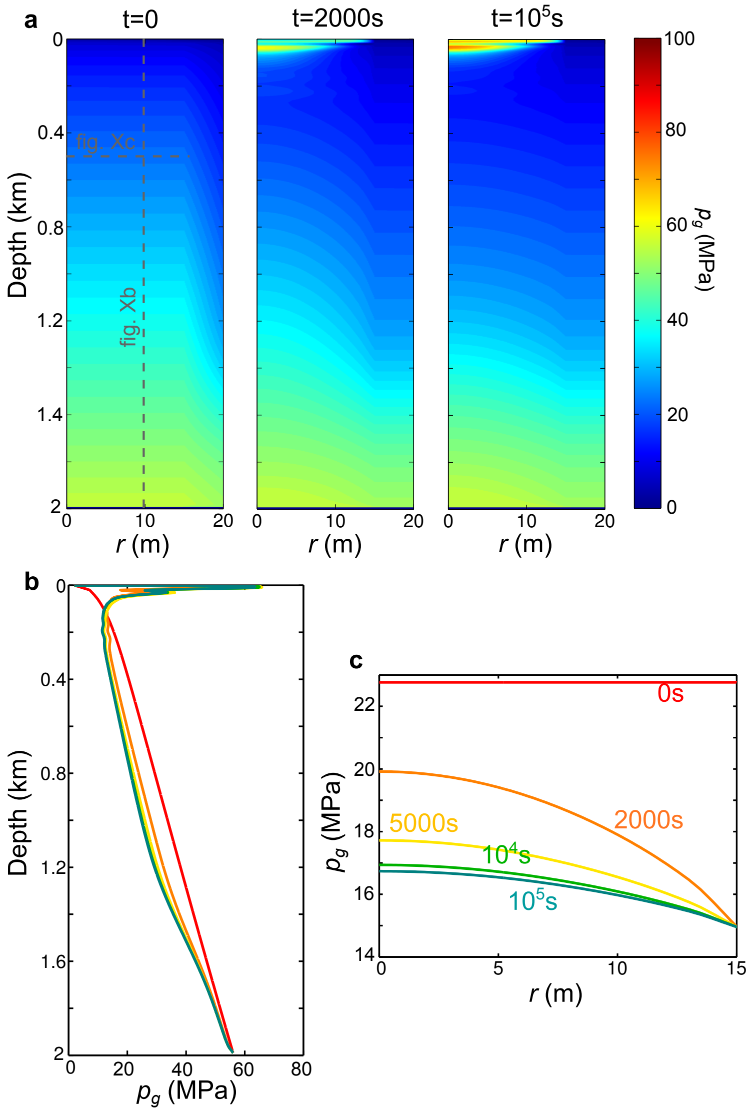

Figure 1.29: Gas pressure evolution with time during degassing. (a) Gas pressure in the conduit at different times. (b) Gas pressure at the conduit center, for different times. (c) Gas pressure in the conduit at a depth of 500m, corresponding to the same solution times as in (b).

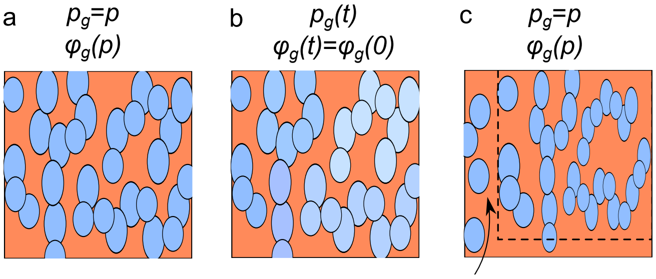

Figure 1.30: Sketch of the assumptions used for coupling magma and gas flow in a steady–state effusive regime. During degassing, the gas pressure varies and we get a new gas mass fraction. For solving magma flow conditions, the new gas volume fraction is calculated assuming that gas pressure is equal to the magma pressure. This supposes an instantaneous adaptation of the magma porosity. This is not compatible with a time–dependent study as magma supply cannot instantaneously accommodate the volume difference created this way.

1.7.7.2 Transient regimes

In transient regimes, boundary conditions evolve with time. Using a gas flow steady–state solution for calculating gas loss is not appropriate here. Indeed, steady–state for the gas is reached in a few hours, along which significant amounts of gas are lost and magma flow conditions likely evolve. We therefore rather deduce gas loss from the gas pressure evolution with time.

Even with this adapted gas loss calculation, we cannot use the same calculation sequence as Collombet (2009). Solving for a steady–state solution does not require to use a pathway that is meaningful for time. In the model from Collombet (2009), magma porosity is constant during gas loss calculation, and the gas and magma pressure are different. During magma flow conditions calculation however, the gas pressure is assumed to be equal to that of the magma, and the porosity is deduced from this assumption. This is equivalent to assuming that, during gas loss calculation, gas flow reaches steady–state with a much shorter time scale than magma flow, and conversely that during magma flow calculation flow conditions adapt instantaneously to gas loss (fig. 1.30). Using such assumptions for calculating a time–dependent evolution of magma flow conditions would be contradictory and lead to results that may not be representative of the real evolution of flow conditions (fig. 1.31).

At the gas flow calculation onset, gas loss would indeed be much more important at the conduit edges (where radial pressure gradients are important) than at the center of the conduit. This would lead, during new magma flow conditions calculation, to a collapse of the magma matrix at the conduit edges. The system would then evolve towards a solution in which magma at the conduit center contains a high amount of gas content, similar to closed conditions, while a very degassed,

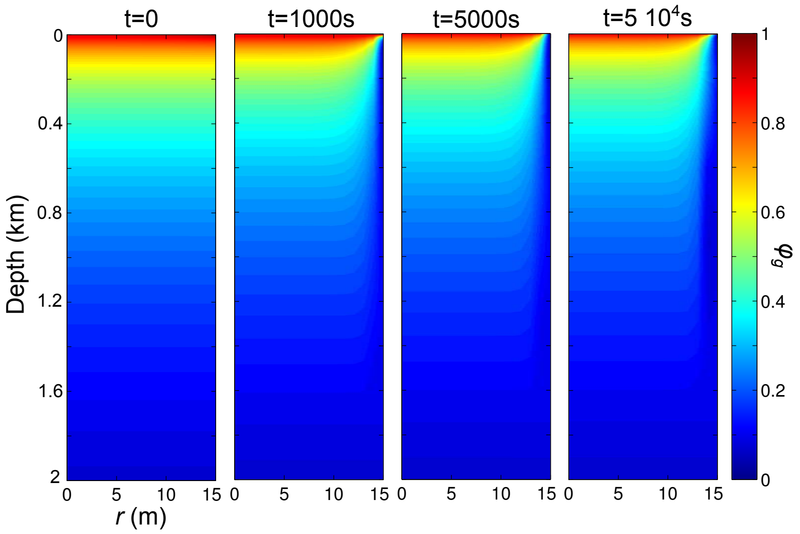

Figure 1.31: Gas volume fraction evolution in the conduit with time using assumptions that (i) during degassing calculation magma flow conditions remain constant and (ii) when calculating new flow conditions, the gas pressure is equal to the magma pressure. The calculation sequence was iterated 50 times, each iteration corresponding to an episode of degassing lasting for 1000s, and the calculation of new steady–state magma flow conditions. Initial conditions are closed system steady–state flow conditions (section 1.4). Using different initial conditions, the system evolves towards similar final conditions.

low permeability layer forms at the conduit margins (fig. 1.31).

In order to couple magma and gas flow, the equations and models need to be adapted using less extreme assumptions. This is the aim of chap. 5. Using effusive initial conditions, the steady–state solution for gas flow can however already provide some interesting information on degassing conditions evolution during an eruption. This is discussed in chap. 2.

1.8 Conclusion

We proposed new models for magma and gas flow conditions in the upper conduit. We provide evidence that the composition of the magma (crystals and water content) has an important influence on flow conditions, while the influence of the conduit geometry is of second–order. We also presented a new time–dependent gas flow model for the upper conduit, that is suitable for studying gas flow conditions in transient regimes. This model is used in chap. 2 for identifying the controlling parameters for gas loss during an eruption, and quantify their influence on volcanic activity evolution.

These models still need to be adapted so that magma and gas flow can be fully coupled in transient regimes. This aspect is discussed in details in chap. 5, in which we give a proposition of adaptation.

Chapter 2

Effects of dome emplacement on magma flow and degassing conditions

Contents

2.1 Introduction

Gas flow in the upper conduit of silicic volcanoes mainly depends on two parameters that are the permeability and the pressure gradient within the conduit and surrounding environment. These two parameters evolve both with time and with space. Magma permeability evolves with magma decompression and bubble coalescence. It can also be very different from permeability in the rock surrounding the conduit. Along with an eruption, permeability and pressure conditions in the conduit and in the surrounding rock may evolve, as well as the volcanic edifice structure, inducing variations of degassing conditions in the upper conduit.

During effusive phases at andesitic volcanoes, a dome often forms as highly viscous, gas depleted magma extrudes from the conduit. Although being associated with relative quiescent periods, domes sometimes collapse, generating pyroclastic flows that can be devastating (Newhall and Melson, 1983; Sato et al., 1992; Ogburn et al., 2015). Hazard during dome growth episodes is mainly related to degassing conditions in the conduit and dome. Pyroclastic flows intensity indeed depends on the gas overpressure within dome rocks (Kueppers et al., 2006; Mueller et al., 2011). Besides, in the case of a major dome collapse, decompression of the conduit may trigger a much more destructive event, depending on conditions in the upper conduit (Druitt et al., 2002; Robertson, 1998). Quantifying the evolution of gas loss along with dome formation is of great interest for evaluating hazard evolution during dome emplacement.

Studying degassing conditions evolution during dome growth is also the occasion of estimating the influence of conduit and surrounding rock conditions on gas flow. Dome growth is indeed associated with pressure loading at the top of the conduit, that causes pressure and permeability evolution both within the conduit and within the surrounding rock. In addition, its presence at the top of the conduit prevents gas leakage to the atmosphere. Here we quantify the influence of each of these effects on gas loss, separately. Starting from steady–state effusive conditions (Collombet, 2009), we solve time–dependent gas flow under varying conditions.

This work resulted in one article (Chevalier et al., 2017) that is attached to this chapter. In the following sections, we give some precision on the conditions and models we use here.

2.2 Initial conditions: Steady–state effusive conditions from Collombet (2009)

Though we proposed numerical models adapted for magma flow and gas flow modelling, we demonstrated in chap. 1 that they cannot be used in a fully coupling way

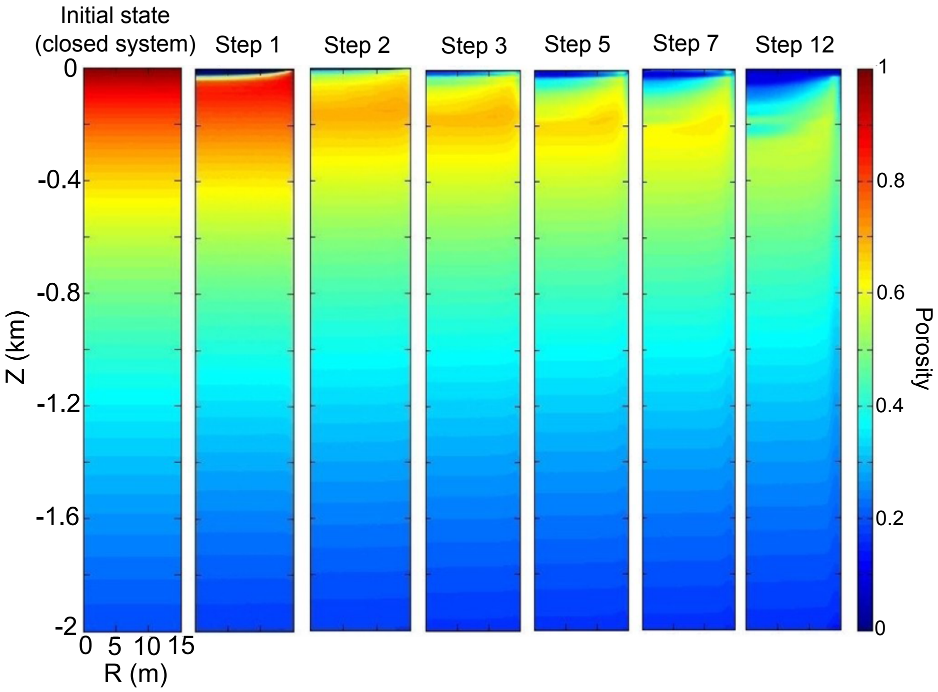

Figure 2.1: Evolution of magma porosity with calculation iterations, from Collombet (2009). Each iteration (step) corresponds to the succession of (1) gas loss calculation, using the steady–state solution for gas flow, and (2) integration of the resulting new magma volatile content to magma flow conditions calculation. The final solution is reached when the two models (gas loss and magma flow) converge. We use this final solution as an initial condition for calculating gas loss evolution with dome growth.

because of some assumptions made for solving magma flow conditions. This aspect will be discussed further in chap. 5, where an adaptation of the models is proposed so that magma flow and gas loss can be fully coupled in transient regimes. The model we developed for degassing with time–dependence is however a great tool to study and discriminate the major controls on gas loss, and get some clues for the interpretation of more complex numerical models (such as a fully coupling model).

We here use as initial condition a steady–state effusive solution from Collombet (2009) for magma and gas flow within the conduit. This solution was obtained by coupling iteratively magma flow with gas flow, until convergence of the two models is obtained (fig. 2.1). Each iteration step does not follow a real time–dependent path, which is valid here because the model aims at reaching a steady–state solution. The two models for magma flow and for gas flow are slightly different from the models we proposed in chap. 1, and these differences are specified here.

2.2.1 Magma flow

The model used by Collombet (2009) for solving steady–state magma flow conditions in the conduit is close to the one proposed by Collier (2005). The major differences between these models and the magma flow model we presented in chap. 1 come from:

- Magma composition: in the model used by Collombet (2009), the initial volume fraction of crystals accounts for 42% of the ground mass, versus 40% in the model we presented in chap. 1.
- Crystallisation: some crystallisation, depending on magma pressure, was included in the model from Collombet (2009). This causes a slight change in the magma viscosity evolution with depth.
- Adaptations due to scientific progress: The models used by Collier (2005) and Collombet (2009) date back to 2006. Since then advances have been made about magma rheology that we included into our magma flow model. This concerns bubble deformation (we use Cx instead of Ca) and crystals influence on viscosity (we do not use the same coefficients in the Einstein–Roscoe equation).
- Evolution of Comsol Multiphysics: The software Comsol Multiphysics that we use for solving our models also evolved a lot since 2009. The solvers, discretisation method, as well as convergence criteria changed between the 3.5 version used by Collier (2005) and by Collombet (2009) and the 4.4 version that is used for solving our models.

The solutions for magma flow from our model and from the model used by Collombet (2009) however remain quite similar, at least in closed system conditions (see chap. 1, section 1.4.3).

2.2.2 Gas flow

The model and method used by Collombet (2009) for gas loss are however quite different from ours, the major differences being:

- Gas loss is calculated using steady state gas velocities. This assumption is suitable in the model proposed by (Collombet, 2009), since a steady–state solution is searched, in which gas flow is at steady–state, without considering any significant temporal evolution. It is however no longer appropriated when studying gas loss in eruptive conditions that vary with time. This is why we rather solve a time–dependent equation for gas flow in our model.

- The source term corresponding to gas exsolution from the melt is neglected.
- Comsol software evolution. Again, the evolution of the comsol software may impact the solutions of the models. In particular, we show in the chap. 1, section 1.7.5, that the steady–state solution calculated with the comsol version 3.5 looks to correspond to the time–dependent solution we get for gas flow at 1500s, which is not equal to the steady–state solution we would get with our model.

Our gas flow model is therefore quite different from the one used by (Collombet, 2009), mainly because we consider time–dependence for gas flow conditions.

2.3 Calculation sequence for studying the possible dome effects

2.3.1 Gas flow model adaptation

In order to study the possible effects dome emplacement may have on gas flow within the conduit, we need to adapt some aspects of the model we presented in chap. 1. The presence of the dome impacts on gas flow conditions by (1) loading the top of the conduit and the surrounding rock and (2) limiting gas leakage to the atmosphere at the top of the conduit by the presence of new permeable material above the conduit. In our model, the presence of the dome is modelled either by setting the top of the conduit boundary condition to the pressure at the base of the dome, or by adding to the model domain a permeable domain that accounts for the dome presence (Chevalier et al., 2017, fig. 1).

Boundary conditions at the edges of the rock shell that surrounds the conduit domain are also modified to take into account permeability evolution in the surrounding rock by fracture closing, and pressure conditions evolution due to dome loading (Chevalier et al., 2017, sections 2.5.4–2.5.5).

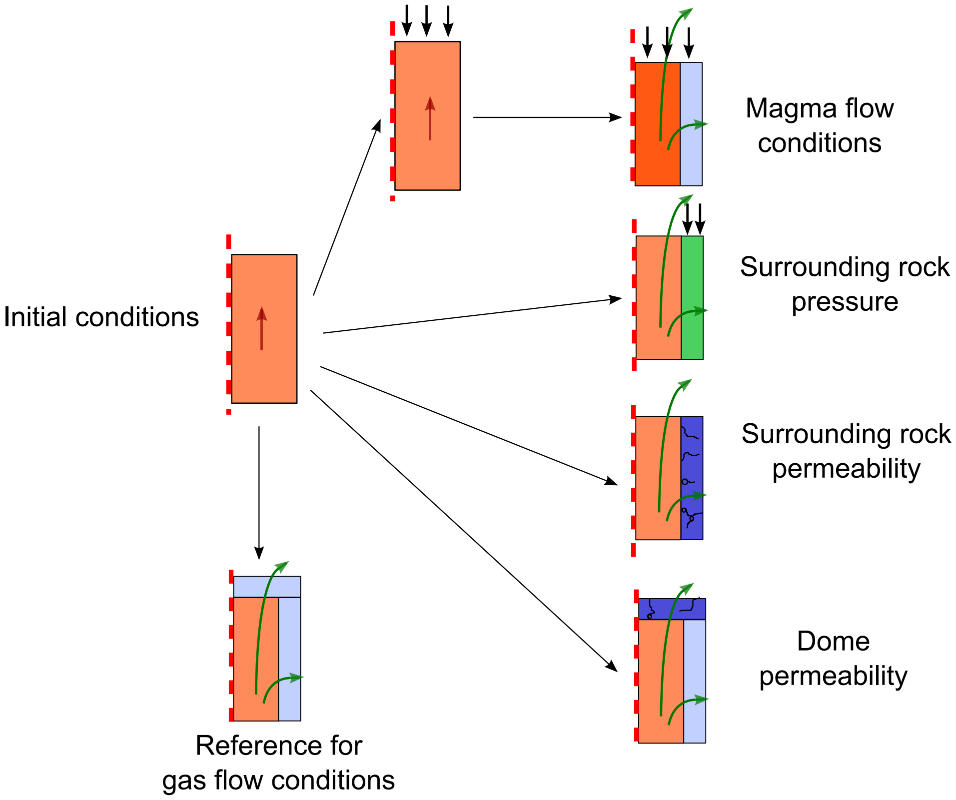

Figure 2.2: Sketch of the different calculation sequences used for evaluating the influence on gas loss of the possible effects associated with dome growth. The possible effects (flow conditions evolution, permeability and pressure in the surrounding rock, permeability in the dome) are tested separately. Their influence on flow conditions is then obtained by comparison with a reference case, that corresponds to effusive extrusion without dome formation. We then finally compare their relative importance.

2.3.2 Calculation sequence

Figure 2.2 resumes the calculation sequence used for evaluating the influence on gas flow of the different effects of dome growth:

- Evolution of magma flow conditions. New magma flow conditions are first calculated using the magma flow model from Collombet (2009). We then use these flow conditions as new initial conditions for gas flow calculation.
- Pressure increase in the surrounding rock. In this case, pressure conditions at the surrounding rock edges are adapted to account for dome loading.
- Surrounding rock permeability. Permeability in the surrounding rock here evolves because of fracture closing due to dome loading. The new permeability conditions are calculated using the same law as in Taisne and Jaupart (2008).
- Dome permeability. We here vary the permeability of the domain representing the dome.

We then compare the influence of these different parameters on gas pressure evolution in the conduit and on gas loss. Results are presented in Chevalier et al. (2017) (see section 2.4).

2.4 Temporal evolution of magma flow and degassing conditions during dome growth, insights from 2D numerical modeling

Journal of Volcanology and Geothermal Research 333-334 (2017) 116–133

Contents lists available at ScienceDirect

Journal of Volcanology and Geothermal Research

journal homepage: www.elsevier.com/locate/jvolgeores

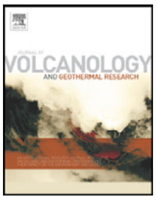

Temporal evolution of magma flow and degassing conditions during dome growth, insights from 2D numerical modeling

Laure Chevalier*, Marielle Collombet, Virginie Pinel

Institute of Earth Sciences (ISTerre) - IRD, Université Savoie Mont Blanc, Campus Scientifique, Le Bourget-du-Lac cedex 73376, France

ARTICLE INFO

Article history:
Received 5 February 2016
Received in revised form 13 January 2017
Accepted 19 January 2017
Available online 21 January 2017

Keywords:
Dome emplacement
Andesitic volcano
Magma flow
Magma degassing
Numerical modeling

ABSTRACT

Understanding magma degassing evolution during an eruption is essential to improving forecasting of effusive/explosive regime transitions at andesitic volcanoes. Lava domes frequently form during effusive phases, inducing a pressure increase both within the conduit and within the surrounding rocks. To quantify the influence of dome height on magma flow and degassing, we couple magma and gas flow in a 2D numerical model. The deformation induced by magma flow evolution is also quantified. From realistic initial magma flow conditions in effusive regime (Collombet, 2009), we apply increasing pressure at the conduit top as the dome grows. Since volatile solubility increases with pressure, dome growth is then associated with an increase in magma dissolved water content at a given depth, which corresponds with a decrease in magma porosity and permeability. Magma flow evolution is associated with ground deflation of a few μrad in the near field. However this signal is not detectable as it is hidden by dome subsidence (a few mrad). A Darcy flow model is used to study the impact of pressure and permeability conditions on gas flow in the conduit and surrounding rock. We show that dome permeability has almost no influence on magma degassing. However, increasing pressure in the surrounding rock, due to dome loading, as well as decreasing magma permeability in the conduit limit permeable gas loss at the conduit walls, thus causing gas pressurization in the upper conduit by a few tens of MPa. Decreasing magma permeability and increasing gas pressure increase the likelihood of magma explosivity and hazard in the case of a rapid decompression due to dome collapse.

1. Introduction

At silicic volcanoes (e.g. Soufrière Hills Volcano, Montserrat, Mount St Helens, United States, Merapi, Indonesia, Volcán de Colima, Mexico) periods of relative quiescence, with effusive lava flows and dome emplacement, alternate with explosive, sometimes very violent events. A dome forms when highly viscous, gas depleted lava, is extruded from the vent. Such activity may last for months to years, with each of several extrusion episodes lasting several days to a few weeks (Odbert et al., 2014; Ogburn et al., 2015; Sparks et al., 1998; Swanson and Holcomb, 1990). Domes are composed of a malleable core, surrounded by a brittle carapace that sometimes breaks out, feeding the talus apron around the dome (Hale et al., 2009a,b; Wadge et al., 2009). The internal part, the core, might contain pressurized gas, whereas the external part, the carapace and the talus are expected to be highly fractured and degassed. The dome shape depends on the relative proportion of the core and the talus as evidenced by the numerical modeling of the endogenous growth (Hale et al., 2009b) but generally has a flat, rounded shape, and can be a few hundred meters high (Swanson and Holcomb, 1990). Superficial dome failures often generate pyroclastic flows, sometimes associated with vulcanian explosions (Newhall and Melson, 1983; Ogburn et al., 2015; Sato et al., 1992). Less frequently, major dome collapses can trigger huge decompression inside the dome and the upper conduit, leading to major explosive eruptions that destroy the dome (Druitt et al., 2002; Robertson, 1998). Field observations (Johnson et al., 2008; Watts et al., 2002), as well as experimental dome rock characterization (Kendrick et al., 2013; Lavallée et al., 2013) and numerical modeling of dome emplacement (Ball et al., 2015; Hale et al., 2009b; Hale and Wadge, 2008) improved our understanding of dome structure and possible causes of collapse. Although those results clearly helped for dome collapse risk assessment (location and frequency), they give little information on explosion intensity. Besides these studies do not take into account how the dome growth might influence the magma flow within the conduit and the associated extrusion rate.

Explosive activity at andesitic lava domes is caused by the fragmentation of low porosity magma, which occurs when strain rate

---

* Corresponding author.
E-mail address: laure.chevalier@univ-smb.fr (L. Chevalier).

http://dx.doi.org/10.1016/j.jvolgeores.2017.01.016

or bubble overpressure, in case of a rapid decompression, exceed the magma tensile strength (Alidibirov and Dingwell, 1996, 2000; Spieler et al., 2004). Decompression experiments on pyroclasts of various porosity and composition evidenced that, on the one hand, the decompression rate needed for magma fragmentation decreases as porosity increases (Spieler et al., 2004) and increases as permeability increases (Mueller et al., 2005, 2008; Spieler et al., 2004). On the other hand, explosion intensity is positively correlated with porosity and bubble overpressure (Kueppers et al., 2006; Mueller et al., 2011). These experimental observations are in agreement with statistical observations at andesitic lava domes (Ogburn et al., 2015), which point out that explosion intensity increases with extrusion rate, which is thought to control magma degassing ability. Gas emission monitoring and field observations at Soufrière Hills Volcano (Edmonds et al., 2003; Watson et al., 2000), Santiaguito (Johnson et al., 2008), Galeras (Stix, 1993) and Lascar (Matthews et al., 1997) silicic lava domes provide evidence that degassing rates were correlated with observed volcanic activity and geophysical signal (seismicity, ground deformation). These variations in degassing regime were attributed to dome and superficial surrounding rock permeability evolution, arguing that dome permeability could have a major impact on magma degassing and gas pressurization, and then on explosion intensity (Edmonds et al., 2003). However, although bubble overpressure build up (Melnik and Sparks, 2005; Sparks, 1997) and degassing (Collombet, 2009; Diller et al., 2006) have been investigated through conduit flow numerical models, possible effects of dome growth on degassing conditions, which may result in magma explosivity evolution and feedback relationships, have not been estimated yet.

The presence of a less permeable dome above the conduit could be responsible for gas pressurization inside the conduit (Collinson and Neuberg, 2012). Aside from controlling degassing via its own permeability, the forming dome exerts pressure loading on the volcanic system and surrounding rock. Pressure loading causes a permeability decrease in the rock surrounding the conduit by closing fractures, possibly limiting gas leakage at the conduit, then causing gas pressurization (Taisne and Jaupart, 2008). Moreover, pressure increase in the conduit may cause a porosity and permeability decrease, as water solubility is pressure dependent, resulting in important changes in magma degassing ability. Further, open-system gas loss not only depends on rock and magma permeability but also on the pressure gradient between the magma and the surrounding rocks. Pressure gradient evolution in the conduit and surrounding rock induced by dome formation will thus also influence degassing. Such effects on magma flow and degassing conditions, and their implications for magma explosivity have never been modeled in realistic dome forming conditions.

The purpose of this article is to quantify the possible effects, and their relative importance, of dome emplacement on magma flow and degassing. As magma flow conditions evolve in the conduit, there may be detectable ground displacement (Albino et al., 2011; Beauducel and Cornet, 2000), which may be relevant for eruption monitoring. We therefore also quantify ground deformation associated with magma flow evolution during dome growth. We develop a numerical model for the magma flow within the conduit beneath the dome, that successively solves for (1) magma flow, (2) surrounding rock deformation, and (3) gas flow through the conduit, surrounding rock and dome, in 2D axisymmetry. Starting from 2D steady state effusive initial conditions from Collombet (2009), we apply evolving boundary conditions according to dome construction. New magma flow conditions are first calculated. Pressure and permeability conditions are then extracted from the resulting flow conditions and used as initial conditions for gas flow calculation in 2D. The reason for modeling magma and gas flow conditions in 2D is that gas flow is extremely dependent on pressure gradient and on magma permeability, which may vary in both horizontal and vertical directions in the conduit, and control the ability of the gas to reach the conduit edges. In addition, 2D modeling gives information about magma gas content and pressurization across the conduit. We comment and discuss the evolution of magma permeability and gas pressure in the conduit during dome growth in terms of magma explosivity and risk assessment in case of a dome collapse.

2. Numerical modeling in 2D axisymmetry

2.1. Conceptual model

We consider an andesitic lava dome forming eruption (Fig. 1a). Magma flows from a shallow reservoir, at a few kilometers depth, in a vertical conduit of a few tens of meters in diameter. It feeds a dome, at the top of the volcano. Note that magma flow is only modeled within the conduit (red part in Fig. 1a), the magma extrusion rate at the conduit top $Q(t)$ is provided by the model and controls the growth of the dome. The reservoir and the dome respectively act as a bottom pressure condition and a top pressure and permeability condition. In the models presented here, we assume a conduit length H of 5 km (Barclay et al., 1998), a conduit radius a_c of 15 m (Swanson and Holcomb, 1990; Voight et al., 1999), and a constant dome aspect ratio D (height over diameter) of 0.25 (Matthews et al., 1997; Swanson and Holcomb, 1990). The dome height H_d varies from 0 to 300 m (Table 1).

Magma flow through the conduit applies pressure p and shear stress σ_t at the conduit walls, which causes conduit and volcano edifice elastic deformation. In addition, the weight of the forming dome induces ground subsidence. As magma rises in the conduit and undergoes decompression, magma porosity increases and its permeability develops: the gas is able to flow in both horizontal and vertical directions, and escapes at the conduit margins and top.

The forming lava dome exerts pressure loading on the conduit and surrounding rock. Due to pressure increase in the conduit, magma flow may evolve. As gas solubility (and then porosity and permeability) are pressure dependent, gas flow within the conduit is modified. Gas flow conditions also depend on pressure gradient evolution in the conduit and surrounding rock. In addition, the pressure exerted by the lava dome on the rock surrounding the conduit possibly causes compaction and fracture closing. This may induce permeability decrease in the surrounding rock, thus further impacting degassing. At the conduit top, the presence of the permeable dome prevents the gas escaping directly into the atmosphere.

2.2. 2D numerical integration strategy

Magma flow, gas flow and ground deformation are calculated in three distinct 2D axisymmetrical numerical models (Fig. 1a–c) that are detailed in the following sections (Sections 2.3, 2.5, 2.4). These three model components are solved with Comsol Multiphysics software. Since magma flow conditions and ground deformation closely interact (Albino et al., 2011; Beauducel and Cornet, 2000; Costa et al., 2009; De' Michieli Vitturi et al., 2008; Green et al., 2006; Nishimura, 2009), these two parts of the model are fully coupled: ground deformation depends on magma flow conditions (normal and shear stress exerted at the conduit edges) that are in turn affected by the deformed conduit geometry. Although magma and gas flow conditions are also extremely interdependent (e.g. Melnik and Sparks, 2005, Schneider et al., 2012), fully coupling magma and gas flow in 2D remains a complicated task due to the complexity of the physical system. Such models currently exist in 2D only for a steady state effusive regime (Collombet, 2009), which does not require time dependance. In the Collombet (2009) case, the steady-state can be reached numerically by a succession of intermediate states, having no temporal meaning. For transient regimes, however, time dependance is mandatory, and makes 2D coupled models even

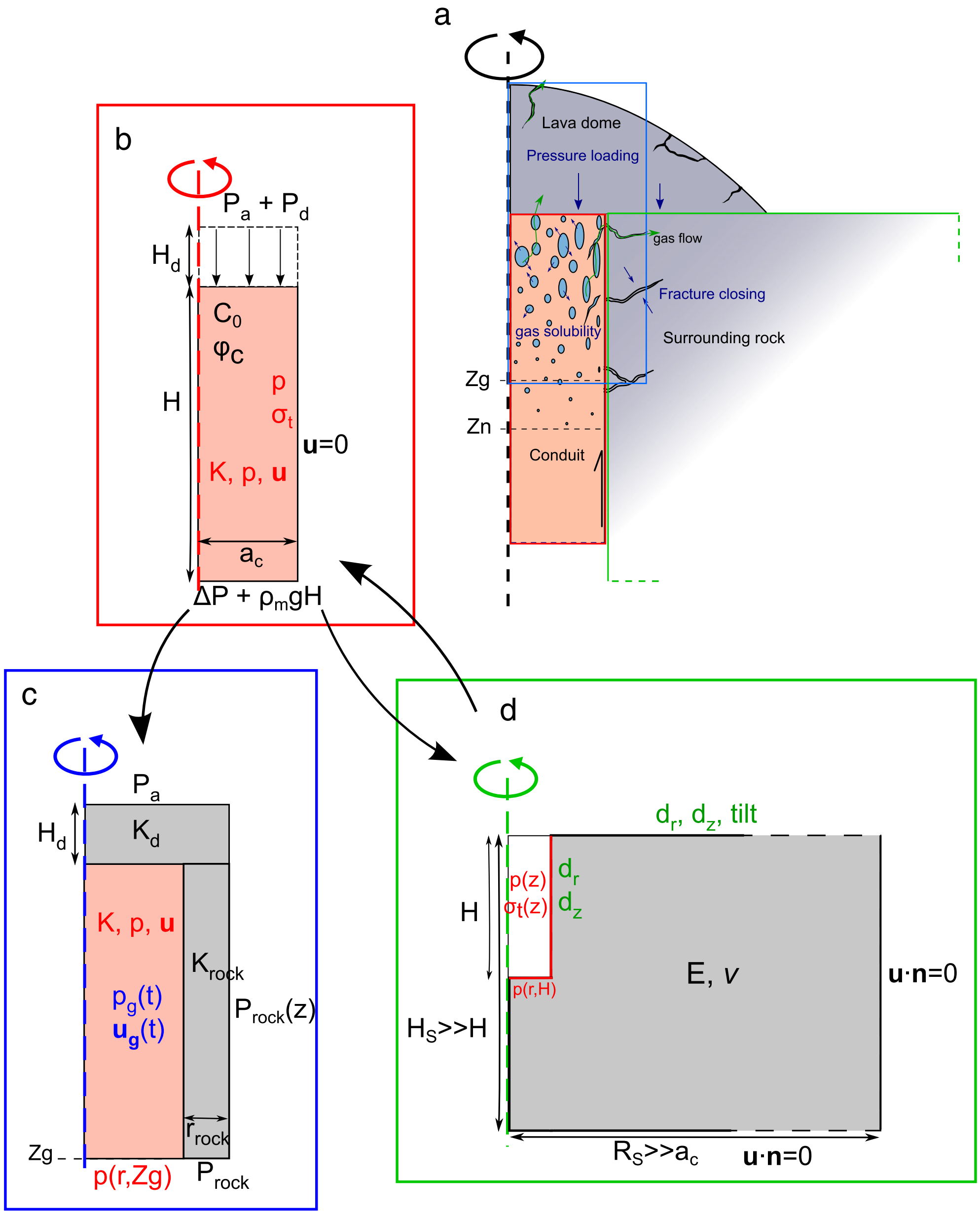

Fig. 1. (a) is a global sketch of magma flow, gas flow and rock deformation location inside the volcano, and their possible interaction. Models for magma flow, gas time-dependent flow through the conduit, surrounding rock and dome, and ground deformation are more specifically represented in (b), (c) and (d), respectively. Boundary conditions as well as entrance and exit parameters are specified. Black font accounts for fixed parameters (see Table 1). They can be constant or depth and radius dependent. Red, blue and green parameters come respectively from magma flow, gas flow, and ground deformation 2D models solutions (see Table 2). They are then both radius and depth dependent. Black arrows between the three models represent currently available coupling.

more complex to solve. No previous work addresses the problem in 2D with time-dependence. Here magma and gas flow conditions are one-way coupled: gas flow depends on magma flow conditions (pressure, velocity and permeability). However, magma flow does not take into account results from gas flow calculation along with dome growth (such as gas mass transfer and pressure), although the initial magma volatile content comes from the Collombet (2009) solution (Section 3).

Meshes used in the three model components were generated with Comsol Multiphysics. For magma flow, we use a mesh made of 1 m wide by 10 m deep rectangles. The mesh used for gas flow is finer, with 0.5 m by 0.5 m squares. For solid deformation of the solid country rock, the mesh is made of triangular elements that are refined at the conduit walls and at the surface (edges shorter than 1 m).

2.3. Magma flow

For numerical calculation cost and model simplicity, silicic magma is represented as a single compressible phase, whose bulk properties (density ρ, dynamical viscosity μ and volume viscosity κ) depend on the properties and interaction of the gas, liquid and solid phases (Collombet, 2009; Lensky et al., 2002; Prud'Homme and Bird, 1978). This assumption is valid at andesitic volcanoes because of the high magma viscosity, that makes the relative velocity of bubbles and crystals in the melt negligible compared with magma bulk velocity. Mass (Eq. (1)) and momentum (Eq. (2)) conservation equations for a single compressible phase are written as follows:

$$\nabla\cdot(\rho\mathbf{u}) = 0 \tag{1}$$

Table 1
Parameters used in the numerical models. Values used in the reference model (effusive regime, no dome is present) are indicated. The range of values used for testing the potential dome effects are specified where needed.

Parameter	Notation	Reference value	Tested values	References
Geometry				
Conduit radius	a_c	15 m		Swanson and Holcomb (1990), Voight et al. (1999)
Conduit length	H	5 km		Barclay et al. (1998)
Maximum dome height	H_d	0 m	0–300 m	Blake (1990), Swanson and Holcomb (1990)
Dome radius	R_d	0 m	0–600 m	
Dome aspect ratio	D	0.25		Matthews et al. (1997), Moriya (1978), Swanson and Holcomb (1990)
Gas exchange zone depth	Z_g	2 km		Collombet (2009)
Nucleation depth	Z_n	3.5 km		Collombet (2009)
Rock shell width	r_{rock}	5 m		Collombet (2009)
Pressure transition depth	Z_{lith}	1.5 km	1–2 km	Fournier (2006)
Constant parameters				
Ideal gas constant	R	$8.314\ \mathrm{J \cdot mol^{-1} \cdot K^{-1}}$		
Gravity acceleration	g	$9.81\ \mathrm{m \cdot s^{-2}}$		
Water molar mass	M	$0.018\ \mathrm{g \cdot mol^{-1}}$		
Atmospheric pressure	P_a	1 bar		
Water density	ρ_{H2O}	$1000\ \mathrm{kg \cdot m^{-3}}$		
Gas viscosity	μ_g	$1.5 \cdot 10^{-5}\ \mathrm{Pa \cdot s}$		
Water solubility coefficient	K_h	$4.11 \cdot 10^{-6}\ \mathrm{Pa^{-1/2}}$		Shaw (1974)
Permeability coefficient	A	$2 \cdot 10^{-19}\ \mathrm{m^2}$		Klug and Cashman (1996)
Permeability exponent	α	3.5		Klug and Cashman (1996)
Magma temperature	T	1100 K		
Rock density	ρ_{rock}	$2500\ \mathrm{kg \cdot m^{-3}}$		
Chamber overpressure	ΔP	10 MPa		Massol (2001), Mastin et al. (2009)
Dome pressure loading	P_d	0 MPa	0–7.36 MPa	
Water weight fraction in melt	C_0	4 wt%		Barclay et al. (1998)
Crystal volume fraction	φ_c	0.42		Barclay et al. (1998), Gardner et al. (1996), Sparks et al. (2000)
Rock permeability	K_{rock}	$10^{-12}\ \mathrm{m^2}$	10^{-12}–$10^{-16}\ \mathrm{m^2}$	Collombet (2009), Farquharson et al. (2015), Ingebritsen and Scholl (1993), Melnik and Sparks (2002)
Dome permeability	K_d	$10^{-12}\ \mathrm{m^2}$	10^{-9}–$10^{-17}\ \mathrm{m^2}$	Edmonds et al. (2003), Kendrick et al. (2016), Kushnir et al. (2016), Melnik and Sparks (2002)

$$\rho(\mathbf{u} \cdot \nabla)\mathbf{u} = -\rho\mathbf{g} + \nabla \cdot \left[-p\underline{I} + \mu\left(\nabla\mathbf{u} + (\nabla\mathbf{u})^T\right)\right] + \nabla \cdot \left[\left(\kappa - \frac{2}{3}\mu\right)(\nabla \cdot \mathbf{u})\underline{I}\right] \tag{2}$$

where $\underline{I}$ is the identity matrix, while p, the magma bulk pressure, and $\mathbf{u}$, the velocity field are unknown variables (Table 2). A detailed description of ρ, μ and κ formulation is given in Collombet (2009). The magma is composed of (i) a liquid phase, hereafter called melt, that contains dissolved water, (ii) a solid phase (Barclay et al., 1998; Gardner et al., 1996; Sparks et al., 2000), composed of a fixed amount of crystals φ_c, and possibly (iii) a gas phase, when specific physical conditions are reached. We assume water to be the only volatile present in the magma, since it is in most cases the most abundant by a significant amount (Wallace et al., 2002). The mass fraction of dissolved water C_m is pressure dependent, following Henry's law (Eq. (3)). Therefore, the exsolved volatile content is a function of C_m, below, and of the initial water mass fraction, C_0.

$$C_m = K_h\sqrt{p} \tag{3}$$

where K_h is the Henry's law solubility constant for water (Shaw, 1974) (Table 1). We assume that there is no additional crystallization during magma ascent, and no temperature variation.

We apply a no-slip condition at the conduit walls (Fig. 1b). The pressure at the bottom of the conduit is fixed, and accounts for magmastatic pressure with an overpressure ΔP in the reservoir (Massol, 2001; Mastin et al., 2009). We assume that ΔP is not affected by dome loading, and therefore remains constant. At the conduit top, the pressure condition accounts for the weight of the dome P_d, added to the atmospheric pressure P_a. In this model, we consider that the dome is flat above the conduit, such that the pressure condition at the conduit exit is laterally constant. Note that magma flow is not coupled with gas flow (see Section 2.2), unlike the effusive solution of Collombet (2009). Consequently, the magma flow solution calculated here is not a steady-state solution, as it is not at equilibrium with gas flow. However it provides a first order estimation for dome loading effects.

2.4. Ground deformation

We consider a cylinder of rock, around the conduit, of depth H_s and radius R_s, large compared with the dome radius (Fig. 1d). We neglect the influence of volcanic edifice topography, and assume an initial flat ground. Roller conditions (tangential movements only) are

Table 2
Variables solved in the models.

Model variables			
Parameter	Notation	Dimensions	Comes from
Magma pressure	p	r,z	Magma flow
Magma velocity	u	r,z	Magma flow
Magma bulk density	ρ	r,z	Magma flow
Magma dynamical viscosity	μ	r,z	Magma flow
Magma volume viscosity	κ	r,z	Magma flow
Shear stress at the conduit walls	σ_t	z	Magma flow
Extrusion rate	Q		Magma flow
Magma water content	C_m	r,z	Initial conditions
Gas pressure	p_g	r,z,t	Gas flow
Gas Darcy velocity	$\mathbf{u_d}$	r,z,t	Gas flow
Gas advection velocity	$\mathbf{u_a}$	r,z	Magma flow
Gas exsolution rate	$Q_{melt \to gas}$	r,z	Magma flow
Gas density	ρ_g	r,z,t	Gas flow
Gas density (magma flow)	ρ_g^i	r,z	Magma flow
Pressure in the surrounding rock	P_{rock0}	r,z	Initial conditions
Pressure in the rock, near the conduit	P_{rock}	r,z	Magma flow
Dissolved water weight fraction in melt	C_m	r,z	Magma flow
Gas mass in a unit volume of magma	m_g	r,z,t	Gas flow
Gas volume fraction	φ_g	r,z	Magma flow
Melt volume fraction	φ_m	r,z	Magma flow
Magma vertical permeability	K_V	r,z	Magma flow
Magma horizontal permeability	K_H	r,z	Magma flow
Initial gas pressure (no dome)	$P_{i,0}$	r,z	Magma flow
Initial gas pressure (under dome)	$P_{i,Hd}$	r,z	Magma flow
Gas pressure at steady-state (no dome)	$P_{eq,0}$	r,z	Gas flow
Gas pressure at steady-state (dome)	$P_{eq,Hd}$	r,z	Gas flow
Gas pressurization	δp	r,z	Gas flow

applied at the bottom and vertical edges of the cylindrical box. The top surface is free. The rock, characterized by its Young modulus E and Poisson's ratio ν deforms elastically.

For ground deformation associated with magma flow, normal and shear stress conditions are applied as boundary conditions at the conduit walls (radius a_c) (Fig. 1d). These applied values come directly from the magma flow solution (conduit of depth H). The deformation field is thus more complicated than the classical pressure source model in an elastic half-space used in most of geodetic studies performed on volcanoes and known as the Mogi solution (Mogi, 1958). It would correspond to a vertical alignment of Mogi sources with a strength increasing with depth plus the additional shear component induced by the magma flow.

Dome loading also induces subsidence, which is calculated by applying pressure loading at the top of the rock cylinder. The pressure loading depends on the dome height ($P_d = \rho_{rock} g h_d$), that is radius dependent according to Eq. (4):

$$h_d = H_d \frac{(R_d^2 - r^2)}{R_d^2} \tag{4}$$

for $0 < r < R_d$, with R_d the dome radius (Table 1). We assume that the rock's Young modulus and Poisson's ratio are respectively 1 GPa (Voight et al., 1999; Widiwijayanti et al., 2005) and 0.25. The complete deformation calculation provides a new conduit geometry, radial and vertical ground displacement, and the corresponding tilt. The conduit geometry doesn't change much here (radial deformation is less than 0.5% of the conduit diameter, for realistic elastic parameters). The coupled solution for ground deformation is then very close to a one-way coupling solution (in which ground deformation is calculated from flow conditions with no feedback effects).

2.5. Gas flow

2.5.1. Model description

During ascent, magma undergoes a decreasing pressure gradient and becomes oversaturated in volatiles. Gas exsolves from the melt as bubbles nucleate. Their growth due to further exsolution and decompression, and shear conditions can induce bubble coalescence: the magma becomes permeable. Gas then flows through the connected network of bubbles and escapes at the conduit walls and top, proportionally to pressure gradients and permeability conditions in the conduit (discussed in Section 2.5.3) and in the surrounding rock (discussed in Sections 2.5.4–2.5.5).

At a given, fixed point in the conduit, magma gas content evolves due to (i) volatile exchanges between the melt and gas phases (dissolution or exsolution), (ii) magma flow that advects bubbles, and (iii) gas flow through the permeable magma and surrounding rock. In the model presented here, the gas mass conservation law includes these three terms. It is solved in the conduit, in the surrounding rock and in the dome, in 2D axisymmetry (Fig. 1c). We calculate a time dependent solution for gas pressure p_g, which enables us to follow the evolution of gas pressure in the conduit and of gas flux at the conduit edges with time. We carry on the calculation until a new steady-state for gas flow is reached. We use this steady-state solution to quantify the influence of dome loading and dome permeability effects on gas flow. The model here is limited to the uppermost conduit, above Z_g, where most of gas exchanges happen. The conduit is surrounded with a shell of rock, of width r_{rock} (Fig. 1c). The dome is represented as a permeable box of height H_d at the top of the conduit and surrounding rock. We again assume that the dome is flat, such that lateral height variations are negligible above the conduit. Gas pressure is fixed at the top of the dome (atmospheric pressure), at the rock edge ($r = a_c + r_{rock}$) (see Section 2.5.5), and at the bottom of the conduit (magma pressure).

2.5.2. Mass conservation for the gas

We assume that gas flows through the magma matrix and through the surrounding rock with Darcy velocity $\mathbf{u_d}$:

$$\mathbf{u_d} = -\frac{K \nabla p_g}{\mu_g} \tag{5}$$

where K is the magma, surrounding rock or dome permeability, ∇p_g is the gas pressure gradient and $\mu_g = 1.5 \cdot 10^{-5}$ Pa·s is the gas dynamical viscosity. $\mathbf{u_d}$ is averaged on a small volume of magma. Note that $\mathbf{u_d}$ is not the gas absolute velocity due to Darcy flow, which would be $\mathbf{u_d}/\varphi_g$, with φ_g the gas volume fraction. Bubble advection due to magma flow can be equated with a gas flux having the following velocity $\mathbf{u_a}$:

$$\mathbf{u_a} = \mathbf{u}\varphi_g \tag{6}$$

We assume that gas flow does not affect magma flow during the time considered for degassing (a few hours). This hypothesis can be considered as valid as long as magma viscosity is high enough. The magma porosity and permeability are then assumed to be constant with the degassing time, as well as the magma pressure and velocity fields. As a consequence, the gas exsolution flux is constant, and accounts for magma decompression while rising through the conduit. The expression for gas exsolution flux then comes from mass conservation equations for dissolved volatiles in the bulk magma:

$$Q_{melt \rightarrow gas} = -\nabla \cdot (\mathbf{u}\varphi_m C_m \rho_m) \tag{7}$$

where $Q_{melt \rightarrow gas}$ is the volatile mass flux from the melt to the gas phase. φ_m and ρ_m are the melt volume fraction and density. The final mass conservation equation for the gas is given in Eq. (8):

$$\frac{\partial m_g}{\partial t} = -\nabla \cdot ((\mathbf{u_d} + \mathbf{u}\varphi_g)\rho_g) - \nabla \cdot (\mathbf{u}\varphi_m C_m \rho_m) \tag{8}$$

where m_g is the mass of gas in one unit volume of magma. Since magma porosity is constant, m_g is related to gas pressure:

$$p_g = \frac{RTm_g}{M\varphi_g} \tag{9}$$

with $R = 8.314$ J·mol^{-1}· K $^{-1}$ the universal gas constant, and T the gas temperature ($T = 1100$ K). Eq. (8) can then be arranged in:

$$\varphi_g \frac{\partial p_g}{\partial t} + \nabla \cdot (\frac{-K}{\mu_g} p_g \nabla p_g + \mathbf{u}\varphi_g p_g) = -\frac{RT}{M} \nabla \cdot (\mathbf{u}\varphi_m C_m \rho_m) \tag{10}$$

We solve Eq. (10) in the conduit, in the surrounding rock and in the dome.

2.5.3. Magma permeability in the conduit

Many studies, based on permeability measurements for pumice samples, show that permeability has a power-low dependance on porosity (Eichelberger et al., 1986; Klug and Cashman, 1996). Most of these studies assume there is a porosity threshold below which the magma is not permeable, which would be consistent with the percolation theory (Blower, 2001; Lee, 1990; Sahimi, 1994). However, the value of this observed critical porosity varies significantly through the literature and is not sufficient to account for highly permeable samples with very low porosities (Klug and Cashman, 1996; Melnik and Sparks, 2002). These high permeabilities were first interpreted as a consequence either of high magma crystallinity, which confines bubbles to a limited space, such increasing local porosity and permeability, (Blower, 2001; Melnik and Sparks, 2002) or of bubble deformation in viscous flow (Klug and Cashman, 1996), which may enhance bubble coalescence. On the other hand, Rust and Cashman (2004) measured similar permeability values in low crystallinity obsidian samples. They introduced the possibility of an hysteretic relation between permeability and porosity as degassed magma can conserve a high permeability.

We are working in effusive conditions, and assume that magma experienced several degassing events. In these conditions, at the conduit top, low porosity magma should remain permeable. The Klug and Cashman (1996) permeability law (Eq. (11)) assumes that porosity is maintained even for low porosity magma. In addition, it is consistent with a wide range of permeability measurements for silicic lava natural samples. We therefore use this relation to calculate magma permeability inside the conduit, above the initial percolation depth:

$$K_V = 2 \cdot 10^{-19} \alpha^{3.5} \tag{11}$$

Permeability measurements on samples with elongated bubbles show that permeability in the direction of elongation is 0.5 to 3 orders of magnitude higher than perpendicular permeability (Blower, 2001; Bouvet de Maisonneuve et al., 2009; Degruyter et al., 2009; Klug et al., 2002; Rust and Cashman, 2004; Wright et al., 2006). In our case, the capillary number for bubbles is higher than 1 in most of the conduit, when the gas phase is present. Bubbles can then deform and have an elongated shape. We then consider that, in the conduit, horizontal permeability K_H is ten times smaller than vertical permeability K_V.

Recent work on magma rheology evidenced that, at andesitic volcanoes, magma can experience shear fracturing, which would be responsible for the formation of a damage halo at the conduit rim (Holland et al., 2011; Lavallée et al., 2013). Magma permeability in this area would be increased by up to three orders of magnitude in the direction of fractures, such promoting efficient gas transport at the conduit edges. These rheological observations give relevant explanation for degassing observations at Santiaguito (Bluth and Rose, 2004; Holland et al., 2011). Besides, Gaunt et al. (2014) observed the presence of such a damage area around spines extruded at Mount St Helens, were vertical permeability was up to four orders of magnitude higher than horizontal permeability. Magma fracturing may be of great importance for understanding magma permeability and degassing in the conduit uppermost part. However, brittle failure criteria for three phase magma does not exist for pressure ranges we are interested in (Shields et al., 2014). In this study, we thus rely on permeability measurements for silicic lava samples, and do not take into account magma fracturing influence. However, the possible impact of neglecting magma fracturing will be discussed in Section 5.3.2.

2.5.4. Permeability conditions in the surrounding rock and dome

Following Collombet (2009), we assume a constant (10^{-12} m^2) and isotropic permeability in the surrounding rock. During dome growth, pressure loading on the surrounding rock may cause compaction and fracture closing, leading to a permeability decrease. Following Taisne and Jaupart (2008), we estimate the maximum impact on rock permeability associated with a 300 m-high dome, using the Rice (1992) relation:

$$K = K_0 e^{-\frac{\sigma}{\sigma *}} \tag{12}$$

where K is the resulting permeability, K_0 is the initial permeability, σ is the effective normal stress and $\sigma * = 2.5$ MPa is a constant. We obtain a maximum permeability decrease of one order of magnitude beneath the dome, decreasing with depth. It remains significant for a depth equivalent to a few times the dome radius. We test its effect on gas flow, considering a uniform permeability decrease, in order to maximize its influence. We also tested the sensitivity of the model on a wider range of rock permeability values (10^{-16} to 10^{-12} m^2), consistent with measured permeabilities for dome rock samples (Kendrick et al., 2016; Kushnir et al., 2016; Melnik and Sparks, 2002).

Dome permeability can be very complex and depends on the dome formation dynamics and structure (Ashwell et al., 2015; Lavallée et al., 2013) as well as dome rock properties and fracturing (Kendrick et al., 2016; Kushnir et al., 2016; Lavallée et al., 2013). Fractured areas, formed due to strain localization, as well as the formation of tuffisite veins can promote locally high permeability development (Kendrick et al., 2016; Lavallée et al., 2013). Besides, micro-scale permeability depends on magma vesicularity, micro-fracturing and alteration (Farquharson et al., 2015; Kushnir et al., 2016). Permeability measurements on dome natural rocks of Soufrière Hills Volcano (Melnik and Sparks, 2002), Merapi (Kushnir et al., 2016) and Volcán de Colima (Kendrick et al., 2016), that include tuffisite as well as micro-fractured samples, give values ranging from 10^{-16} to 10^{-11} m^2. Besides, Edmonds et al. (2003) interpreted observed S0$_2$ emission variations as a result of permeability evolution in the shallow edifice and dome. Permeability estimates from observed S0$_2$ fluxes ranged from 10^{-12} to 10^{-9} m^2. Here we assume a constant and isotropic permeability for the dome. However, we test a large range of permeability values for the dome ranging from 10^{-17} to 10^{-9} m^2, and compare results with the solution for a reference permeability value of 10^{-12} m^2.

2.5.5. Pressure conditions in the surrounding rock

We assume that, at shallow depth, the volcanic edifice is saturated with water, leading to hydrostatic conditions. This assumption is valid at andesitic “wet” volcanoes in tropical regions, with frequent meteorological water supply (e.g. Soufrière Hills Volcano, Merapi, Santiaguito) (Ball et al., 2015; Hurwitz et al., 2003). Deeper, lithostatic conditions are expected, as rock becomes impermeable to fluid circulations (Fournier, 2006). The transition from hydrostatic to lithostatic pressure occurs at a depth of a hundred meters to a few kilometers (Fournier, 2006). Here we assume such a transition happens at a depth Z_{lith} (purple curve in Fig. 2a), fixed at 1500 m, but its influence is discussed in Section 5.3.3.

Pressure boundary conditions for the surrounding rock P_{rock} (green curve in Fig. 2), at distance r_{rock}, depend on the surrounding rock pressure under loading P_{rock0} (purple curve) and on the conduit pressurizing effect (dP in Fig. 2). The surrounding rock pressure P_{rock0} evolves slightly from hydrostatic to lithostatic (Fig. 2a) with depth as described in Eq. (13), where the density evolves from water density ρ_{H2O} at the surface to crust density at depth and is described by the Comsol step function, f (with a transition zone width of 800 centered at $z = Z_{lith}$).

$$P_{rock0} = P_{atm} + P_d + gzf(\rho_{H2O}, \rho_{rock}) \tag{13}$$

Overpressure in the conduit has a pressurizing effect that depends on the pressure difference between the conduit and the surrounding rock (dP in Fig. 2a), and decreases with the distance from the conduit r_{rock} as expressed in Eq. (14):

$$P_{rock} = P_{rock0} + \frac{r_{rock}^2}{(a_c + r_{rock})^2}(p_{r=ac} - P_{rock0}) \tag{14}$$

Pressure loading associated with a dome emplacement causes a pressure increase in the surrounding rock. Under lithostatic conditions, this pressure loading would be accommodated in the first hundred meters under the dome (Pinel and Jaupart, 2000). Under hydrostatic conditions, we assume that pressure loading causes a constant overpressure in the surrounding rock (Fig. 2b).

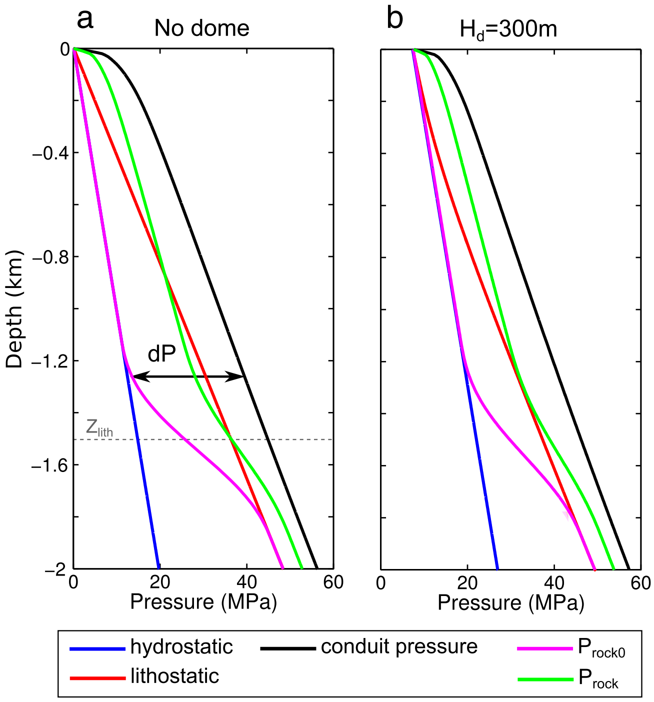

Fig. 2. Pressure P_{rock} in the surrounding rock, at distance r_{rock} ($r_{rock} = 5$ m) (green curve), depends on surrounding rock pressure under loading far from the conduit P_{rock0} (purple curve) and on the conduit pressurizing effect. P_{rock0}, that is not influenced by the conduit, slightly evolves from hydrostatic (blue curve) to lithostatic (red curve), using Comsol smoothed step function (transition of width 800 m centered at $Z_{lith} = 1500$ m). Overpressure in the conduit has a pressurizing effect that depends on the pressure difference dP between the conduit (black curve) and the surrounding rock, and on a radius-dependent coefficient c, that comes from elastic deformation equations: $c = a_c^2/(a_c + r_{rock})^2$ (≈ 0.56 at $r_{rock} = 5$ m, for a conduit radius of 15 m). (a) Pressure boundary conditions with no dome. (b) Pressure boundary conditions for a 300 m high dome. Curves of figure (a) are added in transparency for comparison.

3. Initial conditions

To study the impact of a dome emplacement on magma flow, degassing and ground deformation, we first calculate a steady-state solution for magma flow, deformation and gas flow in an effusive regime without a dome and use this state as an initial condition. We then test how parameters (magma pressure, velocity and permeability, gas flux, ground deformation) evolve in response to dome emplacement.

Collombet (2009), proposed a 2D steady state solution for an effusive regime. This solution takes into account gas flow in both vertical and horizontal directions, and its loss at the conduit walls and at the top of the conduit. Magma and gas flow are fully coupled: gas flow depends on magma flow conditions that in turn depend on gas loss. Porosity and pressure in the conduit, from this solution (Collombet, 2009), are presented in Fig. 3a and b, respectively. Magma degassing leads to the formation of degassed layers of a few tens of meters at the top of the conduit and of a few meters at the conduit walls (Fig. 3a, blue color indicates lower porosities). In the whole conduit, magma porosity remains lower than 60%. The vertical pressure profile shows that most of the magma overpressure is accommodated at the top of the conduit (Fig. 3b). The initial extrusion rate is 13.4 $m^3 \cdot s^{-1}$, which can seem quite large regarding measured extrusion rates during dome forming eruptive regime at Soufrière Hills Volcano (Sparks et al., 1998; Voight et al., 1999) and Mount St Helens (Swanson and Holcomb, 1990). However, this remains in the range of effusive regime conditions (Ogburn et al., 2015; Pallister et al., 2013). This solution provides reasonable and realistic initial conditions for a dome forming eruptive regime. We first adapt these initial magma flow conditions (Collombet, 2009) to 2D axisymmetry, and calculate associated ground deformation and gas flow. These solutions are used as reference cases for interpretation of subsequent runs in which we vary the dome height and other related key parameters. Collombet (2009), used a surrounding rock permeability K_{rock} of 10^{-12} m^2. We use the same value for initial gas flow calculations (case without dome). We also use this value as a reference value for the dome permeability K_d.

4. Results

4.1. Influence of dome height on magma flow

Pressure increase at the top of the conduit due to dome loading causes an overpressure in the whole conduit (Fig. 4). Overpressure reaches up to 7 MPa for a 300 m high dome (dashed curve) at the top of the conduit and remains significant in the uppermost kilometer.

Water solubility in the melt is pressure dependent (Eq. (3)). Therefore, when pressure increases in the conduit, magma porosity decreases and dissolved water content increases, especially at the top of the conduit (Fig. 5a, difference between the dashed and plain curves). The main effect occurs in the top few hundred meters of the conduit (zoom in Fig. 5a,b), where both the initial porosity (plain curve in Fig. 5a) and the increase in pressure (Fig. 4) are important. At the very top of the conduit, we observe the formation of a layer of completely unvesiculated magma (up to 70 m thick for a dome of 300 m) (Fig. 5a, zoom). This porosity decrease will impact magma permeability and therefore influence gas flow within the conduit.

The increase in dissolved water is also associated with a magma viscosity decrease (Fig. 6a, difference between dashed and plain curves), as the melt viscosity is water dependent. For a dome height of 300 m, the maximum observed decrease in viscosity reaches 45% (dashed curve in Fig. 6b), at about 100 m under the dome. This causes a decrease in shear stress within the conduit, thus facilitating magma flow. This effect would tend to increase the extrusion rate. Conversely, a decrease in the vertical pressure gradient due to the dome load (difference in magma pressure between the bottom and top of the conduit), together with an increase in magma density due to the porosity reduction, both act to decrease the extrusion rate.

These latest effects dominate such that we finally observe a strong decrease in extrusion rate during dome formation: from 13.4 m^3 s^{-1} with no dome at the top (initial conditions) to 9 m^3 s^{-1} under a dome height of 300 m. Dome volume increase with time is presented in (plain curve in Fig. 7). With the parameters considered in this study (Table 1) a 300 m high dome is built in 200 days, while it takes only a few hours to build a 50 m high dome.

4.2. Ground deformation

Conduit pressurization and shear stress evolution at the conduit walls cause a small deflation, visible in the tilt evolution around the volcano (Fig. 8a). This deflation is mainly due to the decrease in magma flux rate (Section 4.1), that is responsible for a decrease in shear stress at the conduit walls. A variation in tilt of more than 2.5 µrad occurs at 300 m from the conduit center, for a dome height of 100 m. Farther from the conduit, the deformation signal decreases below the tiltmeters detection threshold (about 1 µrad). The deflation associated with magma flow evolution would therefore be detectable close to the conduit (less than 500 m) only. This deflation is however hidden by the much greater deflation due to subsidence (Fig. 8b). Subsidence amplitude is three orders of magnitude higher than the deflation associated with conduit processes. Unlike plug formation, which can induce ground deformation large enough to be detected, but only by near field measurements (Albino et al., 2011),

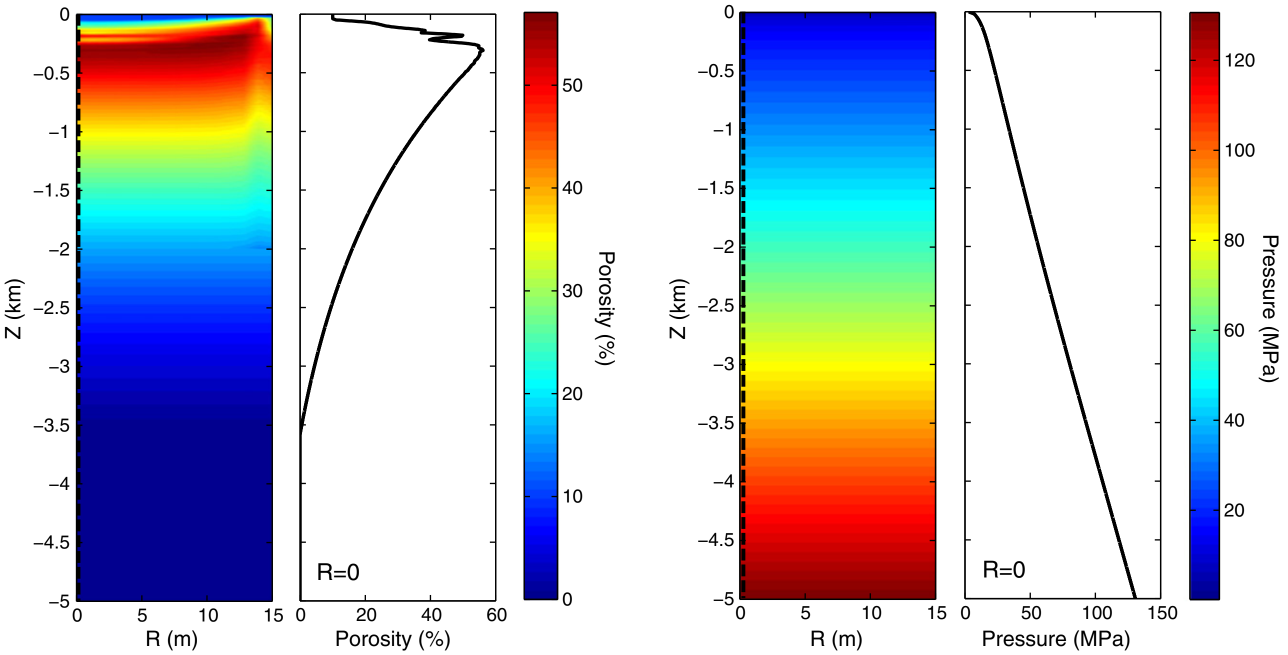

Fig. 3. Initial porosity and pressure conditions in the conduit. A 2D map of the conduit and a vertical profile at the conduit center are presented for both porosity and pressure. These conditions come from Collombet (2009) steady state effusive solution.

conduit pressurization and shear stress evolution induced by dome emplacement appear everywhere to be too small to be detected.

4.3. Magma degassing

For all tested cases, the temporal solution for gas flow is calculated until steady-state is reached. Gas pressure steady-state for the case without a dome is used as a reference to discuss results. Steady-state is reached in about 12 h.

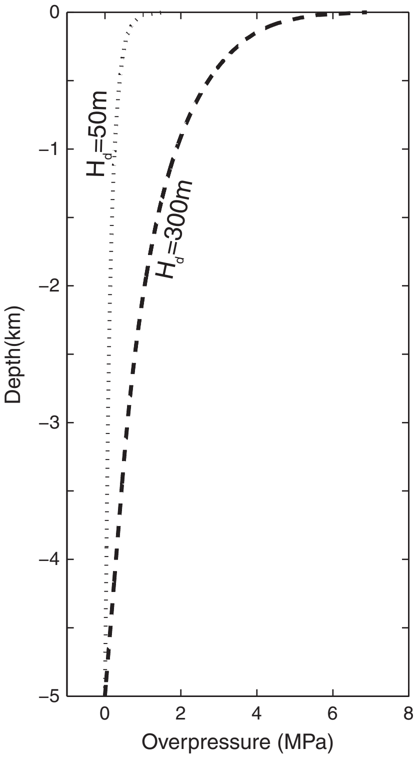

Fig. 4. Overpressure due to dome growth is represented for dome heights of 50 m (dotted curve) and 300 m (dashed curve). The pressure difference from the reference case (without dome) is shown at the conduit center ($r = 0$ m).

4.3.1. Surrounding rock permeability

In this paragraph, we test the influence of decreasing surrounding rock permeability on gas flow. Magma flow conditions used for this calculation correspond to the initial conditions (without a dome). No permeable dome is present at the top of the conduit, where an atmospheric pressure boundary condition is imposed, and pressure conditions in the surrounding rock remain constant. Here we assume a uniform (constant with depth) permeability decrease in the rock. To account for the influence of dome loading on the country rock permeability (compaction and fracture closing), we use a decrease factor of 10 (K_{rock} is set to 10^{-13} m^2 compared to the previous and reference value of 10^{-12} m^2), which corresponds to a dome height of 300 m (Section 2.5.4). The change in conduit pressure δp associated with a permeability decrease in the surrounding rock is calculated as the difference in gas pressure at steady-state between the studied and reference cases (without dome, $K_{rock} = 10^{-12}$ m^2) in Eq. (15), where $P_{eq,Hd}$ and $P_{eq,0}$ are the gas pressure at steady-state for the case with a dome of height H_d (and, here, decreased permeability) (dashed purple and blue curves in Fig. 9) and without dome (black dashed curve), respectively.

$$\delta p = (P_{eq,Hd} - P_{eq,0}) \tag{15}$$

Decreasing the surrounding rock permeability to 10^{-13} m^2, to account for dome loading (see Section 2.5.4), causes an increase in gas pressure in the conduit, at steady-state for gas flow, of a few 0.1 MPa (Fig. 10a, red areas are associated with higher gas pressure increase). This effect is significant in the top 200 m, but it is rapidly attenuated with depth. We also tested the influence of having even lower permeabilities in the rock, using values that remain in the range of measured permeabilities for volcanic rocks (Fig. 10a–d). These lower permeability values lead to a much more significant conduit pressurization (up to 37 MPa for a surrounding rock permeability of 10^{-16} m^2, Fig. 10d). Results are commented upon in the discussion (Section 5.3.1).

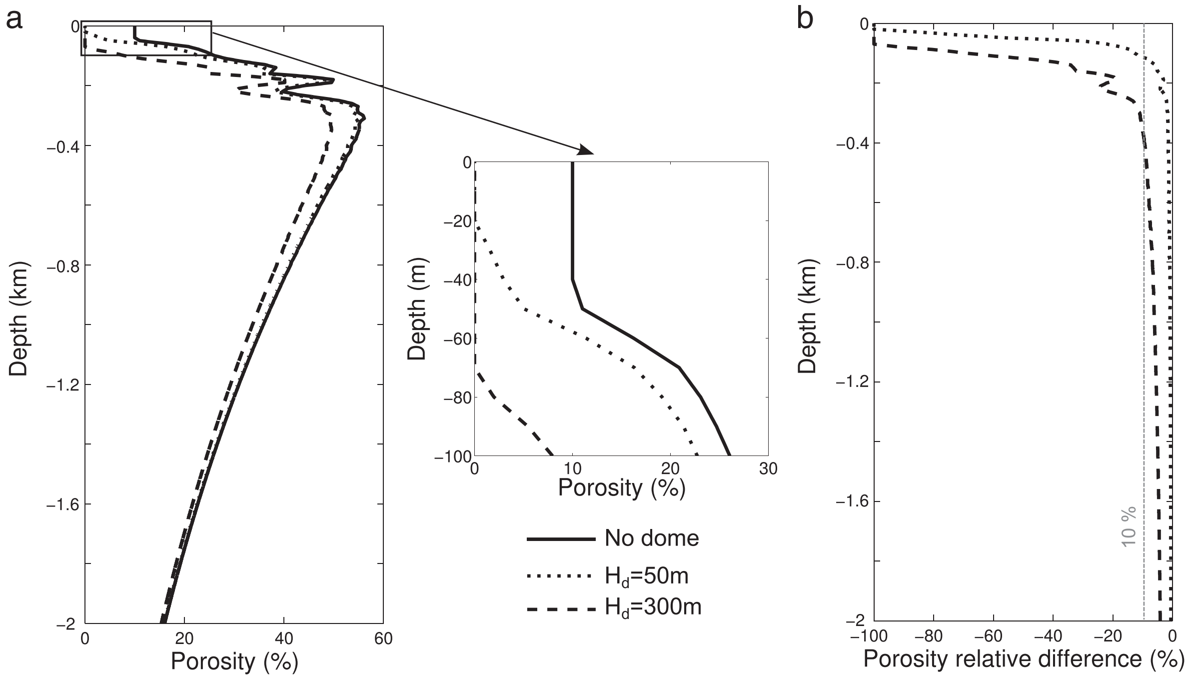

Fig. 5. (a) Porosity at the conduit center ($r = 0$ m) is represented for dome heights of 0 m (plain curve), 50 m (dotted curve), and 300 m (dashed curve). In (b), the porosity relative difference from the reference case is shown at the conduit center, for dome heights of 50 m (dotted curve) and 300 m (dashed curve).

4.3.2. Dome permeability

Initial conditions for the gas pressure and magma permeability again correspond to the reference case, without a dome. We are then able to observe the influence of the dome permeability on gas flow, independently from effects due to magma flow evolution in the conduit. Permeability and pressure conditions in the rock surrounding the conduit also remain constant. The overpressure δp in the conduit associated with a dome permeability of 10^{-17} m^2, compared with a dome permeability of 10^{-12} m^2 is presented in Fig. 11. The presence of the dome appears to have very little effect on gas pressure in the conduit, except for the uppermost few meters. Dome permeability mostly influences dome pressurization (red area in Fig. 11), but has little effect on magma degassing in the conduit.

4.3.3. Surrounding rock pressure

We test here the effect of increasing pressure in the surrounding rock and at the top of the conduit, due to dome loading. For this

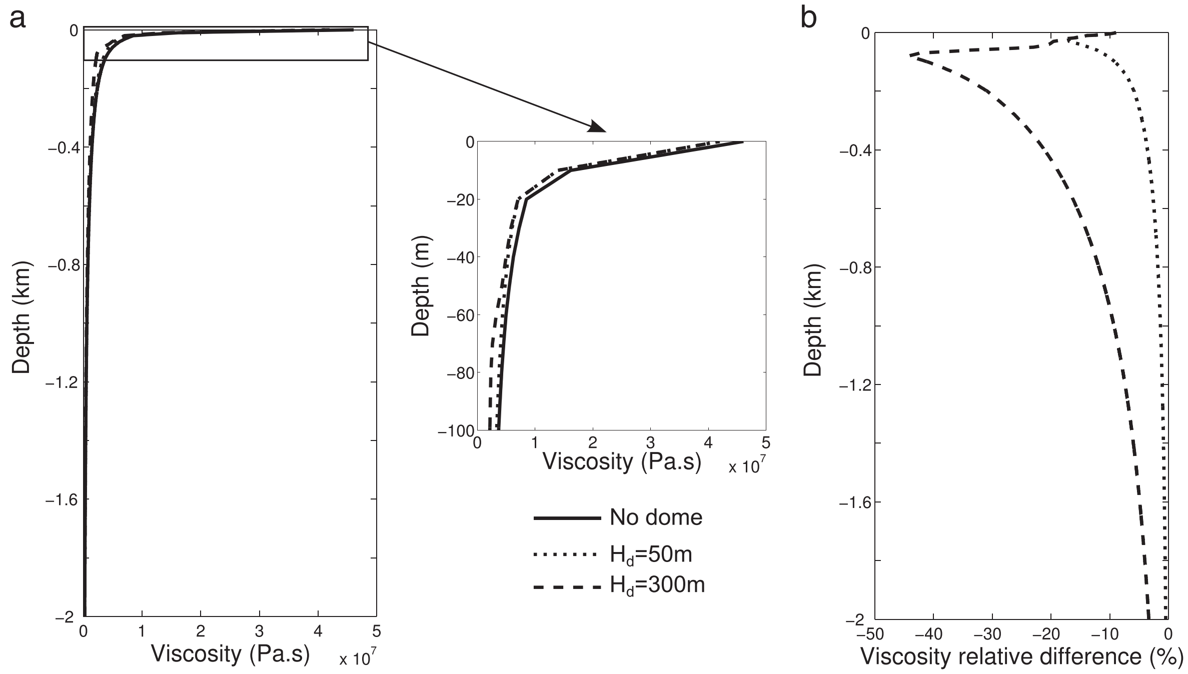

Fig. 6. (a) Viscosity at the conduit center ($r = 0$ m) is represented for dome heights of 0 m (plain curve), 50 m (dotted curve), and 300 m (dashed curve). In (b), the viscosity relative difference from the reference case is shown at the conduit center, for dome heights of 50 m (dotted curve) and 300 m (dashed curve).

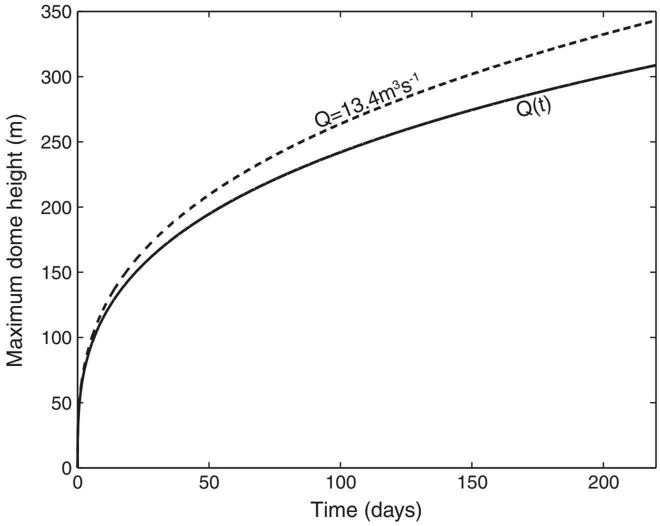

Fig. 7. Dome height evolution with time. Magma extrusion rate Q was extracted from magma flow solutions for dome heights of 0, 50, 100, 150 and 300 m. Results were interpolated to enable calculation of magma extrusion rate evolution with time (plain curve). For comparison, the dashed curve represents the evolution with time of the dome height assuming that the magma extrusion rate remains constant (13.4 m^3 s^{-1} in effusive conditions, without a dome).

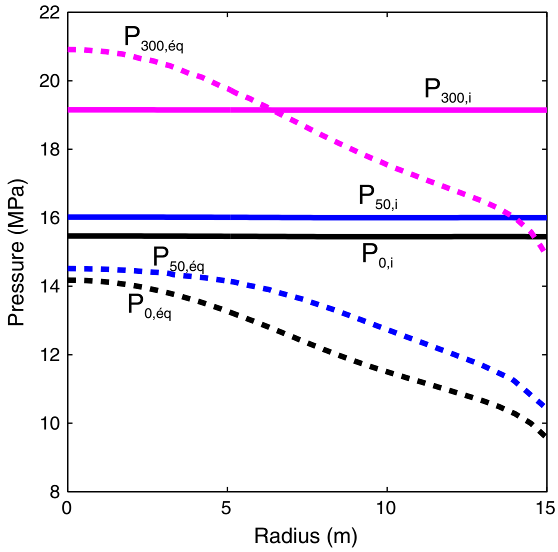

Fig. 9. Radial profiles of gas pressure in the conduit at a depth of 200 m, for dome heights of 0 m (black curves), 50 m (blue curves) and 300 m (purple curves), before degassing (plain curves), and at gas flow steady-state (dashed curves). Model parameters taken are listed in Table 2. Gas overpressure in the conduit δp, represented in Figs. 10–12 and 14, is the difference in gas pressure, at steady-state, between the studied case $P_{Hd,eq}$, and the reference $P_{0,eq}$ ($H_d = 0$ m, $K_r = 10^{-12}$ m^2). For cases with initial and boundary pressure conditions that are different from reference conditions (Fig. 14), the difference of initial gas pressure between the studied case $P_{Hd,i}$ and the reference $P_{0,i}$ is removed: $\delta p = (P_{Hd,eq} - P_{0,eq}) - (P_{Hd,i} - P_{0,i})$. In Figs. 10–12, initial pressure conditions are the same as in the reference case. δp then resumes to gas pressure difference at steady-state.

calculation, the initial gas pressure and porosity in the conduit again come from the initial solution for magma flow (no dome). Rock permeability is constant, and $K_{rock} = 10^{-12}$ m^2. Increasing the surrounding rock pressure causes an increase in gas pressure δp in the conduit of a few tens of MPa, for a dome of 300 m (Fig. 12). This effect is significant in the top first hundred meters of the conduit (up to 12 MPa and 18 MPa for dome heights of 50 and 300 m, respectively). In addition, pressurization is also quite important (up to 4 MPa for a 300-m-high dome) in the rest of the conduit.

Increasing pressure in the rock surrounding the conduit causes a decrease in pressure gradient between the conduit and the surrounding rock. As gas loss depends on the pressure gradient (Eq. (5)), less gas is lost at the conduit walls at the beginning of gas flow (compare dashed and dotted lines with plain line in Fig. 13a). Eventually gas pressurizes in the conduit, increasing the pressure gradient at the conduit walls, until it is high enough to cause gas flux from the conduit to the surrounding rock. Upon examining gas fluxes at the conduit walls at steady-state for the gas (Fig. 13b), we notice that at depth (below 300 m), less gas is lost compared with the reference case, such that gas remains trapped within the conduit. At shallower depths, however, the increased gas fraction in the magma is responsible for a strong increase in conduit pressure (Fig. 12), and gas flux increases at the conduit walls (Fig. 13b).

To summarize, pressure increase in the surrounding rock due to dome loading causes a significant pressurization in the upper conduit.

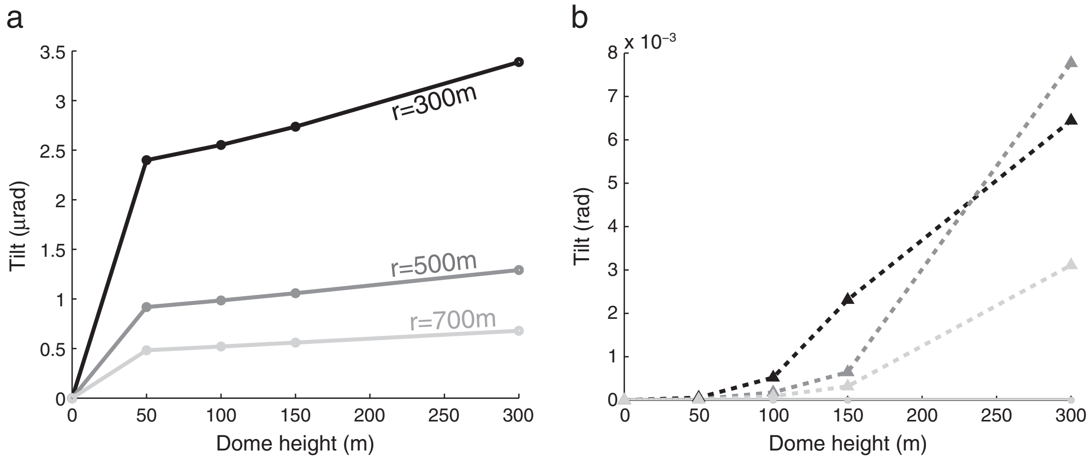

Fig. 8. Tilt evolution during dome growth at 300, 500 and 700 m from the conduit center (black, dark grey and light grey curves). (a) Deflation effect due to magma flow evolution (plain curves). (b) Comparison with dome loading subsiding effect (dashed curves). Positive tilt values are associated with deflation centered at the conduit. Values are obtained for a Poisson's ratio of 0.25 and a Young modulus of 1 GPa (see Table 1). The grid used for the numerical calculation has a depth Hs = 10 km and radius Rs = 20 km.

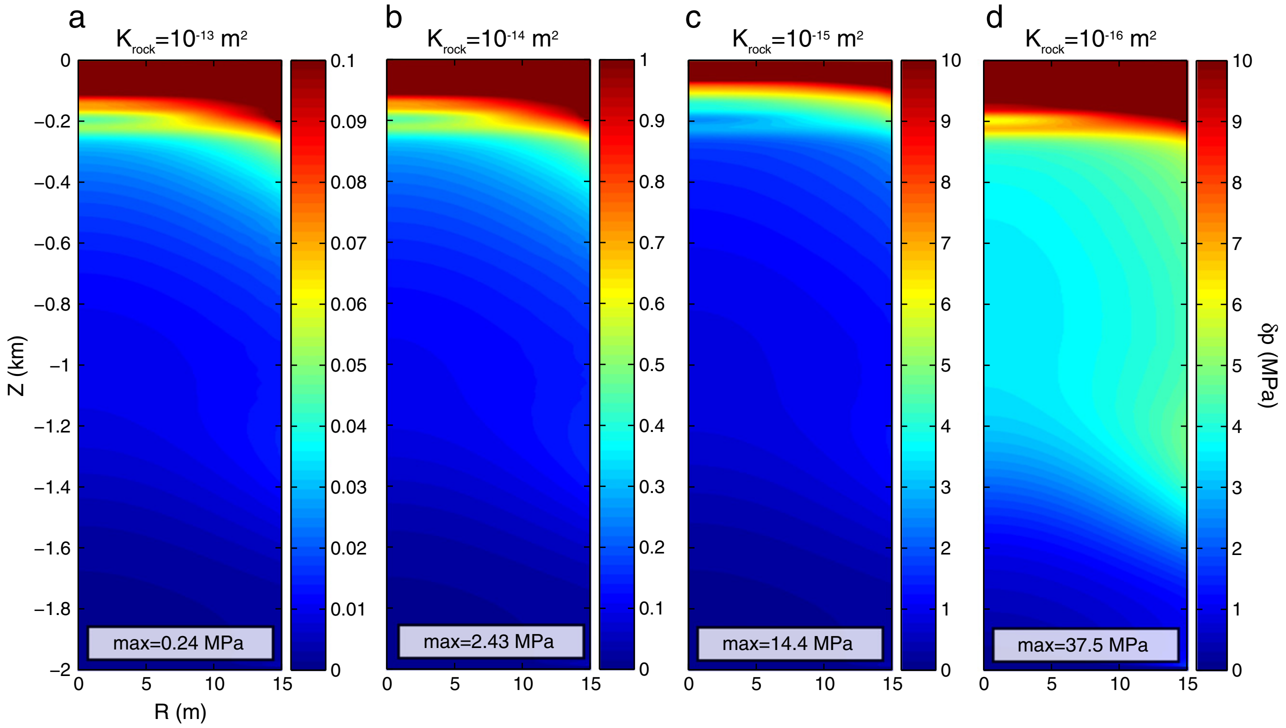

Fig. 10. Gas pressure evolution δp within the first 2 km of the conduit, for surrounding rock permeability varying from 10^{-13} to 10^{-16} m^2. Initial and boundary pressure conditions are constant, as well as magma permeability, and no dome is present above the conduit. Parameters used are listed in Table 1.

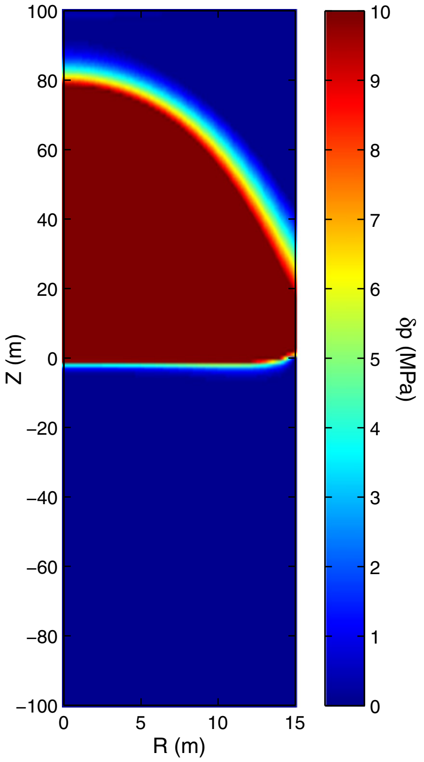

Fig. 11. Effect of dome permeability. Gas pressure evolution δp within the first 100 m of the conduit and in the dome, for a dome permeability of 10^{-17} m^2 (and height 100 m), compared with a reference case in which dome permeability was set to 10^{-12} m^2. Note that δp is defined as previously but here, in the reference case, the conduit is covered with a dome of permeability 10^{-12}m^{-2}. Surrounding rock permeability and pressure conditions remain constant, as well as magma permeability. Parameters used are listed in Table 1.

4.3.4. Magma permeability

The porosity decrease due to the evolution of magma flow in the conduit is associated with a permeability decrease, as magma permeability depends on porosity (Eq. (11)). We here test the influence of this resulting magma permeability decrease on gas flow. Permeability conditions in the surrounding rock, however, are constant ($K_{rock} = 10^{-12}$ m^2). Pressure in the surrounding rock and at the top of the conduit account for the presence of the dome and its pressure loading. Besides, to be consistent with bubble advection and gas exsolution terms, we use here the initial gas pressure and magma porosity and permeability that correspond to magma flow conditions under dome pressure loading. Pressure conditions are then different between cases with or without a dome (plain curves in Fig. 9). The gas pressure difference at steady-state thus takes into account the change in gas pressure due to magma permeability evolution, but also the gas pressure variation due to the dome loading difference. We remove this pressure difference associated with dome loading before calculating gas flow, in order to examine only the effects of permeability on gas loss (Eq. (16)).

$$\delta p = (P_{eq,Hd} - P_{eq,0}) - (P_{i,Hd} - P_{i,0}) \tag{16}$$

$P_{i,Hd}$ and $P_{i,0}$ are the gas pressure, before gas flow, for a case with a dome of height H_d and the reference case (without dome), respectively (Fig. 9). Magma permeability decrease causes important pressurization in the conduit (Fig. 14). As described in Section 4.1 and in Fig. 5, magma porosity, and then permeability decrease were particularly important at the top of the conduit, leading to the formation of a completely unvesiculated layer (a few tens of meters thick, represented in white on Fig. 14). This impermeable layer prevents gas loss from the top of the conduit. Permeability decrease in the rest of the conduit also causes a decrease in degassing efficiency. Gas then accumulates at the top of the conduit, causing a strong increase in gas pressure (up to several tens of MPa, at a depth of 50 to 200 m, for

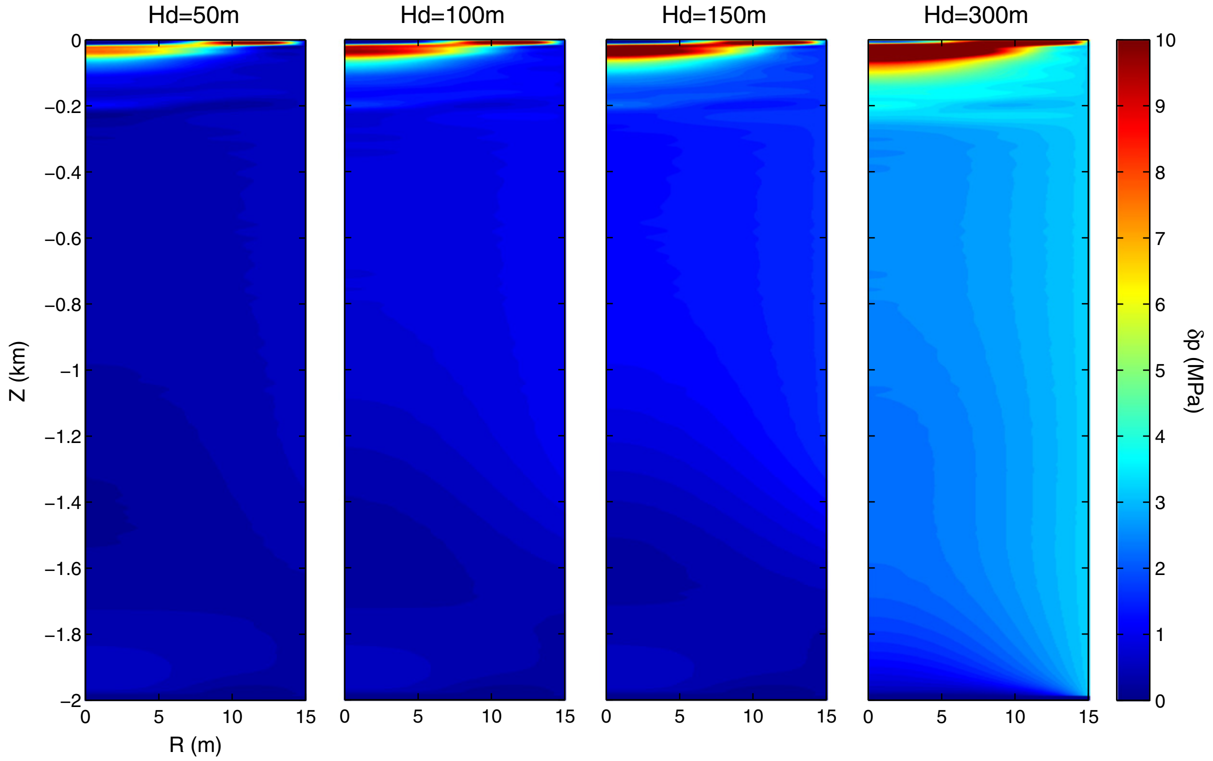

Fig. 12. Effect of rock pressure increase. Gas pressure evolution δp is represented within the first 2 km, for surrounding rock pressure corresponding to dome heights varying from 50 to 300 m. No permeable dome is present above the conduit, and magma and surrounding rock permeability remain constant. Parameters used are listed in Table 1, in particular $Z_{lith} = 1.5$ km.

a 300-m-high dome). At depth (200 to 1500 m), magma permeability decrease also causes a little pressurization, of a few MPa.

5. Discussion

5.1. Magma and gas flow conditions evolution along with dome growth

Our magma and gas flow modeling show that dome pressure loading causes a magma pressure increase in the conduit that is particularly important at the top of the conduit (up to 7 MPa under a 300-m-high dome). The increase in magma pressure is associated with volatile dissolution in the magma inducing an increase in magma dissolved water content, as well as a decrease in magma porosity and permeability as the dome grows. At the top of the conduit, the strong decrease in magma porosity causes the formation of a few-tens-of-meter-thick unvesiculated layer (Section 4.1). In addition, pressure loading decreases permeability and increases pressure in the surrounding rock. Our results from gas flow calculations show that all these effects contribute to limiting gas loss at depth (below 300 m) (e.g. Fig. 13) and increasing gas pressure at the top of the conduit (uppermost hundred meters of the conduit) by several MPa (up to 18 MPa for a 300-m-high dome, see Figs. 10–12 and 14).

However, in our modeling, magma flow is not affected by gas flow, and possible resulting gas content evolution. In our gas flow calculations, steady state is reached in less than 12 h for most of the simulations. Although gas and magma flow may not be in equilibrium at dome growth onset (in our model a 50-m-high dome builds in 6 h), 100 to 300-m-high domes are built in 7 to 200 days (Section 4.1), which is large compared with the time needed for the gas to reach steady-state flow. In a fully coupled model, where magma and gas flow would be interdependent, gas flow would then likely be close to steady-state during most of the dome growth. Our one way coupling model then provides a good first order estimate of gas flow conditions associated with the magma flow and boundary conditions evolution we calculated. However, in a fully coupled model, magma flow conditions, and especially magma volatile content, would be influenced by these degassing conditions. Limited degassing at depth would indeed make the gas to stay longer within the magma, thus causing a relative increase in magma volatile content with time at shallower depth. This would possibly lead to an increase in porosity, and cause a decrease in magma viscosity. The unvesiculated layer we observed in our results, whereas it is absent from field samples, might then be partially removed. Further, due to the increase in porosity, magma permeability may remain important and limit gas pressurization. Gas loss is however extremely dependent on pressure conditions in the surrounding rock, and should remain important in the upper conduit.

To summarize, the model we present here for gas flow conditions provides a good first order estimate of degassing evolution with dome growth, although it maximizes the decrease in magma porosity and the increase in gas pressure. Coupling magma and gas flow in a full way is essential to better quantify magma and gas flow evolution under a forming dome, but it was beyond the scope of this paper.

5.2. Main dome effect: gas pressure and potential explosivity increase

Dome failures and collapses at andesitic volcanoes are frequently associated with explosive activity, caused by the fragmentation of low porosity magma submitted to rapid decompression (Calder et al., 2002; Druitt et al., 2002; Robertson, 1998; Sato et al., 1992). Pyroclastic flows are frequently triggered by superficial dome failure (Calder et al., 2002; Sato et al., 1992), while less frequently, major explosions occur after a major dome collapse that induces magma fragmentation within the dome and the upper part of the conduit (Druitt et al., 2002; Robertson, 1998). Experimental fragmentation of natural silicic rock samples evidenced that the bubble

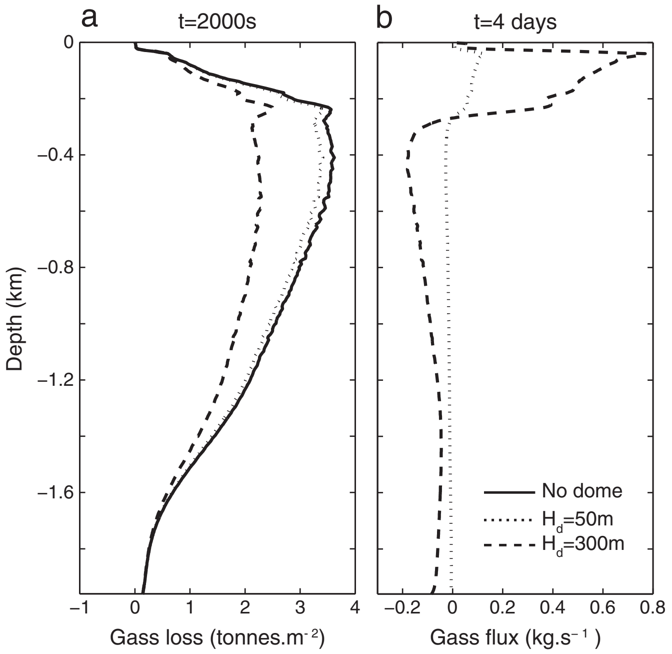

Fig. 13. (a) Cumulative gas loss at the conduit walls during the first 2000 s of gas flow solution. Results are obtained for dome heights of 0, 50 and 300 m (plain, dotted and dashed curves respectively). (b) Difference of gas flux at the conduit walls between cases with domes of 50 m (dotted curve) and 300 m (dashed curve) and the reference case, at steady-state. Parameters used are listed in Table 1, in particular $Z_{lith} = 1.5$ km.

overpressure needed for magma to fragment decreases with increasing magma porosity (Spieler et al., 2004), and that fragmentation intensity increases with increasing magma porosity and bubble overpressure (Kueppers et al., 2006; Mueller et al., 2011). Fragmentation initiation and intensity can also be affected by the magma small scale permeability, however this occurs for permeabilities of more than 10^{-12} m^2 (Mueller et al., 2008; Richard et al., 2013), which are not expected for dome rocks (Kendrick et al., 2016; Kushnir et al., 2016). For a magma porosity of 10%, which is in the range of porosities measured in effusive products (Kendrick et al., 2016; Kushnir et al., 2016), magma fragmentation would happen for a bubble overpressure exceeding 15 MPa (Scheu et al., 2008; Spieler et al., 2004). Important explosive eruptions at Soufrière Hills Volcano were initiated with a major dome collapse, that caused a conduit unloading by 3–6 MPa (Druitt et al., 2002; Robertson, 1998). With such a decompression, magma fragmentation would occur within the conduit for gas overpressures of about 10 MPa (Druitt et al., 2002). Although we do not discuss dome collapses or explosions initiation processes in this article, our results give some insights in magma explosivity and eruption intensity evolution with dome growth.

Our results show that pressure increase in the surrounding rock with dome growth limits gas loss at depth (below 300 m) an causes an increase in gas pressure in the conduit of several MPa (up to 18 MPa for a 300 m-high dome). At silicic volcanoes, microlite crystallization in the magma can also induce an increase in gas pressure at shallow depths of similar importance (Melnik and Sparks, 2005; Sparks, 1997). The gas pressure increase associated with crystallization ranges from a few MPa to several tens of MPa (Melnik and Sparks, 2005; Sparks, 1997), depending on the gas ability to escape from the magma and accommodate the pressure build up. Gas loss limitation with dome growth would favor this additional pressure build up, thus increasing the total change in gas pressure by several MPa. As the dome grows, this important gas pressurization at the conduit top would decrease the decompression range, and then the dome collapse importance needed to trigger magma fragmentation in the conduit. It would also increase the magma explosivity and explosion intensity in the case of a significant dome collapse. In the work presented here, we do not model magma and gas flow conditions inside the dome. However, the gas pressure in the magma extruding from the conduit increases with time. Gas pressure in the inner dome would then likely increase along with dome growth, contributing do high explosion intensity in the case of a major dome collapse.

In addition, the decrease in deep magma degassing we observe would possibly induce an increase in magma porosity at shallower depth if magma flow was coupled with gas flow (Section 5.1). The increase in magma gas content at the top of the conduit, added with a strong increase in gas pressure, would even more favor magma fragmentation in the case of a rapid conduit decompression. In the case of an exogenous dome formation, the magma extruded from the conduit would be further decompressed and feed lobes at shallow depth. This would increase the magma explosivity in the case of a minor dome failure, and may even trigger shallow explosive events of increasing intensity.

5.3. Pathways for magma degassing

5.3.1. Limited influence of the surrounding rock and dome permeability on magma degassing

As the magma rises within the conduit and undergoes decompression, gas exsolves from the magma and permeability develops. Depending on pressure gradients in the conduit (Eq. (5)), surrounding rock and dome, the gas is then able to flow through the magma and escapes at the conduit walls and top. Our results show that gas flow conditions are extremely sensitive to magma permeability and to pressure in the surrounding rock, whose variations under a growing dome can lead to an increase in gas pressure of several MPa (Figs. 12, 14, Sections 4.3.4 and 4.3.3).

We have shown that a decrease in rock permeability around the conduit, due to dome loading, causes little gas pressurization (a few bars) in the conduit (Fig. 10a, Section 4.3.1), although we note that a greater decrease in rock permeability leads to dramatically greater conduit pressurization (up to 37 MPa for a permeability of 10^{-16} m^2) (Fig. 10b–d). To further investigate surrounding rock permeability influence on degassing, we calculated gas flow for rock permeabilities varying over a wide range of values ($K_{rock} = 10^{-9}$–10^{-19} m^2). We find that for the rock permeability values close to magma permeability, conduit average gas pressure varies significantly, increasing by about 8 MPa (dots in Fig. 15b). However, for rock permeability values far from the magma, changing rock permeability by one order of magnitude has little effect on gas flow. The initial rock permeability ($K_{rock} = 10^{-12}$ m^2) we considered in our model is quite high compared with the magma permeability ($K_V = 5 \cdot 10^{-16}$–$3 \cdot 10^{-13}$ m^2, $K_H = 5 \cdot 10^{-17}$–$3 \cdot 10^{-14}$ m^2) (Fig. 15a). Gas flux at the conduit walls is therefore limited by the ability for the gas to extract from the magma, rather than by country rock permeability. However, when initial rock and magma permeabilities are close in value, small variations in rock permeability due to dome loading changes could lead to significant pressure increase in the conduit.

The dome permeability, however, has almost no effect on gas flow, except for pressurizing the dome itself, even for very low dome permeabilities (Fig. 11, Section 4.3.2). These results show that gas flow is much more sensitive to conditions in the surrounding rock than at the top of the conduit (i.e. at the base of the dome, in this particular case), which means that gas is mainly lost at the conduit walls, not through the dome. This outcome can be explained in terms of geometry. The total surface of the conduit walls is two orders of magnitude greater than the conduit cross-sectional area. Furthermore, the distance from the magma to the conduit walls is always, in this case, less than 15 m, whereas the vertical distance required for gas to escape through the dome is significantly larger (a few kilometers). Even with a vertical vs horizontal permeability ratio of 10 in

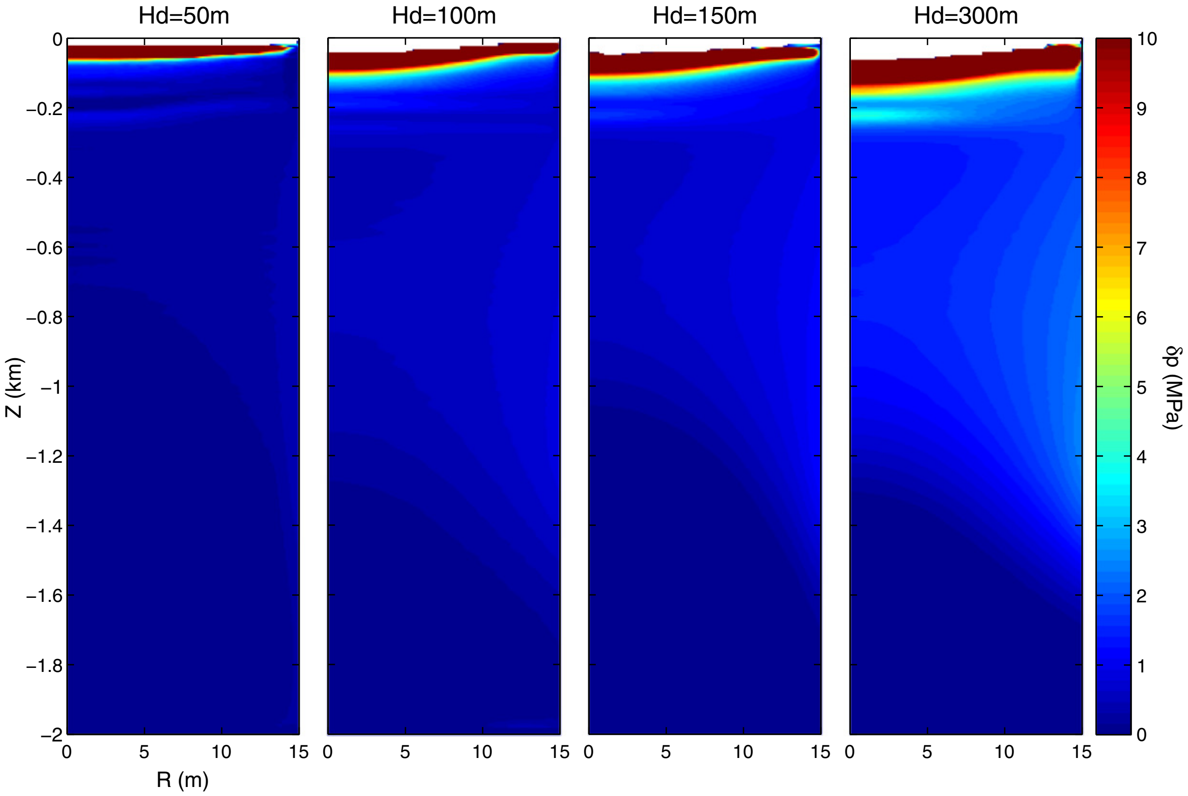

Fig. 14. Effect of magma flow conditions (permeability, porosity) evolution: gas pressure evolution δp within the first 2 km, for conduit permeability and porosity corresponding to dome heights varying from 50 to 300 m. Parameters used for calculation are listed in Table 1. The white area at the conduit top corresponds to the unvesiculated layer observed in Fig. 5, where gas cannot flow. No dome is present above the conduit, and surrounding rock permeability is constant. Surrounding rock pressure conditions account for dome pressure loading in the surrounding rock (Fig. 2b).

the magma, and even though vertical permeability plays a key role in gas mobility through the conduit, gas flow is much more influenced by conditions at the conduit walls.

To summarize, permeability of the magma and pressure conditions in the surrounding rocks have a first order control on magma degassing.

5.3.2. Permeability conditions

Magma permeability dependence on flow conditions. At the conduit margins, magma is submitted to important shear stress that can be responsible for (i) bubble elongation and (ii) magma fracturing. In the magma flow model presented here, we used the Klug and Cashman (1996) permeability law (Eq. (11)) and assumed a constant bubble deformation within the conduit (Section 2.5.3). Permeability development in andesitic effusive flow conditions depends on many parameters, including geometrical characteristics of the bubble network (Degruyter et al., 2009). These geometrical parameters depend on magma flow and shear stress conditions, that evolve both spatially and with time in the conduit. To take into account the bubble deformation influence on permeability in a more accurate way, the magma permeability law would then have to be related to flow conditions.

Due to shear stress conditions, bubble elongation should be limited at the conduit center, where shear stress is minimum, and increase towards the conduit margins. Permeability measurements in andesitic pumice reveal that bubble deformation is associated with permeability anisotropy, as permeability is much higher in the direction of bubble elongation (Bouvet de Maisonneuve et al., 2009; Degruyter et al., 2009; Klug et al., 2002). Important bubble deformation at the conduit margins may then enhance vertical gas flow and magma degassing at the conduit edges. In such degassing conditions, dome permeability might have a greater influence on gas flow, as a smaller dome permeability would possibly limit the release of the gas vertically channeled at the conduit margin.

Fracturing at the conduit margins. In specific parts of the conduit, and especially at the conduit margins, andesitic magma can also experience shear fracturing (Holland et al., 2011; Lavallée et al., 2013). In addition, the rock surrounding the conduit is submitted to important shear stress (Albino et al., 2011; Beauducel and Cornet, 2000; Gaunt et al., 2014; Green et al., 2006) and can also fracture (Gaunt et al., 2014). These two effects would cause the formation of a highly permeable fracture network at the conduit margins. Such a fracture network could significantly increase vertical permeability and facilitate gas vertical flow, thus enhancing degassing efficiency along the conduit margins. Besides, if this fracture network is connected with the atmosphere, which may be the case in exogenous dome growth conditions (Gaunt et al., 2014; Watts et al., 2002) and would be in agreement with observations at Santiaguito (Bluth and Rose, 2004; Holland et al., 2011), degassing would remain efficient during dome growth, leading to less gas pressurization within the conduit. Conversely, if this fracture network was sealed for any reason, gas pressure could rise rapidly. The dome permeability would then play an important role in gas pressurization and explosive activity evolution.

The effect of this high permeability network on magma degassing would however be limited to the conduit margins of the uppermost part of the conduit (uppermost few hundred meters (Holland et al., 2011)), where magma viscosity and shear stress conditions for fracturing are reached. Deeper in the conduit, the influence of

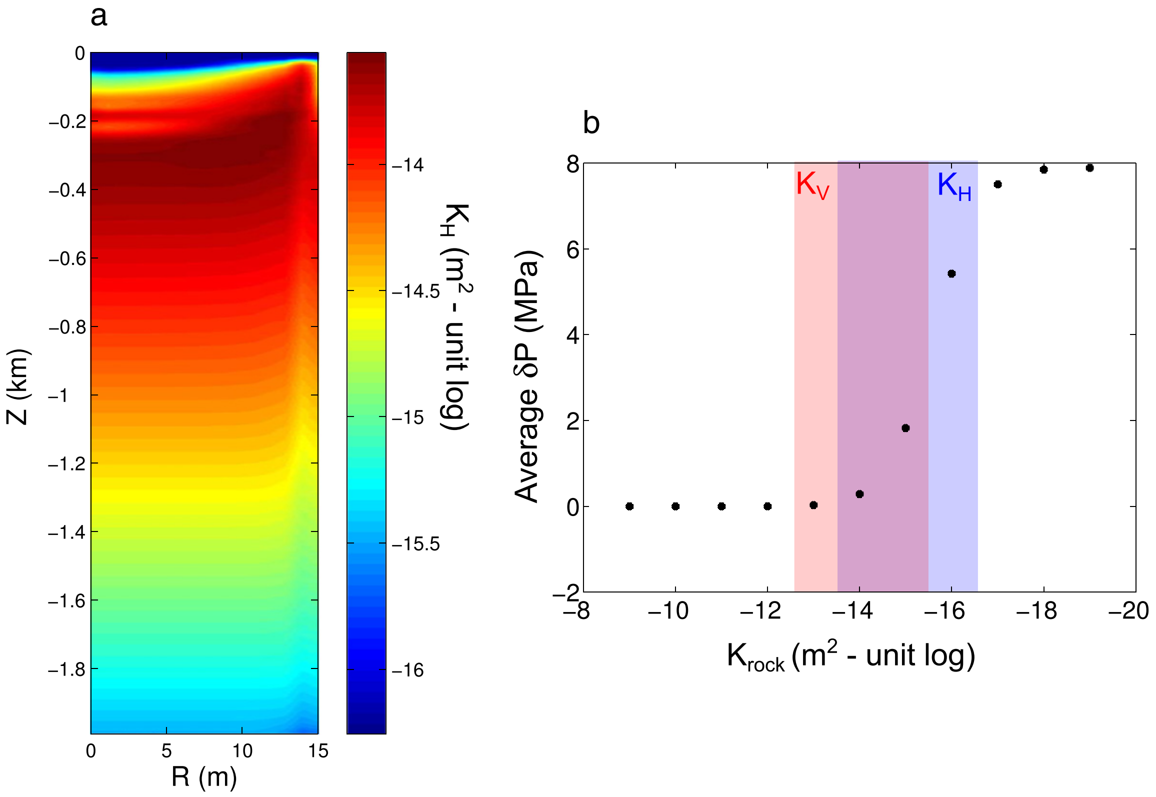

Fig. 15. (a) Horizontal permeability conditions within the conduit (K_H). Note that vertical permeability (K_V) is ten times higher. (b) Mean value of gas overpressure (δp) within the conduit, for rock permeability values ranging from 10^{-9} to 10^{-19} m^2 (unit log). The range of conduit horizontal and vertical permeability values are represented respectively by the blue and red areas.

dome loading on pressure and permeability conditions at the conduit margins would lead to an increase in the volatile content of the magma that reaches the conduit top. In addition, gas flow depends on permeability and pressure conditions within the magma, which means that the volatile content of the magma at the center of the conduit may keep increasing with dome growth if no efficient pathways are created between the center of the conduit and permeable fractures at the borders.

Permeability conditions in the surrounding rock. In the gas flow model presented here, we assumed that surrounding rock permeability was constant with depth. In addition to specific permeability conditions at the uppermost conduit edges, permeability in volcanic edifices, as well as its evolution under pressure loading, is badly constrained and may vary significantly depending on rock texture. Farquharson et al. (2015) measured permeability in andesitic edifice rock samples at Volcán de Colima. They found values ranging from 10^{-15} to 10^{-10} depending on the rock sample textures. Besides, water and gas flow through the rock composing the volcanic edifice, in particular hydrothermal activity can be responsible for rock alteration and permeability variations of several orders of magnitude (Ball et al., 2015; Edmonds et al., 2003; Ingebritsen and Scholl, 1993). The surrounding rock permeability is also influenced by the magmatic system. Shallow reservoirs and intrusions cause surrounding rock heating. Fournier (2006) estimated that in volcanic areas, the heated rock could be ductile close to magmatic intrusions. According to the same authors, the transition from brittle to ductile occurs at a few hundred meters above magmatic intrusions and is associated with a strong decrease in rock permeability.

Depending on the initial permeability conditions in the rock surrounding the conduit, the dome influence on magma degassing could be quite different from our models results. For example, an initial low rock permeability at depth would confine gas loss to the shallowest part of the conduit, where the dome's influence is the most important. The dome loading effect on permeability would then potentially lead to much more important gas pressurization. Conversely, high surrounding rock permeability and enhanced degassing at depth, were the dome's influence is limited, would reduce dome growth impact on degassing.

5.3.3. *Pressure conditions in the surrounding rock*

The pressure transition from hydrostatic to lithostatic in volcanic edifices is related with the brittle/ductile transition of rock, whose depth depends on magmatic activity. Depending on the presence of magmatic intrusions, and on the intensity of volcanic activity in the area, the transition occurs at a depth of a few hundred meters to a few kilometers (Fournier, 2006). Having no precise information on this transition depth in a volcanic edifice, we tested its influence on gas flow conditions. Depending on Z_{lith}, gas flow and loss at the conduit walls change (Fig. 16). For shallower transition depths (dotted curve), gas flux at the conduit walls, below the transition, is strongly decreased (Fig. 16b), causing the gas to remain in solution. Above the transition, this amount of gas escapes, as pressure difference between the conduit and the rock is maximum, and gas flux is therefore higher (Fig. 16b). A shallower transition favors the gas remaining longer within the magma. On another hand, at the top of the conduit, the surrounding rock may not be saturated with ground water, depending on the meteorological conditions (Ball et al., 2015; Hurwitz et al., 2003), and pressure conditions would get closer to atmospheric pressure. This would enhance degassing at the conduit top, and then limit gas pressurization.

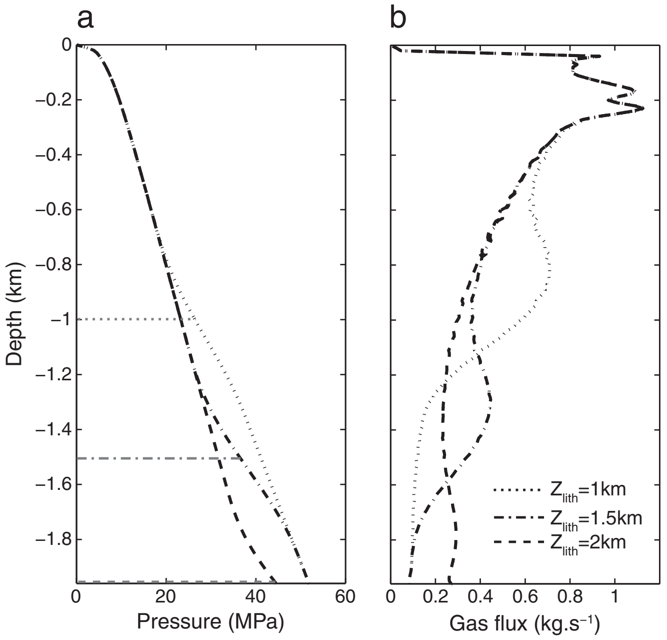

Fig. 16. Effects of transition depth (Z_{lith}) from hydrostatic to lithostatic pressure on gas loss at the conduit wall: (a) pressure condition at a distance $r_{rock} = 5$ m from the conduit in the surrounding rock (P_{rock}). (b) Gas flux at steady-state. Results are shown for Z_{lith} equal to 1 km (dotted curve), 1.5 km (dot-dashed curve) and 2 km (dashed curve).

Having an accurate estimate of the pressure in the rock surrounding the conduit is difficult to achieve. However, it is essential for interpreting regime evolution under a dome. Results from our gas flow model show that pressure increase in the rock due to dome loading may play a key role in conduit pressurization. If surrounding rock pressure is lithostatic, pressure increase due to dome loading would be attenuated with depth (Pinel and Jaupart, 2000). Gas flow would then mostly be affected at the top of the conduit. However, if surrounding rock pressure is hydrostatic, dome pressure loading would not be attenuated with depth, and gas flow might then be much more affected, leading to greater pressurization within the conduit.

5.4. Limited visibility of flow conditions evolution in ground deformation

Our results show that magma flow evolution below a growing dome causes little ground deformation (up to 3 μrad for a dome height of 300 m), compared with the subsidence effect (up to $8 \cdot 10^{-3}$ rad, corresponding with a vertical displacement of a few meters) (Fig. 8). GPS and InSAR measurements of deformation around volcanoes, together with numerical modeling, show that loading by eruptive products (lava flows, explosive deposits) can be responsible for a significant ground subsidence around the volcano (Odbert et al., 2015; Pinel et al., 2011), even at distances of about 1 km from the conduit center. Furthermore, Pinel et al. (2011) have shown that this deposits loading, together with an equivalent decrease in reservoir volume beneath the volcano account for ground deformation observed around Volcán de Colima. However, at Soufrière Hills Volcano, as well as Merapi, tilt and ground displacement observed in the near field evidenced episodes of inflation and deflation that could not be retrieved with such loading deformation sources modeling (Beauducel and Cornet, 2000; Green et al., 2006). For both cases, shear stress at the conduit walls, at shallow depth (Beauducel and Cornet, 2000; Green et al., 2006), or pressurization under a plug (Voight et al., 1998) were proposed as more realistic and reliable deformation sources. In addition, numerical models evidenced that ground deformation associated with shear stress variations due to variable magma degassing or plug formation could account for observed near field ground deformation at Soufrière Hills Volcano (a few hundred meters from the conduit) (Albino et al., 2011; De' Michieli Vitturi et al., 2013; Nishimura, 2006, 2009). Our results show that ground deformation associated with magma flow evolution along with dome growth are detectable close to the conduit only (less than 300 m from the vent), and would be negligible compared with subsidence due to dome loading. In the following paragraphs we discuss some assumptions we made that may impact these results.

Here we estimated ground deformation associated with magma flow using flow conditions that do not integrate magma degassing evolution. In a fully coupled model, gas loss limitation with dome growth would cause an increase of magma porosity and a decrease in magma viscosity, and possibly remove the unvesiculated layer observed in Section 4.1. This would decrease shear stress conditions at the conduit wall and cause important changes in pressure gradients in the whole conduit, possibly leading to significant ground deformation. Albino et al. (2011) provide evidence that the formation of a degassed layer at the top of the conduit induces detectable deformation. The removal of such a degassed layer during a dome forming episode may also be associated with ground deformation detectable in the near field.

Here we modeled ground deformation assuming an initial flat ground. However, around volcanoes, topography can impact significantly ground deformation. We estimated the potential influence of topography considering a dome emplacement on top of a conical volcano. Here the volcano slope is set to 45° in order to maximize the effect of topography. Although tilt evolution with dome height is slightly different from what we observed with a flat topography, it remains of similar amplitude. Furthermore, the deformation signal induced by magma flow within the conduit (up to 3.5 μrad for a dome height of 300 m) remains negligible compared with the subsidence induced by the dome weight (up to $8 \cdot 10^{-3}$ rad). We thus conclude that in the case of a crater-confined dome growth at the top of an andesitic volcano, topography has a limited influence on the ground deformation signal, which is dominated by subsidence.

6. Conclusion

From numerical modeling of magma flow, gas flow and ground deformation in 2D axisymmetry, we quantified the feedback effects of a dome emplacement on magma flow and degassing, as well as the induced ground deformation. Dome growth is associated with a decrease in permeability in the conduit and surrounding rock, and a pressure increase in the surrounding rock. Our results show that magma degassing is extremely sensitive to pressure conditions in the surrounding rock and to permeability and pressure conditions within the conduit, whereas, contrary to the common idea, the dome permeability has no influence. Regarding permeability at the conduit walls, it is only influent when it is within the range of values close to the magma permeability. These results also evidence that gas is mainly lost at the conduit walls, not at its top. Along with dome growth, pressure increase in the surrounding rock and conditions evolution in the conduit are responsible for a decrease in magma degassing at depth (below 300 m). This decrease in gas loss at depth is responsible for both an increase in gas pressure (up to a few tens of MPa) and a relative increase in magma volatile content in the conduit shallower part. These two effects combine to increase magma explosivity in the case of a rapid decompression following a dome collapse, explosions intensity increasing with dome height. Although we did not include magma fracturing in our model, we expect it would not change the main conclusions of our work, since it is only present in extreme conditions at conduit margins, in its top part.

Such results point out the need of an accurate understanding of magma permeability development and evolution in andesitic magmas. Permeability and pressure conditions in the rock surrounding the conduit, and their evolution with pressure loading also need to be better constrained. In addition, the sensitivity of magma degassing to conditions in the conduit emphasizes the importance of taking into account pressure gradient and permeability variations in 2D for gas flow modeling and eruptive regime evolution understanding. The significant impact of dome growth on degassing evolution evidences the need of improving the models by coupling magma flow with gas flow conditions in order to get more accurate estimates of magma porosity, permeability and viscosity variations, as well as gas pressure evolution along with dome growth, such parameters being determinant for risk assessment in the case of a dome collapse. Besides, their evolution might be associated with a significant ground deformation in the near field, more important than what we modeled so far, which could then be discriminated from subsidence effect induced by the dome load and potentially be interpreted in terms of magma flow conditions evolution, such providing key inputs for risk assessment at andesitic volcanoes.

Acknowledgments

This work was supported by the ANR DOMERAPI (ANR-12-BS06-0012). We thank David Cébron and Alain Burgisser for helpful advice on numerical considerations. We are grateful to Steve Ingebritsen, Jessica Ball and many others for rewarding comments and discussions. We also thank Amanda Clarke, an anonymous reviewer, and the Editor Heidy Mader for their comments and suggestions that greatly improved the manuscript.

References

Albino, F., Pinel, V., Massol, H., Collombet, M., 2011. Conditions for detection of ground deformation induced by conduit flow and evolution. J. Geophys. Res. 116, B06201.

Alidibirov, M., Dingwell, D., 1996. Magma fragmentation by rapid decompression. Lett. Nat. 380, 146–148.

Alidibirov, M., Dingwell, D., 2000. Three fragmentation mechanisms for highly viscous magma under rapid decompression. J. Volcanol. Geotherm. Res. 100, 413–421.

Ashwell, P., Kendrick, J., Lavallée, Y., Kennedy, B., Hess, K.-U., von Aulock, F., Wadsworth, F., Vasseur, J., Dingwell, D., 2015. Permeability of compacting porous lavas. J. Geophys. Res. Solid Earth 120, 1605–1622.

Ball, J., Stauffer, P., Calder, E., Valentine, G., 2015. The hydrothermal alteration of cooling lava domes. Bull. Volcanol. 77, 102.

Barclay, J., Rutherford, M., Carroll, M., Murphy, M., Devine, J., Gardner, J., Sparks, R., 1998. Experimental phase equilibria constraints on pre-eruptive storage conditions of the Soufriere Hills magma. Geophys. Res. Lett. 25, 3437–3440.

Beauducel, F., Cornet, F.-H., 2000. Constraints on magma flux from displacement data at Merapi Volcano, Java, Indonesia. J. Geophys. Res. 105, 8193–8203.

Blake, S., 1990. Lava flows and domes. . Ch. Viscoplastic Models of Lava DomesSpringer Berlin Heidelberg., pp. 88–126.

Blower, J., 2001. Factors controlling permeability-porosity relationships in magma. Bull. Volcanol. 63, 497–504.

Bluth, G., Rose, W., 2004. Observations of eruptive activity at Santiaguito Volcano, Guatemala. J. Volcanol. Geotherm. Res. 136, 297–302.

Bouvet de Maisonneuve, C., Bachman, O., Burgisser, A., 2009. Characterization of juvenile pyroclasts from the Kos Plateau Tuff (Aegean Arc): insights into the eruptive dynamics of a large rhyolitic eruption. Bull. Volcanol. 71, 643–658.

Calder, E., Luckett, R., Sparks, R., Voight, B., 2002. The eruption of Soufrière Hills Volcano, Montserrat, from 1995 to 1999 Vol.21. . Ch. Mechanisms of Lava Dome Instability and Generation of Rockfalls and Pyroclastic Flows at Soufrière Hills Volcano, Montserrat The Geological Society of London, Memoirs., pp. 173–190.

Collinson, A., Neuberg, J., 2012. Gas storage, transport and pressure changes in an evolving permeable volcanic edifice. J. Volcanol. Geotherm. Res. 243-244, 1–13.

Collombet, M., 2009. Two-dimensional gas loss for silicic magma flows: toward more realistic numerical models. Geophys. J. Int. 177, 309–318.

Costa, A., Sparks, R., Macedonio, G., Melnik, O., 2009. Effects of wall-rock elasticity on magma flow in dykes during explosive eruptions. Earth Planet. Sci. Lett. 288, 455–462.

De' Michieli Vitturi, M., Clarke, A., Neri, A., Voight, B., 2008. Effects of conduit geometry on magma ascent dynamics in dome-forming eruptions. Earth Planet. Sci. Lett. 272, 567–578.

De' Michieli Vitturi, M., Clarke, A., Neri, A., Voight, B., 2013. Extrusion cycles during dome-building eruptions. Earth Planet. Sci. Lett. 371-372, 37–48.

Degruyter, W., Bachman, O., Burgisser, A., 2009. Controls on magma permeability in the volcanic conduit during the climactic phase of the Kos Plateau Tuff eruption (Aegean Arc). Bull. Volcanol. 72, 63.

Diller, K., Clarke, A., Voight, B., Neri, A., 2006. Mechanisms of conduit plug formation: implications for vulcanian explosions. Geophys. Res. Lett. 33, L20302.

Druitt, T., Young, S., Baptie, B., Bonadonna, C., Calder, E., Clarke, A., Cole, P., Harford, C., Herd, R., Luckett, R., Ryan, G., Voight, B., 2002. The eruption of Soufrière Hills Volcano, Montserrat, from 1995 to 1999, Vol. 21. Ch. Episodes of Cyclic Vulcanian Explosive Activity With Fountain Collapse at Soufrière Hills Volcano, MontserratThe Geological Society of London, Memoirs. pp. 281–306

Edmonds, M., Oppenheimer, C., Pyle, D., Herd, R., Thompson, G., 2003. SO_2 emissions from Soufrière Hills Volcano and their relationship to conduit permeability, hydrothermal interaction and degassing regime. J. Volcanol. Geotherm. Res. 124, 23–43.

Eichelberger, J., Carrigan, C., Westrich, H., Price, R., 1986. Non-explosive silicic volcanism. Nature 323, 16.

Farquharson, J., Heap, M., Varley, N., Baud, P., Reuschlé, T., 2015. Permeability and porosity relationships of edifice-forming andesites: a combined field and laboratory study. J. Volcanol. Geotherm. Res. 297, 52–68.

Fournier, R., 2006. Volcano deformation. Ch. Hydrothermal Systems and Volcano Geochemistry Springer Berlin Heidelberg. pp. 323–341

Gardner, J., Thomas, R., Jaupart, C., 1996. Fragmentation of magma during Plinian volcanic eruptions. Bull. Volcanol. 58, 144–162.

Gaunt, H., Sammonds, P., Meredith, P., Smith, R., Pallister, J., 2014. Pathways for degassing during the lava dome eruption of Mount St. Helens 2004–2008. Geology 42, 947–950.

Green, D., Neuberg, J., Cayol, V., 2006. Shear stress along the conduit walls as a plausible source of tilt at Soufrière Hills Volcano, Montserrat. Geophys. Res. Lett. 33, L10306.

Hale, A., Calder, E., Loughlin, S., Wadge, G., Ryan, G., 2009a. Modelling the lava dome extruded at Soufrière Hills Volcano, Montserrat, August 2005–May 2006. Part II: rockfall activity and talus deformation. J. Volcanol. Geotherm. Res. 187, 69–84.

Hale, A., Calder, E., Wadge, G., Loughlin, S., Ryan, G., 2009b. Modelling the lava dome extruded at Soufrière Hills Volcano, Montserrat, August 2005–May 2006. Part I: dome shape and internal structure. J. Volcanol. Geotherm. Res. 187, 53–68.

Hale, A., Wadge, G., 2008. The transition from endogenous to exogenous growth of lava domes with the development of shear bands. J. Volcanol. Geotherm. Res. 171, 237–257.

Holland, A., Watson, I., Phillips, J., Caricchi, L., Dalton, M., 2011. Degassing processes during lava dome growth: insights from Santiaguito lava dome, Guatemala. J. Volcanol. Geotherm. Res. 202, 153–166.

Hurwitz, S., Kipp, K., Ingebritsen, S., Ried, M., 2003. Groundwater flow, heat transport, and water table position within volcanic edifices. J. Geophys. Res. 108,

Ingebritsen, S., Scholl, M., 1993. The hydrogeology of Kilauea Volcano. Geothermics 22, 255–270.

Johnson, J., Lees, J., Gerst, A., Sahagian, D., Varley, N., 2008. Long-period earthquakes and co-eruptive dome inflation seen with particle image velocimetry. Nature 456, 377–381.

Kendrick, J., Lavallée, Y., Hess, K.-U., Heap, M., Gaunt, H., Meredith, P., Dingwell, D., 2013. Tracking the permeable porous network during strain-dependent magmatic flow. J. Volcanol. Geotherm. Res. 260, 117–126.

Kendrick, J., Lavallée, Y., Varley, N., Wadsworth, F., Lamb, O., Vasseur, J., 2016. Blowing off steam: tuffisite formation as a regulator for lava dome eruptions. Front. Earth Sci. 4, 41.

Klug, C., Cashman, C., Bacon, C., 2002. Structure and physical characteristics of pumice from the climactic eruption of Mount Mazama (Crater Lake), Oregon. Bull. Volcanol. 64, 486–501.

Klug, C., Cashman, K., 1996. Permeability development in vesiculating magmas: implication for fragmentation. Bull. Volcanol. 58, 87–100.

Kueppers, U., Perugini, D., Dingwell, D., 2006. "Explosive energy" during volcanic eruptions from fractal analysis of pyroclasts. Earth Planet. Sci. Lett. 248, 800–807.

Kushnir, A., Martel, C., Bourdier, J.-L., Heap, M., Reuschlé, T., Erdmann, S., Komorowski, J.-C., Cholik, C., 2016. Probing permeability and microstructure: unravelling the role of a low-permeability dome on the explosivity of Merapi (Indonesia). J. Volcanol. Geotherm. Res. 316, 56–71.

Lavallée, Y., Benson, P., Heap, M., Hess, K., Flaws, A., Schillinger, B., Meredith, P., Dingwell, D., 2013. Reconstructing magma failure and the degassing network of dome-building eruptions. Geology 41, 515–518.

Lee, S., 1990. Universality of continuum percolation. Phys. Rev. 42, 4877–4880.

Lensky, N., Lyakhovsky, V., Navon, O., 2002. Expansion dynamics of volatile-supersaturated fluid and bulk viscosity of bubbly magma. J. Fluid Mech. 460, 39–56.

Massol, H., 2001. Ascent and decompression of viscous vesicular magma in a volcanic conduit. J. Geophys. Res. 106, 16233–16240.

Mastin, L., Lisowski, M., Roeloffs, E., Beeler, N., 2009. Improved constraints on the estimated size and volatile content of the Mount St. Helens magma system from the 2004–2008 history of the dome growth and deformation. Geophys. Res. Lett. 36, L20304.

Matthews, S., Gardeweg, M., Sparks, R., 1997. The 1984 to 1996 cyclic activity of Lascar Volcano, northern Chile: cycles of dome growth, dome subsidence, degassing and explosive eruptions. Bull. Volcanol. 59, 72–82.

Melnik, O., Sparks, R., 2002. The eruption of Soufrière Hills Volcano, Montserrat, from 1995 to 1999 Vol. 21. Ch. Dynamics of Magma Ascent and Lava Extrusion at

Soufrière Hills Volcano, MontserratThe Geological Society of London, Memoirs. pp. 153–171

Melnik, O., Sparks, R., 2005. Controls on conduit magma flow dynamics during lava dome building eruptions. J. Geophys. Res. 110, B02209.

Mogi, K., 1958. Relations between the eruptions of various volcanoes and the deformations of the ground surfaces around them. Bull. Earthquake Res. Inst. 36, 99–134.

Moriya, I., 1978. Morphology of Lava Domes. 14. Bulletin Department of Geography Kanazawa University Japan., pp. 55–69.

Mueller, S., Melnik, O., Spieler, O., Sheu, B., Dingwell, D., 2005. Permeability and degassing of dome lavas undergoing rapid decompression: an experimental determination. Bull. Volcanol. 67, 238–526.

Mueller, S., Scheu, B., Kueppers, U., Spieler, O., Richard, D., Dingwell, D., 2011. The porosity of pyroclasts as an indicator of volcanic explosivity. J. Volcanol. Geotherm. Res. 203, 168–174.

Mueller, S., Scheu, B., Spieler, O., Dingwell, D., 2008. Permeability control on magma fragmentation. Geol. Soc. Am. 36, 399–402.

Newhall, C., Melson, W., 1983. Explosive activity associated with the growth of volcanic domes. J. Volcanol. Geotherm. Res. 17, 111–131.

Nishimura, T., 2006. Ground deformation due to magma ascent with and without degassing. Geophys. Res. Lett. 33, L23309.

Nishimura, T., 2009. Ground deformation caused by magma ascent in an open conduit. J. Volcanol. Geotherm. Res. 187, 178–192.

Odbert, H., Stewart, R., Wadge, G., 2014. The eruption of Soufrière Hills Volcano, Montserrat, from 2000 to 2010 Vol. 39. Ch. Cyclic Phenomena at the Soufrière Hills Volcano, MontserratThe Geological Society of London, Memoirs., pp. 41–60.

Odbert, H., Taisne, B., Gottsmann, J., 2015. Deposit loading and its effect on co-eruptive volcano deformation. Earth Planet. Sci. Lett. 413, 186–196.

Ogburn, S., Loughlin, S., Calder, E., 2015. The association of lava dome growth with major explosive activity (VEI ≥ 4): DomeHaz, a global dataset. Bull. Volcanol. 77, 40.

Pallister, J., Scneider, D., Griswold, J., Keeler, R., William, C., Noyles, C., Newhall, C., Ratdomopurbo, A., 2013. Merapi 2010 eruption - chronology and extrusion rates monitored with satellite radar and used in eruption forecasting. J. Volcanol. Geotherm. Res. 261, 144–152.

Pinel, V., Hooper, A., De la Cruz-Reyna, S., Reyes-Davila, G., Doin, M., Bascou, P., 2011. The challenging retrieval of the displacement field from InSAR data for andesitic stratovolcanoes: case study of Popocatepetl and Colima Volcano, Mexico. J. Volcanol. Geotherm. Res. 200, 49–61.

Pinel, V., Jaupart, C., 2000. The effect of edifice load on magma ascent beneath a volcano. . Phylosophical Transactions: Mathematical, Physical and Engineering Sciences 358. pp. 1515–1532.

Prud'Homme, R., Bird, R., 1978. The dilatational properties of suspensions of gas bubbles in incompressible Newtonian and non-Newtonian fluids. J. Non-Newtonian Fluid Mech. 3, 261–279.

Rice, J., 1992. Fault mechanics and transport properties of rocks. . Ch. Fault Stress States, Pore Pressure Distributions, and the Weakness of the San Andrea Fault Academic, London., pp. 475–503.

Richard, D., Scheu, B., Mueller, S., Spieler, O., Dingwell, D., 2013. Outgassing: influence on speed of magma fragmentation. J. Geophys. Res. Solid Earth 118, 862–877.

Robertson, R., 1998. The explosive eruption of Soufrière Hills Volcano, Montserrat, West Indies, 17 September, 1996. Geophys. Res. Lett. 25, 3429–3432.

Rust, A., Cashman, K., 2004. Permeability of vesicular silicic magma: inertial and hysteresis effects. Earth Planet. Sci. Lett. 228, 93–107.

Sahimi, M., 1994. Applications of Percolation Theory. Taylor & Francis Ltd., London.

Sato, H., Fujii, T., Nakada, S., 1992. Crumbling of dacite dome lava and generation of pyroclastic flows at Unzen Volcano. Let. Nat. 360, 664–666.

Scheu, B., Kueppers, U., Mueller, S., Spieler, O., Dingwell, D., 2008. Experimental volcanology on eruptive products of Unzen Volcano. J. Volcanol. Geotherm. Res. 175, 110–119.

Schneider, A., Rempel, A., Cashman, K., 2012. Conduit degassing and thermal controls on eruption styles at Mount St. Helens. Earth Planet. Sci. Lett. 357-358, 347–354.

Shaw, H., 1974. Diffusion of water in granitic liquids: part I. Experimental data; part II. Mass transfer in magma chambers. Carnegie Inst. Wash. Publ. 634, 139–172.

Shields, J., Mader, H., Pistone, M., Caricchi, L., Floess, D., Putlitz, B., 2014. Strain-induced degassing of three-phase magmas during simple shear. J. Geophys. Res. Earth Sci. 119, 6936–6957.

Sparks, R., 1997. Causes and consequences of pressurisation in lava dome eruptions. Earth Planet. Sci. Lett. 150, 177–189.

Sparks, R., Murphy, M., Lejeune, A., Watts, R., Barclay, J., Young, S., 2000. Control on the emplacement of the andesite lava dome of the Soufrière Hills Volcano, Montserrat by degassing-induced crystallization. Terra Nova 12, 14–20.

Sparks, R., Young, S., Barclay, J., Calder, E., Cole, P., Darroux, B., Davies, M., Druitt, T., Harford, C., Herd, R., James, M., Lejeune, A., Loughlin, S., Norton, G., Skerrit, G., Staviusk, M., Stevens, N., Toothill, J., Wadge, G., Watts, R., 1998. Magma production and growth of the lava dome of the Soufrière Hills Volcano, Montserrat, West Indies: November 1995 to December 1997. Geophys. Res. Lett. 25, 3421–3424.

Spieler, O., Kennedy, B., Kueppers, U., Dingwell, D., Scheu, B., Taddeucci, J., 2004. The fragmentation threshold of pyroclastic rocks. Earth Planet. Sci. Lett. 226, 139–148.

Stix, J., 1993. A model of degassing at Galeras Volcano, Colombia, 1988–1993. Geology 21, 963–967.

Swanson, D., Holcomb, R., 1990. Lava flows and domes. Ch. Regularities in Growth of the Mount St. Helens Dacite Dome, 1980–1986Springer Berlin Heidelberg. pp. 3–24

Taisne, B., Jaupart, C., 2008. Magma degassing and intermittent lava dome growth. Geophys. Res. Lett. 35,

Voight, B., Hoblitt, R., Clarke, A., Miller, A., Lynch, L., McMahon, J., 1998. Remarkable cyclic ground deformation monitored in real-time on Montserrat, and its use in eruption forecasting. Geophys. Res. Lett. 25 no. 18, 3405–3408.

Voight, B., Sparks, R., Miller, A.D., Stewart, R., Hoblitt, R., Clarke, A., Ewart, J., Aspinall, W., Baptie, B., Calder, E., Cole, P., Druitt, T., Hartford, C., Herd, R., Jackson, P., Lejeune, A., Lockhart, A., Loughlin, S., Luckett, R., Lynch, L., Norton, G., Robertson, R., Watson, I., Watts, R., Young, S., 1999. Magma flow instability and cyclic activity at Soufrière Hills Volcano, Montserrat, British West Indies. Science 283, 1138–1139.

Wadge, G., Ryan, G., Calder, E., 2009. Clastic and core lava components of a silicic lava dome. Geology 37, 551–554.

Wallace, P., Anderson, A., Davis, A., 2002. Quantification of pre-eruptive exsolved gas contents in silicic magmas. Lett. Nat. 377, 612–616.

Watson, I., Oppenheimer, C., Voight, B., Francis, P., Clarke, A., Stix, J., Miller, A., Pyle, D., Burton, M., Young, S., Norton, G., Loughlin, S., Darroux, B., Staff, M., 2000. The relationship between degassing and ground deformation at Soufrière Hills Volcano, Montserrat. J. Volcanol. Geotherm. Res. 98, 117–126.

Watts, R., Herd, R., Sparks, R., Young, S., 2002. The eruption of Soufrière Hills Volcano, Montserrat, from 1995 to 1999 Vol. 21. . The Geological Society of London, Memoirs, Ch. Growth Patterns and Emplacement of the Andesitic Lava Dome at Soufrière Hills Volcano, Montserrat., pp. 115–152.

Widiwijayanti, C., Clarke, A., Elsworth, D., Voight, B., 2005. Geodetic constraints on the shallow magma system at Soufrière Hills Volcano, Montserrat. Geophys. Res. Lett. 32, L11309.

Wright, H., Roberts, J., Cashman, K., 2006. Permeability of anisotropic tube pumice: model calculations and measurements. Geophys. Res. Lett. 33, L17316.

Journal of Volcanology and Geothermal Research 341 (2017) 371–373

Contents lists available at ScienceDirect

Journal of Volcanology and Geothermal Research

journal homepage: www.elsevier.com/locate/jvolgeores

Corrigendum

Corrigendum to "Temporal evolution of magma flow and degassing conditions during dome growth, insights from 2D numerical modeling" [J. Volcanol. Geotherm. Res. 333–334 (2017) 116–133]

Laure Chevalier *, Marielle Collombet, Virginie Pinel

Institute of Earth Sciences (ISTerre) - IRD, Université Savoie Mont Blanc, Campus Scientifique, 73376 Le Bourget-du-Lac cedex, France

1. False implementation of divergence in 2D cylindrical geometry in the COMSOL Multiphysics PDE

The article "Temporal evolution of magma flow and degassing conditions during dome growth, insights from 2D numerical modeling" (http://dx.doi.org/10.1016/j.jvolgeores.2017.01.016) studies the different effects a dome emplacement may have on gas loss in the upper conduit, using numerical models for solving magma and gas flow conditions. It is made of 3 independent however interacting models that successively solve magma flow, ground deformation and gas flow conditions.

An error has been introduced in the numerical implementation of the gas flow model with the COMSOL Multiphysics software due to the false implementation of the equations in the 2D cylindrical geometry in the COMSOL Multiphysics PDE (belonging to the Mathematics group). We indeed recently found out that the divergence calculation was not implemented correctly despite this error has no visibility in the software documentation and interface. In 2D cylindrical geometry, the expression of the divergence would be expressed as follows:

$$\nabla \cdot A = \frac{\partial A_r}{\partial r} + A_r/r + \frac{\partial A_z}{\partial z} \tag{1}$$

However, in the COMSOL Multiphysics PDE, 2D cylindrical geometry, the middle term of the right member, A_r/r, is missing. Because of this missing term, solutions from the COMSOL Multiphysics PDE, 2D cylindrical geometry, correspond to a 2D Cartesian geometry, rather than cylindrical.

The results we presented for gas flow in the article "Temporal evolution of magma flow and degassing conditions during dome growth, insights from 2D numerical modeling" (http://dx.doi.org/10.1016/j.jvolgeores.2017.01.016) therefore correspond to gas flow in a dike (2D geometry), rather than in a conduit (2D cylindrical), contrary to what was claimed.

2. Corrections

We corrected the gas flow model by adding the missing term for divergence as a source term, in the COMSOL Multiphysics PDE, and compared new results for gas flow (conduit) with those published in JVGR (dike). This change in the geometry used for solving gas flow in the upper conduit has little influence on the conclusions we drew up in the published article. We indeed mainly commented on qualitative observations, while the error mainly affects quantitative results.

We observe significant changes in Figs. 10 and 12 of the article, which are presented here. Fig. 10 concerns changes in the gas pressure due to the evolution of the surrounding rock permeability with dome growth. Here, new results show that the rock permeability influence is significant in the top part of the conduit (first 100 m) even for a permeability change from 10^{-12} m^2 to 10^{-13} m^2 (up to 4 MPa). By decreasing the rock permeability by one order of magnitude, we maximised the effect a dome may have on this parameter. The gas pressure evolution this permeability change causes remains small compared with the influence of pressure in the surrounding rock and of magma flow conditions evolution. Considering larger orders of magnitude of permeability change, the influence on gas pressure is also higher than in the previous article version, but it remains superficial.

Fig. 1,2 presents the influence of pressure conditions in the surrounding rock on gas pressure in the conduit. Compared with the previous article version, the evolution of gas pressure in the top part of the conduit, due to the evolution of pressure conditions in the surrounding rock, is smaller (increase of 8 MPa instead of 17 MPa for a 300 m-high dome). In the rest of the conduit however, pressurisation remains similar (about 4 MPa).

DOI of original article: http://dx.doi.org/10.1016/j.jvolgeores.2017.01.016.

* Corresponding author.
E-mail address: laure.chevalier@univ-smb.fr (L. Chevalier).

http://dx.doi.org/10.1016/j.jvolgeores.2017.06.008

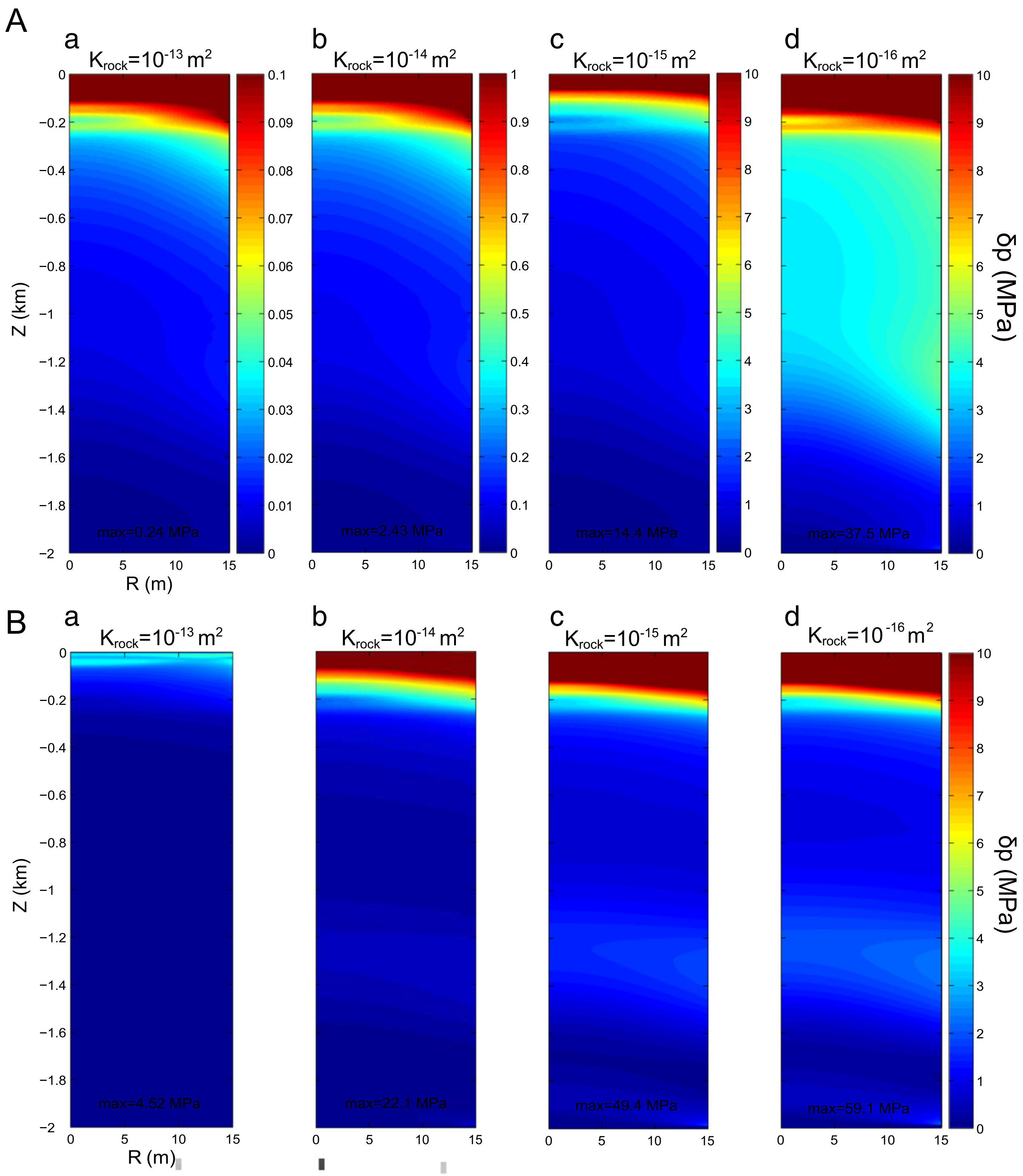

Fig. 1. Changes in Fig. 10. a) Initial version, 2D geometry (dike) b) Corrected version, 2D cylindrical geometry (conduit). Gas pressure evolution δp within the first 2 km of the conduit, for surrounding rock permeability varying from 10^{-13} to 10^{-16} m². Initial and boundary pressure conditions are constant, as well as magma permeability, and no dome is present above the conduit.

Fig. 2. Changes in Fig. 12. A) Initial version, 2D geometry (dike) B) Corrected version, 2D cylindrical geometry (conduit). Effect of rock pressure increase. Gas pressure evolution δp is represented within the first 2 km, for surrounding rock pressure corresponding to dome heights varying from 50 to 300 m. No permeable dome is present above the conduit, and magma and surrounding rock permeability remain constant.

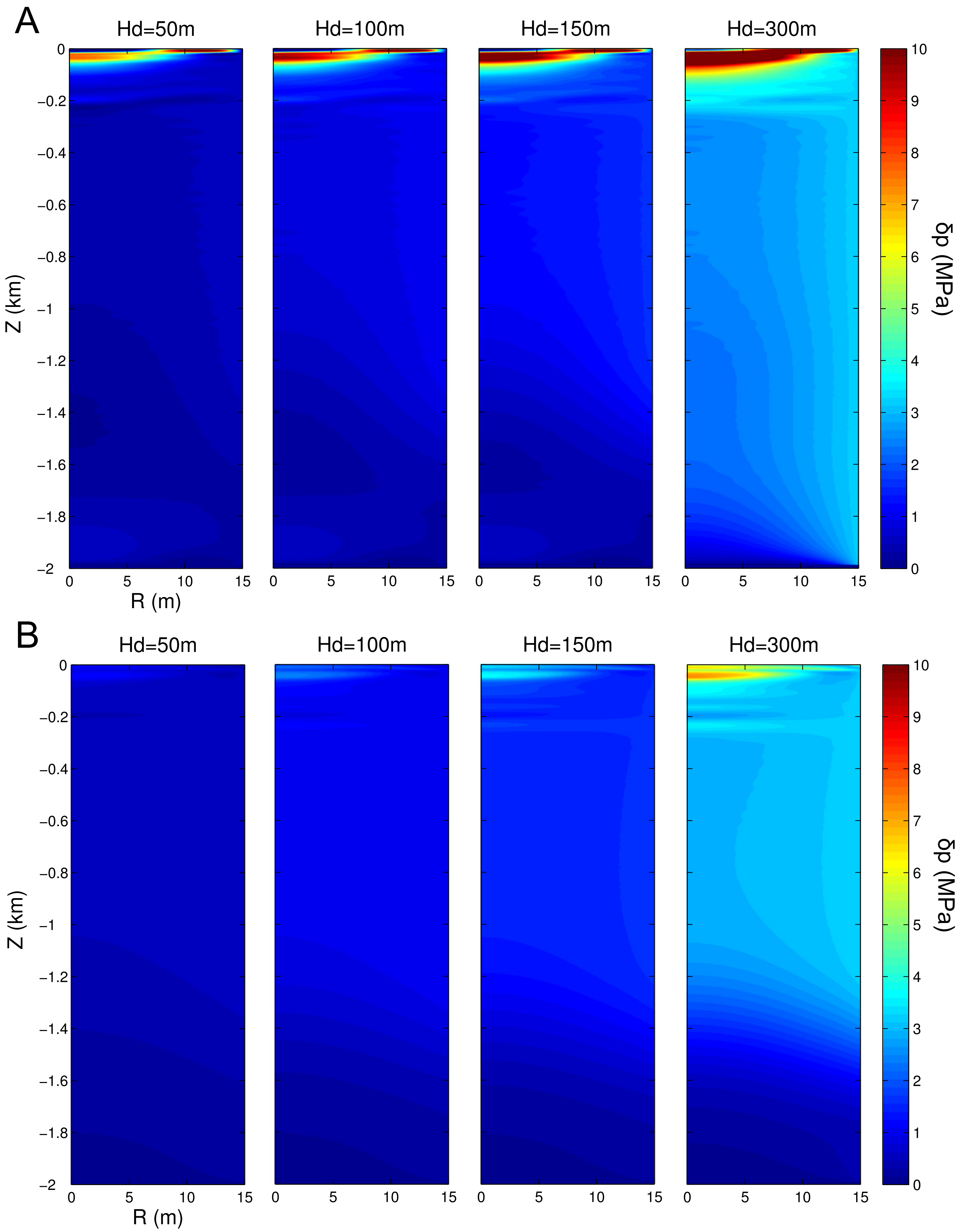
A
Hd=50m
Hd=100m
Hd=150m
Hd=300m
Z (km)
0
−0.2
−0.4
−0.6
−0.8
−1
−1.2
−1.4
−1.6
−1.8
−2
R (m)
0 5 10 15
δp (MPa)
0 1 2 3 4 5 6 7 8 9 10
B
Hd=50m
Hd=100m
Hd=150m
Hd=300m
Z (km)
R (m)
δp (MPa)

2.5 Conclusion

In this chapter, we studied the influence of several parameters on gas flow conditions, that evolve with dome growth. We identified parameters that are controlling for gas loss, and quantified their relative influence. Results presented in Chevalier et al. (2017) provide evidence that gas loss in the upper conduit is controlled by the evolution of magma permeability and pressure conditions in the surrounding rock, while the permeability of the forming dome has little influence. We also observed that gas is mainly lost at the conduit walls, and not at its top.

The evolution of magma permeability within the conduit, and of pressure gradients at the conduit edges with depth are therefore determinant for gas loss. Although we give some insights on the influence of pressure conditions evolution with depth on degassing in Chevalier et al. (2017) (section 5.3.3), permeability development within the conduit, and its evolution with depth is poorly constrained. Permeability development in ascending magma, and its influence on gas loss is discussed in chap. 3.

Although we here focused on dome emplacement consequences for gas loss and flow conditions, the results presented here give insights on the controls that exist on gas loss in transient conditions. This may reveal useful for the interpretation of future, more complex models.

Chapter 3

Magma permeability development and evolution in the conduit

Contents

3.1 Introduction

Measurements for experimental (Takeuchi et al., 2005, 2009) and natural (e.g. Klug and Cashman, 1996; Melnik and Sparks, 2002; Mueller et al., 2005; Rust and Cashman, 2004, 2011) silicic magma samples cover a very large range of porosity-permeability values (Mueller et al., 2005; Gonnermann and Manga, 2007). A variety of empirical permeability-porosity relationships were proposed from these datasets (e.g. Klug and Cashman, 1996; Mueller et al., 2005; Rust and Cashman, 2011). However, they all lack in representing the whole range of observed values. Choosing one permeability law among the others then often results in neglecting part of the existing data. In chapter 2 we show that magma permeability has a huge influence on gas loss. It is therefore of primary importance to better understand permeability development in magmas, and how it can result in such a diversity of permeability-porosity relationships, in order to have some more clues on which permeability law should be used in conduit flow modelling.

In addition, permeability measurements on anisotropic samples provided evidence that bubble deformation is associated with an anisotropy in permeability, the permeability in the direction parallel to elongation being higher than in the orthogonal direction (Wright et al., 2006; Klug et al., 2002; Degruyter et al., 2009; Rust and Cashman, 2004; Blower, 2001; Bouvet de Maisonneuve et al., 2009). In the conduit, magma is submitted to shear stress that can cause important bubble deformation. These shear conditions however evolve in space and time. Being able to link permeability with flow conditions would then be of great interest for modelling degassing in the conduit.

Studies on the connected bubble network evidenced that permeability can be related to several geometrical parameters such as tortuosity or bubble diameter (Bouvet de Maisonneuve et al., 2009; Degruyter et al., 2009). Although the permeability laws developed this way cannot be used in conduit flow models because we do not have access to some of these geometrical parameters, they provide some clues for understanding permeability development. We therefore work on characterising the bubble networks of rhyolitic synthetic samples, and link their characteristics with permeability and with conduit flow parameters, such as porosity, velocity field and water content. This study aims at better understanding how permeability develops in ascending magma, and at integrating observations made from the bubble network characteristics to a permeability law that can be used in a conduit flow model.

For this work I collaborated with Alain Burgisser. I describe the work we have done in greater details in section 3.2, and specify the role I took. This work resulted in one article, currently under review, that is then attached. In this article we provide some clues on the controls of permeability development, especially for percolation, which corresponds to the exact moment when magma becomes permeable. The percolation is often associated with a critical porosity value, called percolation threshold, over which the magma is observed to be permeable. We give a new expression for the percolation threshold that succeeds in separating permeable samples from impermeable ones for a wide range of data. We also develop in this article a permeability law that unifies most of the permeability-porosity relationships made on silicic volcanoes. This permeability law can be easily integrated into a numerical model. Its influence on the magma flow conditions modelling in 1D (Kozono and Koyaguchi, 2009) is discussed in the article. Eventually, I integrate the specific new permeability law to the gas flow model I presented in chap. 2 and discuss possible consequences for conduit flow modelling and eruption dynamics understanding.

3.2 Work on permeability development in decompressed magma

Motivations Results from Chevalier et al. (2017) provide evidence that the magma permeability plays a key role in magma degassing in the conduit, which in turn influences magma explosivity. Knowing the difficulty for current permeability laws to reassemble the whole permeability measurements dataset, I was very interested in working on better understanding permeability development processes. I had heard about permeability laws based on geometrical parameters, and was eager to work on linking those parameters with flow conditions, in order to possibly integrate these permeability laws into numerical modelling. This was the occasion of studying the role of bubble elongation on permeability anisotropy, which I think is a key issue for degassing modelling.

Alain Burgisser was particularly interested in understanding permeability development in magmas, and especially in the very moment when magma becomes permeable, which is called percolation. A percolation threshold had already been defined in several permeability studies as a critical value of the porosity, but their was no agreement on its value.

Analysed material derived from previous experiments We worked on natural samples of rhyolitic composition that had been hydrated and then decompressed with different decompression rates and duration. The resulting bubbly samples had been scanned with 3D X-ray micro-tomography. These experiments had been designed and run by Burgisser and Gardner (2004) and Gardner (2007). We directly worked on the X-ray scans.

Samples characterisation Alain Burgisser and I both worked on characterising the bubble networks of the samples. We also measured their permeability from fluid flow numerical simulations in each direction of the 3D volumes. While Alain worked on the isotropic samples (spherical bubbles), I worked on the anisotropic ones (elongated bubbles). Because of anisotropy, I oriented the samples so that I could measure permeability and geometrical parameters (tortuosity, cross–section anisotropy, bubble elongation) in the directions of the major, intermediate and minor axes of the bubble deformation.

Exploration on parameters relationships We then both worked on linking the different measured parameters (bubbles and throats diameter, porosity, connected porosity, tortuosity, bubble elongation, interbubble distance, Bubble Number Density (BND)) with each other, and with parameters that can be used in the conduit flow numerical models (porosity, bubble diameter, BND, velocity field and pressure). This was the occasion for thinking about the role of physical processes that may affect the permeability and the relations between the different parameters. During this exploratory work, I also evidenced the importance of the Bubble Size Distribution (BSD) spread (σ_a/d_a) for explaining connected porosity development in anisotropic samples.

Pooling observations After this explorative time, we then pooled our observations. We worked together on adapting the relations we had observed so that they are consistent for both anisotropic and isotropic samples. During this time, Alain observed that the BSD spread σ_a/d_a, combined with the interbubble distance z_m, was a relevant parameter for splitting connected samples from impermeable ones (Burgisser et al. (2017), fig. 3).

Comparison with other studies Alain did most of the work for assembling data from other studies and confront them with the relationships we had fitted. I helped extracting porosity, viscous and inertial permeability, bubble diameters and BSD spread from the data presented by Lindoo et al. (2016) for decompressed silicic samples.

Implementation in conduit flow numerical models Since I was particularly interested in integrating our results into numerical models, I did the work to implement our permeability law in the Kozono and Koyaguchi (2009) and in the Chevalier et al. (2017) conduit flow models. Part of the results from the resulting models are

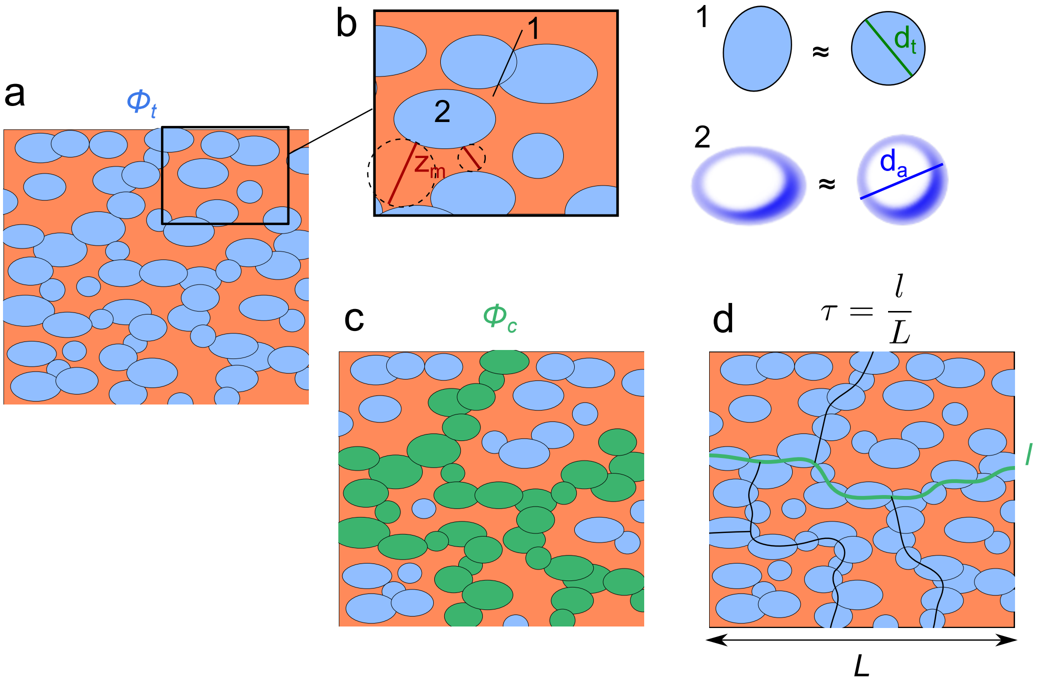

Figure 3.1: Sketch of the geometrical parameters measured in the samples. (a) The total porosity ϕ_t is the ratio between the volume of bubbles and the total volume, expressed in vol% (b) The bubble diameter d_a corresponds to the diameter of the sphere of equivalent volume. The throat diameter d_t corresponds to the diameter of the disc of equivalent surface. z_m is the interbubble distance. (c) The connected porosity ϕ_c is the ratio between the volume of bubbles connected with the sample edges and the total sample volume, expressed in vol%. (d) The tortuosity τ is the ratio between the shorter path between two opposite edges of the sample l, and the Euclidian distance between these two edges L.

presented in the article. They concern the 1D model from Kozono and Koyaguchi (2009). The consequences of implementing our permeability law into a 2D axisymmetric degassing model (Chevalier et al., 2017) are presented in section 3.4.

3.3 The percolation threshold and permeability evolution of ascending magmas

In revision for Earth and Planetary Science Letters.

Earth and Planetary Science Letters 470 (2017) 37–47

Contents lists available at ScienceDirect

Earth and Planetary Science Letters

www.elsevier.com/locate/epsl

The percolation threshold and permeability evolution of ascending magmas

Alain Burgisser [a,*], Laure Chevalier [a], James E. Gardner [b], Jonathan M. Castro [c]

[a] Univ. Savoie Mont Blanc, CNRS, IRD, ISTerre, F-73376 Le Bourget du Lac, France
[b] Department of Geological Sciences, The University of Texas at Austin, Austin, TX 78712-0254, USA
[c] Institute of Geosciences, Johannes Gutenberg University Mainz, Mainz, Germany

ARTICLE INFO

Article history:
Received 5 November 2016
Received in revised form 11 April 2017
Accepted 12 April 2017
Available online xxxx
Editor: T.A. Mather

Keywords:
rhyolite
experimental petrology
conduit flow
volcanic eruption

ABSTRACT

The development of gas permeability in magmas is a complex phenomenon that directly influences the style of a volcanic eruption. The emergence of permeability is linked to the concept of percolation threshold, which is the point beyond which gas bubbles are connected in a continuous network that allows gas escape. Measurements of the percolation threshold, however, range from ∼30 to 78 vol%. No known combination of parameters can explain such a wide range of threshold values, which affects our understanding of the relationship between percolation and permeability. We present permeability calculations on bubble-bearing rhyolitic melts that underwent experimental decompression. Samples were analyzed by X-ray microtomography to image the bubble networks in 3D. We develop a percolation threshold for magmas that depends on the bubble network characteristics of this sample set. This relationship recovers the behavior of a wide range of volcanic samples by separating permeable samples from impermeable ones with a success rate of 88%. We use this percolation threshold to propose simplified permeability relationships that rely on parameters widely used in numerical modeling of magma flow. These relationships are valid within one order of magnitude for the viscous permeability coefficient and within two orders of magnitude for the inertial coefficient. They recover the ranges of values previously covered by isolated relationships, reassembling them within a single framework. We test the implications of such unification on eruptive dynamics with a 1D, two-phase conduit flow model. This test shows that varying the percolation threshold has little influence on vertical gas loss and ascent dynamics.

1. Introduction

During a volcanic eruption, magma ascends towards the surface and loses the volatiles it contains. In viscous magmas, volatiles are lost as gas bubbles that grow during ascent but hardly move relative to each other. The coalescence of the bubbles with each other transforms the bubbly magma into a connected network that is permeable to gas (e.g., Eichelberger et al., 1986). Permeability allows the gas to separate from the magma (e.g., Yoshida and Koyaguchi, 1999). An efficient separation promotes effusive eruptions, whereas bubble accumulation by growth promotes fragmentation and explosive eruptions (e.g., Jaupart and Allègre, 1991).

Studies aimed at understanding magma permeability have established relationships that depend on material properties, such as bubble size, total and connected gas volume fraction, throat size (aperture of inter-bubble connections), bubble aspect ratio, and network tortuosity (Klug and Cashman, 1996; Mueller et al., 2005; Wright et al., 2009; Yokoyama and Takeuchi, 2009; Degruyter et al., 2010a). Focusing on natural data, permeability relationships went from the apparent simplicity of depending only on total gas volume fraction (Klug and Cashman, 1996) to larger degrees of complexity as more data were acquired and more degrees of freedom were needed to describe the relationships (Saar and Manga, 1999). Another degree of complexity was reached when a second permeability coefficient was introduced alongside the original coefficient entering Darcy's law. While the first permeability coefficient, k_1, quantifies the effects of gas flow when viscous effects dominate, the additional coefficient, k_2, takes into account the inertial effects of turbulent flow (Rust and Cashman, 2004). It was also found that the relationships gain in accuracy of permeability prediction when using connected gas volume fraction instead of total gas fraction (Saar and Manga, 1999; Mueller et al., 2005; Gonnermann and Manga, 2007). The relationship between total and connected porosity is directly linked to the threshold at which

---

* Corresponding author. Fax: +33 479 758 742
E-mail address: alain.burgisser@univ-savoie.fr (A. Burgisser).

http://dx.doi.org/10.1016/j.epsl.2017.04.023

Table 1
Symbol list. The mean bubble diameter is based on the diameter distribution and the average bubble diameter is based on volume distribution (see Methods).

Symbol	Description (unit)
A	Proportionality constant
a_i	Semi-axes of ellipsoid (m)
a_{KC}	Constant in Kozeny–Carman equation (m^2)
a_M	Constant in percolation equation (m^2)
B	Proportionality constant
b_{KC}	Exponent in Kozeny–Carman equation
b_M	Exponent in percolation equation
c_d	Percolation constant (m)
c_ϕ	Connected porosity constant
c_p	Connected porosity constant (m)
c_τ	Tortuosity constant
c_z	Percolation exponent
χ_i	Bubble aspect ratio
d_a	Average bubble diameter (m)
d_m	Mean bubble diameter (m)
d_t	Throat diameter (m)
ε_i	Bubble elongation
f_0	Inertial factor
ϕ_c	Connected porosity
ϕ_p	Percolation porosity
ϕ_t	Total porosity
i, k	Indices of spatial direction
k_1	Viscous permeability (m^2)
k_2	Inertial permeability (m)
l_i	Longest semi-axis of ellipsoid orthogonal to i (m)
m	Exponent in Archie's law
μ	Fluid viscosity (Pa s)
n	Exponent in Degruyter equation
N_m	Bubble number density per unit melt (m^{-3})
P	Pressure (Pa)
ρ	Fluid density (kg/m^3)
r_i	Radius of equivalent disk of ellipsoid cross-section orthogonal to i (m)
R_1, R_2, R_3	Sum of residuals
σ_a	Standard deviation of d_a (m)
σ_m	Standard deviation of d_m (m)
τ_i	Tortuosity
v_i	Fluid velocity (m/s)
$\vec{w}$	Vector of components a_i
x_i	Spatial direction
z	Calculated inter-bubble distance (m)
z_m	Measured inter-bubble distance (m)
Z	Scaled inter-bubble distance (m)
Z_p	Percolation threshold on Z (m)

the magma ceases to be impermeable to gas. Drawing from percolation theory (Sahini and Sahimi, 1994), this threshold has mostly been assumed to depend on a constant value of gas volume fraction (Blower, 2001). Characterizing the percolation threshold in natural products (e.g., Eichelberger et al., 1986; Klug and Cashman, 1996; Saar and Manga, 1999; Mueller et al., 2005), experimental magmas (e.g., Takeuchi et al., 2009; Martel and Iacono-Marziano, 2015), and analogue materials (e.g, Namiki and Manga, 2008) led to values ranging from ∼30 to 78 vol%. Several possible controls of such a wide range of values have been proposed: crystal volume fraction, melt viscosity, shear stress, decompression rate, differences in experimental methodology, and the inaccuracy of theoretical models that do not take into account the time needed for interstitial film retraction (Okumura et al., 2013; Rust and Cashman, 2011; Lindoo et al., 2016). Some parameters, such as shear stress, give a partial explanation for the variability of measured percolation thresholds (Caricchi et al., 2011; Okumura et al., 2013), whereas others, such as melt viscosity, do not seem to control this variability (Lindoo et al., 2016). None explain the full spectrum of threshold values.

The transition of magma from being permeable to impermeable controls when gas escape ceases. The amount of gas escape, on the other hand, is controlled by permeability, which directly influences the style of the volcanic eruption (Yoshida and Koyaguchi, 1999; Kozono and Koyaguchi, 2009; Degruyter et al., 2012). Clarifying the relationship between percolation and permeability is thus an important issue.

Here we investigate the role of the bubble network geometry on the percolation threshold and on permeability. (See Table 1.) We use a subset of two series of experiments (Burgisser and Gardner, 2004; Gardner, 2007) on silicate melts in which bubbles grew during isothermal decompression and interacted to various degrees, sometimes creating a permeable network by coalescence. These crystal-free experiments were analyzed by X-ray Computed Tomography (CT) to obtain 3D reconstructions of the bubble networks, as described in Castro et al. (2012). Bubble network parameters and both viscous and inertial permeability coefficients were calculated so as to test the relationship of Degruyter et al. (2010a) against our data set. That relationship assumes that the state of percolation and network parameters are known. We relax these assumptions by making the relationships depend on 1) a percolation threshold related to bubble network geometry and 2) magmatic parameters widely used in conduit flow models. We establish that the percolation depends on bubble separation and on the degree of polydispersity of the bubble size distribution. The resulting relationship links inertial and viscous permeabilities to the average and standard deviation of the bubble size distribution, bubble aspect ratio, and total porosity. We show how the proposed percolation threshold captures the behavior of previously published data sets. Finally, we explore some implications of having a unified framework predicting magma permeability on conduit flow model outputs.

2. Methods

2.1. CT volumes

We analyzed a subset of 36 samples from experimentally decompressed rhyolite melts. Briefly, the Burgisser and Gardner (2004) and the Gardner (2007) experiments consisted of placing samples of rhyolitic glass in sealed Au-capsules with distilled water, and equilibrating them at 150 MPa for five days in order to saturate the melt with water. Some capsules were quenched, removed from the pressure vessel, and opened to extract the hydrated samples. These samples were reloaded into Au capsules without water, but with either silicate glass powder or MgO powder to serve as a sink for expelled water during decompression, allowing open-degassing conditions. Each capsule was then repressurized and reheated at the hydration conditions for 5 min before an applied sudden decompression nucleated small bubbles (mean radius <<10 μm). The other samples – i.e. those that had not been reopened and reloaded – remained in the pressure vessel until the nucleation step was performed, thus ensuring closed-system conditions. All samples were maintained at the nucleation pressure until bubbles reached thermodynamic equilibrium, which was checked by determining the glass water content (Gardner, 2007). Pressure was then released in increments to approximate a constant decompression rate until a final pressure was reached, at which samples were quenched rapidly.

All volumes analyzed by CT (Castro et al., 2012) come from hydrated and foamed cores that underwent decompression in either closed, or open degassing conditions. These samples were sometimes small pieces broken from the original cores and sometimes were parts of thin sections that were recut with a diamond saw so as to leave the smallest possible amount of thin section glass attached to the sample. As a result, while the former samples are often equant and yielded nearly cubic CT volumes, the latter samples were much thinner in one direction and yielded highly flattened volumes (details in Supplementary Text S1 and Fig. S1).

Connected bubbles have retained their original shapes. When these shapes are mostly spherical, we refer to the sample as being isotropic. Some volumes contain ellipsoidal bubbles. They come from the top part of hydrated and foamed samples and we refer to these samples as being anisotropic. Sample deformation is likely due to volumetric expansion of the sample during decompression that forced the melt in the crimped ends of the capsule (Burgisser and Gardner, 2004). In these deformed areas, both bubble elongation amplitude and direction vary significantly. CT volumes were selected so that bubbles have clearly visible and homogeneous orientation fabric. These anisotropic samples were rotated so that the principal directions of elongation correspond to those of the sample edges (x, y and z axes).

2.2. Bubble network parameters

The CT volumes were digitally thresholded in order to distinguish bubbles from glass. Some samples contain <1 vol.% of Fe–Ti oxides, which were grouped with the glass category. The software ImageJ (version 1.49) and associated plugins were used to quantify the three-dimensional network of bubbles. Bubbles are not distributed homogeneously in space. The distance separating two neighboring bubbles is thus best measured by focusing on the glass phase. Bubble separation distance, z_m, is the mean value given by the "Thickness" plugin of the BoneJ (version 1.3.11) bundle (Doube et al., 2010), which measures at each voxel of the glass phase the diameter of the largest sphere that fits within the glass phase and that contains that voxel. Connected porosity was measured by adding all the connected volumes given by the "3D object counter" plugin (Bolte and Cordelières, 2006) that had bounding boxes as large as the CT volume (i.e. that span the volume from side to side). In most samples, bubbles form an interconnected network. Original bubbles can nevertheless be separated because they connect to each other by narrow throats (Supplementary Text S1 and Fig. S2). The software Blob3D (Ketcham, 2005) was used to separate bubbles either by erosion or planar cut. Bubble and throat shapes were measured for the whole sample whenever possible. When the number of bubbles in the CT volume was too large to be fully analyzed with Blob3D, a representative sub-volume was used to determine bubble and throat shape statistics. Throat diameter, d_t, was defined as the diameter of the disk equivalent to the measured throat surface. The throat diameter value used for calculation is the median for the sample and the standard deviation gives the spread of this parameter. Bubble number density with respect to melt volume, N_m, was calculated using the total number of counted bubbles in the sample volume, except for samples where the total number of bubbles was not fully counted. Instead, N_m for those samples are the total bubble number densities reported in Burgisser and Gardner (2004) and Gardner (2007), corrected for sample porosity.

Bubble diameter, d_a, was calculated as the diameter of the equivalent sphere corresponding to the average bubble volume, which is the sum of all bubble volumes divided by the number of bubbles. The uncertainty on bubble diameter, σ_a, corresponds to half the difference between the 16th and 84th percentile of the volume distribution. This measure of standard deviation takes into account that the shape distribution spans from Gaussian to power law (Burgisser and Gardner, 2004). Most studies on bubble size distributions have used the mean bubble diameter, d_m, instead of d_a as the characteristic bubble diameter (e.g., Burgisser and Gardner, 2004; Takeuchi et al., 2009; Bai et al., 2010). We found that d_a yields generally better fits with the permeability relationships we consider herein. Formally, d_a corresponds to the ratio between the 4th and 3rd moments of the bubble diameter distribution, and d_m is the arithmetic mean of the distribution. This ratio fits our measurements, but it needs the full size distribution to convert d_m into d_a. Because most studies report only d_m, and its associated standard deviation, σ_m, we instead use empirical relationships that depend only on these two quantities to retrieve d_a from the published d_m:

$$d_a = A d_m\left(1+\frac{\sigma_m}{d_m}\right) \tag{1}$$

$$\sigma_a = AB\sigma_m\left(1+\frac{\sigma_m}{d_m}\right) \tag{2}$$

These relations fit very well with our measurements when the proportionality constants, A and B, are set to 0.87 and 0.64, respectively. We use the ratio of σ_a to d_a as a measure of the degree of polydispersity of the distribution: $\sigma_a/d_a = B\sigma_m/d_m$.

Some permeability relationships involve a cross-section shape factor, χ_i (Degruyter et al., 2010a):

$$\chi_i = \left(\frac{l_i^2}{r_i^2}+\frac{r_i^2}{l_i^2}\right) \tag{3}$$

where l_i is the longest semi-axis of the ellipsoid cross-section area orthogonal to direction i and r_i is the radius of the equivalent disk of the ellipsoid cross-section area. Because the anisotropic samples were oriented so that the bubble major axes of elongation match the sample edge directions, we define a_i as the semi-axes of the Blob3D best-fit ellipsoids of the bubbles. We assume that l_i corresponds to the maximum of the ellipsoid semi-axes orthogonal to the selected direction i with $k = x, y, z$:

$$l_i = max(a_{k,k\neq i}) \tag{4}$$

The parameter r_i is:

$$r_i = \sqrt{\prod(a_{k,k\neq i})} \tag{5}$$

Equation (3) thus becomes:

$$\chi_i = \left(\frac{max(a_{k,k\neq i})}{min(a_{k,k\neq i})}+\frac{min(a_{k,k\neq i})}{max(a_{k,k\neq i})}\right) \tag{6}$$

Cross-section shape factors were calculated in three directions of space for each bubble in a given sample. The χ_i values of each sample correspond to the median values over all the bubbles. The single χ value of isotropic samples was averaged over the three directions of space.

The parameter ε_i is a measure of the bubble relative elongation in direction i. Considering the vector $\vec{w}$ composed by the bubble best-fit ellipsoid semi-axes, ε_i corresponds to the ith component of the unit vector co-linear with $\vec{w}$:

$$\varepsilon_i = \frac{a_i}{\sqrt{a_k^2}} \tag{7}$$

For each sample, ε_i is the median value over all the bubbles. For spherical bubbles, $\varepsilon_i = 3^{-0.5}$.

For all samples, directional tortuosity, τ_i, was measured using 3dma-rock (Lindquist et al., 1996; Song et al., 2001). 3dma-rock first calculated the sample medial axis network (i.e. the network of paths through the center of bubbles and throats). The two sample faces orthogonal to the selected direction were then taken as entrance and exit faces. For each pair of voxels belonging to each respective face, the shortest path joining them using the medial axis network was calculated. The tortuosity of the voxel pair is the ratio between this shortest path length and the Euclidean distance between the two voxels. For all samples, τ_i is the median tortuosity of all these paths. For isotropic samples, the single tortuosity value, τ, corresponds to the average of the values weighted by the corresponding edge length in the same way as for the permeability values.

2.3. Permeability

Permeability measurements were carried out by numerical simulations of fluid flow within the bubble network. This is now a standard method to measure permeabilities on millimeter-size samples scanned by CT (Wright et al., 2006; Degruyter et al., 2010b; Bai et al., 2010; Polacci et al., 2014). The Lattice Boltzman solver used is Palabos (www.palabos.org), following the procedure described in Degruyter et al. (2010b). Briefly, the CT volumes were considered as a permeable structure where the glass is solid and the bubble space is filled with a fluid of constant density and viscosity. Walls delimiting the porous space are defined as non-slip boundaries. Each simulation was run by applying a pressure difference between two opposite sides orthogonal to the direction of interest, sealing the remaining four sides, and solving for the flow field. The simulations were used to obtain both the viscous, k_1, and inertial, k_2, permeability coefficients according to the Forchheimer equation (Ruth and Ma, 1992; Rust and Cashman, 2004):

$$\frac{dP}{dx_i} = \frac{\mu}{k_1} v_i + \frac{\rho}{k_2} v_i^2 \tag{8}$$

where dP/dx_i is the pressure gradient between two opposite sides of the parallelepipedic sample along direction i, μ is fluid viscosity, ρ is fluid density, and v_i is the average fluid velocity in direction i. Equation (8) is quadratic with respect to v_i, so simulations with different pressure gradients were run in order to find k_1 and k_2. These gradients were such that the Reynolds numbers of the fluid flow through the permeable network were high enough to ensure that inertial effects were present (Table S2 and Supplementary Text S1). The associated Mach numbers were low enough to ensure that the incompressibility assumption was not violated. Six runs were carried out on sample G442 to find the optimal number of simulations. After three simulations, the k_1 value is insensitive to the number of tested pressure gradients, changing by $<0.03\%$ when increasing from 3 to 4 simulations. The value of k_2, however, is more sensitive to the number of tested pressure gradients, changing from 62% to 2% when going from 3 to 4 and then from 4 to 5 simulations, respectively. We chose to interpolate k_1 and k_2 over 4 simulations, which introduces an uncertainty of less than a few percent on both permeability coefficients.

We separately tested the effects of voxel size and CT volume size on permeability (Supplementary Text S1). We used the characteristic number of bubbles across the connected clusters to classify samples as permeable and impermeable. Whether CT volumes are large enough to be representative with respect to permeability was tested following Bai et al. (2010). This analysis suggests that the uncertainty introduced by the finite size of the CT volumes is within a factor 1.5 for k_1 and within a factor 5 for k_2; it is roughly of the same order as the uncertainty given by the three directions of space for nearly equant volumes. It also suggests that the voxel size of the isotropic samples was sufficiently small (edge length is 1–4 μm with bubbles containing an average of 43 voxels across, Table S1) to limit the effect of discretization to $<10\%$ of the permeability values. Because anisotropic samples contain fewer bubbles, the effect of discretization was tested systematically (Table S2). Overall, changing voxel size affects anisotropic permeability values by a factor ranging from 1.4 to 20.

To be able to compare permeability values (k_1 and k_2, respectively) of isotropic samples, regardless of CT volume shape, the three orthogonal directions were measured in turn and a single average value was obtained by weighting each direction by its dimension relative to the three others (i.e. ${}^{avg}k = ({}^{x}k \times x + {}^{y}k \times y + {}^{z}k \times z)/(x + y + z)$, where ${}^{avg}k$ is the average permeability value, x, y, and z are the side lengths of the CT volume, and ${}^{x}k$, ${}^{y}k$, and ${}^{z}k$ are the respective permeabilities). Positive error bars represent the maximum value minus the weighted average and negative error bars represent the weighted average minus the minimum value. No weighting was done for anisotropic samples as permeability in each direction is considered separately. Errors on anisotropic samples represent the effects of grid size. In summary, a total of $4 \times 3 = 12$ simulations were carried out per sample. Simulations were run on the CIMENT computer cluster “gofree” at ISTerre, France, with either 48 or 64 cores, depending on sample size, for a total running time of <3 days per sample.

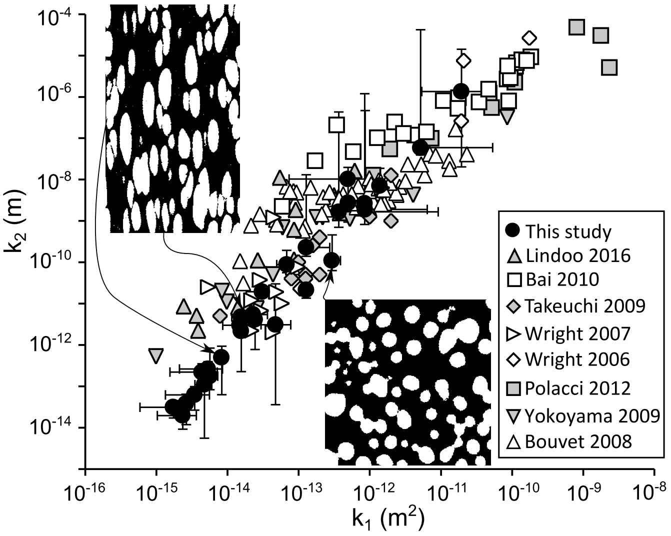

Fig. 1. Viscous permeability (k_1) as a function of inertial (k_2) permeability. Black circles mark our measured values on experimentally decompressed rhyolitic melts, and other symbols represent data from Wright et al. (2006, 2007); Bouvet de Maisonneuve et al. (2009), Yokoyama and Takeuchi (2009), Takeuchi et al. (2009), Bai et al. (2010), Polacci et al. (2012), and Lindoo et al. (2016). Insets show 2D binary images (bubbles are white, glass is black) of an isotropic sample (lower right, G434, sides are 0.81 mm long, permeability indicated with an arrow is measured on a volume of much larger cross-section) and an anisotropic sample (upper left, ABG9b, long side is 0.83 mm, permeabilities along arrow direction indicated).

Because k_1 and k_2 values span as many as 4 orders of magnitude and include 0, fitting by minimizing the ℓ_2-norm (squared Pearson’s correlation coefficient, R^2) on the log values of k_1 and k_2 is not possible. We chose instead cubic-root data transformation to calculate the residuals for these two variables and minimized the ℓ_1-norm so that residuals are not dominated by outliers (Horn and Johnson, 1985). The sums of residuals from each fitted equation were normalized by the maximum values of the respective measured variable to ensure that each equation was given comparable weight. Using m and c indices to differentiate between calculated and measured quantities, the residual sums are:

$$\begin{aligned} R_1 &= \frac{\sum |(k_1)_m^{1/3} - (k_1)_c^{1/3}|}{max((k_1)_m^{1/3})} \\ R_2 &= \frac{\sum |(k_2)_m^{1/3} - (k_2)_c^{1/3}|}{max((k_2)_m^{1/3})} \\ R_3 &= \frac{\sum |(\phi_c/\phi_t)_m - (\phi_c/\phi_t)_c|}{max((\phi_c/\phi_t))} \end{aligned} \tag{9}$$

where ϕ_c and ϕ_t are connected and total porosity, respectively.

3. Results

Fig. 1 shows the calculated viscous and inertial permeability coefficients (Eq. (8)). Viscous permeabilities range from 1.7×10^{-15} to 1.9×10^{-11} m^2, whereas inertial coefficients range from 2.0×10^{-14} to 1.4×10^{-6} m (Table S2). These permeabilities will be referred to as “measured permeabilities” although they are the result

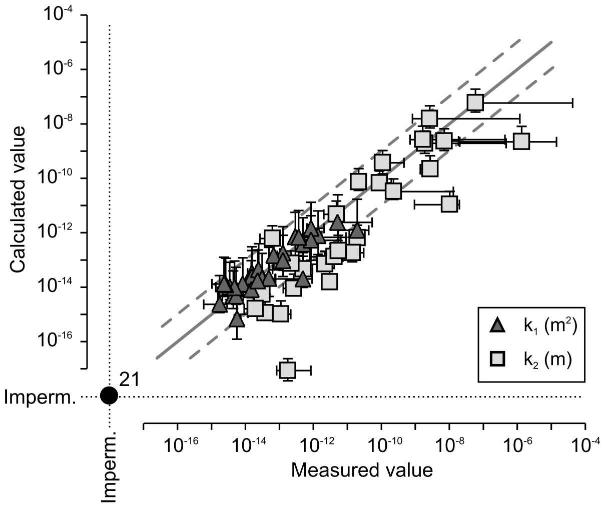

Fig. 2. Measured versus calculated permeabilities (k_1 and k_2). Calculated permeabilities are from Eqs. (10)–(11). The continuous gray line marks the 1:1 ratio and the two dashed gray lines mark the 1:10 and 10:1 ratios, respectively. The two axes labeled “Imperm.” represent permeability coefficients of zero and the filled circle with the label “21” represents 21 samples correctly identified as being impermeable.

of computations, so as to differentiate them from values calculated by simplified relationships, which are herein referred to as “calculated permeabilities”. The coefficients are correlated and can be fitted by a power law ($k_2 = 4.73 \times 10^{14} k_1^{1.91}$ with $R^2 = 0.97$ on the log values). Such a correlation is consistent with the findings of other studies on natural and experimental products (Fig. 1). This consistency has two consequences. First, it gives confidence in the permeabilities computed from CT volumes, and second it shows that even samples with low (<20) numbers of connected bubbles across one direction yield permeabilities that follow the trend defined by samples that have many connected bubbles. This method is therefore applicable to experimental bubble studies with small sample volumes.

Relationships proposed by Degruyter et al. (2010a) link both permeability coefficients to physical parameters of the permeable network:

$$k_1 = \frac{\phi_c^n d_t^2}{16\chi\tau^2} \tag{10}$$

$$k_2 = \frac{\phi_c^{4n} d_t^2}{2 f_0 \tau^3} \tag{11}$$

where d_t is the characteristic diameter of the bubble connections (throats), χ is the channel circularity here measured on the bubbles, τ is the tortuosity of the connected bubble network, and f_0 is an inertial friction coefficient. For anisotropic samples, ϕ_c, τ, and χ should henceforth be replaced by ϕ_{c-i}, τ_i and χ_i, where $i = x$, y, or z is the direction considered. Compared to Degruyter et al. (2010a), we changed 1 into n in the exponent of ϕ_c in Eq. (10) and 2 into $4n$ in the exponent of ϕ_c in Eq. (11) because, although k_1 and k_2 are related to first order by a power law, the ratio k_2/k_1 has a second-order dependence on ϕ_c^4 (Fig. S3). Our measurements of the bubble network provide values for every parameters of Eqs. (10)–(11), except n and f_0. A two-parameter regression minimizing $R_1 + R_2$ (Eq. (9)) yields best fits values of $n = 2.49$ and $f_0 = 1.21$ with $R_1 = 1.69$ and $R_2 = 1.47$ (Fig. 2). The fit is better for k_1 than for k_2, with 26 out of 28 samples having calculated values within one log unit of the measured k_1 value and only 13 out of 28 calculated k_2 being within one log unit of the measured k_2. The k_2 value of sample G437 is an outlier for which no explanation has been found.

The core of the percolation concept is that not all gas bubbles belong to the connected network. By depending on the connected porosity, Eqs. (10)–(11) assume that the percolation state of the sample is known. Were it not the case, ϕ_c would be unknown and no impermeable samples would be correctly identified as such. This implies that these equations correctly identify the permeability state of only 57% of the samples if percolation information is missing. Equations (10)–(11) also rely on network parameters that are not traditionally available in most studies and in conduit flow models, such as bubble throat diameters or tortuosity. We relax these assumptions by linking the variables ϕ_c, d_t, and τ to a combination of ϕ_t, d_a, and σ_a.

Polacci et al. (2014) suggested that throat diameters can be related to average bubble diameters. In each of our samples, the distribution of the ratios of throat dimension over the diameter of the neighboring bubble is wide and mostly unimodal (Fig. S4), which drove us to characterize each sample by a median throat/bubble ratio. Bringing all samples together, these ratios have values clustering around 0.4 (Fig. 3A): $d_t = 0.4 \times d_a$.

Tortuosity can be related to connected porosity by Archie’s law (Wright et al., 2009; Degruyter et al., 2010a):

$$\tau^2 = \phi_c^{1-m} \tag{12}$$

where m is a constant named the formation factor ($m \geq 1$). Tortuosity depends on bubble shape (Degruyter et al., 2010a). Bubbles elongated parallel to the main gas flow direction decrease the tortuosity in that direction. Conversely, bubbles elongated perpendicular to gas flow increase tortuosity. Here we add an empirical pre-factor to Eq. (12) to take into account bubble anisotropy, using i indices for clarity:

$$\tau_i^2 = \frac{c_\tau \chi_i}{2\sqrt{3}\varepsilon_i}\phi_c^{1-m} \tag{13}$$

where c_τ is an empirical constant, ε_i is a measure of bubble elongation in direction i, χ_i is the cross-section shape factor orthogonal to i, and the factor $2\sqrt{3}$ is such that the pre-exponential factor is equal to c_τ for isotropic samples. We find that the best-fit factor, c_τ, and exponent, m, are 4 and 1, respectively (Fig. S5). Dropping the i indices, tortuosity in a given direction is thus equal to:

$$\tau^2 = (2\chi)/(\sqrt{3}\varepsilon) \tag{14}$$

with $R^2 = 0.64$. Equation (14) no longer depends on ϕ_c. This fit thus ensures a better representation of the effect of bubble elongation on τ at the expense of capturing the influence of ϕ_c on τ.

The lack of a single porosity threshold for percolation found by previous studies suggests that the threshold does not depend solely on porosity. The observation that bubble size distributions are more disperse in permeable samples than in impermeable samples (Burgisser and Gardner, 2004) led us to explore the idea that inter-bubble melt thickness may be a controlling parameter for bubble connectivity. We found that the measured bubble separation distance, z_m, weighted by the normalized degree of polydispersity of the bubble size distribution, σ_a/d_a, (i.e. the quantity $z_m(\sigma_a/d_a)^{c_z}$ with c_z a constant) is an excellent discriminant between permeable and impermeable samples (Fig. 3B). All samples but two can be correctly assigned to a permeability state, based on a critical value of $z_m(\sigma_a/d_a)^{-1}$.

One difficulty is that the inter-bubble distance involved in the discriminatory quantity $z_m(\sigma_a/d_a)^{-1}$ is not traditionally measured in magmatic products, because bubble spacing is generally deduced from bubble size and total porosity in different ways (e.g., Lensky et al., 2004; Castro et al., 2012; Mancini et al., 2016). Our data allow us to re-evaluate such relationships (Fig. 3C), and we

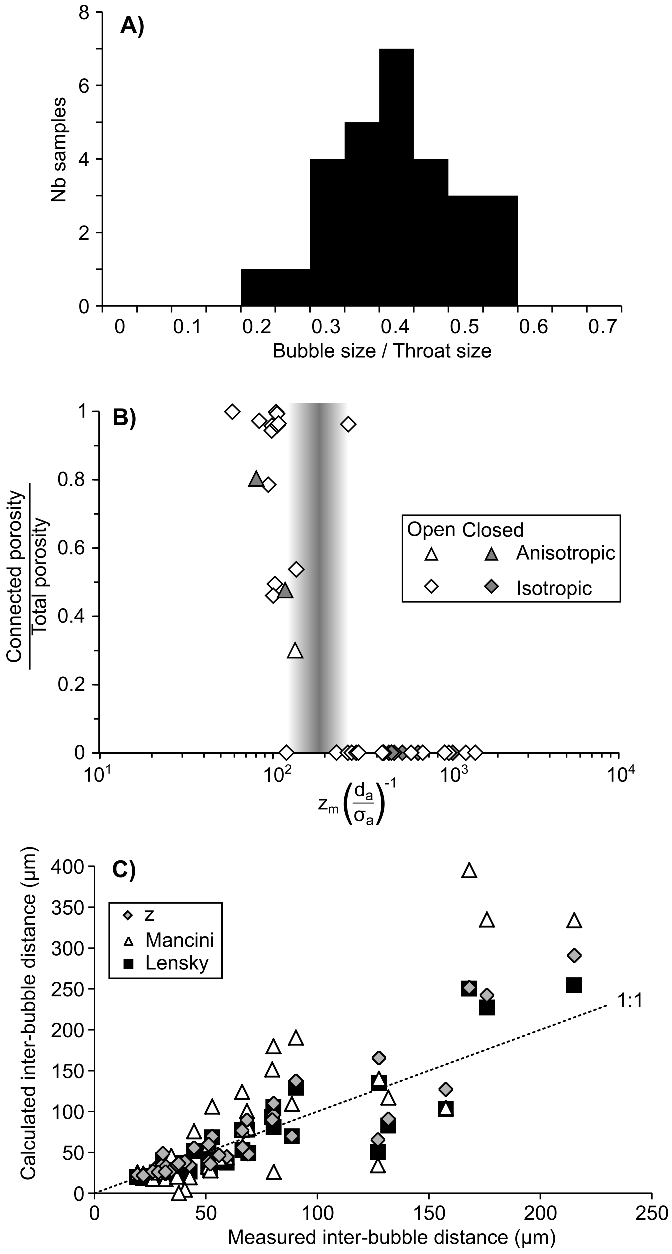

Fig. 3. Relationships between parameters of the bubble networks. A) Histogram of the median ratio d_a/d_t. B) Sorting criteria in µm (inter-bubble distance, z_m, divided by σ_a/d_a) as a function of connectivity (ϕ_c/ϕ_t). Samples are sorted in decompression style ("open" vs. "closed" system) and bubble shapes ("isotropic" vs. "anisotropic"). The shaded vertical area suggests a limit between permeable and impermeable samples. C) Measured inter-bubble distance as a function of calculated inter-bubble distance. Symbols mark three calculation methods: "z" is that of Eq. (15), "Mancini" is that of Mancini et al. (2016) (their z_1 with $o = 6$ and $\alpha_p = 0.63$), and "Lensky" is that of Lensky et al. (2004).

found that the following expression is a good compromise between algebraic simplicity and accuracy:

$$z = 1.5d_a(\phi_t^{-1/3} - 1) \tag{15}$$

which fits our data with $R^2 = 0.8$. A percolation threshold can thus be defined using $Z = z(\sigma_a/d_a)^{c_z}$, instead of $z_m(\sigma_a/d_a)^{-1}$. Moreover, the behavior of ϕ_c/ϕ_t can be described by a logistic function that tends to 1 for small values of Z and to 0 for large Z values:

$$\frac{\phi_c}{\phi_t} = \frac{1}{1+\exp(-c_\phi(Z-c_p))} \tag{16}$$

where c_ϕ and c_p are fit parameters.

Summarizing these simplifications, we can write a viscous permeability relationship that depends only on the average and standard deviation of the bubble size distribution, the average bubble aspect ratio, and the total porosity:

$$k_1 = \frac{\phi_c^n d_a^2 \sqrt{3}\varepsilon}{200\chi^2} \tag{17}$$

where tortuosity is derived using Eq. (14), and n is a constant to be determined. Similarly, the inertial permeability can be expressed as:

$$k_2 = \frac{\phi_c^{4n} d_a}{5 f_0}\left(\frac{\sqrt{3}\varepsilon}{2\chi}\right)^{3/2} \tag{18}$$

The connected porosity is obtained by using Eq. (16) with the inter-bubble distance z from Eq. (15):

$$\phi_c = \frac{\phi_t}{1+\exp(-c_\phi(1.5d_a(\phi_t^{-1/3}-1)-c_p))} \tag{19}$$

There are thus five parameters (c_z, c_ϕ, c_p, n, and f_0) that need to be determined, whereas five measured geometric quantities (ϕ_t, d_a, σ_a, χ, and ε) can be entered into Eqs. (17)–(19) to calculate three quantities (ϕ_c/ϕ_t, k_1, and k_2) that can be compared with their measured counterparts. Five parameters to be regressed simultaneously are too many degrees of freedom for the two-parameter linear regression used to fit Eqs. (10)–(11) in Fig. 2. We instead used a grid search technique to minimize the ℓ_1-norm (Eq. (9)). The sum $R_1 + R_2 + R_3$ was minimized by nested grid search within the bounds $-1 < c_z < 0$, $-10^6 < c_\phi < 0$, $10^{-5} < c_p < 10^{-4}$, $2 < n < 4$, and $10^{-2} < f_0 < 10^2$. To keep grid points within a computationally manageable number, the grid search was conducted with a precision on each parameter that yielded three significant digits, which gave $c_z = -0.128$, $c_\phi = -0.342 \times 10^6$, $c_p = 33.2 \times 10^{-6}$, $n = 2.73$, and $f_0 = 0.790$ with $R_1 = 2.59$, $R_2 = 1.73$, and $R_3 = 5.65$.

Fig. 4A shows ϕ_c/ϕ_t as a function of Z and the fit of Eq. (19) with the above values of c_z, c_ϕ, and c_p (the goodness of fit of ϕ_c is shown on Fig. S6). By definition, $\phi_c/\phi_t = 0.5$ when $Z = c_p$, and the absence of percolation corresponds to ϕ_c/ϕ_t approaching 0. A percolation threshold can thus be defined as a critical value of either ϕ_c/ϕ_t or Z. For simplicity, we chose to define the percolation threshold as $Z_p = c_p + c_d$, where c_d is an additional parameter to be determined. This implies that the threshold value of ϕ_c/ϕ_t is $(1+\exp(-c_\varphi c_d))^{-1}$. We varied c_d to maximize the number of successfully attributed permeability states and found that c_d values from 3×10^{-6} to 8×10^{-6} ensure that the permeability state of all samples but two are correctly identified (Fig. 4A). Using Eq. (15) in conjunction with the discriminant $Z_p = z(\sigma_a/d_a)^{c_z}$ we can define the percolation porosity threshold, ϕ_p, as:

$$\phi_p = \left[1+\frac{c_p+c_d}{1.5d_a}\left(\frac{\sigma_a}{d_a}\right)^{0.128}\right]^{-3} \tag{20}$$

where $c_p + c_d = 39.2 \pm 3 \times 10^{-6}$ m marks the percolation threshold for our samples that correctly identifies the permeability state of 96% of the samples.

Fig. 4B compares calculated and measured permeabilities for the fitted relationships (Eqs. (17)–(19)). Overall, Fig. 4B suggests that most viscous permeability coefficients are predicted within one order of magnitude (88% of the cases), but that only 54% of the inertial permeability coefficients are predicted within one order of magnitude (88% within a factor 100). The same k_2 outlying value as in Fig. 2 is present because the calculated values

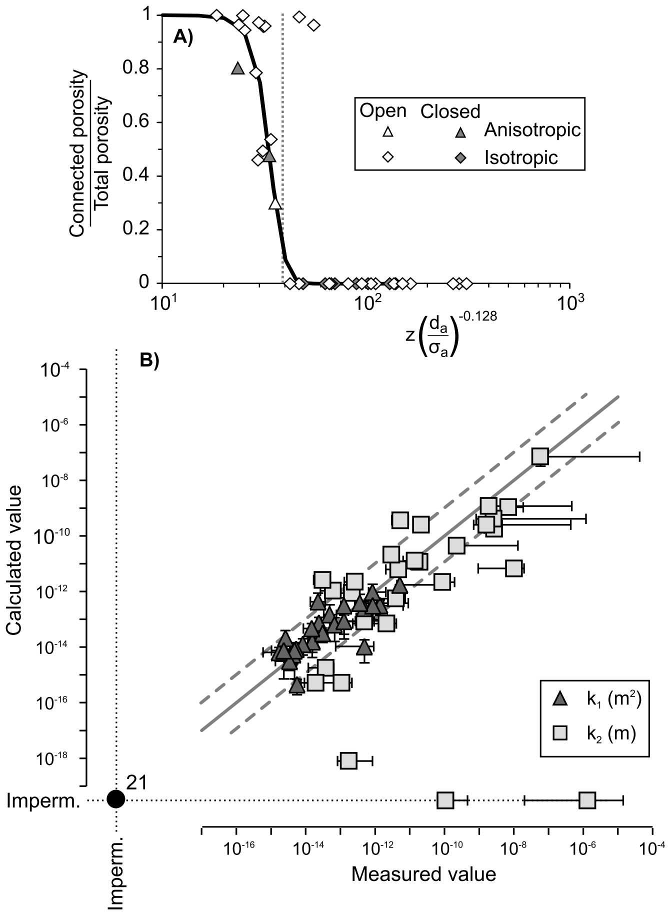

Fig. 4. Results of the fitting procedure. A) Sorting criteria in µm (calculated inter-bubble distance, z, times a power law of σ_a/d_a) as a function of connectivity (ϕ_c/ϕ_t). Samples are sorted in decompression style ("open" vs. "closed" system) and bubble shapes ("isotropic" vs. "anisotropic"). The bold curve is Eq. (19). The vertical dashed line marks the critical value that defines percolation and distinguishes all impermeable samples from permeable samples except two. B) Measured versus calculated permeabilities (k_1 and k_2). The continuous gray line marks the 1:1 ratio and the two dashed gray lines mark the 1:10 and 10:1 ratios, respectively. The two axes labeled "Imperm." represent permeability coefficients of zero and the filled circle with the label "21" represents 21 samples correctly identified as being impermeable. Two samples incorrectly identified as being impermeable are on the horizontal impermeable axis.

of ϕ_c, d_t, and τ for that sample (G437) are close to the corresponding measurements. For isotropic samples, permeabilities can simply be expressed as $k_1 = \phi_c^{2.73} d_a^2/800$ and $k_2 = \phi_c^{10.92} d_a/(8 f_0)$. For strongly anisotropic samples, k_1 could be more than one order of magnitude below the isotropic equivalent value (at most by a factor 20 if χ and ε have the highest measured values of 6 and 0.25, respectively).

4. Discussion

4.1. Comparison of permeability relationships

We evaluate our results against two widely used relationships that aim at quantifying permeability from geometrical measurements of the porous network. The first is a Kozeny–Carman relationship between viscous permeability and porosity (e.g., Eichelberger et al., 1986; Klug and Cashman, 1996; Rust and Cashman, 2011):

$$k_1 = a_{KC}\phi_c^{b_{KC}} \tag{21}$$

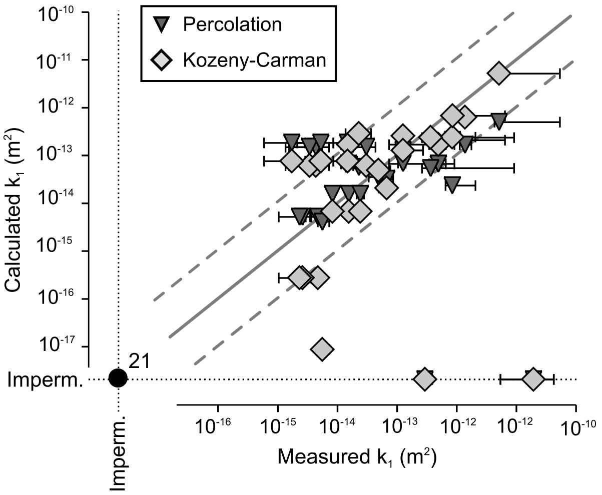

Fig. 5. Measured versus calculated permeability (k_1) from Eq. (21) ("Kozeny–Carman") and Eq. (22) ("Percolation"). Errors are only reported for measured quantities. The continuous gray line marks the 1:1 ratio and the two dashed gray lines mark the 1:10 and 10:1 ratios, respectively. The two axes labeled "Imperm." represent permeability coefficients of zero and the filled circle with the label "21" represents 21 samples correctly identified as being impermeable. Two samples incorrectly identified as being impermeable are the horizontal impermeable axis.

where a_{KC} and b_{KC} are fitted constants. Using Eq. (19) to express ϕ_c, a two-parameter best fit yields $a_{KC} = 8.27 \times 10^{-11}$ m^2 and $b_{KC} = 6.02$ with $R_1 = 2.75$ (Fig. 5).

The second relationship highlights that total porosity and connected porosities are distinct by explicitly depending on total porosity, ϕ_t, and the percolation threshold, ϕ_p (e.g., Feng et al., 1987; Sahini and Sahimi, 1994; Saar and Manga, 1999; Mueller et al., 2005):

$$k_1 = a_M(\phi_t - \phi_p)^{b_M} \tag{22}$$

where a_M and b_M are fitted constants. Setting $\phi_p = 15$ vol.% ensures that all permeable samples are correctly identified as such, but only 2 out of the 21 impermeable samples are correctly identified. Conversely, setting $\phi_p = 60$ vol.%, only 2 out of 28 permeable samples, yet all impermeable samples, are correctly identified. This illustrates that no single value of ϕ_p explains the variation of our data (Mueller et al., 2005). Using Eq. (20) to express ϕ_p, all samples but two are correctly identified and a two-parameter best fit yields $a_M = 1.85 \times 10^{-11}$ m^2 and $b_M = 2.49$ with $R_1 = 3.64$ (Fig. 5).

In summary, the original Degruyter Eq. (10) yields the best fits for the viscous permeability, followed by our simplified Eq. (17), the Kozeny–Carman relationship, and the percolation relationship (R_1 values of 1.69, 2.59, 2.75, and 3.64, respectively). Much of the predictive capability is lost when network parameters such as ϕ_c or τ are not available. When these parameters are missing, regression results give a slight advantage to our relationship compared to that of Kozeny–Carman.

4.2. Testing the percolation threshold against other data sets

Our percolation threshold can be evaluated against published data sets by comparing the calculated threshold to measured values of ϕ_c/ϕ_t. We selected five studies on natural and experimental magmas with various crystal contents and bubble elongations that provide independent estimates of ϕ_c, ϕ_t, d_a, and σ_a (Burgisser and Gardner, 2004; Bouvet de Maisonneuve et al., 2009; Takeuchi et al., 2009; Okumura et al., 2012; Lindoo et al., 2016). Values of d_a and σ_a were recalculated from the original size distributions when necessary. The percolation threshold depends on an empirical constant, c_p, that our data constrain to be between 3×10^{-6}

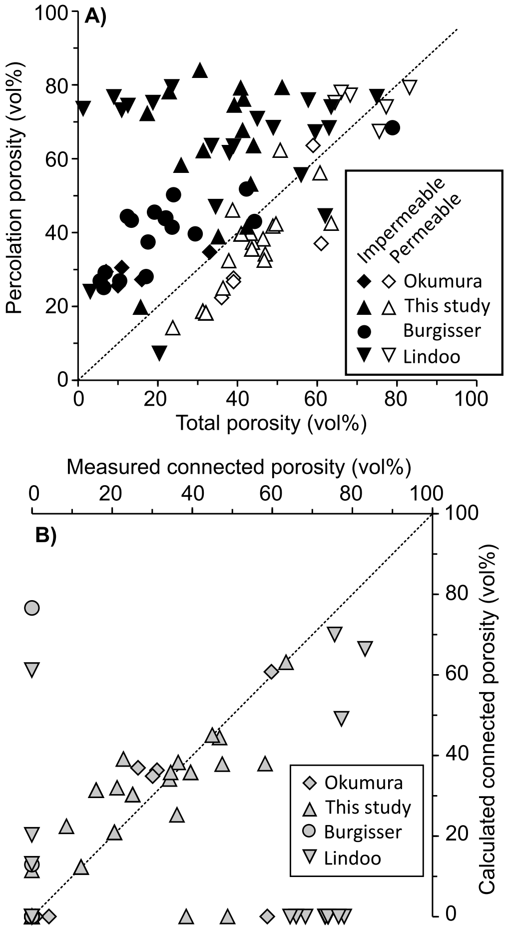

Fig. 6. Applications of the percolation relationship. Data are from Okumura et al. (2012), Burgisser and Gardner (2004), Lindoo et al. (2016), and this study. A) Total porosity (ϕ_t) as a function of percolation porosity (ϕ_p). The dotted line indicates the 1:1 ratio that separates permeable (upper left) from impermeable (lower left) fields. Open symbols are permeable samples and closed symbols are impermeable samples. B) Measured vs. calculated connected porosity (ϕ_c).

and 8×10^{-6} m. This range of c_p values correctly discriminates >87% of all the data points (88% when $c_d = 4 \times 10^{-6}$, Fig. 6A) and Eq. (19) recovers the ϕ_c values of the permeable samples with $R^2 = 0.77$ (Fig. 6B). A global permeability relationship can thus be defined by setting that ϕ_c is given by Eq. (19) when $\phi_t \geq \phi_p$ (or $z \times (\sigma_a/d_a)^{-0.128} \leq 3.72 \times 10^{-5}$) and zero when $\phi_t < \phi_p$. The fact that a success rate of 100% cannot be achieved is partly due to the extreme simplicity of Eqs. (19)–(20), which seek to characterize with a single scalar the percolation state of a complex bubble network where bubbles have heterogeneous shapes and spatial distributions.

Our simplified relationships are more accurate for k_1 than for k_2. Unfortunately, we found no published data set providing independent measures of all the parameters used in Eqs. (17)–(18) to conduct a rigorous evaluation of our relationships. We note, however, that no technical obstacle prevents collecting the relevant data using CT imaging (e.g., Castro et al., 2012), traditional image analysis (e.g., Gardner et al., 1999), or stereology methods (e.g., Martel and Iacono-Marziano, 2015). Because k_2 involves an additional independent parameter, f_0, the lower accuracy on k_2 suggests that considering f_0 as a constant is an oversimplification. This is in agreement with the findings of Degruyter et al. (2010a) and Bouvet de Maisonneuve et al. (2009), which not only indicate that 0.8 is in the low range of inferred f_0 values but also suggest that f_0 should be linked to measurable parameters of the permeable network.

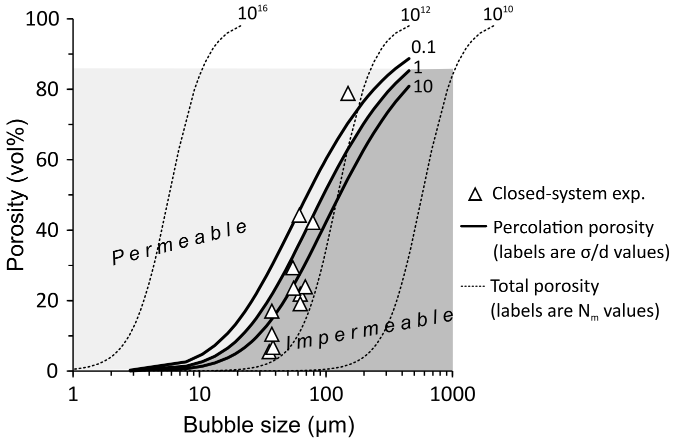

Fig. 7. Total (ϕ_t) and percolation (ϕ_p) porosities as a function of bubble size. Triangle are experimental samples. Dotted curves are total porosities for three bubble number densities (labels 10^{10}, 10^{12}, and 10^{16}). Thick solid curves are percolation porosities for three σ_a/d_a values (labels 0.1, 1, and 10). The light gray field is above the percolation threshold corresponding to $\sigma_a/d_a = 1$ ("permeable") and the dark gray field is below that threshold ("impermeable").

In summary, the simplified relationships we propose give a close representation of the percolation threshold in both experimental and natural products at the expense of a moderate precision on the permeability values compared to laws depending on bubble network parameters. Our laws are related to the connection between gas bubbles in magmas, which means that they are not valid when brittle fracturing occurs (Farquharson et al., 2016; Heap and Kennedy, 2016; Kushnir et al., 2016).

4.3. Implications for magma degassing and eruptions

Having a relationship that estimates percolation has implications for determining at which point gas escapes from magma during ascent. Total porosity and bubble size can be related to the bubble number density per amount of melt, N_m, if the bubble size distribution is monodisperse. The percolation porosity, on the other hand, depends on bubble size and σ_a/d_a. Fig. 7 shows the evolution of ϕ_p and ϕ_t as a function of bubble size for different values of N_m and σ_a/d_a. One trend of percolation porosity is shown for $N_m = 10^{12}$ m^{-3} and three values of σ_a/d_a (0.1, 1, and 10), which approach the conditions of a subset of our data that underwent closed-system decompression and remained impermeable until very large (~80 vol%) porosities. Fig. 7 illustrates how percolation is expected to vary in natural cases. The natural range of N_m is 10^{10}–10^{16} m^{-3} (Rust and Cashman, 2011). The lower bound of σ_a/d_a is 0.1 (our data; Gardner et al., 1999), and the upper bound can be set to 10 by considering that natural pumice often have log normal to exponential distributions (e.g., Polacci et al., 2014). The natural range of parameters can thus be represented by the three ϕ_p curves of Fig. 7 and two additional ϕ_t curves for $N_m = 10^{10}$ and 10^{16} m^{-3}. Fig. 7 shows that high bubble number densities favor percolation at low porosity and early gas loss during ascent whereas low number densities hinder percolation and yield late gas leakage during ascent. The transition predicted by Eq. (20) between impermeable behavior at depth and permeable behavior more shallowly thus spans the full range of percolation porosities inferred in previous studies (Rust and Cashman, 2011; Lindoo et al., 2016).

Fig. 8A represents k_1 versus ϕ_t for our permeability formulation alongside four relationships that are representative of those currently used in conduit flow modeling (Klug and Cashman, 1996; Mueller et al., 2005; Kozono and Koyaguchi, 2009). Increasing N_m in our relationship causes both the percolation threshold and permeability to decrease, whereas, at constant N_m, decreasing σ_a/d_a

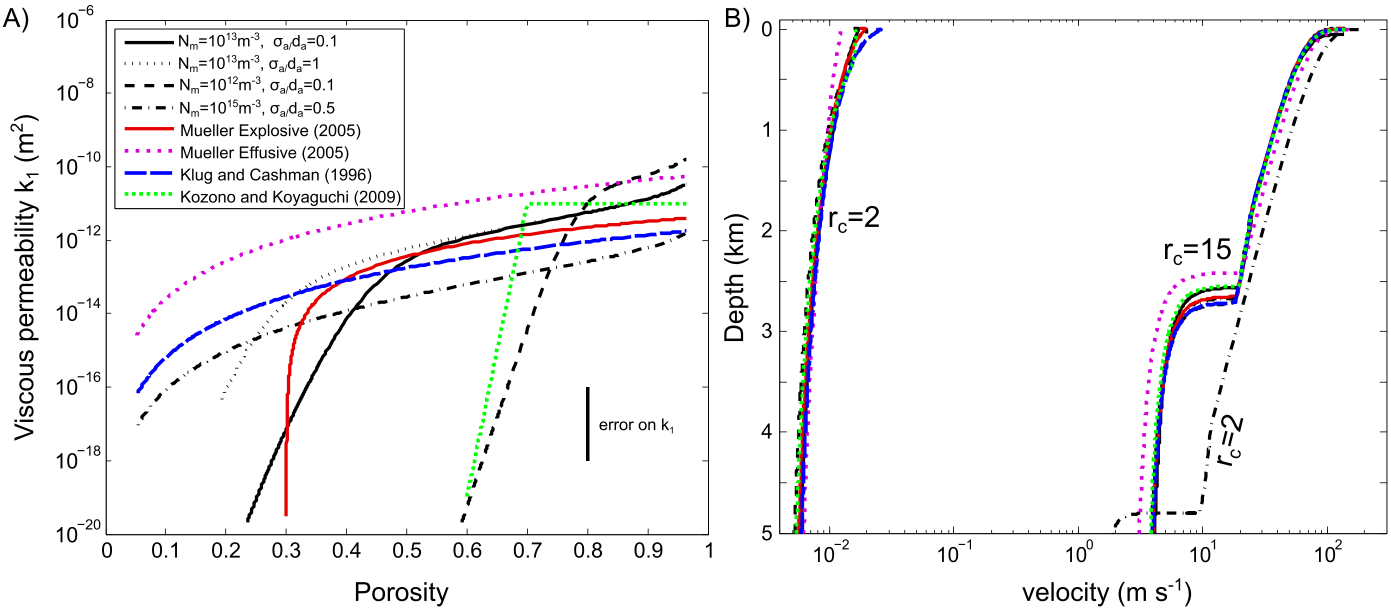

Fig. 8. Influence of various permeability relationships on conduit flow modeling. A) Permeability versus total porosity. B) Model outputs (ascent velocity vs. depth) from the 1D conduit flow model with a conduit radius of 2 and 15 m (labels r_c) and a conduit length of 5 km, a lithostatic pressure at the conduit base with 5 wt.% total water in the magma, and a magma temperature of 950 °C with 45 vol.% crystals. Only liquid velocities are shown. Gas and liquid have velocities that very similar for all runs except effusive runs at depth <1 km, where gas velocities sharply increase to 1–10 m/s. Permeability relationships are from Mueller et al. (2005) for effusive samples ($a_M = 6.3 \times 10^{-11}$ m^2, $b_M = 3.4$) and explosive samples ($a_M = 9 \times 10^{-12}$ m^2, $b_M = 2$), Klug and Cashman (1996, $a_{KC} = 2 \times 10^{-12}$ m^2, $b_{KC} = 3.5$), Kozono and Koyaguchi (2009, $k_1 = 10^{-11}$ m^2 if $\phi_t > 0.7$ with a smooth increase to that constant value when $0.6 < \phi_t < 0.7$), and this study (labels indicate respective values of N_m and σ_a/d_a).

increases the percolation threshold. Setting, for instance, N_m to 10^{15} m^{-3} and σ_a/d_a to 0.5 results in a permeability–porosity relationship that is close to that of Eq. (21). Fig. 8A shows that varying both N_m and σ_a/d_a results in permeability–porosity relationships that cover the same range as those currently used in conduit flow models, except at low porosities ($\phi_t < 0.2$).

Because our relationship depends on parameters widely used in conduit flow modeling, it can be integrated to such numerical models. We implemented it in a 1D two-phase (gas and liquid) conduit flow model tailored to the eruptive conditions prevailing at Merapi volcano in 2010 (e.g., Costa et al., 2013; Erdmann et al., 2016). We used the Kozono and Koyaguchi (2009) model, as modified by Degruyter et al. (2012), to include inertial permeability and the effect of dissolved water on melt viscosity. The effect of crystals on magma viscosity was calculated using Krieger and Dougherty (1959) with a maximum packing 0.65 and an Einstein coefficient of 2.5. Equations (17)–(20) require the specification of d_a, ϕ_t, ε, χ, and σ_a/d_a. Bubble diameter and ϕ_t were calculated from N_m and the melt water content. To be consistent with Fig. 8A, N_m was varied from 10^{12} to 10^{15} m^{-3} and σ_a/d_a was varied from 0.1 to 1. Parameters ε and χ can be estimated using relationships between flow conditions and bubble elongation and orientation (e.g. Rust et al., 2003). In 1D modeling, however, assigning a single preferential orientation at each depth is complex, because the amounts of simple and pure shear have to be averaged over the conduit cross-section. Using the constant values of $\varepsilon = 3^{-0.5}$ and $\chi = 2$ is acceptable because ε and χ have only a second-order influence on permeability. We assume that gas flow was laminar for the four published permeability relationships because they do not include k_2.

Fig. 8B presents model results as liquid (melt + crystals) velocities versus depth. Although we used permeability relationships that cover a wide range of percolation thresholds and permeabilities, model outputs are similar for the eruptive conditions we considered. When the conduit radius is set to 15 m, all runs are in the explosive regime with differences in velocity profiles within 0.15 log units of each other. They have similar fragmentation depths of 2580 ± 170 m and mass fluxes of 5.21–6.91 × 10^6 kg/s. When conduit radius is set to 2 m, all runs are effusive with mass fluxes ranging from 157 to 185 kg/s, except for the run corresponding to $N_m = 10^{15}$ m^{-3} and $\sigma_a/d_a = 0.5$, which is explosive with a mass flux of 5.67 × 10^4 kg/s and a fragmentation depth of 4800 m. With only one run over sixteen having a distinct behavior, the influence of permeability and percolation is thus small under such conditions. The model we use assumes that gas separates from the magma by flowing only in the vertical direction, although a significant part of gas losses during ascent could occur through leakage at the conduit walls (Jaupart and Allègre, 1991; Collombet, 2009). Although such a characterization is beyond the scope of this work, we intuit that our percolation and permeability relationships have more influence in other types of conduit flow models.

In the anisotropic samples we use to establish the percolation threshold, the deformation is due to sample decompression that induced pure shear (Burgisser and Gardner, 2004). The amplitude of this deformation remains relatively low (maximum aspect ratio of 6). Several studies have shown that simple shear can significantly decrease the percolation threshold when it reaches high amplitudes (e.g., Caricchi et al., 2011; Okumura et al., 2009, 2013). Unlike pure shear, simple shear involves bubble rotation that enhances bubble interaction and coalescence. As simple shear is expected to occur in volcanic conduits during magma ascent, it may affect percolation and permeability development in a way that is not captured by our data set.

5. Conclusions

We present results on permeability and bubble network determinations of experimental samples that were decompressed at 6×10^{-3}–10 MPa/s from 150 MPa down to 60–15 MPa. Samples were crystal-free rhyolitic melts bearing 10–64 vol% of H_2O bubbles with aspect ratios of 2–6, sizes of 4–350 μm, and number densities of 5×10^{10}–5×10^{13} m^{-3}. Samples were analyzed by X-ray microtomography to image the bubble networks in 3D. From measurements of the 3D images and geometrical considerations, we develop a percolation threshold for magmas that depends on the bubble network characteristics. This relationship, which is calibrated on our sample set, recovers the behavior of a wide range of experimental and natural volcanic samples, from basaltic andesite to rhyolite, and from crystal-free to crystal-rich. It separates permeable samples from impermeable ones with a success rate of 88%.

We propose simplified permeability relationships based on the percolation threshold that rely on parameters widely used in magma flow numerical modeling. They are calibrated on our sample set and they are valid within one order of magnitude for the viscous permeability coefficient and within two orders of magnitude for the inertial permeability coefficient. They recover the ranges of values previously covered by isolated relationships, reassembling them within a single framework. The implications of such a unification on eruptive dynamics is tested by using a 1D, two-phase conduit flow model constrained by conditions prevailing during the 2010 eruption of Merapi volcano. Results suggest that varying the percolation threshold has little influence on vertical gas loss and ascent dynamics.

Acknowledgements

We appreciated the thorough and helpful reviews by W. Degruyter, the editor, and an anonymous reviewer. This project was partially funded by the European Research Council (grant 202844 under the European FP7), by the ANR DoMerapi (ANR-12-BS06-0012), and by a grant from Labex OSUG@2020 (Investissements d'avenir – ANR10 LABX56). JMC is supported by the VAMOS research centre, University of Mainz, Germany.

Appendix A. Supplementary material

Supplementary material related to this article can be found online at http://dx.doi.org/10.1016/j.epsl.2017.04.023.

References

Bai, L., Baker, D.R., Hill, R.J., 2010. Permeability of vesicular Stromboli basaltic glass: lattice Boltzmann simulations and laboratory measurements. J. Geophys. Res. 115. http://dx.doi.org/10.1029/2009JB007047.

Blower, J.D., 2001. Factors controlling permeability–porosity relationships in magma. Bull. Volcanol. 63, 497–504.

Bolte, S., Cordelières, F.P., 2006. A guided tour into subcellular colocalization analysis in light microscopy. J. Microsc. 224, 213–232. http://dx.doi.org/10.1111/j.1365-2818.2006.01706.x.

Bouvet de Maisonneuve, C., Bachmann, O., Burgisser, A., 2009. Characterization of juvenile pyroclasts from the Kos Plateau Tuff (Aegean Arc): insights into the eruptive dynamics of a large rhyolitic eruption. Bull. Volcanol. 71, 643–658. http://dx.doi.org/10.1007/s00445-008-0250-x.

Burgisser, A., Gardner, J.E., 2004. Experimental constraints on degassing and permeability in volcanic conduit flow. Bull. Volcanol. 67, 42–56. http://dx.doi.org/10.1007/s00445-004-0359-5.

Caricchi, L., Pommier, A., Pistone, M., Castro, J., Burgisser, A., Perugini, D., 2011. Strain-induced magma degassing: insights from simple-shear experiments on bubble bearing melts. Bull. Volcanol. 73, 1245–1257. http://dx.doi.org/10.1007/s00445-011-0471-2.

Castro, J.M., Burgisser, A., Schipper, C.I., Mancini, S., 2012. Mechanisms of bubble coalescence in silicic magmas. Bull. Volcanol. 74, 2339–2352. http://dx.doi.org/10.1007/s00445-012-0666-1.

Collombet, M., 2009. Two-dimensional gas loss for silicic magma fows: toward more realistic numerical models. Geophys. J. Int. 177, 309–318.

Costa, F., Andreastuti, S., Bouvet de Maisonneuve, C., Pallister, J.S., 2013. Petrological insights into the storage conditions, and magmatic processes that yielded the centennial 2010 Merapi explosive eruption. J. Volcanol. Geotherm. Res. 261, 209–235. http://dx.doi.org/10.1016/j.jvolgeores.2012.12.025.

Degruyter, W., Bachmann, O., Burgisser, A., 2010a. Controls on magma permeability in the volcanic conduit during the climactic phase of the Kos Plateau Tuff eruption (Aegean Arc). Bull. Volcanol. 72, 63–74. http://dx.doi.org/10.1007/s00445-009-0302-x.

Degruyter, W., Burgisser, A., Bachmann, O., Malaspinas, O., 2010b. Synchrotron X-ray microtomography and lattice Boltzmann simulations of gas flow through volcanic pumices. Geosphere 6, 470–481.

Degruyter, W., Bachmann, O., Burgisser, A., Manga, M., 2012. The effects of outgassing on the transition between effusive and explosive silicic eruptions. Earth Planet. Sci. Lett. 349–350, 161–170. http://dx.doi.org/10.1016/j.epsl.2012.06.056.

Doube, M., Kłosowski, M.M., Arganda-Carreras, I., Cordelières, F.P., Dougherty, R.P., Jackson, J.S., Schmid, B., Hutchinson, J.R., Shefelbine, S.J., 2010. BoneJ: free and extensible bone image analysis in ImageJ. Bone 47, 1076–1079. http://dx.doi.org/10.1016/j.bone.2010.08.023.

Eichelberger, J.C., Carrigan, C.R., Westrich, H.R., Price, R.H., 1986. Non-explosive silicic volcanism. Nature 323, 598–602.

Erdmann, S., Martel, C., Pichavant, M., Bourdier, J.-L., Champallier, R., Komorowski, J.-C., Cholik, N., 2016. Constraints from phase equilibrium experiments on pre-eruptive storage conditions in mixed magma systems: a case study on crystal-rich basaltic andesites from Mount Merapi, Indonesia. J. Petrol. 57, 535–560. http://dx.doi.org/10.1093/petrology/egw019.

Farquharson, J.I., Heap, M.J., Lavallée, Y., Varley, N.R., Baud, P., 2016. Evidence for the development of permeability anisotropy in lava domes and volcanic conduits. J. Volcanol. Geotherm. Res. 323, 163–185. http://dx.doi.org/10.1016/j.jvolgeores.2016.05.007.

Feng, S., Halperin, H.I., Sen, P.N., 1987. Transport properties of continuum systems near the percolation threshold. Phys. Rev. B 35, 197–214.

Gardner, J.E., 2007. Bubble coalescence in rhyolitic melts during decompression from high pressure. J. Volcanol. Geotherm. Res. 166, 161–176.

Gardner, J.E., Hilton, M., Carroll, M.R., 1999. Experimental constraints on degassing of magma: isothermal bubble growth during continuous decompression from high pressure. Earth Planet. Sci. Lett. 168, 201–218.

Gonnermann, H.M., Manga, M., 2007. The fluid mechanics inside a volcano. Annu. Rev. Fluid Mech. 39, 321–356.

Heap, M.J., Kennedy, B.M., 2016. Exploring the scale-dependent permeability of fractured andesite. Earth Planet. Sci. Lett. 447, 139–150. http://dx.doi.org/10.1016/j.epsl.2016.05.004.

Horn, R.A., Johnson, C.R., 1985. Norms for vectors and matrices. In: Matrix Analysis. Cambridge University Press.

Jaupart, C., Allègre, C., 1991. Gas content, eruption rate and instabilities of eruption regime in silicic volcanoes. Earth Planet. Sci. Lett. 102, 413–429.

Ketcham, R.A., 2005. Computational methods for quantitative analysis of three-dimensional features in geological specimens. Geosphere 1, 32–41.

Klug, C., Cashman, K.V., 1996. Permeability development in vesiculating magmas: implications for fragmentation. Bull. Volcanol. 58, 87–100.

Kozono, T., Koyaguchi, T., 2009. Effects of relative motion between gas and liquid on 1-dimensional steady flow in silicic volcanic conduits: 1. An analytical method. J. Volcanol. Geotherm. Res. 180, 21–36.

Krieger, I.M., Dougherty, T.J., 1959. A mechanism for non-Newtonian flow in suspensions of rigid spheres. Trans. Soc. Rheol. III, 137–152.

Kushnir, A.R.L., Martel, C., Bourdier, J.-L., Heap, M.J., Reuschle, T., Erdmann, S., Komorowski, J.-C., Cholik, N., 2016. Probing permeability and microtexture: unravelling the role of a low-permeability dome on the explosivity of Merapi (Indonesia). J. Volcanol. Geotherm. Res. 316, 56–71.

Lensky, N.G., Navon, O., Lyakhovsky, V., 2004. Bubble growth during decompression of magma: experimental and theoretical investigation. J. Volcanol. Geotherm. Res. 129, 7–22.

Lindoo, A., Larsen, J.F., Cashman, K.V., Dunn, A.L., Neill, O.K., 2016. An experimental study of permeability development as a function of crystal-free melt viscosity. Earth Planet. Sci. Lett. 435, 45–54. http://dx.doi.org/10.1016/j.epsl.2015.11.035.

Lindquist, W.B., Lee, S.-M., Coker, D.A., Jones, K.W., Spanne, P., 1996. Media axis analysis of void structure in three-dimensional tomographic images of porous media. J. Geophys. Res. 101, 8297–8310. http://dx.doi.org/10.1029/95JB03039.

Mancini, S., Forestier-Coste, L., Burgisser, A., James, F., Castro, J., 2016. An expansion–coalescence model to track gas bubble populations in magmas. J. Volcanol. Geotherm. Res. 313, 44–58. http://dx.doi.org/10.1016/j.jvolgeores.2016.01.016.

Martel, C., Iacono-Marziano, G., 2015. Timescales of bubble coalescence, outgassing, and foam collapse in decompressed rhyolitic melts. Earth Planet. Sci. Lett. 412, 173–185. http://dx.doi.org/10.1016/j.epsl.2014.12.010.

Mueller, S., Melnik, O., Spieler, O., Scheu, B., Dingwell, D.B., 2005. Permeability and degassing of dome lavas undergoing rapid decompression: an experimental determination. Bull. Volcanol. 67, 526–538.

Namiki, A., Manga, M., 2008. Transition between fragmentation and permeable outgassing of low viscosity magmas. J. Volcanol. Geotherm. Res. 169, 48–60. http://dx.doi.org/10.1016/j.jvolgeores.2007.07.020.

Okumura, S., Nakamura, M., Takeuchi, S., Tsuchiyama, A., Nakano, T., Uesugi, K., 2009. Magma deformation may induce non-explosive volcanism via degassing through bubble networks. Earth Planet. Sci. Lett. 281, 267–274.

Okumura, S., Nakamura, M., Nakano, T., Uesugi, K., Tsuchiyama, A., 2012. Experimental constraints on permeable gas transport in crystalline silicic magmas. Contrib. Mineral. Petrol. 164, 493–501.

Okumura, S., Nakamura, M., Uesugi, T., Tsuchiyama, A., Fujioka, T., 2013. Coupled effect of magma degassing and rheology on silicic volcanism. Earth Planet. Sci. Lett. 362, 163–170.

Polacci, M., Baker, D.R., La Rue, A., Mancini, L., Allard, P., 2012. Degassing behaviour of vesiculated basaltic magmas: an example from Ambrym volcano, Vanuatu Arc. J. Volcanol. Geotherm. Res. 233–234, 55–64. http://dx.doi.org/10.1016/j.jvolgeores.2012.04.019.

Polacci, M., Bouvet de Maisonneuve, C., Giordano, D., Piochi, M., Mancini, L., Degruyter, W., Bachmann, O., 2014. Permeability measurements of Campi Flegrei pyroclastic products: an example from the Campanian Ignimbrite and Monte Nuovo eruptions. J. Volcanol. Geotherm. Res. 272, 16–22.

Rust, A.C., Manga, M., Cashman, K.V., 2003. Determining flow type, shear rate and shear stress in magmas from bubble shapes and orientations. J. Volcanol. Geotherm. Res. 122, 111–132. http://dx.doi.org/10.1016/S0377-0273(02)00487-0.

Rust, A.C., Cashman, K.V., 2004. Permeability of vesicular silicic magma: inertial and hysteresis effects. Earth Planet. Sci. Lett. 228, 93–107.

Rust, A.C., Cashman, K.V., 2011. Permeability controls on expansion and size distributions of pyroclasts. J. Geophys. Res. 116.

Ruth, D., Ma, H., 1992. On the derivation of the Forchheimer equation by means of the averaging theorem. Transp. Porous Media 7, 255–264.

Saar, M.O., Manga, M., 1999. Permeability–porosity relationship in vesicular basalts. Geophys. Res. Lett. 26, 111–114.

Sahini, M., Sahimi, M., 1994. Applications of Percolation Theory. CRC Press.

Song, S.-R., Jones, K.W., Lindquist, W.B., Dowd, B.A., Sahagian, D.L., 2001. Synchrotron X-ray computed microtomography: studies on vesiculated basaltic rocks. Bull. Volcanol. 63, 252–263.

Takeuchi, S., Tomiya, A., Shinohara, H., 2009. Degassing conditions for permeable silicic magmas: implications from decompression experiments with constant rates. Earth Planet. Sci. Lett. 283, 101–110.

Wright, H.M.N., Roberts, J.J., Cashman, K.V., 2006. Permeability of anisotropic tube pumice: model calculations and measurements. Geophys. Res. Lett. 33.

Wright, H.M.N., Cashman, K.V., Rosi, M., Cioni, R., 2007. Breadcrust bombs as indicators of Vulcanian eruption dynamics at Guagua Pichincha volcano, Ecuador. Bull. Volcanol. 69, 281–300.

Wright, H.M.N., Cashman, K.V., Gottesfeld, E.H., Roberts, J.J., 2009. Pore structure of volcanic clasts: measurements of permeability and electrical conductivity. Earth Planet. Sci. Lett. 280, 93–104.

Yokoyama, T., Takeuchi, S., 2009. Porosimetry of vesicular volcanic products by a water-expulsion method and the relationship of pore characteristics to permeability. J. Geophys. Res. 114.

Yoshida, S., Koyaguchi, T., 1999. A new regime of volcanic eruption due to the relative motion between liquid and gas. J. Volcanol. Geotherm. Res. 89, 303–315.

The percolation threshold and permeability evolution of ascending magmas

Alain BURGISSER[1,2*], Laure CHEVALIER[2], James E. GARDNER[3], Jonathan M. Castro[4]

[1] CNRS, ISTerre, F-73376 Le Bourget du Lac, France.

[2] Université Savoie Mont Blanc, ISTerre, F-73376 Le Bourget du Lac, France.

[3] Department of Geological Sciences, The University of Texas at Austin, Austin, TX 78712-0254, USA.

[4] Institute of Geosciences, Johannes Gutenberg University Mainz, Mainz, Germany.

* Corresponding author: Phone: (+33) 479 758 780. Fax: (+33) 479 758 742. Email: alain.burgisser@univ-savoie.fr

Supplementary Information

This Supplementary Information includes text detailing how the representative nature of the CT volumes was assessed (Text S1), 2 tables with bubble network parameters (Tables S1-S2), and 6 figures with specific geometry analyses and parameter correlations (Fig. S1-S6).

Text S1.

Some CT volumes of isotropic samples are images of thin sections, which yield flattened parallelepipedic shapes. The shortest analysis dimension of these samples often contains fewer than 5-10 bubbles, which is below the minimum required to obtain a representative permeability value (e.g., Blower, 2001; Rust and Cashman, 2004). Figure S1 shows the number of bubble across each dimension as a function of the respective k_1 value along that dimension for all the isotropic samples. Flattened volumes (e.g., G442) have two large dimensions containing 20-50 bubbles that give similar permeability values whereas the third, shorter dimension contains <10 bubbles and gives a significantly different (generally higher) permeability. If all samples were either cubes or flattened parallelepipeds, ignoring the shortest dimension and averaging the permeabilities of the two other dimensions would have been conceivable, but Fig. S1 shows that CT volumes contain a continuum of the number of bubbles per dimension (i.e. the cuboids have a wide range of aspect ratios). This drove us to use an average permeability value that is weighted per edge length and to quantify the uncertainty of each sample by using the minimum and maximum permeability values.

Bubble coalescence proceeds by creating bubble chains that evolve into connected clusters. When these clusters are large enough, they fill the available space and leave only a few isolated bubbles. In impermeable samples, clusters contain only a few bubble and they reach <0.5 mm in diameter. In permeable samples, clusters involve many bubbles and reach up to 2.5 mm in diameter. The CT volumes, however, are sometimes smaller than 0.5 mm across. These volumes may contain an incomplete permeable network. We used the characteristic number of bubbles across the connected clusters to select sample volumes representative with respect to permeability.

The minimum characteristic length of bubble chains forming a connected network is given in units of number of bubbles. It was measured by dividing the shortest edge of the box enclosing the permeable network by the average bubble diameter, d_a, of the sample volume. The average number of bubbles along the corresponding edge of the sample volume is obtained by dividing the edge length by d_a. If the sample is connected in that direction, the ratio between the number of connected bubbles and the average number of bubbles in the sample is equal to one. This ratio is thus a minimum measure of connectivity. We used both this connectivity and the characteristic number of bubbles across the connected network to decide if the sample volume was representative with respect to permeability. Both measures are reported in Table S1. All isotropic samples deemed permeable have connected networks >10 bubbles across except G328. The permeable network of G328 is 6 bubbles across in its shortest dimension and it is impermeable along that dimension because its connectivity is 0.74. The two other directions of space of G328, however, are connected with similar permeability values. This fact and 3D observations of the raw, irregularly shaped CT volume led us to keep it as a permeable sample. The only impermeable sample with connected sides and a connectivity of one is PPE5. It is a very small CT volume with only 3 bubbles across, which led us to consider it as impermeable. Although the present data set shows that the development of connected bubble networks ranges from 2-5 bubbles across in impermeable samples to large networks >50 bubbles across in permeable samples, a quantification of how bubble chains create large connected clusters is hindered by an insufficient number of samples with large enough CT volumes to properly characterize the size of the bubble clusters. The sample G437 has the largest connected cluster that fits within two dimensions of the CT volume (66 bubbles across and a connectivity of 0.84). It was used to test the influence of taking smaller subsets of the connected cluster on permeability.

Whether CT volumes are representative with respect to permeability was tested following Bai et al. (2010). We choose the isotropic sample G437 because the largest connected network bubbles it contains is smaller than the original CT volume in two directions (x and y) of space (this sample was cut from a thin section and its z direction is only 339 voxels thick). Two sub-volumes were extracted from the original volume so that both comprised a bubble network connected in the three directions . The first sub-volume is 700×700×339 voxels, which corresponds to ~66 bubbles across the *x* and *y* directions, and it yields $k_1 = 5.65^{+1.6}_{-0.96} \times 10^{-15}$ m^2 and $k_2 = 1.76^{+6.6}_{-0.93} \times 10^{-13}$ m. These are the values reported in Table S1 and used in the rest of the study. The second sub-volume is 350×350×339 voxels, which corresponds to ~43 bubbles across the *x* and *y* directions, and it yields $k_1 = 8.05^{+1.2}_{-1.5} \times 10^{-15}$ m^2 and $k_2 = 8.3^{+11}_{-3.8} \times 10^{-13}$ m. The uncertainty introduced by varying CT volume size is thus within a factor 1.5 for k_1 and within a factor 5 for k_2; it is roughly of the same order as the uncertainty given by the three directions of space for nearly equant volumes. Besides G437, three other isotropic samples have a connected network smaller than the CT volume (Table S1). Their permeabilities were also computed on sub-volumes that ensured percolation and they have between 10 and 24 connected bubbles across their largest dimension. The other isotropic permeable samples (Table S1) have between 23 and 79 bubbles across their largest dimension, which ensures that the CT volumes are representative with respect to permeability (Blower, 2001). This is not always true for anisotropic samples, which have between 5 and 15 bubbles across each dimension (Table S1).

Whether voxel size was sufficiently small (edge length is 1 - 4 µm with bubbles containing an average of 43 voxels across, Table S1) was tested on the representative isotropic sample G455 using the viscous permeability in the *y* direction at small pressure differential following Degruyter et al. (2010b) for three voxel sizes. The original CT volume had a voxel size of ~2.85 µm^3 and a permeability k_1 of 5.35×10^{-11} m^2. A coarser resolution of 5.7 µm^3 was obtained by halving the sampling of the original volume, which yielded a permeability of 5.94×10^{-11} m^2. The finer resolution of ~1.43 µm^3 was obtained by doubling the sampling of the original volume, which yielded a permeability of 5.12×10^{-11} m^2. Given resolutions of the other isotropic samples of between 1.1 and 3.2 µm^3, we consider that the effect of discretization is <10% on permeability values. The effect of discretization on anisotropic samples was tested systematically and is reported in Table S2.

An additional test of whether the CT volumes have a sufficient resolution was done on throat and bubble shapes. Figure S2 shows comparisons between our CT volumes and images taken either by SEM, or by X-Ray tomography on a synchrotron. The synchrotron image of sample PPE1 was taken at the ID-19 beamline at ESRF (Grenoble, France) under the conditions described in Degruyter et al. (2010b), which yielded a voxel size of 1.12 μm/voxel. This resolution is half that of the Nanotom volume we analyzed (2.33 μm/voxel, Table S1). Figure S2 shows that bubble shapes are correctly captured by the Nanotom image. A representative throat is slightly larger (30 instead of 24 μm) in the Nanotom image compared to that in the synchrotron. This is mostly because the thinning of the inter-bubble film that defines the throat edges is not fully resolved at the coarser resolution. Imaging the same location in the SEM and by tomography is difficult, and so the comparison was done on bubbles of similar sizes on sample G435 (Fig. S2C-D). In both images, throats are visible at the bottom of cut bubble walls. Representative measurements indicated on the images show that both bubble and throat sizes are captured by the Nanotom volumes within an uncertainty of a couple of voxels (2 to 8 μm, depending on the sample, Table S1).

Our Lattice Boltzmann simulations assume that the fluid is incompressible. The Mach number of the simulations should therefore be <1. The Mach number, *Ma*, is equal to $\sqrt{3}$ times the fluid velocity. It is thus maximum where the fluid velocity is maximum in the narrowest channels of the network. The narrowest channels in our samples are bubble throats. Our permeability calculations are, however, based on v_i, which is the average Darcian fluid velocity in direction i (Eq. (8)). The maximum fluid velocity can be estimated using mass conservation between the bubbles and the throats ($\pi/4 d_a^2 v_i/\phi_c = \pi/4 d_{tmin}^2 v_{max}$, where v_{max} is the maximum fluid velocity and d_{tmin} is the 16th percentile of the throat diameter distribution, Table S2). Table S2 indicates that all *Ma* values for our samples are below 0.1, which indicates that the incompressibility assumption was not violated in our runs.

Inertia effects appear when the Reynolds number of the simulated flow through the permeable network reaches 10^{-2} – 10^{-1} (Andrade et al., 1999). Following the same reasoning as that used for *Ma*, the Reynolds number, *Re*, is comprised between $\rho v_i d_a / \mu$ and $\rho v_{max} d_{tmin} / \mu$. Constant fluid viscosity and density were set to 1/6 kg/lu/s and 1 kg/lu^3, respectively. The symbol lu is the lattice unit length, which was set to the voxel edge length. Table S2 reports the *Re* numbers at the largest pressure gradient applied to each sample. They range from 4.4×10^{-3} to 10. The lowest pressure gradient applied to each sample yields *Re* numbers that are typically 4 orders of magnitude lower than the *Re* reported in Table S2. The overall range of *Re*, from 10^{-7} to 10, indicates that inertial effects were present in our runs because $Re>10^{-2}$ at the large pressure gradients. This is corroborated by the fact that the relationship between dP/dx_i and v_i was nonlinear for all samples and could be fitted by quadratic regressions with $R^2>0.9$.

References S1.

Andrade, J.S., Costa, U.M.S., Almeida, M.P., Makse, H.A., Stanley, H.E., 1999. Inertial Effects on Fluid Flow through Disordered Porous Media. Phys. Rev. Lett. 82, 5249–5252. doi:10.1103/PhysRevLett.82.5249

Table S1: Sample physical parameters. Symbol ϕ_t is the total porosity, ϕ_c is the connected porosity, z_m is the inter-bubble distance, d_a is the average bubble diameter, d_m is the mean bubble diameter, and N_m is the bubble number density (Table 1). The label "Min Nb Conn." refers to the average number of connected bubbles across the shortest side of the CT volume. It is calculated as the smallest diameter of the largest connected volume divided by d_a. Label "Connect." refers to the average number of connected bubbles across the shortest side of the CT volume divided by the average number of bubbles along that side. Labels "Size X", "Size Y", and "Size Z" correspond to the number of voxels along each respective side of the CT volume. The label "Voxel" is the length of the voxel edge of the CT volume. Suffixes x, y, z in the anisotropic sample labels refer to the direction of space considered, x corresponding to the maximum elongation and z to the minimum elongation.

Sample	ϕ_t (vol%)	ϕ_c (vol%)	z_m (μm)[a]	d_a (μm)[b]	d_a 16% (μm)[c]	d_a 84% (μm)[c]	d_m (μm)[b]	N_m ($\times 10^{12}$ m^{-3})	Min. Nb Conn.	Connect.	Size X	Size Y	Size Z	Voxel (μm)
Permeable - anisotropic														
ABG9ax	43.6	34.6	28 (14)	52 (0.32)	30	63	48 (0.34)	10.46	3	1.00	202	382	98	1.82
ABG9ay	43.6	39.6	28 (14)	52 (0.32)	30	63	48 (0.34)	10.46	3	1.00	202	382	98	1.82
ABG9az	43.6	39.6	28 (14)	52 (0.32)	30	63	48 (0.34)	10.46	3	1.00	202	382	98	1.82
ABG9bx	43.2	20.6	31 (13)	58 (0.26)	38	68	56 (0.28)	7.39	7	1.00	536	912	458	1.82
ABG9by	43.2	20.6	31 (13)	58 (0.26)	38	68	56 (0.28)	7.39	7	1.00	536	912	458	1.82
ABG9bz	43.2	20.6	31 (13)	58 (0.26)	38	68	56 (0.28)	7.39	7	1.00	536	912	458	1.82
ABG11ax	31.3	25.1	19 (9)	27 (0.24)	19	32	27 (0.25)	40.88	6	1.00	86	196	200	1.8
ABG11ay	31.3	25.1	19 (9)	27 (0.24)	19	32	27 (0.26)	40.88	6	1.00	86	196	200	1.8
ABG11az	31.3	25.1	19 (9)	27 (0.24)	19	32	27 (0.26)	40.88	6	1.00	86	196	200	1.8
ABG11bx	32.1	16	22 (9)	27 (0.23)	19	32	26 (0.24)	46.16	7	1.00	109	200	119	1.8
ABG11by	32.1	16	22 (9)	27 (0.23)	19	32	26 (0.24)	46.16	7	1.00	109	200	119	1.8
ABG11bz	32.1	16	22 (9)	27 (0.23)	19	32	26 (0.24)	46.16	7	1.00	109	200	119	1.8
G303ax	40.9	12.3	51 (25)	61 (0.38)	22	68	37 (0.72)	5.95	5	1.00	129	356	180	2.29
G303ay	40.9	12.3	51 (25)	61 (0.38)	22	68	38 (0.72)	5.95	5	1.00	129	356	180	2.29
G303az	40.9	12.3	51 (25)	61 (0.38)	22	68	38 (0.72)	5.95	5	1.00	129	356	180	2.29
Permeable - isotropic														
PPE11	50.8	48.9	127 (67)	131 (0.46)	28	150	89 (0.73)	0.04	15	1.00	909	958	280	1.59
G323	43	21.3	52 (25)	58 (0.51)	14	73	30 (0.92)	0.53	13	0.83	200	300	186	2.35
G327	46.4	36.5	37 (18)	58 (0.39)	21	66	32 (0.72)	1.27	18	1.00	89	251	264	3.98
G328	49.7	22.9	43 (21)	67 (0.43)	4	61	23 (1.64)	0.72	6	0.74	230	341	300	1.89
G455	63.5	63.4	32 (17)	70 (0.55)	13	89	51 (0.68)	8.5	28	1.00	609	673	33	2.85
G432	46.9	46.9	26 (11)	48 (0.25)	32	56	45 (0.30)	2.64	33	1.00	312	670	621	2.36
G434	38.8	38.5	31 (12)	72 (0.29)	45	87	69 (0.28)	2.12	36	1.00	788	248	581	3.25
G435	37.8	36.2	32 (13)	47 (0.32)	27	58	48 (0.32)	1.22	32	1.00	394	712	1262	1.17
G442	36.4	34.3	29 (14)	36 (0.29)	22	43	38 (0.21)	1.57	41	1.00	134	1302	1195	1.13
G437	16.1	8.6	34 (12)	23 (0.25)	16	27	22 (0.25)	8.1	66	0.84	700	700	339	1.59
G468	60.7	58.2	41 (21)	103 (0.28)	48	127	98 (0.33)	3.82	23	1.00	960	1102	201	2.12
G439	46.7	45	32 (11)	47 (0.30)	29	56	43 (0.33)	5.63	48	1.00	32	1113	976	2
G443	48.9	47.5	37 (16)	66 (0.44)	24	82	54 (0.52)	5.48	27	1.00	74	1328	729	1.36
Impermeable														
G470	15.3	0	38 (13)	28 (0.16)	n.a	n.a	26 (0.25)	11.22	14	0.20	1263	117	1093	1.67
ABG2	16.1	0	66 (25)	61 (0.12)	n.a	n.a	60 (0.18)	2.03	4	0.31	848	426	473	1.9

Sample	ϕ_t (vol%)	ϕ_c (vol%)	z_m (µm)[a]	d_a (µm)[b]	d_a 16% (µm)[c]	d_a 84% (µm)[c]	d_m (µm)[b]	N_m ($\times 10^{12}$ m^{-3})	Min. Nb Conn.	Connect.	Size X	Size Y	Size Z	Voxel (µm)
ABG25	10.4	0	80 (25)	62 (0.12)	n.a	n.a	61 (0.18)	1.02	4	0.84	396	441	99	3.17
ABG16	14.5	0	80 (29)	68 (0.07)	n.a	n.a	71 (0.11)	1.29	2	0.14	481	491	185	1.9
ABG30	36.2	0	59 (26)	61 (0.12)	n.a	n.a	60 (0.18)	5.49	8	0.72	312	412	190	2.2
ABG27	15.1	0	69 (26)	37 (0.15)	n.a	n.a	35 (0.23)	6.6	15	0.50	505	342	156	3
ABG28	23.5	0	45 (18)	55 (0.09)	n.a	n.a	56 (0.14)	3.27	4	0.23	688	684	458	1.5
ABG31	22.5	0	66 (27)	55 (0.15)	n.a	n.a	51 (0.24)	1.94	3	0.41	200	200	99	2
ABG33	18.7	0	53 (22)	61 (0.12)	n.a	n.a	59 (0.19)	2.21	2	0.26	198	198	99	1.75
G393	25.9	0	132 (47)	97 (0.10)	n.a	n.a	97 (0.16)	0.71	6	0.48	177	1128	208	1.14
PPE2	22.9	0	176 (83)	238 (0.17)	n.a	n.a	218 (0.26)	0.08	1	0.53	397	282	121	2.06
PPE4	31.4	0	68 (25)	110 (0.09)	n.a	n.a	111 (0.14)	0.85	4	0.61	276	208	156	2.48
PPE5	40.8	0	128 (57)	257 (0.20)	n.a	n.a	226 (0.31)	0.08	3	1.00	247	274	196	2.12
PPE7	41.7	0	158 (74)	202 (0.11)	n.a	n.a	200 (0.17)	0.65	4	0.65	101	312	218	4
PPE1	17.4	0	168 (78)	210 (0.62)	n.a	n.a	124 (0.96)	0.05	4	0.62	329	330	268	2.33
G391	58.1	0	80 (38)	271 (0.28)	n.a	n.a	218 (0.44)	1.19	6	0.84	960	1310	189	1.15
PPE10	30.6	0	215 (79)	350 (0.22)	n.a	n.a	302 (0.34)	0.06	3	0.73	539	574	337	2.43
G318	22.7	0	90 (36)	134 (0.30)	n.a	n.a	106 (0.46)	0.7	2	0.27	317	539	79	1.5
G321	36.3	0	51 (22)	83 (0.12)	n.a	n.a	81 (0.19)	2.15	4	0.50	400	400	300	2
G300	17.6	0	89 (36)	59 (0.28)	n.a	n.a	47 (0.44)	1.33	7	0.57	268	299	165	2.16
G303	38.6	0	56 (26)	68 (0.47)	n.a	n.a	46 (0.72)	1.45	10	0.65	320	320	300	2.29

[a] Values in parenthesis are standard deviations.

[b] Values in parenthesis are σ/d.

[c] Respective percentiles of the bubble size distribution.

Table S2: Bubble network parameters. Symbol τ is the tortuosity, d_t is the throat diameter, χ is the bubble aspect ratio, ε is the bubble elongation, *Re* is the Reynolds number, *Ma* is the Mach number, k_1 is the viscous permeability, and k_2 is the inertial permeability (Table 1).

Sample	τ	d_t (μm)	χ	ε[a]	*Re*	*Ma*	k_1 (m^2)	k_2 (m)
Permeable - anisotropic								
ABG9ax	4.9 (0.9)	25 (-18,+27)	3.7	0.2	2.5×10^{-2}	1.7×10^{-3}	1.6×10^{-14} $(-4.0\times10^{-15},+4.0\times10^{-15})$	4.7×10^{-12} $(-2.7\times10^{-12},+2.7\times10^{-12})$
ABG9ay	2.1 (0.6)	25 (-18,+27)	2.4	0.9	3.8×10^{-1}	2.6×10^{-2}	5.0×10^{-13} $(-1.5\times10^{-13},+1.5\times10^{-13})$	2.7×10^{-9} $(-1.3\times10^{-9},+1.3\times10^{-9})$
ABG9az	5.8 (3.0)	25 (-18,+27)	6	0.3	1.5×10^{0}	1.0×10^{-1}	4.9×10^{-13} $(-4.2\times10^{-13},+4.2\times10^{-13})$	1.0×10^{-8} $(-9.4\times10^{-9},+9.4\times10^{-9})$
ABG9bx	3.6 (0.8)	26 (-18,+26)	2.6	0.3	8.2×10^{-2}	5.6×10^{-3}	1.6×10^{-14} $(-5.0\times10^{-16},+5.0\times10^{-16})$	2.2×10^{-12} $(-2.0\times10^{-12},+2.0\times10^{-12})$
ABG9by	2.9 (0.8)	26 (-18,+26)	2.2	0.9	8.7×10^{-2}	6.0×10^{-3}	2.4×10^{-14} $(-3.5\times10^{-15},+3.5\times10^{-15})$	4.1×10^{-12} $(-3.3\times10^{-12},+3.3\times10^{-12})$
ABG9bz	4.1 (1.5)	26 (-18,+26)	3.7	0.4	5.3×10^{-2}	3.6×10^{-3}	8.3×10^{-15} $(-1.6\times10^{-16},+1.6\times10^{-16})$	5.0×10^{-13} $(-4.4\times10^{-13},+4.4\times10^{-13})$
ABG11ax	5.5 (2.5)	14 (-8,+13)	2.8	0.2	2.0×10^{-2}	1.8×10^{-3}	4.4×10^{-15} $(-2.8\times10^{-15},+2.8\times10^{-15})$	2.2×10^{-13} $(-1.3\times10^{-13},+1.3\times10^{-13})$
ABG11ay	2.7 (0.9)	14 (-8,+13)	2.7	0.9	2.7×10^{-2}	2.4×10^{-3}	3.1×10^{-14} $(-1.3\times10^{-14},+1.3\times10^{-14})$	1.9×10^{-11} $(-5.4\times10^{-12},+5.4\times10^{-12})$
ABG11az	2.7 (0.6)	14 (-8,+13)	5.5	0.4	4.4×10^{-3}	3.9×10^{-4}	3.5×10^{-15} $(-2.1\times10^{-15},+2.1\times10^{-15})$	6.2×10^{-14} $(-3.6\times10^{-14},+3.6\times10^{-14})$
ABG11bx	2.2 (0.5)	10 (-7,+14)	2.7	0.2	4.1×10^{-2}	7.5×10^{-3}	5.3×10^{-15} $(-3.2\times10^{-15},+3.2\times10^{-15})$	2.6×10^{-13} $(-1.3\times10^{-13},+1.3\times10^{-13})$
ABG11by	1.9 (0.4)	10 (-7,+14)	2.3	0.9	4.1×10^{-2}	7.4×10^{-3}	1.5×10^{-14} $(-6.4\times10^{-15},+6.4\times10^{-15})$	3.0×10^{-12} $(-1.3\times10^{-12},+1.3\times10^{-12})$
ABG11bz	2.6 (0.3)	10 (-7,+14)	3.9	0.4	2.3×10^{-2}	4.2×10^{-3}	1.7×10^{-15} $(-1.2\times10^{-15},+1.2\times10^{-15})$	3.1×10^{-14} $(-1.4\times10^{-14},+1.4\times10^{-14})$
G303ax	2.4 (0.5)	20 (-12,+22)	2.4	0.4	2.7×10^{-2}	2.3×10^{-3}	4.8×10^{-15} $(-1.3\times10^{-15},+1.3\times10^{-15})$	1.1×10^{-13} $(-1.0\times10^{-13},+1.0\times10^{-13})$
G303ay	2.4 (0.0)	20 (-12,+22)	2.1	0.8	4.7×10^{-3}	4.0×10^{-4}	2.6×10^{-15} $(-3.1\times10^{-16},+3.1\times10^{-16})$	3.8×10^{-14} $(-2.6\times10^{-14},+2.6\times10^{-14})$
G303az	2.1 (0.3)	20 (-12,+22)	2.4	0.4	9.2×10^{-3}	7.8×10^{-4}	2.3×10^{-15} $(-1.3\times10^{-15},+1.3\times10^{-15})$	2.0×10^{-14} $(-1.0\times10^{-14},+1.0\times10^{-14})$
Permeable - isotropic								
PPE11	2.2 (0.3)	34 (-21,+59)	2.1	0.6	1.0×10^{1}	3.7×10^{-1}	1.9×10^{-11} $(-1.4\times10^{-11},+2.3\times10^{-11})$	1.3×10^{-6} $(-1.3\times10^{-6},+1.3\times10^{-5})$
G323	2.3 (0.4)	13 (-6,+23)	2.1	0.6	9.0×10^{-2}	8.7×10^{-3}	4.9×10^{-14} $(-1.6\times10^{-14},+2.8\times10^{-14})$	1.4×10^{-11} $(-7.6\times10^{-12},+1.6\times10^{-11})$
G327	2.0 (0.4)	17 (-8,+19)	2.1	0.6	3.9×10^{-2}	5.0×10^{-3}	1.3×10^{-13} $(-2.4\times10^{-14},+1.1\times10^{-14})$	2.1×10^{-11} $(-7.9\times10^{-12},+9.8\times10^{-12})$
G328	2.8 (0.2)	13 (-10,+23)	2.2	0.6	1.7×10^{-1}	2.6×10^{-2}	2.3×10^{-14} $(-9.4\times10^{-15},+1.3\times10^{-14})$	5.4×10^{-12} $(-2.4\times10^{-12},+3.7\times10^{-12})$
G455	1.6 (0.1)	25 (-12,+31)	2.2	0.6	7.2×10^{-1}	4.4×10^{-2}	5.2×10^{-12} $(-8.8\times10^{-13},+4.8\times10^{-11})$	5.9×10^{-8} $(-2.0\times10^{-8},+4.2\times10^{-5})$
G432	1.6 (0.1)	20 (-9,+17)	2.1	0.6	3.7×10^{-1}	2.2×10^{-2}	1.4×10^{-12} $(-2.6\times10^{-13},+3.8\times10^{-13})$	7.1×10^{-9} $(-2.7\times10^{-9},+1.2\times10^{-8})$
G434	1.6 (0.1)	26 (-10,+21)	2	0.6	7.6×10^{-2}	4.6×10^{-3}	2.9×10^{-13} $(-3.6\times10^{-14},+9.3\times10^{-14})$	1.1×10^{-10} $(-4.6\times10^{-11},+3.5\times10^{-10})$
G435	2.0 (0.2)	15 (-8,+12)	2	0.6	1.4×10^{-1}	6.8×10^{-3}	6.8×10^{-14} $(-1.9\times10^{-14},+1.8\times10^{-14})$	8.8×10^{-11} $(-3.2\times10^{-11},+1.1\times10^{-10})$
G442	2.0 (0.2)	13 (-7,+12)	2	0.6	1.6×10^{0}	7.8×10^{-2}	1.3×10^{-13} $(-6.3\times10^{-15},+1.5\times10^{-13})$	2.3×10^{-10} $(-8.8\times10^{-11},+1.3\times10^{-8})$
G437	2.8 (0.4)	9 (-4,+6)	2	0.6	1.2×10^{-2}	1.1×10^{-3}	5.7×10^{-15} $(-9.6\times10^{-16},+1.6\times10^{-15})$	1.8×10^{-13} $(-9.3\times10^{-14},+6.6\times10^{-13})$
G468	1.9 (0.1)	26 (-12,+26)	2.2	0.6	2.5×10^{0}	1.1×10^{-1}	8.5×10^{-13} $(-2.0\times10^{-13},+1.2\times10^{-12})$	2.7×10^{-9} $(-1.8\times10^{-9},+1.2\times10^{-6})$
G439	1.3 (0.1)	15 (-7,+13)	2.2	0.6	2.4×10^{0}	1.6×10^{-1}	8.6×10^{-13} $(-1.1\times10^{-13},+5.5\times10^{-12})$	1.9×10^{-9} $(-6.0\times10^{-10},+4.7\times10^{-7})$
G443	1.5 (0.1)	18 (-8,+20)	2.1	0.6	1.6×10^{0}	6.4×10^{-2}	3.7×10^{-13} $(-1.1\times10^{-13},+8.7\times10^{-12})$	1.7×10^{-9} $(-9.6\times10^{-10},+4.3\times10^{-7})$

[a] Values for isotropic samples are assumed to be $3^{-0.5}$ because χ values are close to the theoretical value of 2.

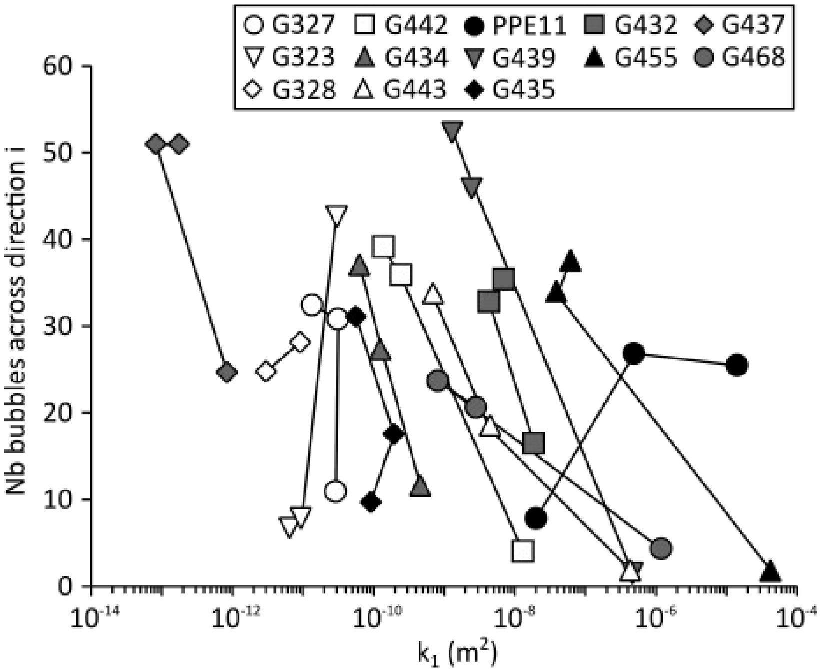

Figure S1: Number of bubbles across each analysis direction as a function of k_1 for isotropic samples. Lines link the three respective directions of each sample. Sample G328 is represented by two points instead of three because it is impermeable along one dimension.

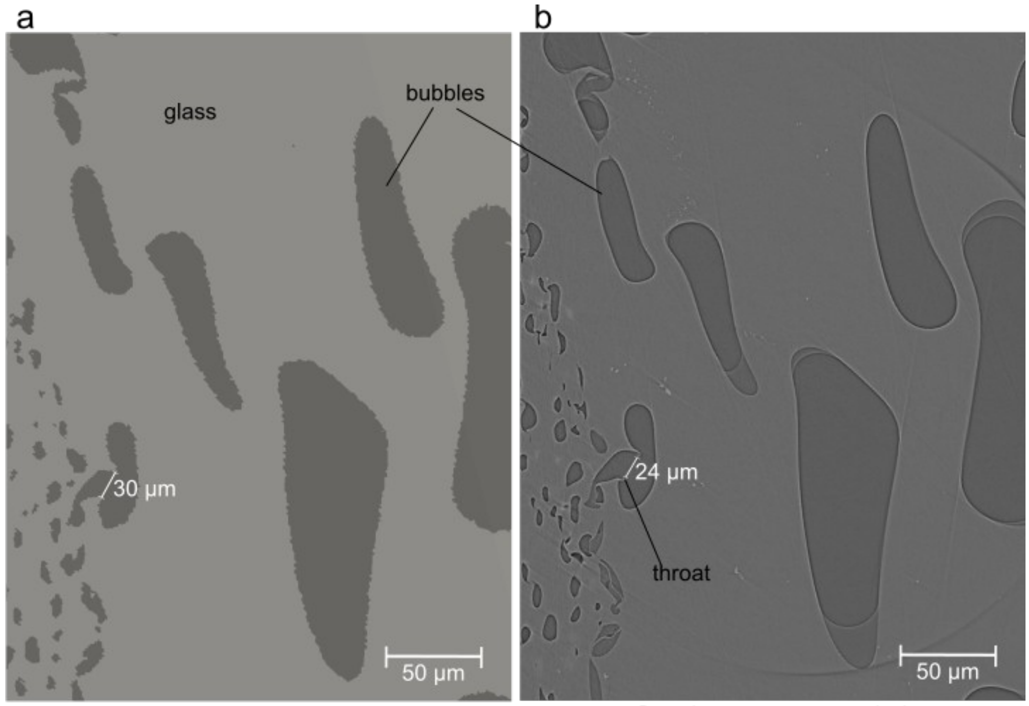

Nanotom, binary image

Synchrotron, greyscale image

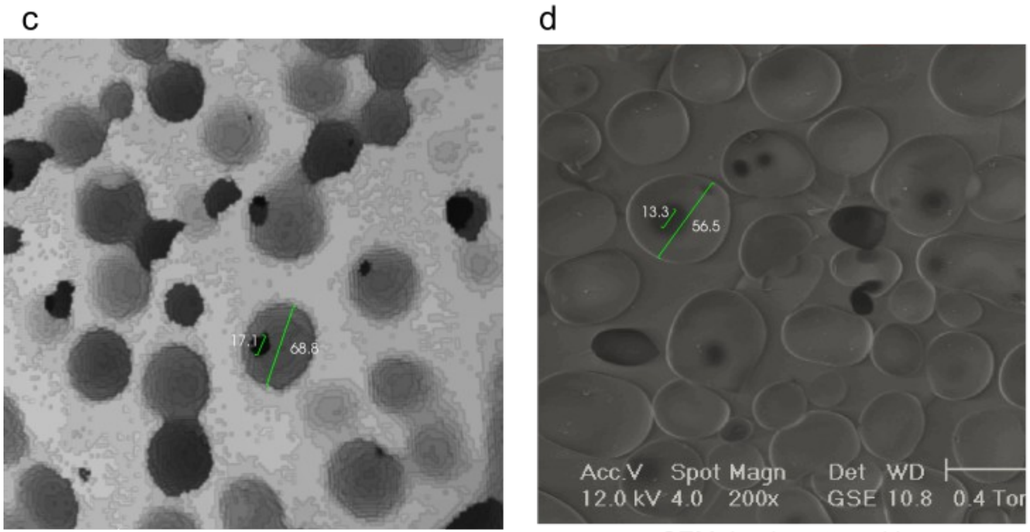

Nanotom, binary image

SEM, backscattered image

Figure S2: Comparison between images of the CT volumes analyzed and images acquired by synchrotron and SEM. A) Cross section of the thresholded Nanotom volume of sample PPE1. B) Greyscale slice of the synchrotron volume of sample PPE1 at the same location as A. C) 3D shaded rendering of a cross section of thresholded Nanotom volume of sample G435. D) SEM backscattered electron image of sample G435 at a different location than C but featuring similarly sized bubbles and throats. Measured distances (green lines) in C and D are in µm.

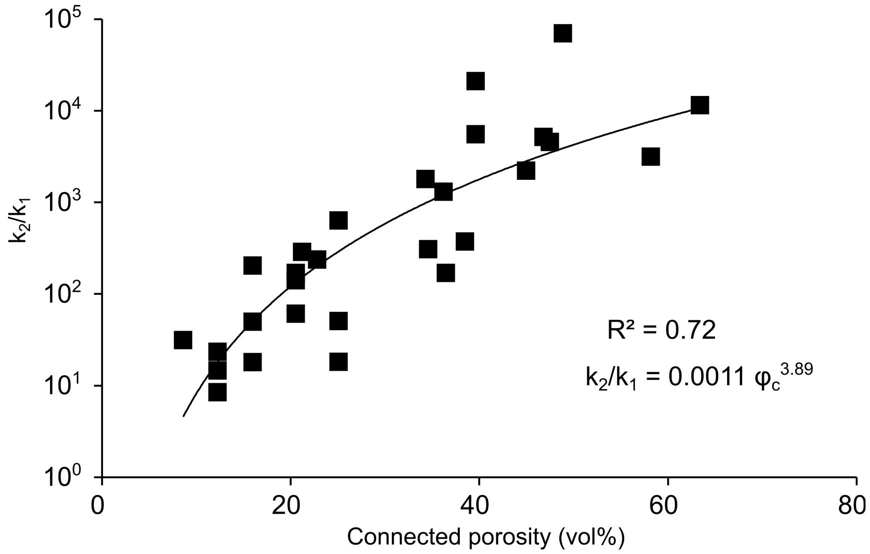

Figure S3: Ratio of inertial to viscous permeability (k_2/k_1) as a function of connected porosity (φ_c). A power law fit with its R^2 value are given as labels.

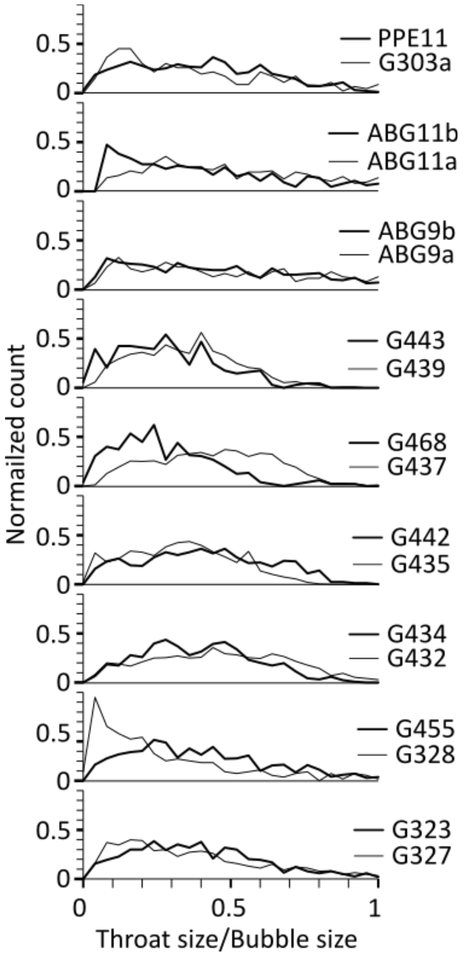

Figure S4: Distributions of throat diameter over bubble diameters for each analyzed pairs of bubble and throat in each samples.

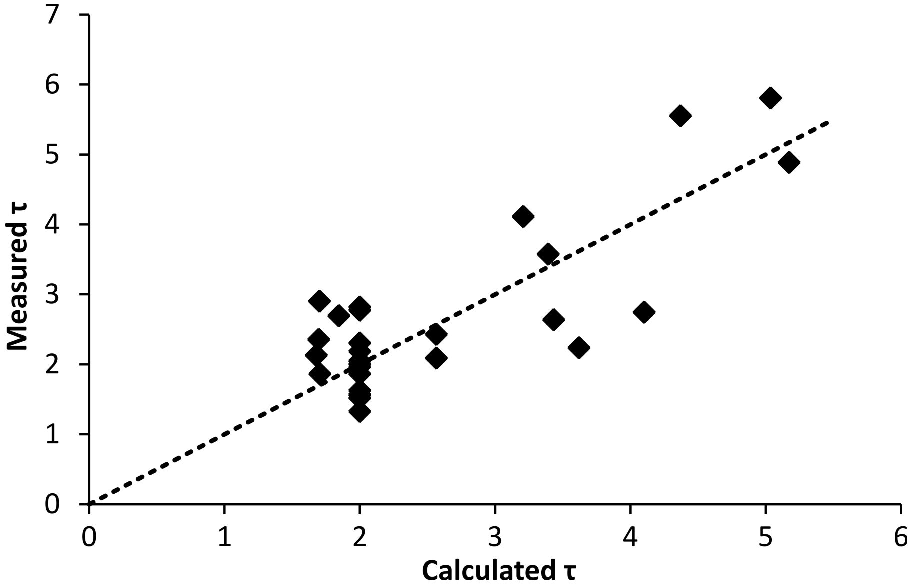

Figure S5: Calculated vs. measured values of tortuosity (τ).

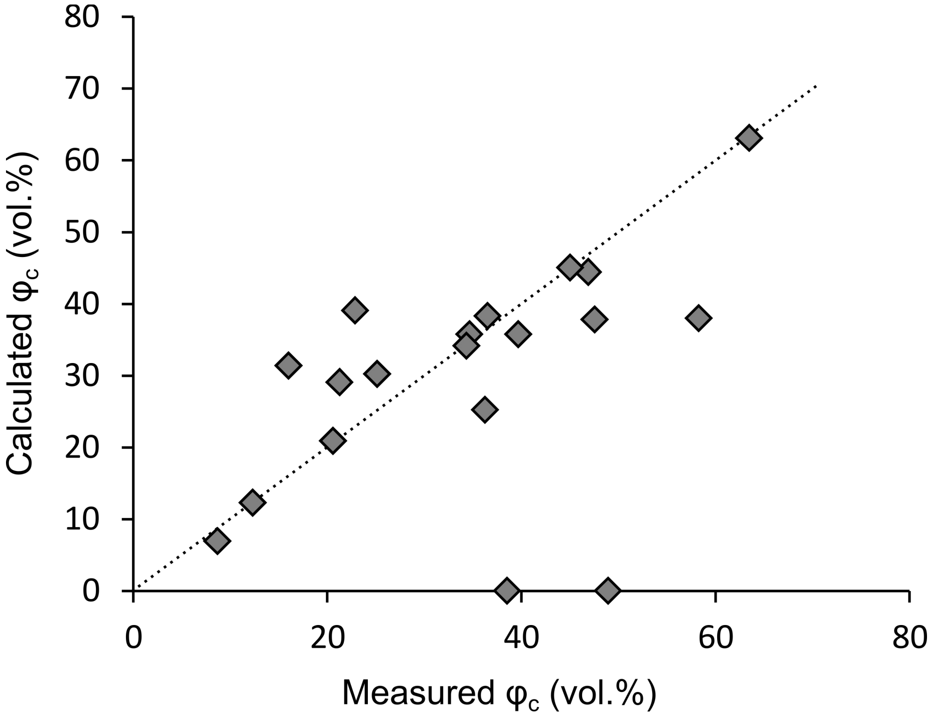

Figure S6: Measured vs. calculated values of connected porosity (*φ_c*).

3.4 Integration of the new permeability law into 2D modelling

3.4.1 Integration of the bubble deformation in the permeability expression

3.4.1.1 Bubble deformation at andesitic volcanoes

Along with magma ascent within the conduit, bubbles present in the magma undergo shear stress and then deform. The importance of this deformation depends on the bubble capillary number Ca, and on the nature of the shear stress. Two end-member natures of shear can affect bubbles in the conduit: simple shear and pure shear. Simple shear is caused by velocity variations that are perpendicular to the flow lines (fig. 3.2b). For example, close to the conduit walls, the vertical velocity varies a lot with the distance to the wall. This causes simple shear. Pure shear is present when the velocity varies along the flow line (fig. 3.2c). This occurs at the top of the conduit, where the increase in porosity due to gas exsolution causes the magma velocity to increase.

In the 2D axisymmetric conduit flow model presented in chap. 1, pure shear is only significant at the very top (a few tens of meters) of the conduit, whereas simple shear is important in the whole conduit. For simplicity, and since no bubble deformation models exist for a combination of pure and simple shear, we here assume that bubbles in the conduit are only deformed due to simple shear.

Bubble deformation under simple shear conditions has been studied for a wide range of capillary numbers, from experimental (e.g. Canedo et al., 1993; Rust and Manga, 2002a; Kameda et al., 2008) and numerical models. The bubble elongation in response to shear stress has been first described by Taylor (1932, 1934), for low Ca ($Ca << 1$) conditions:

$$D = Ca \tag{3.1}$$

where $D = (l-b)/(l+b)$, with l and b the semi-major and the semi-minor axes of the ellipsoidal bubble, respectively. Later, Hinch and Acrivos (1980) found that for higher deformations, and $Ca >> 1$, the bubble deformation was well represented by:

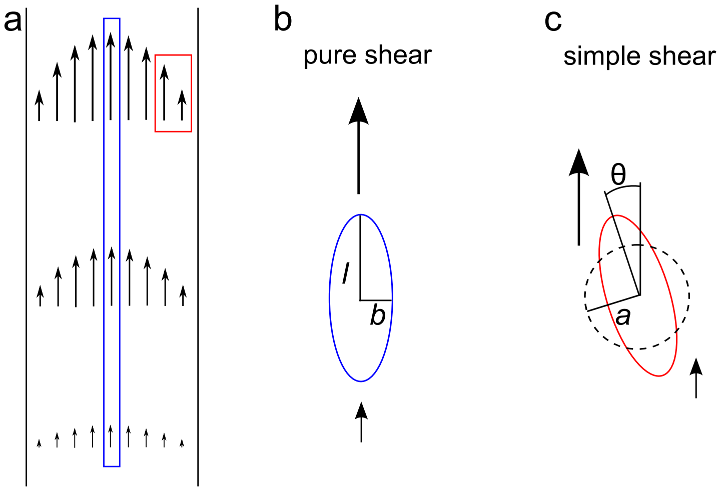

Figure 3.2: Different natures of shear in the conduit. (a) Sketch of the velocity field in the conduit (black arrows). (b) Simple shear is caused by the presence of velocity variations perpendicular to the flow lines. Bubbles submitted to simple shear are elongated and have an orientation angle θ with the flow line. (c) Pure shear is caused by velocity variations along a same flow line. Bubbles are elongated in the direction of flow. l and b represent respectively the deformed bubble semi-major and semi-minor axes, and a is the radius of the spherical, undeformed bubble.

$$\frac{l}{a} = 3.45Ca^{1/2} \tag{3.2}$$

where a is the bubble equivalent sphere diameter. Canedo et al. (1993) measured experimentally the deformation of bubbles with Ca ranging from 3 to 50, and found that bubble deformation was slightly lower than predicted by Hinch and Acrivos (1980). Their data were well represented by the following equation:

$$\frac{l}{a} = 3.1Ca^{0.43} \tag{3.3}$$

Bubbles submitted to simple shear do not deform parallel to the flow lines, but have an orientation angle that varies with the importance of shear (and with Ca value). For low Ca bubbles, Rallison (1980) predicted the following relation for bubble orientation, which was confirmed by Guido and Greco (2001) experiments:

$$\theta = \frac{\pi}{4} - 0.6Ca \tag{3.4}$$

where θ is the angle between the direction of flow and the ellipsoidal bubble major axis. For high capillary numbers, Hinch and Acrivos (1980), and Canedo et al. (1993) agree on the following expression:

$$\theta = \tan^{-1}(0.359Ca^{-3/4}) \tag{3.5}$$

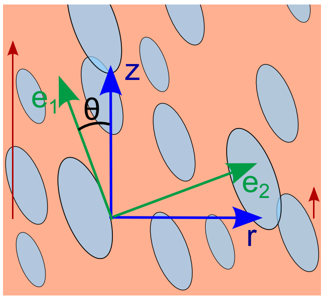

Figure 3.3: Principal directions of permeability due to bubble elongation: direction parallel to elongation e_1 and orthogonal e_2. Because of bubble orientation due to simple shear, these directions are different from the radial r and vertical z directions.

All these equations were obtained from experimental and numerical observations of bubble deformation in steady shear conditions. Llewellin et al. (2002a); Llewelling et al. (2002b); Llewellin and Manga (2005) provided evidence that a bubble submitted to unsteady shear conditions would deform differently, depending on the value of the dynamic capillary number Cd (see chap. 1 section 3.2.3). Instead of Ca, we therefore rather use Cx, with $Cx = \max(Ca, Cd)$.

3.4.1.2 Permeability in the bubble reference frame

The permeability law we developed in (Burgisser et al., 2017) (section 3.3) provides the expressions of both the viscous and inertial permeabilities. The inertial permeability affects gas flow only in turbulent regimes, with high Reynolds numbers Re (> 2300). In our 2D conduit flow model, Re remains very low (<0.6). The momentum equation for gas flow we use in our model is therefore simply a Darcian equation. We therefore only describe here the expression for k_1 implementation. However, this calculation sequence also applies to k_2, if needed.

In this paragraph, we develop the expression of permeability along the directions of the major and minor axes of the bubble, assuming that locally, for a small volume of magma all bubbles in suspension within this volume are deformed in the same way (fig. 3.3). In the permeability law we developed in the attached article, we use two deformation parameters: ε and χ, defined as follows along the directions of the major, intermediate and minor axes directions:

$$\varepsilon_i = \frac{a_i}{\sqrt{\sum a_k^2}} \tag{3.6}$$

$$\chi_i = \left(\frac{\max(a_{k,k\neq i})}{\min(a_{k,k\neq i})} + \frac{\min(a_{k,k\neq i})}{\max(a_{k,k\neq i})} \right) \tag{3.7}$$

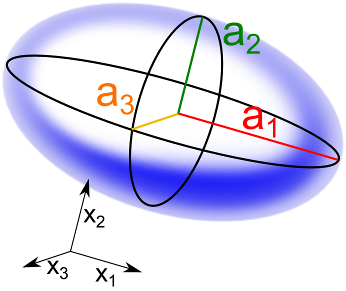

$$\varepsilon_1 = \frac{a_1}{\sqrt{a_1^2 + a_2^2 + a_3^2}}$$

$$\chi_1 = \left(\frac{a_2}{a_3} + \frac{a_3}{a_2}\right)$$

Figure 3.4: Major, intermediate and minor semi-axes in a deformed bubble, and calculation of the ε_i and χ_i parameters corresponding to the direction of elongation.

with i the selected direction, and a_i the semi-axis value corresponding to this direction. We here assume that the minor and intermediate axes are equal.

Having information on bubble elongation from the empirical deformation relationships (3.1) and (3.3), we calculate the expressions of χ (3.9) and ε ((3.10) and (3.11)) corresponding to the directions of the major and minor axes of the deformed bubble (e_1 and e_2, respectively).

Assuming that the minor and intermediate axes are equal,

$$\begin{aligned} \chi_{e1} &= 2 \\ \chi_{e2} &= \left(\frac{l}{b} + \frac{b}{l}\right) \end{aligned} \tag{3.8}$$

For $Cx >> 1$,

$$\begin{aligned} \varepsilon_{e1} &= \frac{l}{\sqrt{l^2 + 2 * b^2}} \\ \varepsilon_{e2} &= \frac{b}{\sqrt{l^2 + 2 * b^2}} \end{aligned} \tag{3.9}$$

For $Cx << 1$,

$$\begin{aligned} \varepsilon_{e1} &= \frac{\left(\dfrac{1+D}{1-D}\right)}{\sqrt{2+\left(\dfrac{1+D}{1-D}\right)^2}} \\ \varepsilon_{e2} &= \frac{1}{\sqrt{2+\left(\dfrac{1+D}{1-D}\right)^2}} \end{aligned} \tag{3.10}$$

We then calculate $k_{1|e1}$ and $k_{1|e2}$ (and $k_{2|e1}$ and $k_{2|e2}$) using the relations developed in Burgisser et al. (2017) (attached paper).

3.4.1.3 Permeability in the conduit

We now develop the expression of the permeability in the conduit, i.e. in the (r,z) framework. In the conduit, the variations of permeability with spacial direction can be represented as an ellipsoid, associated with a permeability tensor whose principal directions are the permeability values along the major, intermediate and minor semi-axes directions of the ellipsoid (fig. 3.5). In the permeability law we developed, the principal values for the permeability tensor are obtained for the spacial directions that correspond to the principal values of the bubbles deformation tensor (see (Burgisser et al., 2017), attached paper). In the principal framework for bubble deformation, the permeability tensor k_1 is therefore diagonal, and the principal permeability values are $k_{1|e1}$ and $k_{1|e2}$:

$$k_{1|(e1,e2)} = \begin{pmatrix} k_{1|e1} & 0 \\ 0 & k_{1|e2} \end{pmatrix}$$

The permeability tensor $k_{1|(r,z)}$ in the conduit reference frame (r,z) can be calculated from $k_{1|(e1,e2)}$ using the relation:

$$k_{1(r,z)} = P^T k_{1|(e1,e2)} P \tag{3.11}$$

where P is the transformation matrix associated with the change of basis from (e_1,e_2) to (r,z), and P^T is its transpose.

$$P = \begin{pmatrix} -\sin\theta & \cos\theta \\ \cos\theta & \sin\theta \end{pmatrix} \tag{3.12}$$

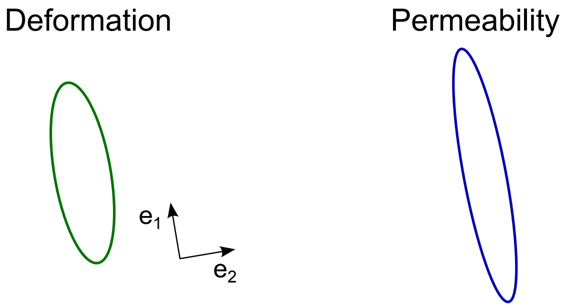

$$S_{e1,e2} = \frac{l}{a}\begin{pmatrix} \varepsilon_{e1} & 0 \\ 0 & \varepsilon_{e2} \end{pmatrix} \qquad K1_{e1,e2} = \begin{pmatrix} K1_{e1} & 0 \\ 0 & K1_{e2} \end{pmatrix}$$

Figure 3.5: Sketch of the deformation and permeability ellipsoids and tensors in the (e_1,e_2) framework.

We then get

$$k_{1|(r,z)} = \begin{pmatrix} \cos^2\theta k_{1|e2} + \sin^2\theta k_{1|e1} & \sin\theta\cos\theta(k_{1|e2} - k_{1|e1}) \\ \sin\theta\cos\theta(k_{1|e2} - k_{1|e1}) & \cos^2\theta k_{1|e1} + \sin^2\theta k_{1|e2} \end{pmatrix} \tag{3.13}$$

Calculations to get $k_{2|(r,z)}$ follow the same reasoning. In the 2D numerical model, we use the Darcy equation to solve for gas flow:

$$\nabla p_g = -\frac{\mu_g}{k_1}u \tag{3.14}$$

Considering a non isotropic permeability, this equation should be written:

$$\nabla p_g = -\mu_g {k_{1|(r,z)}}^{-1}u \tag{3.15}$$

This is valid provided k_1 is invertible. A square matrix is invertible if, and only if, its determinant is not 0.

$$\det k_{1|(r,z)} = k_{1|e1}k_{1|e2}(\cos^2\theta + \sin^2\theta) \tag{3.16}$$

k_1 is therefore invertible for any value of θ and we get:

$$\begin{aligned} &{k_{1|(r,z)}}^{-1} = \\ &\qquad \frac{1}{k_{1|e1}k_{1|e2}}\begin{pmatrix} \cos^2\theta k_{1|e1} + \sin^2\theta k_{1|e2} & -\sin\theta\cos\theta(k_{1|e2} - k_{1|e1}) \\ -\sin\theta\cos\theta(k_{1|e2} - k_{1|e1}) & \cos^2\theta k_{1|e2} + \sin^2\theta k_{1|e1} \end{pmatrix} \end{aligned} \tag{3.17}$$

3.4.2 Constant bubble deformation

We first observe the effects of the BND (N_m) and of the spread of the BSD (σ_a/d_a) on gas flow in the conduit. We use the same 2D axisymmetric model for gas flow calculation as presented in Chevalier et al. (2017) (chap. 2). Starting from steady-state effusive conditions for magma flow (Collombet, 2009), we solve a mass conservation equation for gas flow in the conduit and surrounding rock that takes into account gas permeable flow through the magma, bubble advection by the magma, and gas exsolution from the melt. Boundary conditions are imposed on gas pressure. At the bottom of the conduit (2km depth), the gas pressure equates magma pressure. At the surrounding rock edges we impose a pressure varying with depth, whose expression is fully described in chap. 1. Pressure at the top of the conduit is set to atmospheric. Permeability in the surrounding rock is isotropic and is set to 10^{-12}m^2.

In this section, we set the values of ε_i and χ_i so that the permeability ratio in the conduit $k_{1|z}/k_{1|r} = 10$, and we assume $\theta = 0$. This is indeed the permeability ratio and orientation we used in chap. 2 for gas flow calculation with the Klug and Cashman (1996) law. Using the same permeability anisotropy allows straightforward comparison with our results for gas flow. With our permeability law, a permeability ratio of 10 is reached for $\varepsilon_z = 0.9154$, $\varepsilon_r = 0.2847$, $\chi_z = 2$, $\chi_r = 3.5268$, and corresponds to a vertical elongation of the bubbles with an aspect ratio of 3.2 which is in the low range of deformation measured on real samples (Rust et al., 2003). We vary progressively the BND N_m from 10^{13} to 10^{15}m^{-3}, and σ_a/d_a from 0.1 to 10. For each case we get a time-dependent solution for gas flow through the conduit and surrounding rocks. We present the evolution of permeability obtained in the conduit for the different cases. We also compare the gas pressure at steady state with the steady state solution using the Klug and Cashman (1996) law ($k1 = 2 \cdot 10^{-12}(\varphi_g)^{3.5}$), presented in chap. 2. We also present the results obtained using the average Mueller et al. (2005) permeability law for effusive samples ($k1 = 6.3 \cdot 10^{-11}(\varphi_g)^{3.4}$), with the same permeability ratio of 10.

Figures 3.6 and 3.7 present the evolution of the vertical permeability in the conduit with N_m and σ_a/d_a, respectively. The vertical permeability profiles corresponding to the Klug and Cashman (1996) and the Mueller et al. (2005) permeability-porosity relationships are also presented. As discussed in Burgisser et al. (2017) (attached to this article), fig. 8, decreasing N_m causes a global increase in the permeability, although it also causes an increase in the percolation threshold value (fig. 8a in Burgisser et al. (2017)), thus restricting permeable gas flow to a smaller part of the conduit. In fig. 3.6, the permeability distribution for a BND of 10^{13}m^{-3}

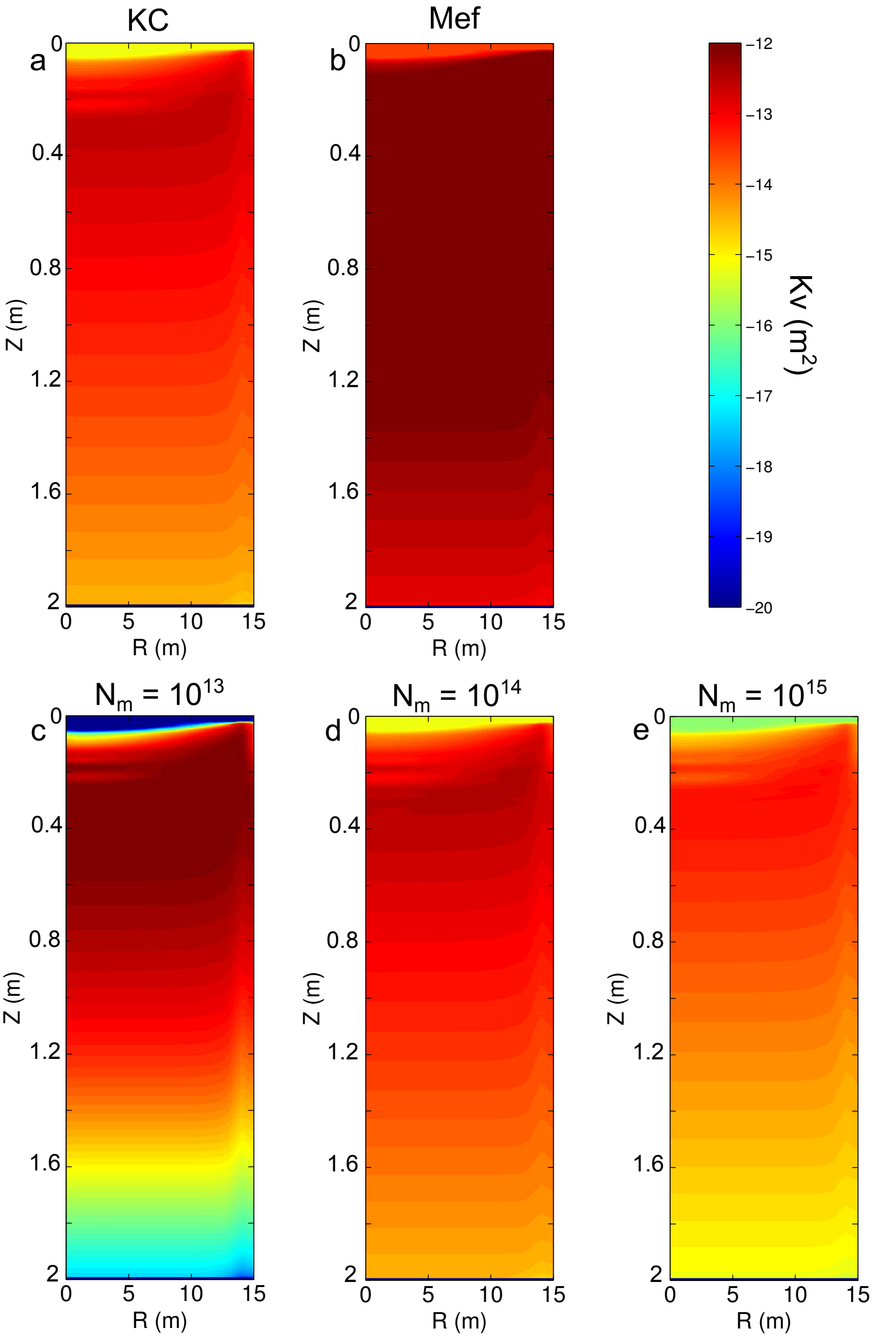

Figure 3.6: Vertical permeability within the conduit calculated from several permeability laws. (KC): Klug and Cashman (1996), (Mef): Mueller et al. (2005), others: Burgisser et al. (2017) (attached article), with N_m varying from 10^{13} to $10^{15}\mathrm{m}^{-3}$ and $\sigma_a/d_a = 1$. Red color indicates high permeability, whereas blue indicates low permeability. In all these simulations $k_{1|z}/k_{1|r} = 10$.

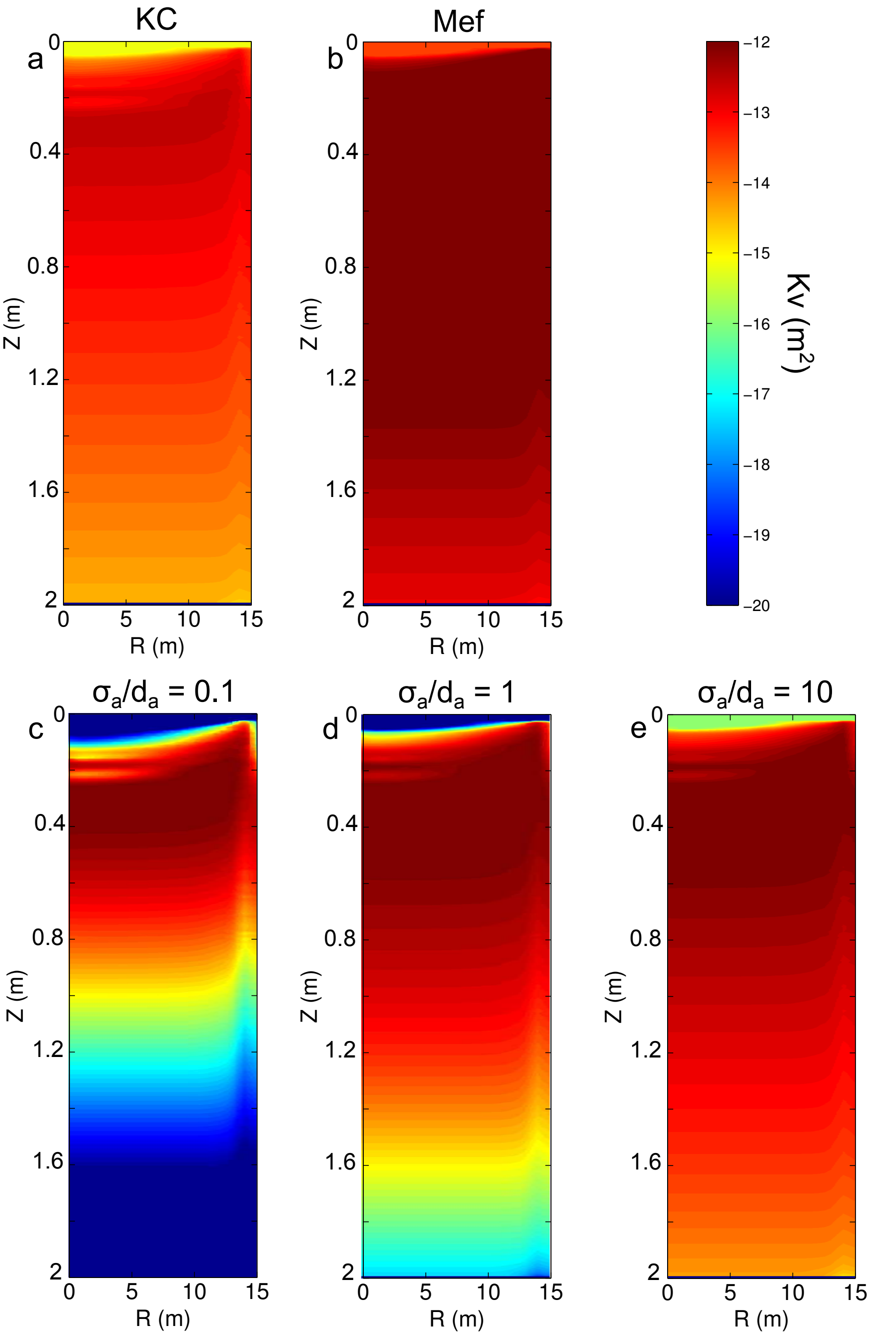

Figure 3.7: Vertical permeability within the conduit calculated from several permeability laws. (KC): Klug and Cashman (1996), (Mef): Mueller et al. (2005), others: Burgisser et al. (2017) (attached article), with σ_a/d_a varying from 0.1 to 10 and $N_m = 10^{13}\mathrm{m}^{-3}$. Red color indicates high permeability, whereas blue indicates low permeability. In all these simulations $k_{1|z}/k_{1|r} = 10$.

indeed evidences the presence of an impermeable zone at the very top of the conduit (until a depth of about 70m), as well as a low permeability zone at the conduit base (below a depth of 1600m). Increasing σ_a/d_a causes a strong decrease in the percolation threshold, as one can see on fig. 3.7, therefore extending the zone permeable to gas flow. We indeed notice that, with a wide BSD (σ_a/d_a=10), the magma is permeable in the whole conduit (depth up to 2000m), whereas a narrow BSD (σ_a/d_a=0.1) is associated with an elevated percolation threshold, causing the presence of impermeable zones at the top (100m) and bottom (below 1.5km) of the conduit. These results confirm observations made by Burgisser et al. (2017). We also see from these figures, that the permeability law obtained with $N_m = 10^{14}\text{m}^{-3}$ and $\sigma_a/d_a = 1$ is very close to the Klug and Cashman (1996) law, while the Mueller et al. (2005) permeability-porosity relationship is nearly recovered for $N_m = 10^{13}\text{m}^{-3}$ and $\sigma_a/d_a = 10$.

Figures 3.8 and 3.9 present the influence of the different permeability laws presented before on gas pressurization within the conduit. The gas pressure difference δp presented here is the difference between the steady-state solution for gas flow for the permeability law studied $P_{eq,X}$ and that for the Klug and Cashman (1996) law $P_{eq,KC}$ (3.18).

$$\delta p = (P_{eq,X} - P_{eq,KC}) \tag{3.18}$$

Lower permeabilities limit gas flow and then gas loss, then favouring gas pressurization within the conduit. This is visible on fig. 3.8 and 3.9, in which the highest gas pressures in the conduit (a few tens of MPa) are obtained for a high BND and small σ_a/d_a, which, as shown in fig. 3.6 and 3.7, are associated with lower permeability values in the conduit. The permeability-porosity relationship from Mueller et al. (2005) causes the gas pressure to be lower than in the Klug and Cashman (1996) law case, since it is associated with a higher permeability in the conduit.

3.4.3 Free bubble deformation

We now calculate bubble deformation within the conduit depending on flow conditions (section 3.4.1.1). Figure 3.10 presents the evolution of bubble deformation and orientation within the conduit. Results for our 2D axisymmetric conduit flow model evidence that bubble shapes range from undeformed to strongly deformed, with an aspect ratio l/b reaching up to 125. Their orientation varies from 45°, at the conduit center at depth, to less than 5°, in the upper part of the conduit, where

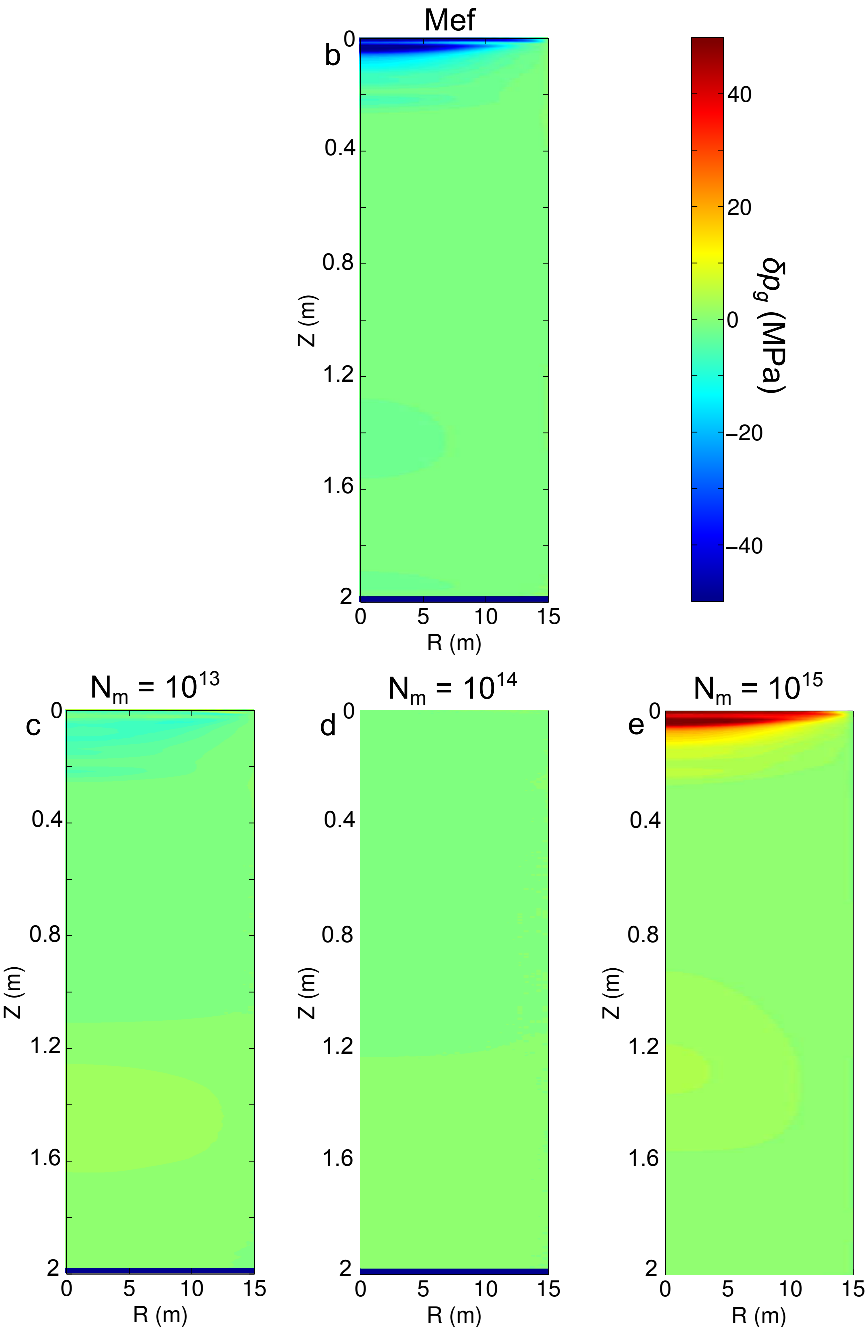

Figure 3.8: Steady-state gas pressure within the conduit, compared with the steady state gas pressure solution using the Klug and Cashman (1996) law, for several permeability laws. (Mef): Mueller et al. (2005), others: Burgisser et al. (2017) (attached article), with N_m varying from 10^{13} to 10^{15}m^{-3} and $\sigma_a/d_a = 1$. Red color indicates that gas pressure is higher than in the solution using the Klug and Cashman (1996) law, whereas blue indicates it is lower.

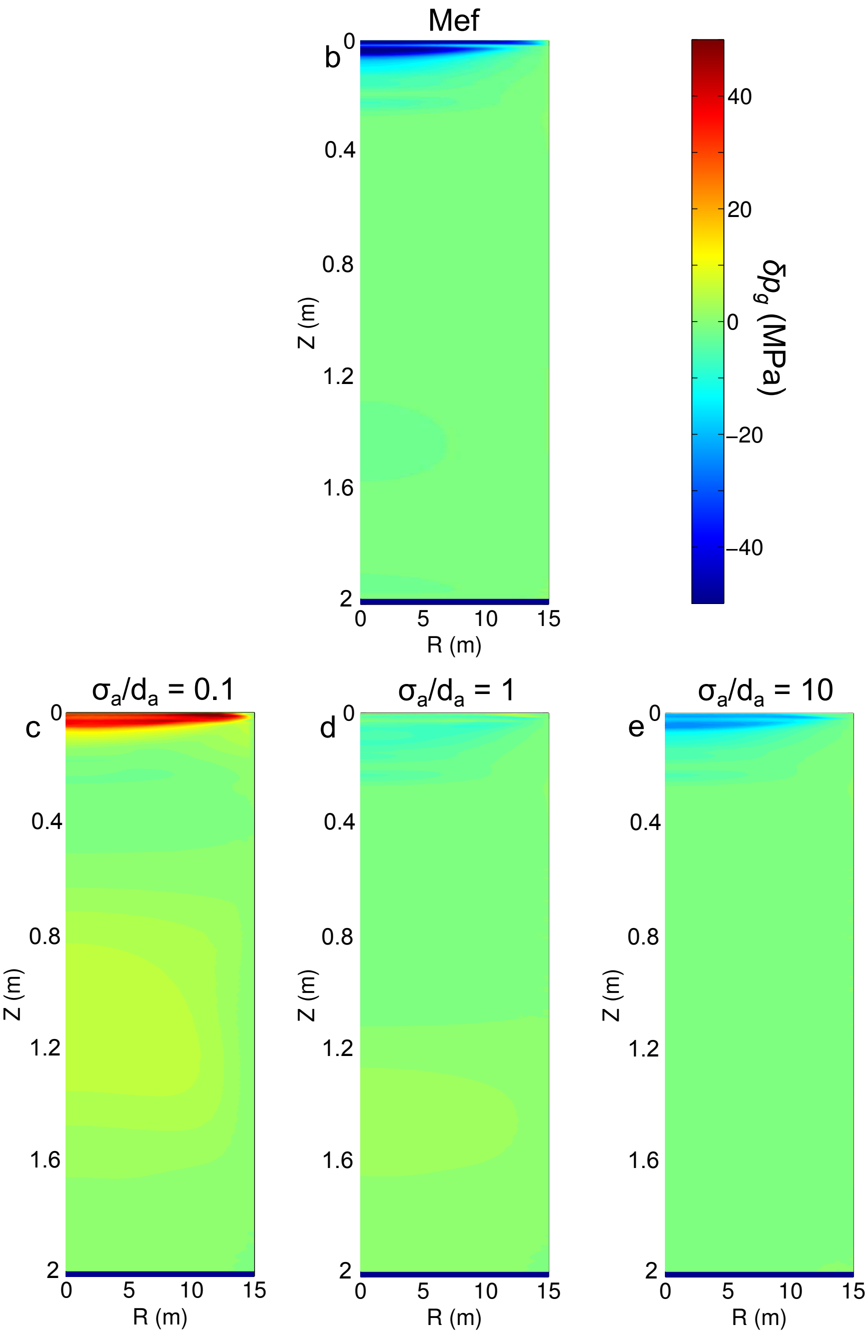

Figure 3.9: Steady-state gas pressure within the conduit, compared with the steady state gas pressure solution using the Klug and Cashman (1996) law, for several permeability laws. (Mef): Mueller et al. (2005), others: Burgisser et al. (2017) (attached article), with σ_a/d_a varying from 0.1 to 10 and $N_m = 10^{13}\mathrm{m}^{-3}$. Red color indicates that gas pressure is higher than in the solution using the Klug and Cashman (1996) law, whereas blue indicates it is lower.

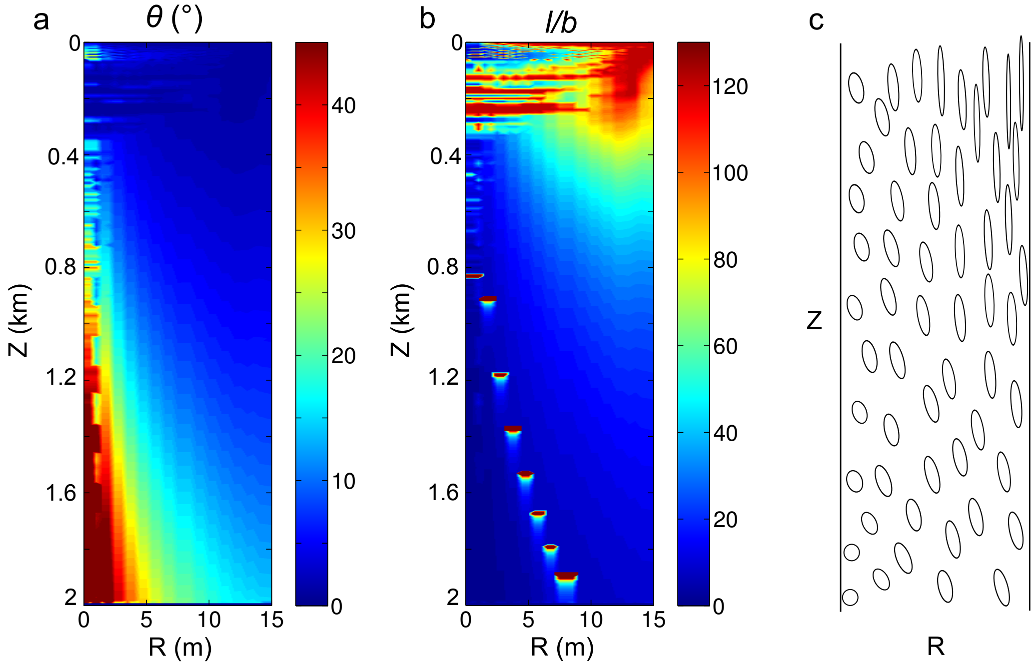

Figure 3.10: (a) Bubble orientation (θ) and (b) aspect ratio (l/b) evolution in the conduit. (c) is a Sketch of evolution of bubble deformation in the conduit to illustrate results presented in (a) and (b).

simple shearing is maximum.

We then apply these deformation parameters to obtain magma radial and vertical permeability as described in section 3.4.1.3 and use it to solve gas flow within the conduit. We here set a BND of 10^{14}m^{-3} and a BSD σ_a/d_a of 1, because the associated permeability is the closest to a Klug and Cashman (1996) law (section 3.4.2, fig. 3.6). Results show that the strong bubble deformation described earlier is associated with a very important difference in permeability between the parallel and orthogonal directions to bubble elongation. It reaches more than 4 orders of magnitude in most of the conduit, and results in a very large permeability anisotropy within the conduit (fig. 3.11).

Some strong, short scale variations in the l/b ratio and in permeability values are visible in fig. 3.10 and 3.11. They result from the second order derivation of the velocity solution from Collombet (2009), required for the calculation of Cd, and are probably linked with the discretisation order used for the velocity field calculation in this model. We therefore do not take into account these small scale variations in the results interpretation, and focus on global variations in the conduit.

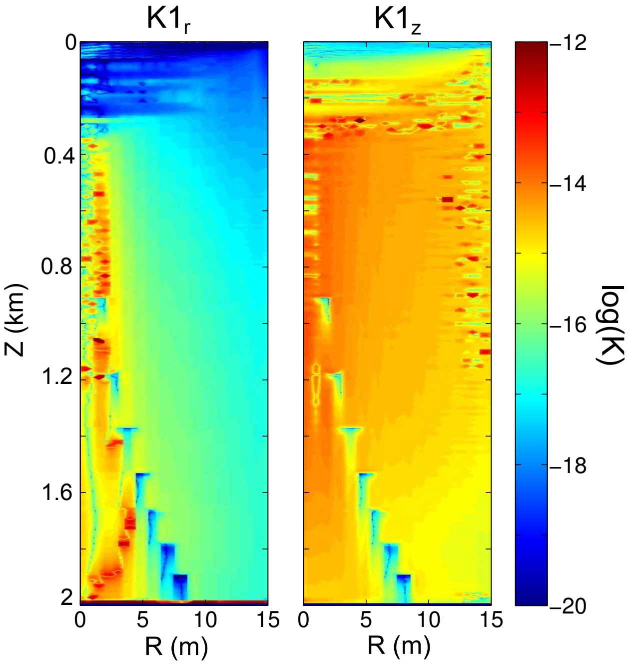

Figure 3.11: Radial ($k_{1|r}$) and Vertical ($k_{1|z}$) viscous permeability evolution within the conduit. Permeabilities are given in m^2 and represented using a logarithmic scale for more visibility.

3.5 Discussion

3.5.1 Influence of magma permeability on volcanic activity

Results obtained for a moderate, constant bubble deformation show that, depending on the BND and BSD spread, the evolution of permeability within the conduit varies significantly. These permeability variations are associated with changes in degassing conditions, which cause pressure changes that sometimes are even greater than those observed during dome growth (Chevalier et al., 2017) (a few tens of MPa). This provides evidence that the way permeability develops in the magma rising towards the surface is key to understand the eruptive regime and explosivity hazard.

Depending on the bubble nucleation and growth history in the magma rising towards the surface, the magma permeability, and then the efficiency of degassing varies a lot. A lower BND, together with a spread BSD, is associated with an efficient degassing, and may favour effusive eruptions, as long as the gas can be lost at the conduit walls. A high number of bubbles, however, would retard permeability development, and be associated with a less permeable bubble network. This would limit gas flow from the conduit center to the conduit edges, where it can be lost, therefore decreasing gas loss. This would trigger a relative increase in the magma gas content, thus making the volcanic activity to evolve towards larger amounts of gas within the magma, eventually leading to more explosive regimes. Integrating N_m and σ_a/d_a to conduit flow therefore looks important. These parameters cannot be deduced from the flow dynamics, however they both can be constrained from erupted samples analysis and studies on bubbles populations evolution in the magmas (e.g. Massol and Koyaguchi, 2005; Kedrinskiy, 2009; Giachetti et al., 2010).

The permeability law we presented does not take into account the influence of fractures in the magma, that would control permeability at low porosity (Kushnir et al., 2016). In addition, the relation between porosity and permeability is known to be hysteretic (Tuffen et al., 2003; Rust and Cashman, 2004). This also is not present in our permeability law, and would require more investigations.

3.5.2 Permeability anisotropy within the conduit

Considering bubble deformation calculated from the modelled flow conditions in the conduit, we get a huge permeability anisotropy (up to 4 orders of magnitude) in most of the upper conduit area. Such a permeability anisotropy seems exaggerated compared with permeability measurements made from pyroclastic samples, especially for effusive regimes (Wright et al., 2006; Klug et al., 2002; Degruyter et al., 2009; Rust and Cashman, 2004; Blower, 2001; Bouvet de Maisonneuve et al., 2009), that report permeability differences between the direction of bubble elongation and the orthogonal direction of up to 3 orders of magnitude in extreme cases. Our integration of bubble deformation within the permeability law is however based on a reduced dataset of 5 samples that had experienced deformation. The bubble aspect ratio in these samples does not exceed 6, which is small compared with aspect ratios present in our conduit flow model (l/b ranges up to 125). More experimental work would be needed to observe the influence of strong bubble deformation on permeability and adapt our permeability law to these extreme conditions.

In addition, the bubble deformation we observed in our samples was mainly caused by pure shear due to volumetric expansion along with decompression. In the conduit, however, deformation is likely mainly caused by simple shear, that involves bubble rotation and may enhance bubble coalescence. Several studies on permeability development in experimental samples have shown that simple shear can significantly decrease the percolation threshold when it reaches high amplitudes (e.g., Caricchi et al., 2011; Okumura et al., 2009, 2013). Further bubble coalescence due to simple shear may have a significant impact on permeability and may be associated with a less pronounced anisotropy than that we observed using the permeability law we developed.

Besides, we calculated bubble deformation using empirical laws calibrated for two-phase flow conditions (melt and bubbles). In the case of conduit flow, a significant amount of crystals is also present, and may affect bubble deformation and response to shear.

3.6 Conclusion

We used geometrical parameters to characterise the connected bubble network of experimental samples and better understand the development of permeability in silicic magmas during decompression. We were able to define a percolation threshold that depends on the BND and on the BSD. This percolation threshold expression succeeded in classifying a wide range of data from natural to experimental samples. Using this percolation threshold, we developed an expression for permeability that can be integrated into conduit flow models. The presence of anisotropic samples in our dataset also provided the opportunity to study the influence of bubble deformation on permeability, and integrate these observations into the permeability law. The permeability law we developed unifies a wide range of pre-existing empirical permeability-porosity relationships, and therefore improves degassing modelling in conduit flow models.

We integrated this permeability law into conduit flow models, in 1D and in 2D axisymmetry. The percolation threshold seems to have little influence on the results based on the 1D conduit flow model of Kozono and Koyaguchi (2009), modified after Degruyter et al. (2012). However, this model does not take into account gas loss at the conduit walls. The 2D conduit flow model, on the other hand, simulates gas loss both at the conduit walls and at the conduit top. Using this model, we were able to provide evidence that the percolation threshold and permeability law have an important influence on degassing conditions, by possibly limiting gas flow toward the conduit edges. A low permeability within the conduit is associated with a gas pressurization at the conduit top of a few tens of MPa, which is sufficient to trigger some explosive events.

The permeability law we proposed may however not be fully suitable for the range of bubble deformation observed within the conduit. It is indeed based on a few samples with limited bubble deformation, and, applied to real deformation in the conduit, results in permeability anisotropies that are huge compare with measurements for natural samples in effusive conditions. Some more investigations are needed to extend our observations to a wider range of samples, and discuss the influence of stronger bubble deformation on permeability.

Chapter 4

Interpretation of near field ground deformation recorded before the Merapi 2006 eruption

The island of Java was once crooked, and the gods had to fix this. They called a meeting and decided to move the Mount Jamurdipo, a massive mountain located on the southern coast at the island west end, to the center of Java, in order to ensure balance. Meanwhile, however, at the chosen location, two powerful smiths, Empu Rama and Empu Permadi, had set about forging a sacred kris. The gods warned them, but Empu Rama and Empu Permadi refused to leave. In anger, Gods buried them under Mount Jamurdipo, their spirit becoming the eternal guardians of the mountain. Their hearths turned into a crater, and Mount Jamurdipo, turned into a volcano, was renamed Mount Merapi, which literally means "the one making fire" in old Javanese. The legend has it that when the volcano is about to erupt, the guardians make an appearance in the form of a cloud above the summit as a warning sign.

Figure 4.1: During the Labuhan ceremony, which is believed to help preventing the balance of nature and is celebrated every anniversary of the Sultan's coronation, Javanese people bring offerings to the South sea, Gunung Merapi and Gunung Lawu. (credit Tarko Sudiarno)

Contents

4.1 Introduction

Numerical modelling of conduit flow conditions and of degassing helps understanding how magma flow, and consequently the eruptive regime evolve from effusive to more explosive conditions. In the precedent chapter, we identified parameters that control gas loss in the conduit, thus controlling the amount of gas present in the magma extruding at the volcanic vent. Although such numerical models are extremely important to better understand processes happening in the conduit and anticipating the eruptive regime evolution trend during an eruption, they are not sufficient, on their own, to forecast a precise event. Processes happening in the nature are extremely complex and multiple. Numerical models, although they help interpreting the observed evolution, need constant feedback from observation data to be adapted to the real events evolutions.

The magma gas content is a key parameter for understanding the eruptive regime evolution at andesitic volcanoes. However we cannot have a direct access to this gas content within the conduit. The analysis of erupted samples reveals precious informations on past conditions within the conduit (e.g. Erdmann et al., 2014, 2016; Drignon et al., 2016), but collecting them during an on–going eruption is almost impossible for safety reasons. In addition, they may not be representative for current conditions within the conduit. The possibilities for monitoring flow conditions and degassing therefore depend on their translation through other observable parameters. The magma gas content evolves due to the importance of gas loss. It may therefore be possible to track the evolution of degassing conditions and then on the magma gas content from gas emissions measurements at the volcanic vent (Watson et al., 2000; Edmonds et al., 2003; Allard, 2014). Besides, the amount of gas present within the magma impacts on the magma viscosity and density, thus affecting the applied normal and shear stress at the conduit walls. This could be visible in ground deformation data (Albino et al., 2011). Eventually, the evolution of flow conditions can be associated with some seismic activity (e.g. Beauducel and Cornet, 2000).

Ground deformation has been observed at volcanoes for a long time and has been proven to be tightly linked with volcanic activity. For example, inflation and deflation trends have been observed to be associated with eruptions onsets. It also provided useful information on the volcano plumbing systems. More recently, deformation data recorded in the near field at Merapi and Montserrat appeared to be linked with conditions in the conduit (Beauducel and Cornet, 2000; Albino et al., 2011). Conduit pressurisation was first invoked to explain the observed deformation. Later, the shear stress applied by magma flow at the conduit walls was proven to be responsible for part of the deformation observed in the near field at Merapi during a dome–forming eruption (Beauducel and Cornet, 2000). The ascent rate deduced from these models was well correlated with the amount of multiphasic seismic events, which is thought to be linked with the importance of magma supply to the forming dome. The models from Beauducel and Cornet (2000), however, used simplified shear stress and pressure conditions, that are not related to realistic magma flow conditions. More recently, Albino et al. (2011), studied ground deformation associated with the formation of a plug within a volcanic conduit, using a conduit flow model coupled with ground deformation. They provided evidence that such flow conditions account for the deformation observed in the near field during effusive eruptions at the Soufrière Hills Volcano (Montserrat). Ground deformation recorded in the near field at andesitic volcanoes could therefore provide clues on conduit flow conditions.

The DOMERAPI ANR, that supported part of this Ph.D., aims at improving the instrumentation and data acquisition at Merapi. The objective is to better understand processes happening in the deep plumbing systems (magma reservoir), shallow conduit and superficial dome, and in the hydrothermal system. Among silicic volcanoes, the Merapi is characterised by a hot supplying magma of basaltic to andesitic composition, that is rich in CO_2 (Borosiva et al., 2013; Troll et al., 2013b, e.g.), and has a high crystallinity (about 70% of the erupted material). Its activity mainly consist in dome growth episodes associated with passive degassing. The effusive extrusion rate varies between low and very high velocities (up to $25\text{m}^3\text{s}^{-1}$) (Newhall et al., 2000; Voight and Elsworth, 2000; Pallister et al., 2013). These dome growth episodes are punctuated with dome collapses that generate pyroclastic flows of varying importance, and less frequently with violent explosive episodes. My Ph.D. particularly aims at better understanding degassing and magma flow evolution in the conduit, and at linking these conditions with observed ground deformation. In this scope, we here interpret the ground deformation observed in the near field at Merapi before the 2006 eruption using conduit flow models.

Several kinematic GNSS measurement campaigns were carried out at the Merapi summit between 1993 and 2006 (Beauducel and Cornet, 2000; Beauducel et al., 2006) using a dense benchmark network (about 25m spacing between the benchmarks). A major part of these data have not been analysed yet. The density of the benchmark network however provides a unique opportunity to study the expression of conduit conditions in near field ground deformation, and evaluate its usefulness for monitoring the eruptive regime evolution. In this chapter, we first introduce some background knowledge on the Merapi formation, activity and monitoring. We then focus on the interpretation of ground deformation data recorded a few days before the 2006 eruption onset. We use a 3D numerical model that couples simple flow conditions with elastic ground deformation in the Merapi edifice. The flow conditions used here account for the formation of a degassed plug at the top of the conduit as proposed by Albino et al. (2011). Results provide evidence that conduit flow modelling is key for understanding near field ground deformation at Merapi. However, the complexity of the summit geology and rheology, together with the sparsity of the data, make it complex to use ground deformation for monitoring flow conditions evolution in this precise case.

4.2 The Merapi volcano

4.2.1 The Merapi, a killer volcano

Gunung Merapi is located in central Java (Indonesia)(fig. 4.2). It is currently considered as one of the most active and dangerous volcanoes worldwide, and the most dangerous among the 129 Indonesian Volcanoes, according to the Volcanological Survey of Indonesia (VSI). Merapi was designated as one of the *Decade Volcanoes* by the International Association of Volcanology and Chemistry of the Earth's Interior (IAVCEI) in 1990. Its activity consists in dome growth episodes and collapses that generate devastating pyroclastic flows, and less frequently in more violent explosions (Voight 2000, Newhall2000). During the rainy season, frequent lahars re–mobilise pyroclastic deposits, causing additional damages (Lavigne, 2000, De Bélizat, 2013). Merapi activity has caused more than 1300 fatalities over the last century, and the destruction of many villages and infrastructures. It is considered as one of the world top ten deadly volcanoes (Witham, 2005).

Merapi is located in a very densely populated area, about 25km northern from the major city of Yogyakarta ($\approx$ 4M inhabitants). Despite the threat of pyroclastic surges and lahars, the local population continues to increase, with thousands of people living on the Merapi's flanks. Being able to anticipate the Merapi activity evolution is therefore of first concern. The early warning system at Merapi, and at all the Indonesian volcanoes, comprises four alert levels, based on instrumental and visual observations: Aktif (normal), Waspada (unusual activity, imminent eruption expected), Siaga (increased activity, eruption expected within two weeks), and Awas (gas and ash emissions, main eruption expected within 24h). The alert level is declared to the population through the National Agency for Disaster Management (BNBP) and the local government. Together with the Indonesian Center of Volcanology and Geological Hazard Mitigation (CVGHM), they give recommendations and evacuation orders.

In 2010, the alert level was raised to Waspada on September 20, and to Siaga on October 21. As seismicity and deformation raised unprecedented levels, the alert level was raised to Awas on October 25, and evacuation was called for the several tens of thousands of people living within 10km around the summit. The evacuation zone was then extended successively to 15 and 20km on the 3 and 4 November (Surono et al., 2012). Pyroclastic flows on November 4 reached up to 17km from the summit.

Although the 2010 eruption caused 367 fatalities, about 10 000 to 20 000 lives were saved due to prompt evacuation. Despite this success, forecasting Merapi activity remains extremely complex and uncertain, and relies on the interpretation of instrumental and visual observations. The population safety around the Merapi volcano does not only depends on the correct interpretation of activity evolution. The efficiency of the evacuation plan, as well as the population awareness and trust in the CVGHM and government previsions are also of first importance. During the 2010 eruption, most of the 367 fatalities were from a village where evacuation had not taken place yet, and 35 others had refused to evacuate their own villages. Besides, a sounding from Mei et al. (2013) revealed that 50 to 70% of the displaced persons had returned into the danger zone during the crisis, despite evacuation orders.

Based on historical records of the Merapi activity, on recent observations and on magma chemistry, Gertisser and Keller (2003) argued that Merapi is currently at the beginning of a major phase of increased activity. Being able to anticipate eruptive activity evolution and give robust estimates to the population is then of increasing importance.

4.2.2 Merapi formation and history

Mount Merapi is a 2930m high andesitic stratovolcano located in center Java, Indonesia (fig. 4.2). It is part of the Sunda volcanic arc, which extends from northern Sumatra to the Banda sea and results from the northward subduction of the Indo–Australian plate beneath the Eurasian plate, at a rate of about 6.5 to 7 cm/yr (Hamilton, 1979; Jarrard, 1986; De Mets et al., 1990). Merapi belongs to a group of four volcanoes (Ungaragan, Telemojo, Merbabu and Merapi) aligned NE (fig. 4.3), of which it is the youngest and most active. It rises on an immature arc crust about 25km thick, whose upper part is composed of a thick sequence of cretaceous to tertiary limestones and marls (van Bemmelen, 1949) that can be found as thermally metamorphosed xenoliths in recent lavas (Camus et al., 2000; Troll et al., 2013b; Chadwick et al., 2007).

The Merapi geological evolution has been widely studied since the 1990's, when the Merapi was designated as one of the 16 Decade Volcanoes (Berthommier et al.,

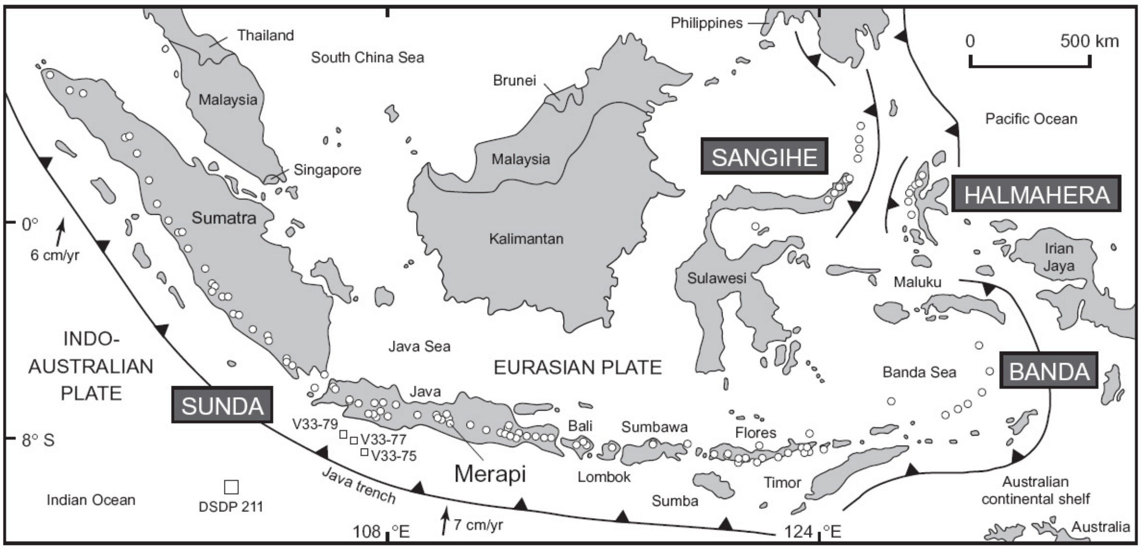

Figure 4.2: Mount Merapi is located in central Java, close to the Sunda arc. (after Gertisser and Keller, 2003)

Figure 4.3: View of Mount Merapi (forefront) and Merbabu, from the SE. Mount Ungaragan is visible in the right background. On the left G.Slamet, G. Sumbing and G. Sindoro are also visible. (credit Anak Tangga)

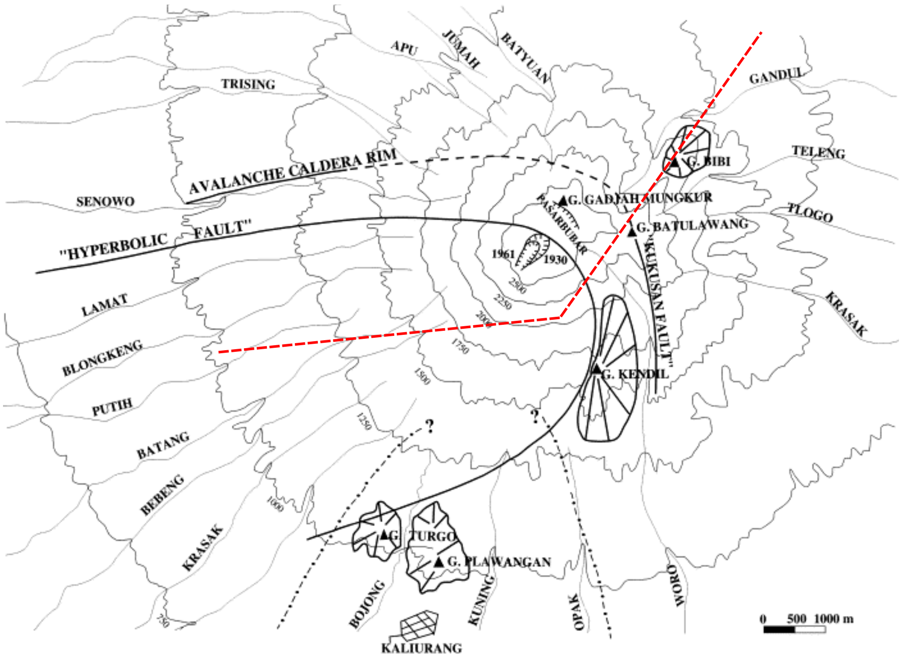

Figure 4.4: Major structures at Merapi, from Camus et al. (2000). The red dashed line indicates the orientation of the section presented in fig.4.5

1990; Camus et al., 2000; Newhall et al., 2000; Gertisser et al., 2012). Gertisser et al. (2012) provided new volcanoclastic samples datation, constraining the different growth stages of Merapi. A few proto–Merapi volcanic structures existed at the north–east of the actual Merapi: Gunung Bibi (”Gunung”, hereafter abbreviated G., is an Indonesian word meaning ”Mount”), which was dated to 109 +/- 60ka, and, at the south–west, G. Turgo and G. Plawagan that were dated to 138 +/- 3ka and 135+/-3ka respectively (fig. 4.4) (Gertisser et al., 2012). G. Merapi started to grow about 30–40 thousands years ago, building an edifice of basaltic andesite lava flows intercalated with pyroclastic deposits. A major, St. Helens–like collapse occurred about 4.8+/- 1.6ka (Gertisser et al., 2012) ago and triggered the explosion of a shallow cryptodome. This event marked the end of the old–Merapi. The western part of the volcano was completely destroyed, leaving a horse–shoe shaped crater in which the new–Merapi started to grow (fig. 4.5). The new–Merapi activity was marked by a compositional change about 2 thousand years ago. Since then, Merapi activity was almost continuous, evolving toward the actual typical Merapi activity. The most recent (three past centuries) domes and lava flows formed within the Pasarbubar crater (Camus et al., 2000).

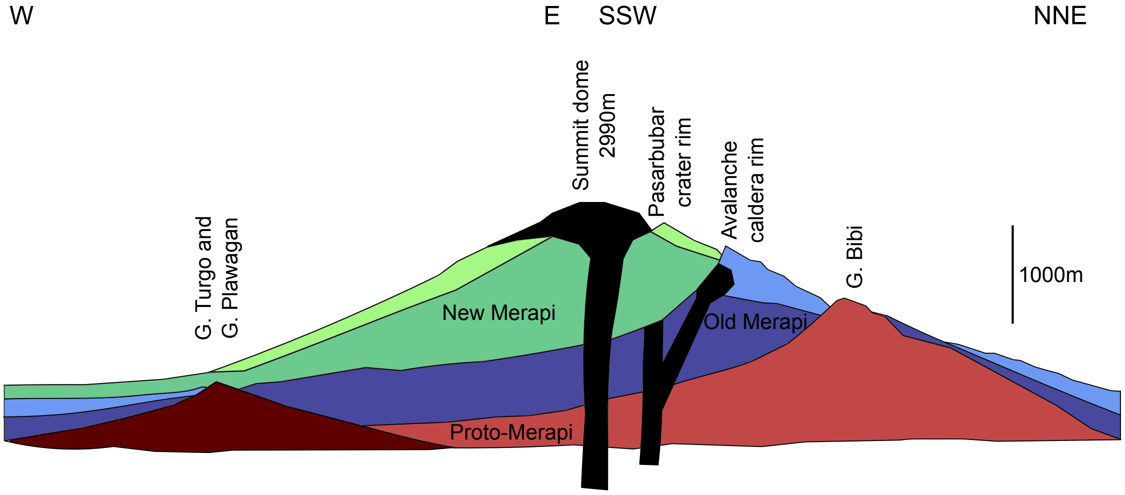

Figure 4.5: Sketch of the actual Merapi global structure, from Camus et al. (2000), modified after Gertisser et al. (2012)

4.2.3 Current activity

Over the past three centuries, the Merapi activity mainly consisted in endogenous dome growth (fig. 4.6a) (extrusion rate ranging from 7000 to 300000 m^3/day (Newhall and Melson, 1983; Voight et al., 2000)). It is punctuated with dome collapses that generate pyroclastic flows (Volcanic Explosivity Index (VEI) 2), known as the "Merapi–type nuées ardentes" (fig. 4.6b) (e.g. 2001–2002, 2006), that are mainly directed toward the southern and western flanks of the volcano. More exceptionally, explosions of relatively high intensity (VEI 3–4) (fig. 4.6c) cause the dome destruction and generate major pyroclastic flows that can reach up to 17km from the summit (e.g. 1872, 2010). These periods of increased volcanic activity alternate with quiescence phases, every few years (Voight et al., 2000; Newhall et al., 2000). During the rainy season, lahars are frequent, and transport primary pyroclastic deposits over distances of a few kilometers.

The actual Merapi summit topography is marked, at the north and east, by the 1961 and 1930 eruptions crater rims (fig. 4.4). Domes forming at Merapi have very steep slopes (up to 60°). This results in gravitational instabilities, generating regularly small rockfalls, named guguran in Indonesian, that generally reach no more than 1–2km from the summit. The number of gugurans is directly related to dome growth and magma extrusion rate (Ratdomopurbo and Poupinet, 2000). Since the Merapi 1961 crater floor slopes 35° to the SW, domes generally spread in that direction, and have an ovoid shape.

Figure 4.6: Photographs of Mount Merapi taken during several eruptive phases. (a) Dome growth, 2006, view from the south. Note also the presence of a little guguran rockfall (incandescent strip). (AP photo) (b) Pyroclastic surges associated with dome collapse in June 2006 (AP photo). (c) 2010 vulcanian explosion (credit Irwin Fedriansyah).

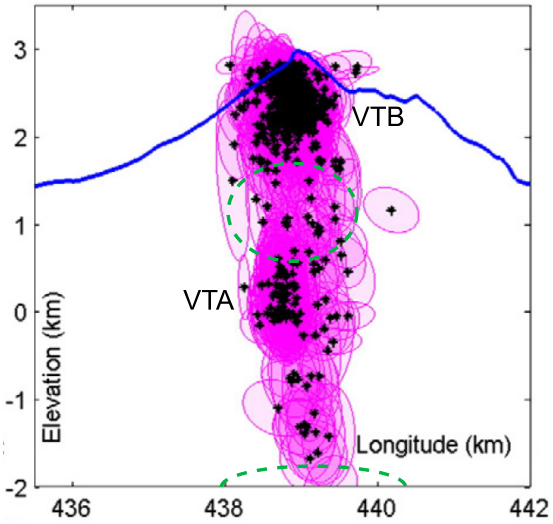

Figure 4.7: Earthquakes hypocenter retrieval for the 2010 eruption. (modified from Budi-Santoso et al. (2013)

4.2.4 Understanding the volcanic system to mitigate risks

The accuracy of the previsions for future eruptions scenario and intensity at Merapi relies not only on a good interpretation of instrumental and visual monitoring, but also on our well understanding of the Merapi volcanic plumbing system. A variety of geophysical, geochemical and petrological methods exist and have been used to constrain the Merapi internal structure and the magmatic processes occurring in there.

4.2.4.1 Geophysical imagery

Geophysical methods such as seismic tomography, gravity, electromagnetism and ground deformation are of great interest for identifying the main bodies composing the volcanic system. Ratdomopurbo and Poupinet (1995, 2000), identified the presence of one superficial reservoir, at a depth from 1.5 to 2.5km beneath the summit, and another shallow reservoir, at depths greater then 5km, from Volcano Tectonic (VT) earthquakes hypocenters retrieval. VT volcanoes are indeed thought to be associated with rock failure caused by magma propagation between the reservoirs and the surface. Their presence therefore reveals pathways for magma where no reservoir is present. The same observations were renewed by Budi-Santoso et al. (2013) (fig. 4.7) from earthquakes that occurred during the 2010 eruption. A pressure source at about 9km under the Merapi summit was also identified by Beauducel and Cornet (1999) from ground displacement and tilt observations.

Such shallow reservoirs are not visible from gravimetric and electromagnetic

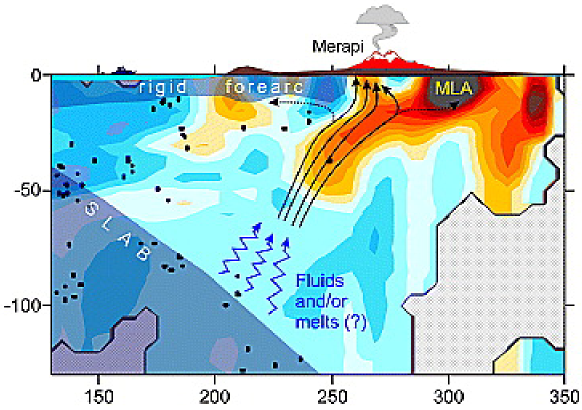

Figure 4.8: Seismic tomography has evidenced the presence of a strong velocity anomaly aside Mount Merapi, diving eastwards, probably related to fluid extraction from the subducted Indo–Australian slab. The background in this figure represents the S velocity anomaly. Figure from Koulakov et al. (2007).

data (Tiede et al., 2007; Müller et al., 2002; Commer et al., 2006; Byrdina et al., 2017), from which were only identified anomalies around the conduit and in the volcanic edifice. These anomalies were interpreted as resulting from altered rocks and from the possible presence of an hydrothermal system. Recent results from seismic tomography using ambient noise correlation, recorded within the MERAMEX project, however provided evidence for the possible presence of a shallow reservoir in the south–west part of the Merapi edifice, extending down to a depth of 8km (Koulakov et al., 2016). In the scope of the DOMERAPI project, a more localised seismic network was installed around Merapi and Merbabu, aiming at imaging the volcanic system with more precision. About 45 Sismob seismic stations were installed from September 2013 to April 2015. Data are currently being analysed using a combination of body wave analysis and ambient noise correlation (Abdullah et al., 2017).

At greater scales, seismic tomography revealed the presence of a strong negative velocity anomaly beneath the Merapi (fig. 4.8), that should be associated with the presence of at least 15–25vol% of melt (Wagner et al., 2007; Koulakov et al., 2007; Luehr et al., 2013; Koulakov et al., 2016). This anomaly is sloping to the east, towards the Indo–Australian slab, and is interpreted as the result of fluid extraction from the subducted plate. Another, separated, large low velocity anomaly has been observed in the center of Java (Koulakov et al., 2016), that may be caused by the presence of a large magmatic reservoir feeding Merapi and Lawu volcanoes.

4.2.4.2 Constraints from petrology

Erupted lavas bring to the surface a lot of information on the magma history. In particular, mineral assemblages and composition are powerful tools to retrieve the pressure and temperature conditions present when crystallisation occurred. Phase equilibrium and mineral barometry, (Chadwick et al., 2013; Costa et al., 2013; Nadeau et al., 2013; Erdmann et al., 2014, 2016), associated with petrological observations (Troll et al., 2013b; Chadwick et al., 2007), evidenced the presence of a shallow main storage system, about 5–18km beneath the Merapi summit (fig. 4.9), in agreement with seismic and ground deformation observations. Moreover, the stability of the crystal size distribution within products erupted during the last centuries (Innocenti et al., 2013b; van der Zwan et al., 2013), associated with geochemical considerations (Preece et al., 2013), proved that the Merapi magmatic system is in quasi–steady state.

The magma present in this large magmatic system is of basaltic–andesitic composition (52–57wt% SiO2). The observation of basaltic inclusions in erupted lavas, as well as geochemical constraints on mineral crystallisation suggest it is supplied with a hotter, more basaltic magma (Chadwick et al., 2007; Borosiva et al., 2013; Troll et al., 2013b). This supplying material has however never erupted, which evidences the important volume of the Merapi magma storage system. The importance of mingling and mixing textures observed in erupted samples suggest that magma experiences crystal fractionation, with recurrent remobilisation of the crystal rich mushes. These mixing textures also suggest that the main storage system could possibly be composed of a network of magma pockets (Chadwick et al., 2007; Borosiva et al., 2013; Troll et al., 2013b) (fig. 4.9a), which would give a satisfying explanation for its poor visibility on geophysical tomography data (Wagner et al., 2007; Koulakov et al., 2007; Luehr et al., 2013).

The presence of thermally metamorphosed, calcareous xenolithic inclusions in erupted lavas also suggest a significant assimilation of shallow crustal limestones in the storage area (Chadwick et al., 2007; Borosiva et al., 2013; Troll et al., 2013b). The assimilation of these calcareous sediments would be responsible of a substantial increase in the magma CO_2 content, which could trigger explosions. Geochemical analyses of fumarolic gas in the volcano crater confirmed the important role of assimilation in the magma CO_2 budget (Allard, 1983; Deegan et al., 2010, 2011; Troll et al., 2012, 2013a; Nadeau et al., 2013). Drignon et al. (2016) however recently questioned the importance of the assimilation implication in volcanic activity. They provide evidence, in the specific case of the 2010 explosive event, that the eruption

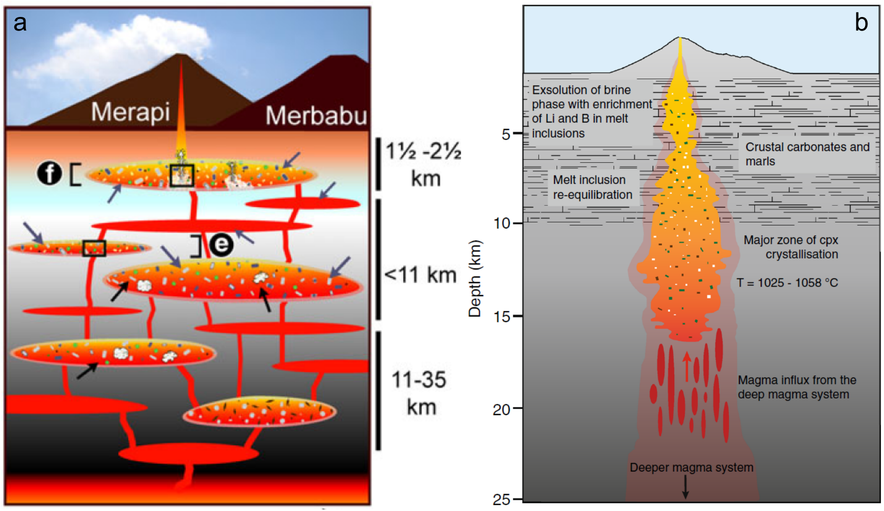

Figure 4.9: Examples of models of the storage system beneath Merapi deduced from petrological and geochemical constraints. (a) Multiple pockets reservoir from van der Zwan et al. (2013). (b) Single reservoir from Preece et al. (2014)

may not have been triggered by CO_2 assimilation, but rather by the supply of hot basaltic volatile–rich magma to the storage reservoir.

4.2.5 Monitoring volcanic activity

In association with a good understanding of the processes occurring in the volcanic system, the interpretation of instrumental and visual monitoring observations can help anticipating the volcanic activity.

4.2.5.1 Visual observation

Visual observation of the volcano summit is probably the most ancient monitoring method. For ages, the presence of clouds at the Merapi summit prior to eruptions was already considered as a warning signal, as the Merapi mythology testifies. The observation of a plume of ash and vapour is still a criteria for raising the alert to its maximum level. Lava flows and dome formation are other usual signs that a new eruption period has started (e.g. Ratdomopurbo et al., 2013). After the 2010 eruption, two visual observation stations were installed within the scope of the DOMERAPI project. These two stations capture pictures, but also visual and IR videos of the volcano summit. Using these observations may help understanding pyroclastic flows initiation during future events. Besides, the video cameras have a stereoscopic position, allowing to retrieve deformation and displacements at the dome surface (Karim Kelfoun, personal communication). These information may be very helpful to understand and prevent future dome destabilisation and collapse (Walter et al., 2013). Eventually, during an eruption, the evolution of the volcanic activity can be monitored using satellite imaging. The ash cloud evolution, as well as changes at the Merapi summit can be monitored using visual images (Pallister et al., 2013; Carr et al., 2016). Besides, satellite radar imagery helps monitoring the emplacement of lava deposits, as well as dome growth (Pallister et al., 2013; Solikhin et al., 2015).

4.2.5.2 Gas

The magma gas content is a controlling parameter for the magma explosivity and the eruptive regime. A way to monitor the evolution of degassing conditions at depth and to get clues on the magma gas content is to observe gas releases at the volcano summit. Both the amount of gas released and its composition can reveal changes in the magma conditions at depth. Gas release can be monitored using satellites measurements (Clarisse et al., 2008; Carn et al., 2008; Prata and Bernardo, 2007) and remote measurements from nearby stations (E.G. Differential Optical Absorption Spectroscopy (DOAS) (Galle et al., 2003)).

DOMERAPI, in collaboration with the DCO (Deep Carbon Observatory) financed the observation of gas release at Merapi after the 2010 eruption. A first measurement campaign was carried on in 2014, in order to characterise gas releases at the Merapi summit from a combination of Open–Path Fourier Transform InfraRed (OP–FTIR) spectrometry, MultiGas analysis, UV video observation and DOAS. Results from this first campaing motivated in September 2015 the installation, of a MultiGas permanent station at the Merapi summit. It measures gas emissions and composition (ratios between H_2O, CO_2, SO_2, H_2S and H_2) during half an hour, four times a day. These data allow monitoring of deep degassing conditions (Patrick Allard, personal communication). Two DOAS stations were also installed in summer 2015 in nearby observation posts.

4.2.5.3 Seismicity

Seismicity has been used for monitoring volcanic activity at Merapi since 1924, when a first Weichert mechanical seismograph was installed. An increase in seismic activity was recorded on this seismograph before the major 1930 explosion (Van Padang, 1933). Later, a network of short period seismographs was installed, in 1982, by the VSI, in collaboration with the United States Geological Survey (USGS). In addition to this early network, digital recording systems have been installed since 1991 (Ratdomopurbo and Poupinet, 2000).

A variety of seismic signals are recorded at Merapi volcano and have been related to different processes possibly happening into the volcanic system. Since 1984, they are classified as follows (Ratdomopurbo and Poupinet, 2000):

- Volcano Tectonic (VT) events, of type A (deep) and B (shallow). Those events are microtectonic earthquakes that are supposedly associated with the injection of magma in the upper part of the volcano, and with high gas pressure regimes. A large number of VTA and VTB preceded the 2010 eruption (Budi-Santoso et al., 2013).
- Multiphase (MP) events. They are associated with dome growth and with the supply of magma and gas to the dome. Their hypocenters are very shallow, beneath the dome.
- Rockfalls (*Guguran* in Indonesian) are caused by small avalanches of rock from the dome and summit area. They are correlated with Multiphase events as they also depend of the importance of dome growth.
- Low frequency events and tremor. They are associated with fluid resonance within the plumbing system.

An increase of the seismic activity is often observed before eruptions (Van Padang, 1933; Ratdomopurbo et al., 2013; Budi-Santoso et al., 2013), which helps determining when to rise the alert level. From 2013, DOMERAPI financed the installation of 6 seismic antennas as well as 3 stations that record continuously the seismic activity.

4.2.5.4 Ground deformation

The volcanic activity is also associated with ground deformation, which may provide useful informations on processes happening in the volcanic edifice. At Merapi, the ground deformation is monitored using Electronic Distance Measurement sensors (EDM), Tiltmeters, and Global Navigation Satellite System (GNSS) measurements. An EDM network was installed at Merapi since the early 1980s by the VSI, in collaboration with the United States Geological Survey (USGS) and the Merapi Volcano Observatory (MVO) (Siswowidjoyo et al., 1985). It was reinforced in 1988 (Voight, 1988; Voight et al., 1989). EDM consist in determining the distance between a reference point (observatory) and a fixed prism, located at the volcano summit.

Summit deformation can therefore be observed from remote observatories, with a relative precision on measured distance of 10^{-6}. At Merapi, the EDM observatories are 7 to 4km from the summit (slope distance), allowing distance measurements with a precision of 7 to 4mm. They are still used today to monitor the summit deformation (Young et al., 2000; Ratdomopurbo et al., 2013; Surono et al., 2012).

The VSI also installed since 1988 several tiltmeters, both close to the summit and on the volcano flanks. This first network was reinforced several times (Beauducel and Cornet, 1999; Young et al., 2000; Rebscher et al., 2000). After the 2010 eruption, the Indonesian team installed 5 permanent high–precision tiltmeters, in 2011. This new network was completed in 2013–2014 with three more high–precision tiltmeters, installed in the framework of the DOMERAPI project. Tilt measurements consist in monitoring volcano deformation from ground slope evolution. High–precision tiltmeters can detect inflations and deflations of the volcano with a precision up to 10^{-8}rad. This precision is however extremely dependent on the installation and is limited by the ambient noise, such as daily thermal dilatation and contraction.

GNSS measurements have been widely used at Merapi since the 1990s. This method gives the real time position of a GNSS receiver with a precision of a few meters, with the advantage that it is not bothered with clouds and rain (unlike EDM). At Merapi volcano, in order to increase precision, a set of at least two receivers is used simultaneously, providing a precision of about 2 and 6 mm for horizontal and vertical positions, respectively (Botton et al., 1997). GNSS permanent stations have been installed and used since 1993 (Beauducel and Cornet, 1999; Rebscher et al., 2000). This network is sensitive to ground deformation caused by deep sources. A shallow reservoir, at a depth of about 9km, was identified from these data Beauducel and Cornet (1999). At the volcano summit, kinetic GNSS measurements at benchmarked positions have been done from time to time during field campaigns (Beauducel and Cornet, 2000; Beauducel et al., 2006). After the 2010 eruption, three permanent GNSS stations were installed by the Indonesian and Japanese teams, in addition with a reference station at the Yogyakarta observatory (BPPTK). 5 more permanent stations have been installed with DOMERAPI.

In the near field, EDM measurements from nearby observatories, together with GNSS and inclinometry measurements revealed inflations occurring prior to the Merapi eruptions, and followed by deflations after the eruption started (Ratdomopurbo et al., 2013; Surono et al., 2012). More recently, pressure and shear stress conditions in the conduit were proven to be responsible for an important part of the deformation observed close to the summit (Beauducel and Cornet, 2000). The deformation caused by magmatic activity is however distorted by fractures and faults present at the Merapi summit, as evidenced by (Beauducel et al., 2006), and by the summit rheology inhomogeneity (Young et al., 2000).

4.2.5.5 WEBOBS DOMERAPI

The DOMERAPI project has helped funding and installing numerous stations for seismic, geodetic, visual and geochemical measurements. All the data recorded by these stations are assembled on the WEBOBS website. They are available continuously to the DOMERAPI collaborators, with informations on the stations location, installation and maintenance.

4.3 Case study : summit deformation prior to the 2006 dome growth

In the following sections, we focus on the ground deformation observed from kinematic GNSS measurements prior to the 2006 eruption. During this period, Merapi activity progressively increased, and was associated with significant displacements in the near field. We use 3D finite element models to retrieve this ground deformation, considering either point source or conduit sources. In particular, we estimate the potential for conduit flow models, from which depend shear stress and pressure conditions at the edges of the conduit, to account for the deformation observed at the summit of Merapi volcano.

4.3.1 Data collection and treatment

GNSS positions for a set of benchmarks were collected by François Beauducel and by the MVO team, during several field campaigns between October 2002, just after the end of the 2001–2002 eruption, and March 2006, a few days after the seismic activity started to increase prior to the Merapi 2006 eruption (table 4.1). All the benchmarks were installed on the northern and eastern parts of the crater rim (fig. 4.10). A few of them are part of the geodetic network installed in 1988 by the VSI and USGS, for EDM measurements (Voight, 1988), and 50 were added to this previous network in 1997, in order to improve kinematic GNSS displacement monitoring at the Merapi summit (Beauducel et al., 2006). No GNSS position measurement was done on the southern and western parts of the summit, because of the steep topography and the dome activity.

Date	Nb of points	eastern RMSE	northern RMSE	vertical RMSE	Merapi activity
20/10/2002	50	0.0095	0.0078	0.0040	End of 2001–2002 eruption
01/08/2003	35	0.0274	0.0242	0.0019	
08/08/2004	43	0.0980	0.0781	0.0117	
16/12/2004	42	2.1931	2.0778	0.1159	
22/06/2005	50	0.0340	0.0318	0.0024	
13/07/2005	50	0.0508	0.0472	0.0044	First seismic precursors
11/09/2005	54	0.3613	0.2909	0.0614	
28/03/2006	48	0.1302	0.1352	0.0100	Activity acceleration

Table 4.1: Field campaigns for GNSS position measurement at the Merapi summit from 2002 to 2006. The eastern, northern and vertical RMSE (m) are the mean Root Mean Square Errors (RMSE) on position measurement at all measured points, for the east north and vertical position coordinates (UTM-49), respectively.

In order to optimize the time needed for measuring GNSS positions, a kinematic measurement method was used (static measurements require a 2 to 6 hour record for each baseline (Beauducel and Cornet, 1999)). Kinematic measurements combine one static receiver that stays at the reference station, recording at a 1s sampling rate. A second receiver is moved along the benchmarks, describing a loop that ends at the starting point (fig. 4.11 and 4.12). This receiver records at the same 1s sampling rate, and the trajectory is repeated for redundancy. Benchmarks positions calculated from kinematic measurements yield errors of about 5cm. In addition, rapid–static GNSS measurements are done for selected points that form a triangle, during 15 min. They give more reliable baselines, with errors on positioning of about 1cm. The station LUL is used as the reference because of its stability during the observed period 1993–1997, and because of its central position in the benchmarks network (Beauducel et al., 2006)(fig. 4.10). The whole GNSS measurement method is fully described in Beauducel et al. (2006).

Final benchmarks GNSS positions, and corresponding Root Mean Square Errors (RMSE), are retrieved by processing the rapid–static baselines and chronological kinematic baselines (i.e. baselines between two benchmarks for which positions were measured consecutively) (fig. 4.11b). The position of the reference station is fixed. Rapid–static baselines are more reliable than chronological ones and then control the network adjustment (fig. 4.11). More details on the solving system are available in Beauducel et al. (2006). The global RMSE uncertainties on positioning are about 0.85cm, with a lower vertical (0.4cm) than horizontal (1.2cm) uncertainty. The moving receiver position is indeed acquired with a manually stabilized antenna (fig. 4.12), that may oscillate horizontally during acquisition, in the case of windy conditions. Displacements are finally calculated by comparing two measurement sessions.

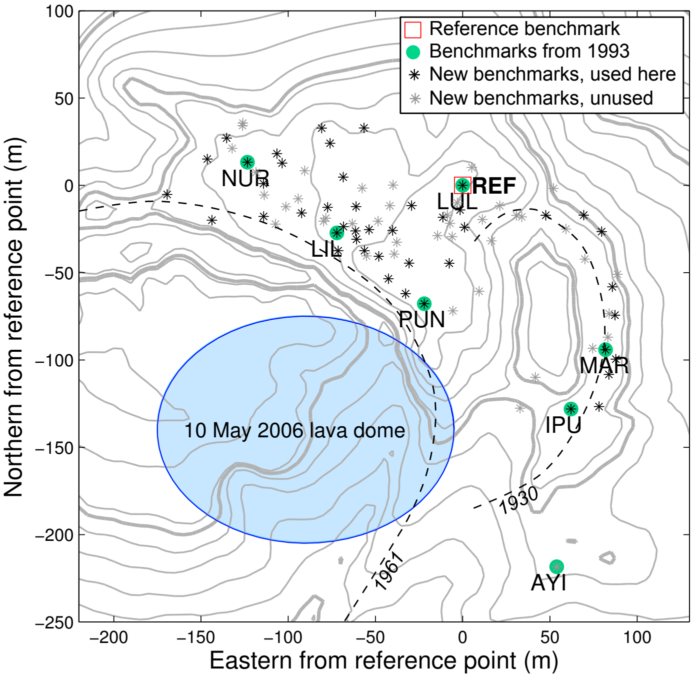

Figure 4.10: Location of the benchmarks. The red square indicates the location of the reference benchmark, LUL, while green circles mark the position of the old EDM benchmarks, and stars mark the position of benchmarks installed after 1997. Black stars are the benchmarks that were used for displacement measurement between July 2005 and March 2006. The blue ellipse indicates the emplacement of the lava dome observed on May 10 (fig.4.14). The topography dates back to 1993.

The precision on GNSS positions is insured by (i) the three rapid–static baselines, that form a closed triangle, (ii) the repetition of the moving receiver trajectory, and (iii) the fact that this trajectory is a closed loop. Because of hard meteorological conditions or increased alert level, the entire procedure may not have been respected for each campaign, leading sometimes to much higher errors on positions (e.g. December 2004, September 2005 see table 4.1).

4.3.2 Deformation at the Merapi summit before the 2006 eruption

4.3.2.1 Summit morphology after the 2001–2002 eruption

The Merapi summit morphology has remained relatively similar over the last decades. Domes build up inside the 1961 crater. They are associated with lava flows and rockfalls directed towards the South and West directions. Collapse of these lava domes and small vulcanian explosions generate pyroclastic surges, also directed SW. This activity results in malleable deposits that pile up on the western and southern flanks of the volcano and induce changes in the topography there and around the dome.

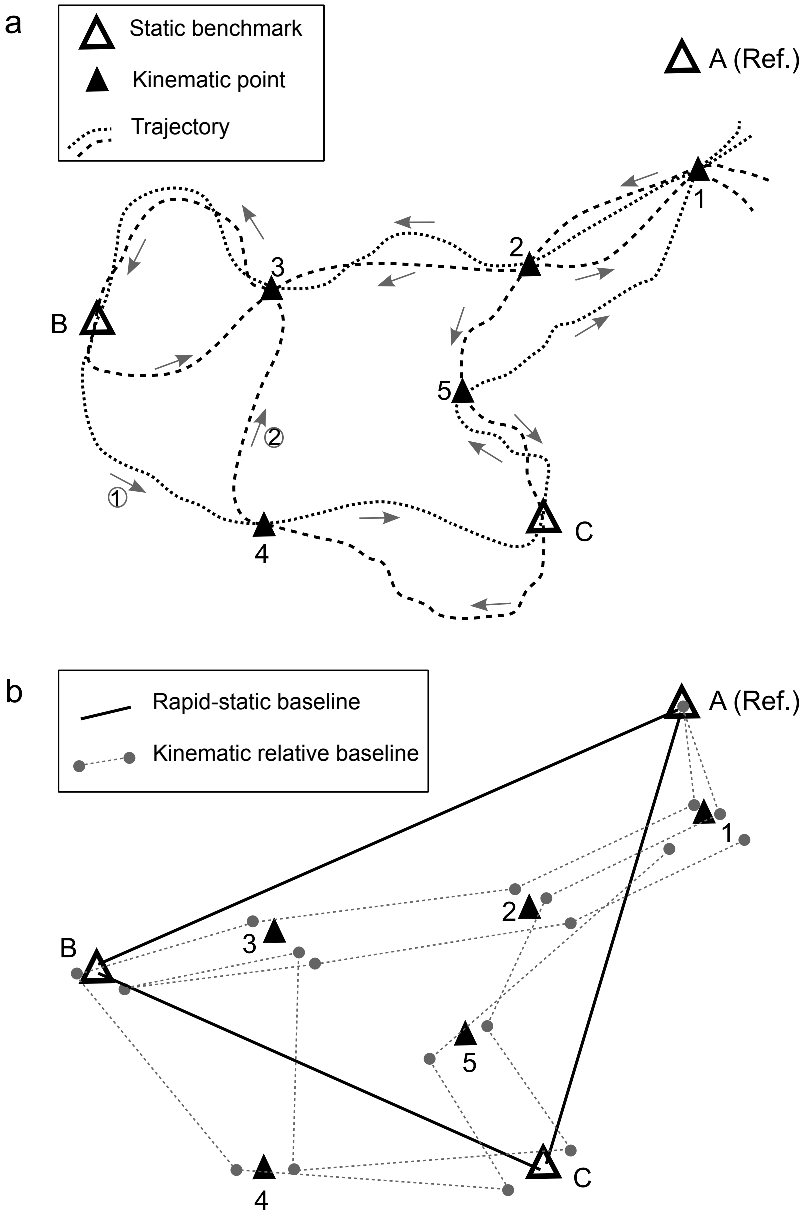

Figure 4.11: Kinematic GNSS position measurement method. a) Example of trajectories through the benchmarks to measure positions. Black triangles represent the benchmarks. Larger empty triangles represent benchmarks for which a rapid–static position measurement was done. b) Baselines used to retrieve the benchmarks positions. (Figure from Beauducel et al. (2006))

Figure 4.12: Kinematic GNSS acquisition at the AYI point (fig. 4.11). The receiver 2m–high antenna is positioned on the benchmark and stabilised by the operator. (From Beauducel et al. (2006))

Fig. 4.13 presents the deposits associated with extrusive episodes that occurred in 1996–1997, 1998 and 2001. The northern and eastern parts of the summit, conversely, have undergone few topographic changes. They are marked by the presence of the 1961 and 1930 crater rims (fig. 4.13).

The summit rheology is highly inhomogeneous, with malleable dome and pyroclastic deposits at the SW, and more consolidated deposits that form the crater floor and the remnant crater rim. In addition, several fractures were identified during field campaigns at the Merapi summit. Major faults are presented on fig. 4.13. The northern part of the crater rim is surrounded with two faults that were identified from both visual observation during field work and interpretation of observed deformation during the 1999–2002 period (Beauducel et al., 2006). The Gendol fault, at the south east, and oriented towards the south east, was identified by the MVO from previous field observations and deformation records.

4.3.2.2 The 2006 Merapi eruption

The first seismic and deformation precursors of the 2006 eruption were recorded in July 2005 (Ratdomopurbo et al., 2013). The seismicity and ground deformation then remained stable until mid–March 2006, when it started increasing again. This increase in activity accelerated until the 26 April 2006, when it dropped down (Ratdomopurbo et al., 2013). The seismic activity recorded during March and April mainly

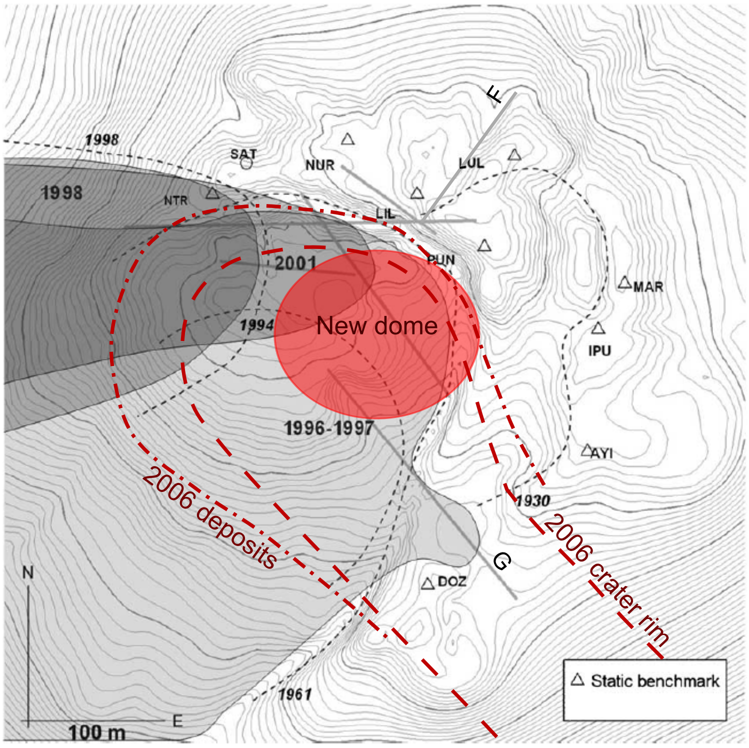

Figure 4.13: Deposits from previous eruptions (gray shading), and emplacement of the 2006 deposits. Red shade: new lava dome observed on May 10 (Ikonos Satellite). Dashed–dotted red curve: dome in early June 2006, dashed red curve: crater rim after the June collapses. Dashed grey curve: contours of the 1961 and 1930 crater rims. Grey lines: observed faults, G: Gendol fault, F: fault used for July 2005–March 2006 displacement retrieval.

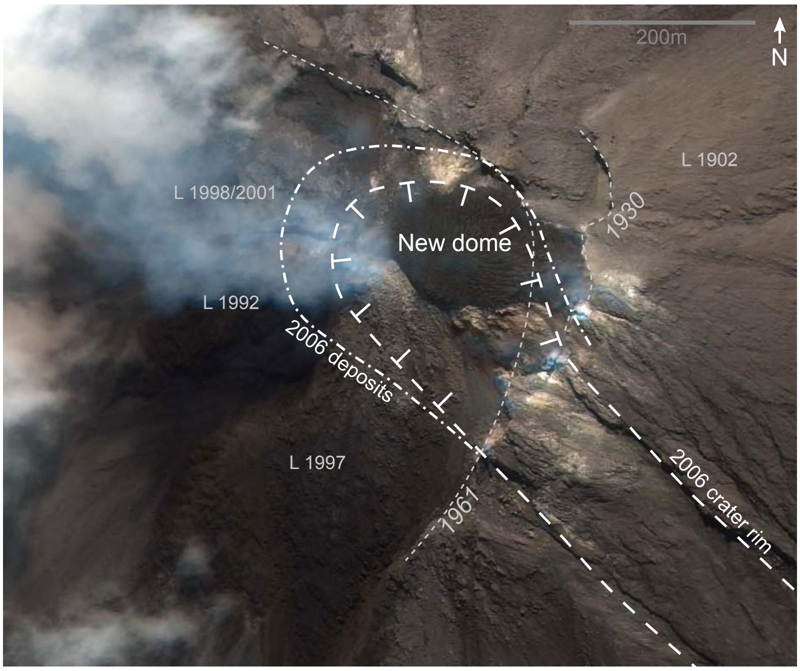

Figure 4.14: Photograph from the Ikonos satellite, on May 10. The new lava dome is visible (dark rounded shape). Dashed thin grey curves: countours of the 1961 and 1930 crater rims. Dashed–dotted thick white curve : dome in early June 2006, dashed thick white curve : crater rim after the June collapses. L xxxx: Previous deposits.

consisted in MP events, generally associated with dome growth or magma/gas supply to the dome. An increase in Guguran events, which are caused by rockfalls generally related to dome growth, was observed concurrently. Although lava was observed at Pasarbubar in early April, no official report of lava observations exist before lava flow fronts were heard for the first time on April 21. On April 26, seismic activity and deformation dropped down. On April 28, photographs of the summit revealed the presence of new blocks of rock. The growth of a new lava dome was confirmed on May 10, as the new dome was visible on an Ikonos satellite photograph (fig. 4.14).

Dome growth carried on until June 8, with an extrusion rate increasing from $1m^3s^{-1}$ per day, in early May, to about $3.3m^3s^{-1}$ per day in early June. On June 4, part of the crater rim (called *Gegerbuaya* "crocodile back" in Indonesian), located SE, collapsed. Two major dome collapses occurred on the 9 and 14 June, removing most of the dome. They initiated series of pyroclastic flows that reached distances of up to 7km from the summit, in the Gendol valley, on the southern flank. A new dome formed in late June and kept growing until October 2006. Deposits associated with the 2006 eruption are visible on fig 4.13.

4.3.2.3 Observed deformation at the Merapi summit

The 2006 eruption, whose first precursors where detected since July 2005, succeeded to a repose period of more than 32 months, from October 2002 to July 2005. During this period of quiescence, some displacements were observed at the summit. They were not associated with a volcanic activity and should rather have been caused by gravity movements and faults activity. Between 0ctober 2002 and June 2005, the eastern part of the crater rim had a significant (about 20cm) upward displacement. This displacement is also visible on the 2002–2003 and 2002–2004 displacement maps (fig. 4.15a and b, fig. 4.16), although few benchmarks positions are available. This uplift might then have occurred as soon as early 2003. Between August 2003 and August 2004, the northern part of the crater rim moved towards north–west (fig. 4.15a). These displacements look very inhomogeneous, since only part of the crater is involved, and evidence the presence of a few faults, that uncouple the displacements at the north and at the east of the crater. Some fractures were indeed observed during field campaigns, including in the area between the northern and eastern parts of the crater rim.

Between October 2002 and July 2005 some downward displacement is visible at a few benchmarks that are close to the crater rim edges (fig. 4.15b). The displacement observed between October 2002 and May 2006 also evidence downward movements at a few more benchmarks located in the north part of the crater rim, close to the margin too (fig. 4.15c). These downward movements, at the margins of the crater rim are probably due to gravity movements in eroding or faulted areas.

Between July 2005 and March 2006, when the activity at Merapi increased, we observe a significant displacement at the Merapi summit (fig. 4.15d). This displacement is mainly radial, away from the domes area, with a small vertical component. Around the reference station, however, we observe highly non homogeneous displacements. These displacements that are extremely different from movements recorded at the north and east parts of the crater rim, could be caused by the presence of more malleable, highly fractured rocks there. A fracture had indeed been observed in this area (fig. 4.13) (Beauducel et al., 2006). Within the scope of the DOMERAPI project, recent temperature and $C0_2$ flux data were recorded at the Merapi summit. They also provide evidence for the possible presence of a faulted area, at this location, that separates the eastern and northern parts of the crater (Byrdina et al., 2017) (Svetlana Byrdina, personal communication).

The inflating displacement observed between July 2005 and March 2006 was associated with an increased MP seismic activity and might have been caused by

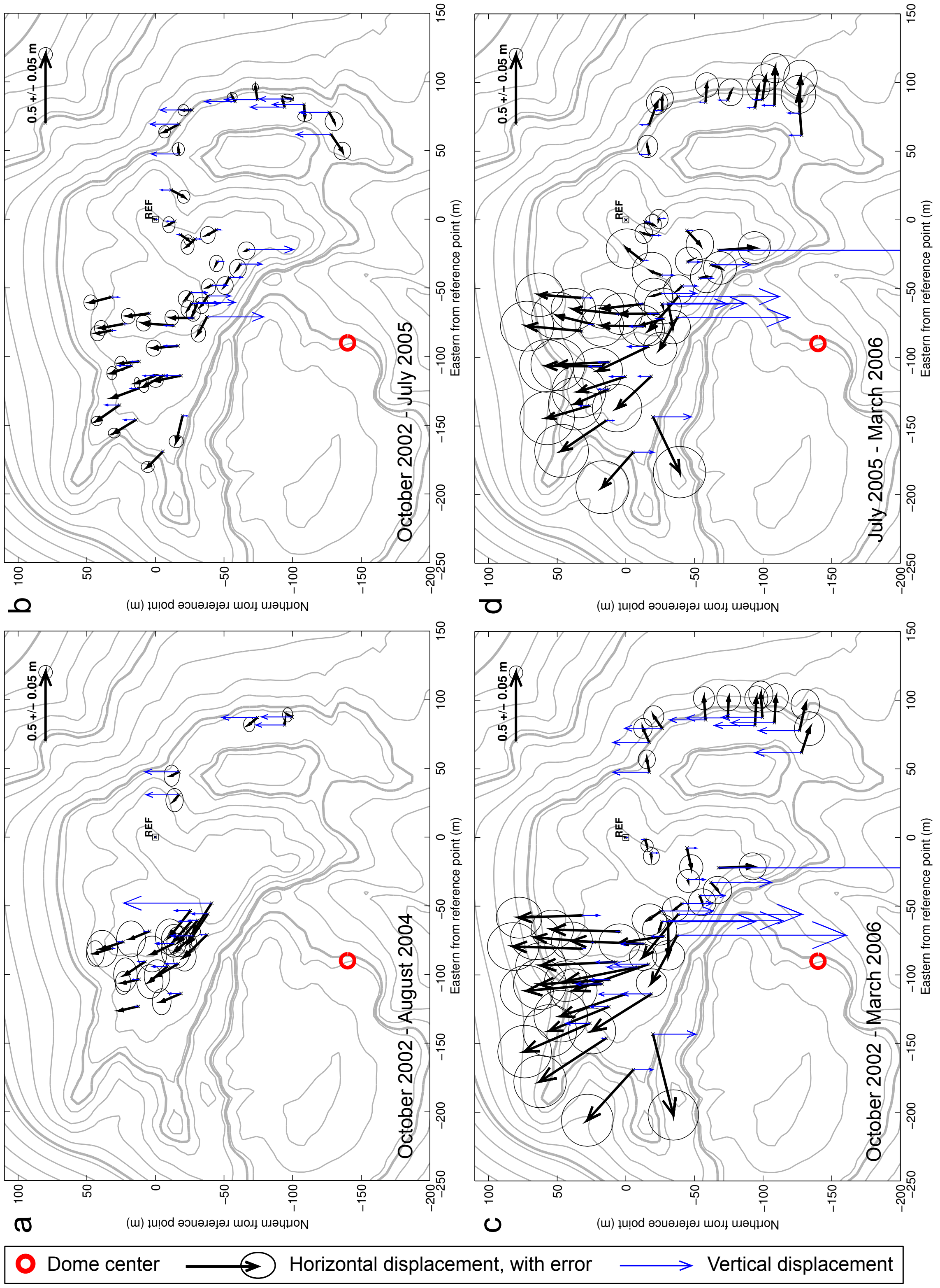

Figure 4.15: Displacement recorded at the Merapi summit between October 2002 and March 2006. Horizontal displacement is represented with dark arrows, and dark ellipses indicate the error on this displacement. Blue arrows represent the vertical displacement (positive towards the North). The red circle marks the center of the 10 May 2006 lava dome. (a) October 2002–August 2004. The crater rim northern part has moved NW. (b) October 2002–June 2005: the upward movement of the eastern crater rim is visible, as well as a gravity downward displacement close to the crater rim margin. (c) October 2002–March 2006: added to the previous displacement, deformation associated with the increased volcanic activity is visible. (d) Focus on the July 2005–March 2006 period, to which will be compared modeled displacement in the following sections.

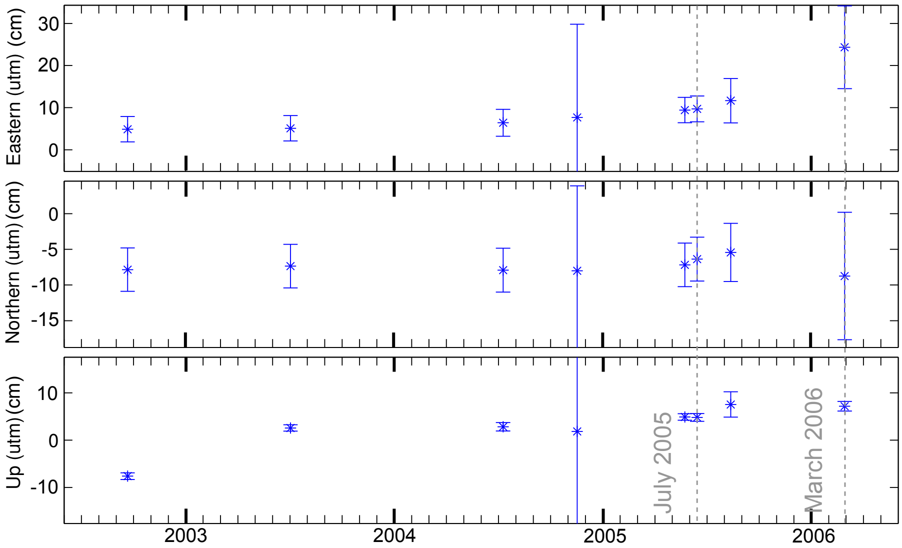

Figure 4.16: Example of GNSS position time series, for the benchmark MAR. Positions are given relative to the 1999 position.

magma progression in the edifice before the 2006 eruption and associated dome emplacement onset. We aim at identifying how volcanic activity, especially conduit flow conditions, affect ground deformation in the near field. We therefore focus on the displacements recorded at the Merapi summit between July 2005 and March 2006, i.e. before the beginning of the 2006 eruption. At first, we do not take into account the displacements observed around the reference station. The influence on ground displacement of the presence of a faulted area there, however, will be tested in a second time.

4.4 Methods

4.4.1 Deformation sources

4.4.1.1 Mogi

Since its first use for volcanology in 1958 by Kiyoo Mogi (Mogi, 1958), dilatation point sources, known today as Mogi sources, have been widely used for interpreting ground deformation associated with volcanic activity (e.g. (Beauducel and Cornet, 1999; Sanderson et al., 2010)). The Mogi model consists in a dilatation point source in a homogeneous, semi–infinite elastic space. This dilatation can be related to a volume or pressure increase. In this way, the point source is generally represented as a sphere of radius a_m and depth H_m, to witch edges is applied either a pressure P_m or a displacement, corresponding to a volume change ΔV of the sphere (fig. 4.17).

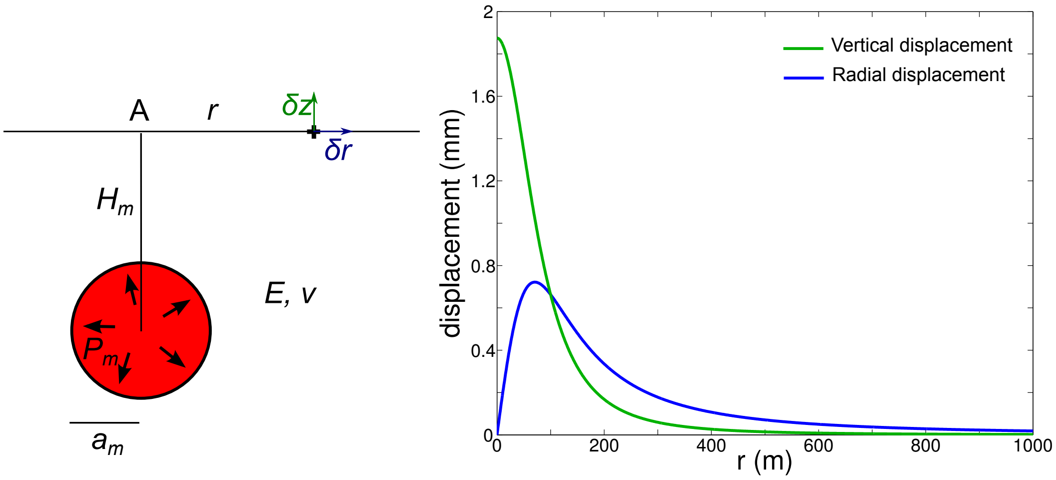

Figure 4.17: Mogi model considering a pressure increase. a) Sketch of the mogi source and principal parameters. b) Ground radial and vertical displacement, for a_m=10m, H_m=100m, P_m=10MPa, E=1GPa and ν=0.25

Analytical solutions for the associated radial δr and vertical δz displacements at the half–space surface exist (4.1) and depend on a_m, P_m or ΔV, the depth of the sphere center, H_m, and on the field elastic properties: the Young's modulus E and the Poisson's ratio ν:

$$\begin{aligned} \delta r &= \frac{3a_m^3 P_m(1+\nu)}{2E}\frac{r}{(H_m^2+r^2)^{3/2}} \\ \delta z &= \frac{3a_m^3 P_m(1+\nu)}{2E}\frac{H_m}{(H_m^2+r^2)^{3/2}} \end{aligned} \tag{4.1}$$

r is the distance to the Mogi source position projected on the surface (fig. 4.17).

Deformation around volcanoes is in many cases attributed to magma displacements, generating local volume or pressure variations. Mogi sources have first been used to retrieve magma reservoirs location, and follow their replenishment or emptying along with eruptive activity. In the volcanic edifice, local deformation can be caused, for example, by sill and dyke emplacements, magma flow in the conduit or pressurisation under a plug. In such cases, the deformation source can hardly be represented by a simple point source. However, the Mogi model remains a simple and efficient tool to evaluate the location of the deformation sources and constrain their nature.

At volcanoes, local topography is far from a flat ground. The models used for retrieving deformation at volcanoes are then slightly different from the original Mogi model. A solution for correcting the effect of topography from the analytical solution, using a varying depth difference between observation points and the source rather than a constant depth difference, has been proposed by William and Wadge (1998, 2000). It gives, however, inexact results, especially for shallow sources beneath relatively steep slopes (Beauducel and Carbone, 2015). Here we rather use a 3D finite element model of a spherical pressure source beneath the volcano edifice. The associated displacement is no longer calculated analytically, but is a result of the edifice deformation calculation, in response to this pressure. Since the observed deformation is very local, we expect the deformation source to be small, and caused by changing conditions in the conduit or by small intrusions. We therefore choose a sphere radius of 15m, which is approximately the estimated radius for the Merapi conduit. A constant and uniform pressure of 1MPa is applied to the sphere edges. The modelled ground displacement is proportional to this pressure, which will be adjusted in a second time (see section 4.4). With this near–Mogi model, we aim to constrain the main deformation source location and nature.

4.4.1.2 Magma flow in a conduit

Magma flow in the volcanic conduit applies pressure and shear stress at the conduit walls. This causes a volcanic edifice deformation, possibly detectable close to the volcano summit. Beauducel and Cornet (2000) needed to invoke pressurisation and shear stress inside a conduit to retrieve observed deformation at the Merapi summit from 1993 to 1997. The pressure and shear stress conditions they used were constant with depth and therefore hardly consistent with realistic conduit flow conditions. Their results however evidenced that magma flow in the conduit is key to understand volcanic ground deformation in the near field. Later, studies by Green et al. (2006), Nishimura (2006, 2009) and Albino et al. (2011) also argued that flow conditions in the conduit could be of first importance to understand ground deformation observed in the near field.

At andesitic volcanoes, during effusive eruption phases, the magma undergoes degassing, crystallization, and cooling as it rises towards the surface. This can result in the formation of a more viscous plug at the top of the conduit. This is consistent with expected flow conditions at the onset of a new effusive phase at Merapi. Here we use the same plug flow conditions as Albino et al. (2011). An incompressible newtonian magma with constant density (we neglect gas and crystals volume fractions variations) and depth dependent viscosity flows within a cylindrical conduit, in response to an overpressure P_c in the magma reservoir. The viscosity profile is a step function of depth, and corresponds to the presence of a viscous plug at the top of the conduit (fig. 4.18a).

The overpressure and shear stress associated with these flow conditions can be calculated analytically. They depend on the ratio between magma μ_m and plug μ_p viscosities, the plug thickness H_p, the conduit height H and radius a_c, and on the overpressure at the bottom of the conduit P_c.

$$
\begin{aligned}
P &= \begin{cases} P_p + (z - H_p)\dfrac{(P_c - P_p)}{(H - H_p)} & \text{if} \quad z \leq H_p \\ z\dfrac{P_p}{H_p} & \text{if} \quad z \geq H_p \end{cases} \qquad (4.2) \\
\sigma &= \begin{cases} \dfrac{(P_c - P_p)}{(H - H_p)}\dfrac{a_c}{2} & \text{if} \quad z \leq H_p \\ \dfrac{P_p}{H_p}\dfrac{a_c}{2} & \text{if} \quad z \geq H_p \\ \end{cases} \\
\text{with } P_p &= \frac{H_p}{(H_p + \dfrac{\mu_m}{\mu_p}(H - H_p)} P_c
\end{aligned}
$$

P_p is the pressure under the plug. The overpressure and shear stress calculated here correspond to the pressure and shear stress conditions difference from a reference case of stagnant magma in the conduit (P_c=0, no magma flow and therefore no shear stress). These magma flow conditions are associated with the extrusion rate given in (4.3). The conduit is modelled as an empty vertical cylinder, to which edges are applied the overpressure and shear stress corresponding to the flow conditions (fig. 4.18).

$$
Q = \frac{\pi a_c^4 P_c}{8(\mu_p H_p + \mu_m(H - H_p))} \qquad (4.3)
$$

4.4.2 Numerical modelling

We model ground deformation at Merapi using the Comsol Multiphysics software. We use a 3D finite element domain of 5x5km which extends to 5km bellow the sea level (fig. 4.19a). The upper surface is a combination of a relatively precise (precision 5m) topography of the Merapi summit dating from 1993, interpolated with a less precise (precision 30m) SRTM topography from February 2000. Roller conditions are applied at the bottom edges of the domain, and a no displacement condition is applied to its lateral edges (fig. 4.19b). The upper surface is free. The deformation

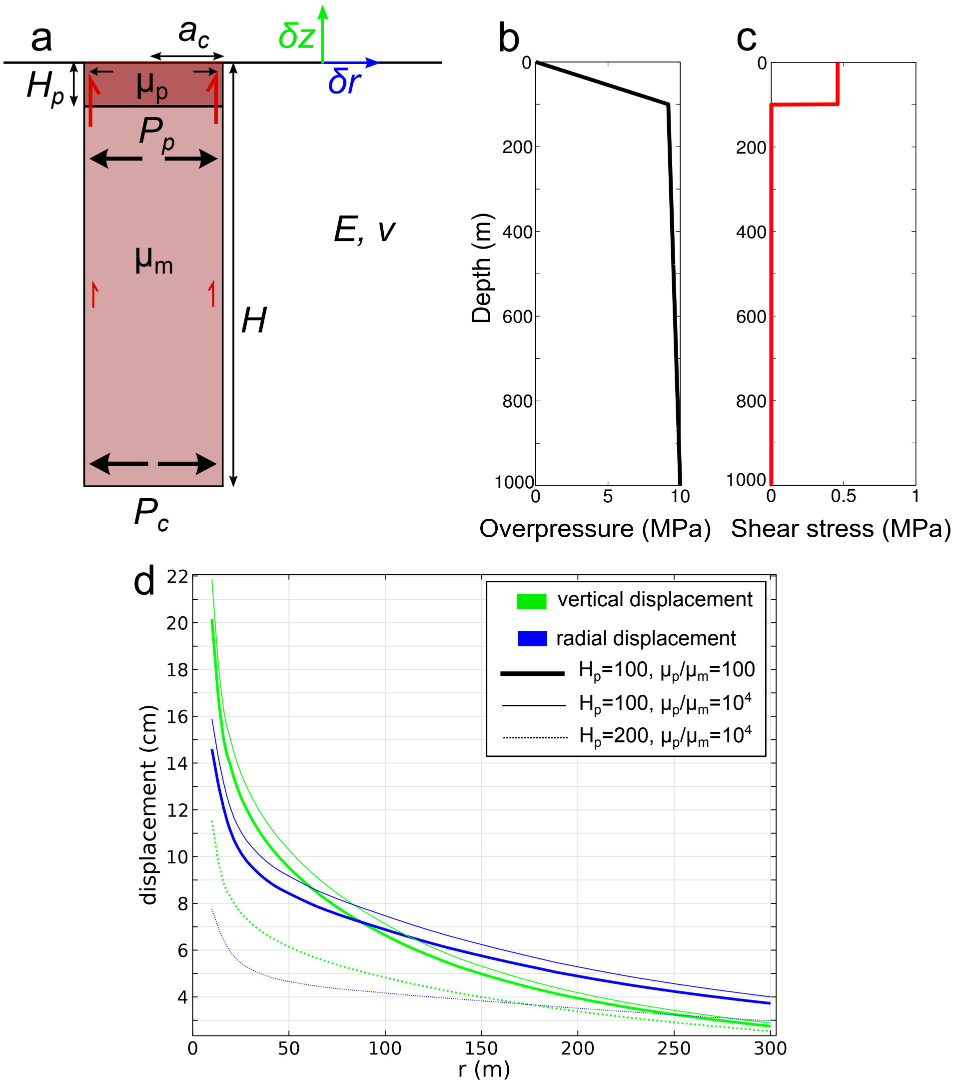

Figure 4.18: Shear stress and pressure conditions associated with a plug. (a) Sketch of plug flow conditions and associated parameters. (b) Pressure profile and (c) shear stress associated with magma flow with H_p=100m, H=1km, a_c=10m, P_c=10MPa, μ_m=10^6Pa·s, μ_p=10^8Pa·s. (d) Ground radial (green) and vertical (blue) displacement for conduit flow models with H_p=100m and μ_p/μ_m=100 (thick curves), H_p=100m and μ_p/μ_m=10^4 (thin curves), and H_p=200m and μ_p/μ_m=100 (dotted curves). The values for H, a_c, P_c and μ_m are the same as in (c).

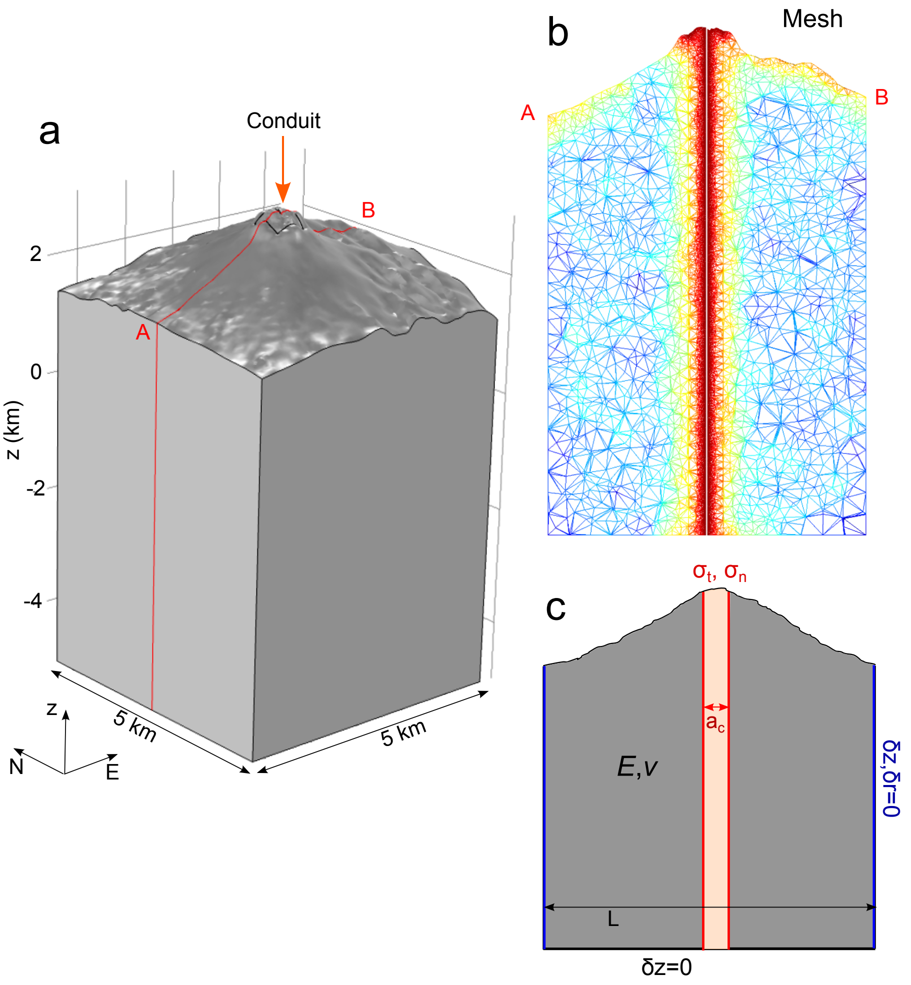

Figure 4.19: Ground deformation numerical model for a conduit deformation source. a) Elastic domain, with the 3D topography from the combination of 1993 and 2000 data. The location of the conduit is indicated. b) Detail of the mesh used for deformation calculation, corresponding to the section A–B indicated on (a). Red to blue colors correspond respectively to fine to wider mesh elements (20m–400m). c) Sketch of a section of the model, with specification of the boundary conditions.

source, either a Mogi spherical source or a conduit cylindrical source, is added to this domain. We consider that the volcanic edifice is elastic, and is characterised by its Young's Modulus E ($E = 0.1$GPa (Beauducel and Cornet, 2000)) and Poisson's ratio ν ($\nu = 0.25$). These values are suitable at the volcano summit, where deposits are poorly consolidated and highly malleable. Beauducel and Cornet (2000) used similar Young's modulus values (E=0.2–0.7GPa). We here chose a very small value for the Young's modulus, however the displacement we calculated is inversely proportional with the ratio between E and the source pressure, and displacements in the case of a higher E can easily be calculated from our results. The mesh is fine (20m wide elements) around the deformation source and the volcano summit, and larger at greater distance (up to 400m wide elements) (fig. 4.19b).

Several dome growth and collapses occurred between 1993 and 2005. This has generated deposits that have partly filled the summit area, and covered the SW flanks, changing the volcano topography by a few meters. These deposits, however, mainly consist in pyroclastic flows and dome clasts, that are very malleable. They will therefore have little influence on the ground deformation observed at the NE crater rim, except by loading the edifice. Since no deposits were added during the July 2005 – May 2006 period, we neglect this effect on ground deformation for this period.

4.4.3 Model best solution

The resulting displacement is extracted for all the benchmarks coordinates. For both deformation sources, the ground displacement is proportional to the overpressure either at the sphere edges, for Mogi sources, or at the bottom of the conduit, for conduit flow conditions. We therefore solve the ground deformation model for a fixed pressure condition and then minimise the Root Mean Square Error (RMSE) R for the model by varying an amplitude factor f for the modelled displacements, in order to find the model that best fits the data. The product of f and the pressure used for ground calculation gives the overpressure conditions needed, at the sphere edges or at the bottom of the conduit, to best explain the data.

$$R = \sqrt{\sum_i \frac{(m_i - f d_i)^2}{\varepsilon_i \sum\limits_i 1/\varepsilon_i}} \tag{4.4}$$

d_i and m_i are the observed and calculated displacements for station i, respectively, ε_i is the error on measured displacement.The minimised error R is then compared for all the deformation models, in order to determine which configuration is in best agreement with the data.

4.5 Results

4.5.1 Mogi models

We calculated ground deformation associated with spherical sources located beneath the 2006 dome and the north–east part of the crater. Tested source locations have depths ranging from 50 to 200m beneath the surface, and are spaced by 20m in the three directions.

The Mogi source that best accounts for the deformation observed on the crater rim is very superficial (30m beneath the ground surface), with a RMSE of 16.15cm (without any model the RMSE is 26.62cm) (fig. 4.20). The pressure needed to best fit the data is 87MPa, which is huge for such a superficial source. In comparison, the resistance of volcanic rocks to traction has been estimated to about 10MPa (Albino, 2011), and in a volcanic conduit, overpressures are expected to reach 25MPa only, in extreme cases. The value of the pressure needed to fit data also depends on the spherical source radius (here r=15m). However here we expect the deformation to be caused by a superficial source, that should therefore be quite small, especially at a depth of 30m only.

Since the volcanic edfice, at the summit, can be very malleable, and the ground deformation is inversely proportional to the Young's modulus, the pressure needed to fit observed deformation, if the Young's modulus is smaller at the summit, could be less important. In order to get rid of pressure and Young's Modulus considerations, we calculated the corresponding volume increase it would represent in the sphere. We get a volume variation of about 40000 m^3, which is huge as it represents about three times the volume of the initial sphere (15m radius). The mean displacement at the sphere edges is of 8.75m. In comparison, fractures opening usually observed on the crater rim is only about a few tens of cm.

To summarize, pressurised spherical sources provide some explanation for the observed deformation, though an important part remains unretrieved. The best sources are extremely shallow and highly pressurised, which is hardly realistic in regard with processes that can happen in the summit area.

4.5.2 Conduit flow Models

The deformation associated with magma flow in the conduit depends on the thickness of the plug, the viscosity ratio between plug and conduit, the pressure at the bottom of the conduit, and the location of the conduit. We first discuss the location of the conduit, and then determine the model, for the selected location, that best fits the data by varying the plug thickness and viscosity, and minimising the RMSE.

4.5.2.1 Conduit localisation

The magma that formed the dome observed on May 10 must have extruded from a vent located beneath the dome. Since the dome has a rounded shape, a first assumption would be to place this vent centered beneath the dome (fig. 4.21). Deformation

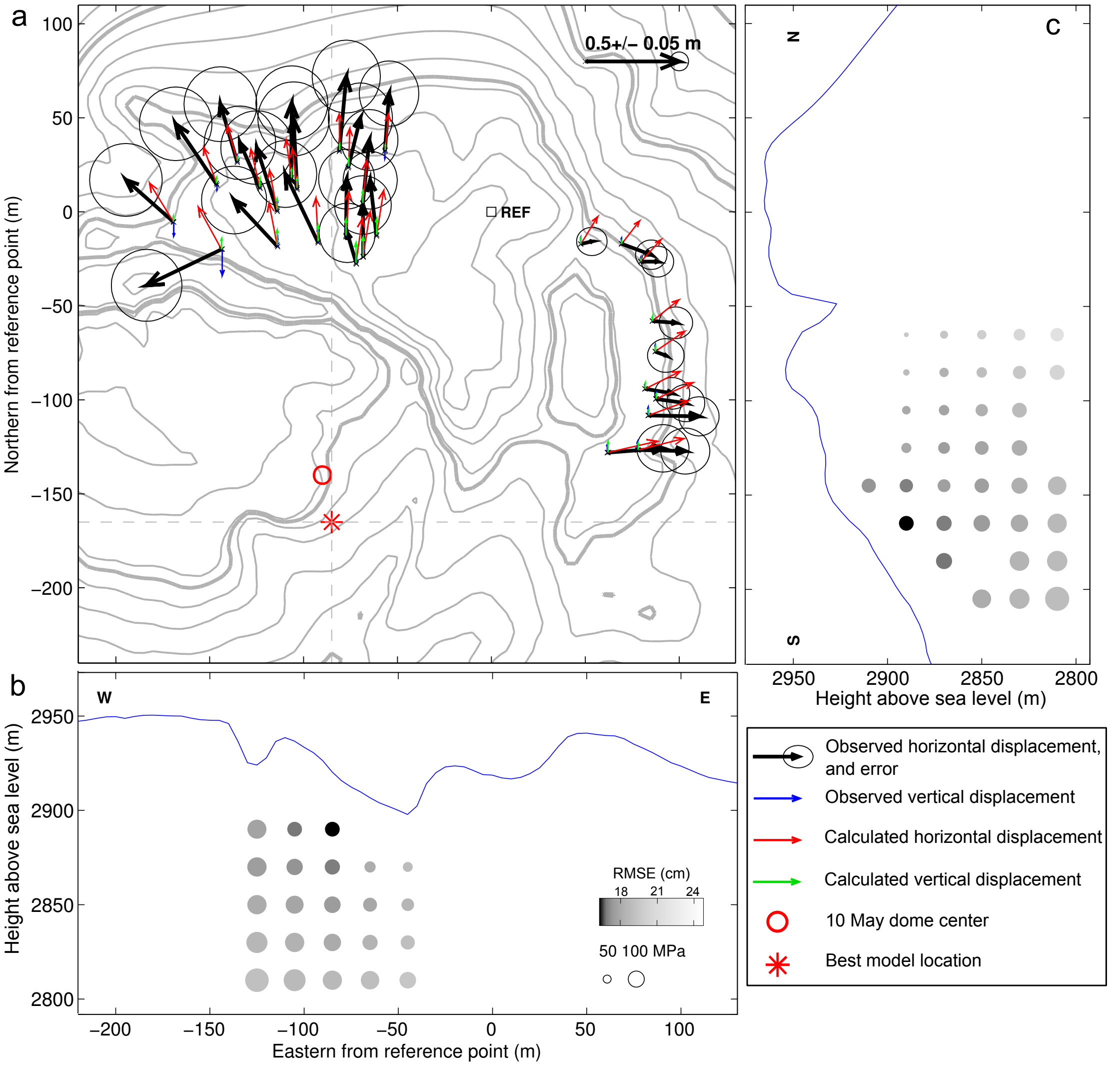

Figure 4.20: Ground displacement solution for the best model of pressurised sphere (Mogi). (a) Ground displacement. Black and blue arrows: horizontal and vertical (positive towards north) observed displacement. Black ellipses correspond to the error on horizontal displacement. red and green arrows: horizontal and vertical displacement from the best model solution. red circle : 10 May 2006 dome center. red star: ”epicenter” of the best spherical deformation source. (b) Other pressurised spherical source models, following the SN cross section passing by the best model. (c) Other tested models, following the WE cross section passing by the best model. The markers sizes increase with the pressure needed to minimise the RMSE. The markers colours depend on the model RMSE. The best model (lowest RMSE) appears in black. (Best model: P_c=87MPa, H_m=30m, RMSE: 16.15cm (no model RMSE: 26.62cm))

retrieval with pressurised, spherical sources may also give clues on the location of the vent, since the best superificial sources may coincide with the conduit exit. Using a typical conduit flow model (H_p=100m, μ_p/μ_m=100), we also determined the position for which the deformation associated with magma flow would best explain (i) the total observed displacement or (ii) the observed horizontal displacement. All the conduit positions determined following these four methods (dome center, mogi results, deduction from total and horizontal displacement) are located beneath the 10 may 2006 lava dome (fig. 4.21), in an area of 90m in diameter.

4.5.2.2 Best conduit flow model

For these four possible locations, we determined the conduit flow model that best fits the observed deformation, by varying the plug thickness from 30 to 150m, the plug vs conduit viscosity ratio from 5 to 10^4, and the pressure at the bottom (depth of 5km) of the conduit. The conduit flow model that minimises the RMSE is obtained for the conduit position determined using the third possibility we described above (typical conduit flow model, total displacement), with a plug thickness of 30m and a viscosity ratio of 10^4 (fig. 4.22). For this model, the RMSE is 19.95cm, and the pressure at the bottom of the conduit is 8.5 MPa, corresponding to an extrusion rate of 14.2 m^3 per day, which is consistent with a very little lava extrusion in early April.

The pressure and corresponding extrusion rate needed to retrieve the observed deformation amplitude are much more realistic than the conditions associated with a pressurised sphere model. However, the vertical displacement obtained with conduit flow models is much higher than that observed. The ratio between vertical and horizontal displacements decreases with a decreasing (but non–zero) plug thickness and an increasing viscosity ratio. Consequently the best model corresponds to the lowest plug thickness and highest viscosity ratio we tested, and would tend to even more extreme values, although the vertical displacement remains too high. Because of the high vertical displacement it is associated with, magma flow within a conduit under a viscous plug does not provide a fully satisfying explanation for the observed ground deformation.

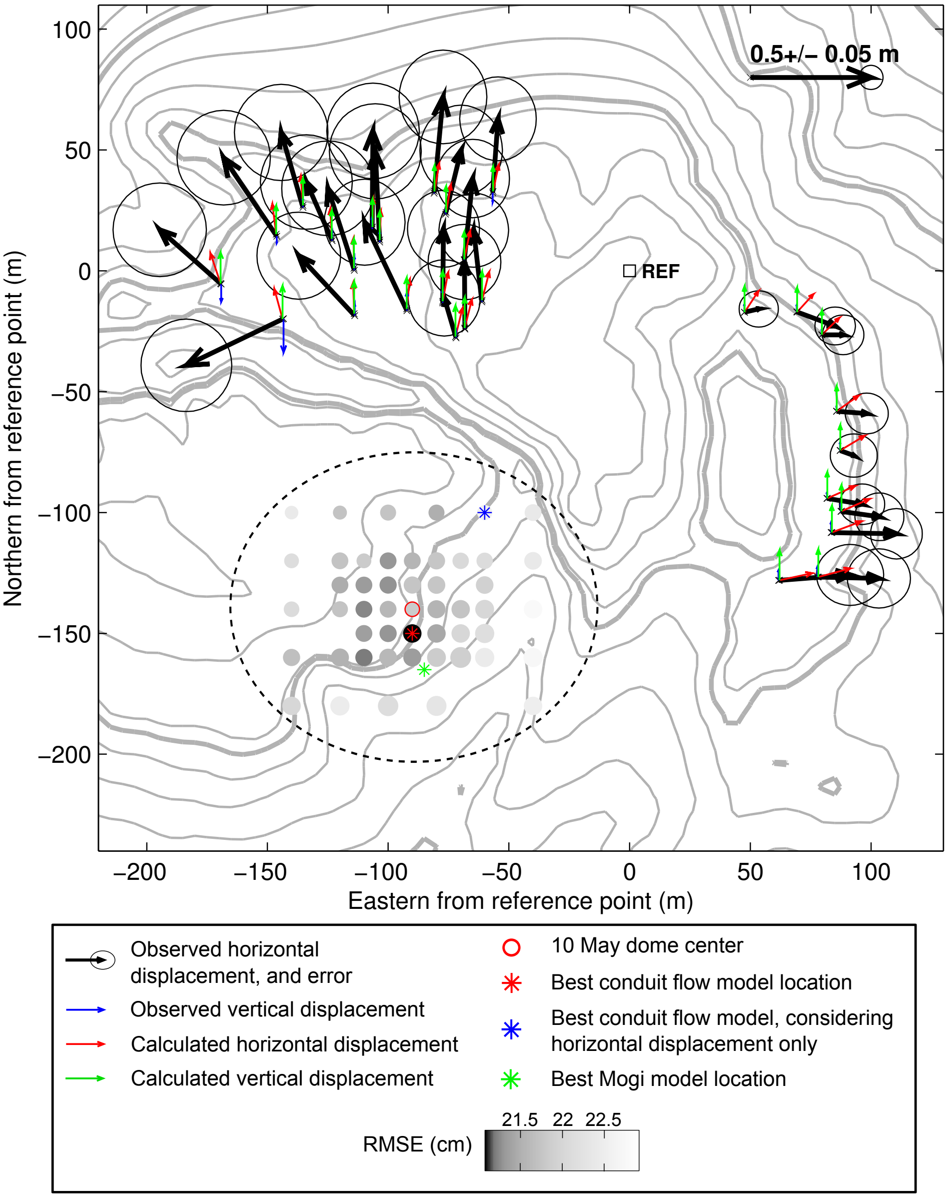

Figure 4.21: Best conduit position from visual observation from the 10 may 2006 Ikonos photograph (red circle), determined from pressurised spheres models results (green star), minimisation of the RMSE for a typical conduit flow model (H_p=100m, μ_p/μ_m=100) for the total (red star), or horizontal (blue star) displacement. The grey markers indicate the location of other tested positions for a conduit flow source deformation, with shades of grey depending on the associated RMSE for the total displacement. The model displacement drawn here with red and green arrows (the color legend is the same as in figure 4.20) corresponds to the best conduit flow model position (red star).

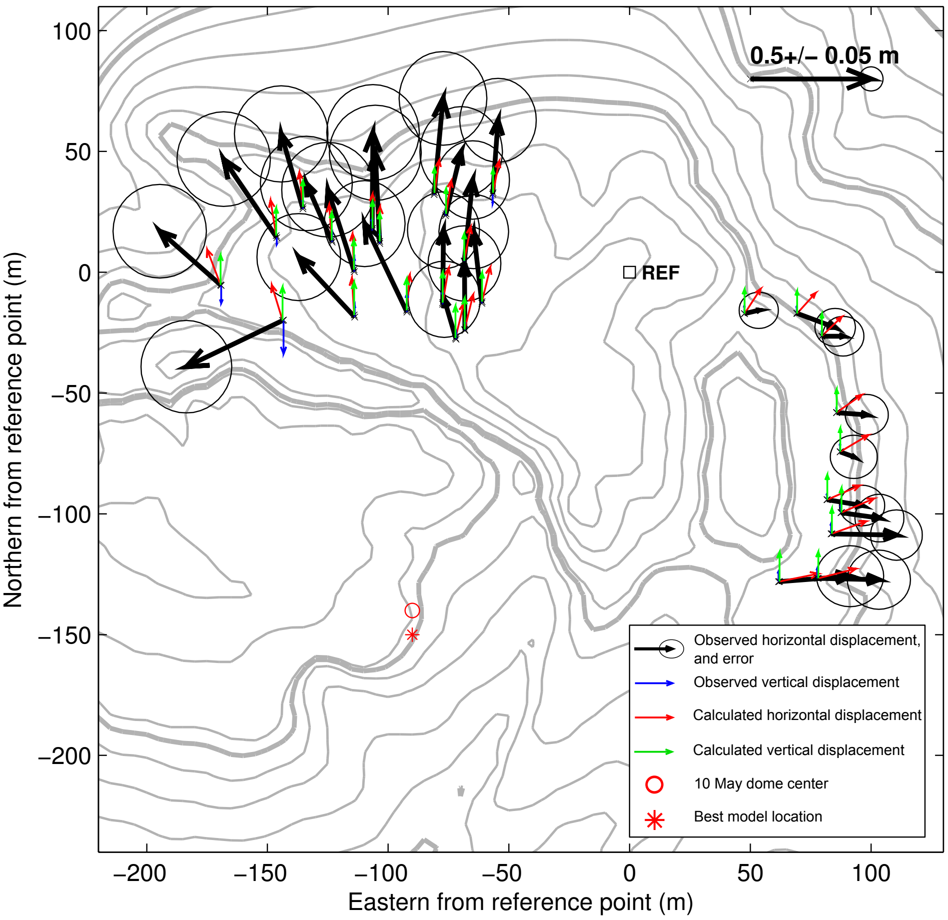

Figure 4.22: Ground deformation associated with the best conduit flow model (H_p=30m, μ_p/μ_m=10^4, P_c=8.5MPa, RMSE: 19.95cm (no model RMSE: 26.62cm)).

4.6 Discussion

4.6.1 Influence of faults

In the models we presented here, we assumed that the volcanic edifice, and particularly the summit area, was elastic, with a homogeneous rheology. However, we know from previous studies (Young et al., 2000; Beauducel et al., 2006), that the real summit has a heterogeneous rheology, and is fractured (section 4.3.2). This is known to influence the observed deformation (Young et al., 2000; Beauducel et al., 2006). In particular, the presence of a fractured zone and some faults were observed between the northern and eastern parts of the 1961 crater rim (section 4.3.2, fig. 4.15).

4.6.1.1 Mogi best models for the eastern part of the crater

Several faults were observed in the northern part of the crater rim and may have contribute to the deformation observed there. We here look for the spherical source model that best retrieves the displacements observed in the eastern part of the crater only, in order to get rid of the faults influence. The best spherical source is located north–east from the source that best fits both eastern and northern stations displacement, with a RMSE of 9.39cm (no model RMSE: 17.40cm), for a pressure of 27MPa (fig. 4.23). Although the displacement at the east is better retrieved, the model results poorly fit the displacement at the north. In the following paragraph, we further investigate the influence of having a faulted zone between the northern and eastern parts of the crater rim.

4.6.1.2 Presence of a faulted zone

We add a highly deformable area to the previous model, located around the reference station, and representing the probably highly faulted and deformable area observed there (section 4.3.2). The highly deformable domain is 170 long, 50m large and 100 to 200m deep. Its Young's modulus is 100 to 10 times lower than that of the rest of the edifice.

We calculate ground deformation associated with magma flow in a conduit, using the best fit parameters we got from previous calculation (H_p=30m, viscosity ratio: 10^4, best location for plug flow). We only vary the highly deformable domain's depth and Young's modulus. The best fit with observed deformation we obtain corresponds to a deformable domain of depth 100m and a Young's modulus 100 times

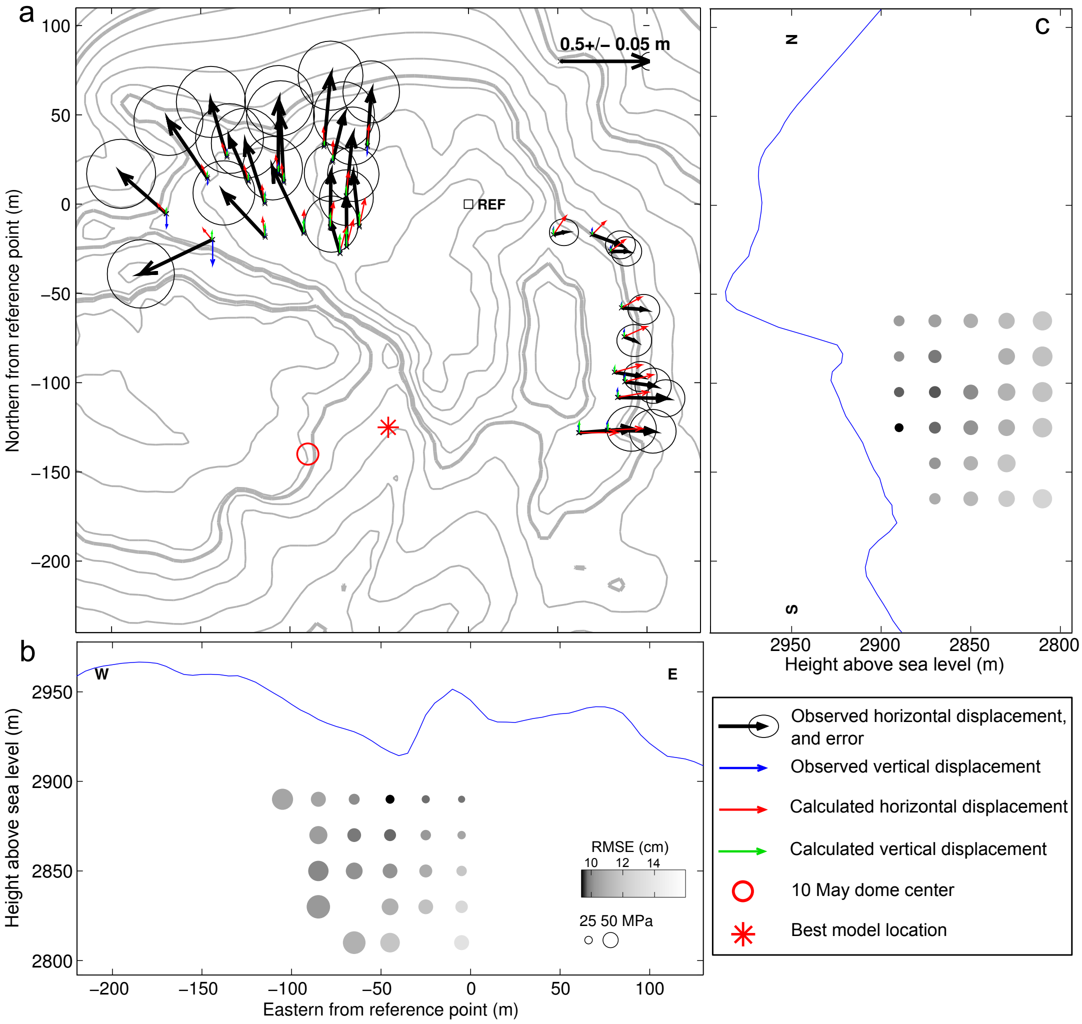

Figure 4.23: Best solution for deformation associated with a pressurized sphere, for the eastern part of the crater rim only. (P_c=27MPa, RMSE: 9.39cm (no model RMSE: 17.40cm))

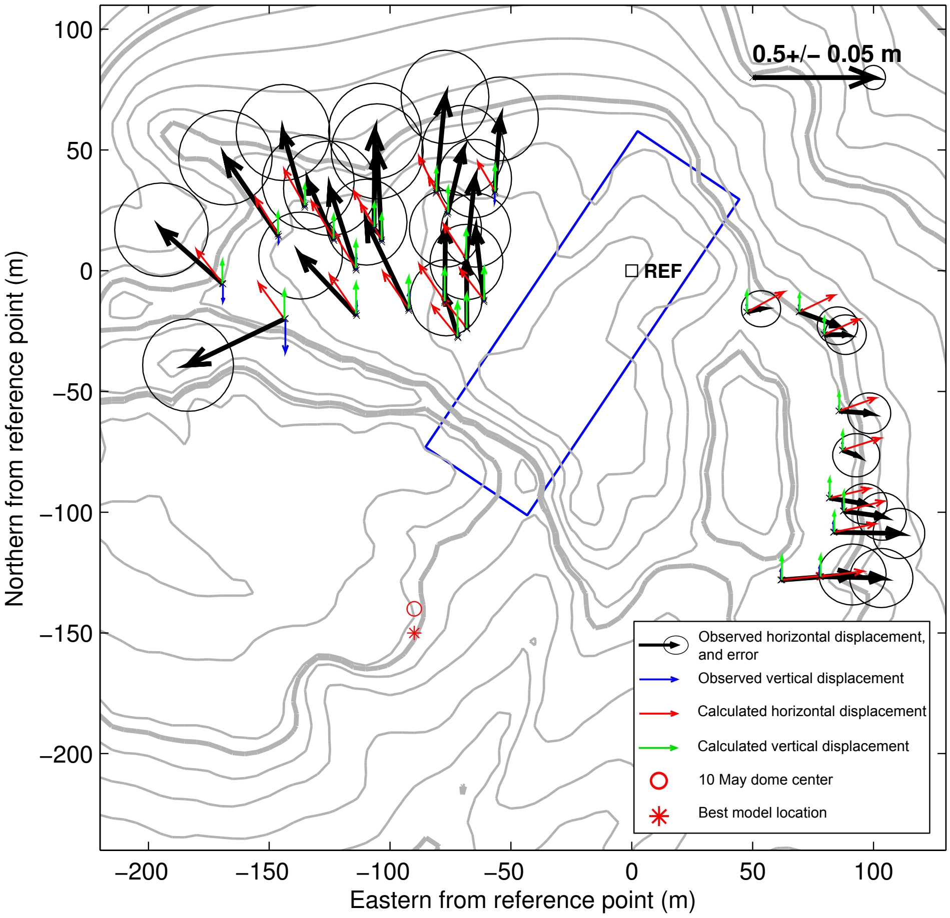

Figure 4.24: Modelled displacement for a conduit flow with $H_p = 30$ and $\mu_p/\mu_m = 10^4$, with a more malleable area (blue rectangle) of depth 100m, and Young's Modulus 1MPa. RMSE: 18.50cm (no model RMSE: 26.62cm).

lower than in the rest of the edifice (fig. 4.24). The RMSE is 18.50 cm. although it remains quite high, it is significantly lower than what we got using a homogeneous edifice rheology. This is partly due to the fact that with the faulted zone influence the resulting displacement has a smaller vertical component, compared with the horizontal one, than in the uniform rheology model. Here we did not discuss the location of the conduit, and only compared results with our best conduit flow model for a uniform rheology. However, with the influence of faults, the best conduit location may be different, and the associated displacement might fit even better observations.

The results presented in these two sections (4.6.1.1 and 4.6.1.2) provide evidence that the presence of faults at the volcano summit can have a huge impact on observed ground deformation and make its interpretation complex. Aside from the faulted zone we modelled here, several other faults have been identified in the summit area (Beauducel and Cornet, 2000; Beauducel et al., 2006) (fig. 4.13 and 4.3.2).

In addition, the geology of the summit also causes inhomogeneities in the rocks response to stress. Materials erupted recently are indeed much more malleable than the older crater rims (Young et al., 2000). Taking into account these rheological elements in ground deformation may help retrieving and interpreting observations. It is however complex, as precise field observations are needed.

4.6.2 Deformation source

Our results show that conduit models give a satisfying retrieval of the observed deformation, especially if the summit complex rheology is taken into account. Besides, the corresponding extrusion rate and the overpressure at the bottom of the conduit are in agreement with observations, contrary to the huge pressures needed to retrieve observations using Mogi source models. However, the conduit flow models that best fit the observed deformation are those with the most extreme values for plug thickness and plug vs conduit viscosity ratio. Besides, the transition between conduit flow and plug flow in our model is sharp, and poorly realistic.

In this paragraph, we explore how the deformation associated with a uniform pressure applied at the conduit edges may fit the data. This constant pressure model would be equivalent to imposing a radial displacement at the conduit edges, and may correspond to an opening of the rock along the conduit. The best model we obtain corresponds to a conduit located northern from the dome center, with a pressure of 8.2 MPa within the conduit (fig. 4.25), corresponding to a mean radial displacement at the conduit edges of about 1.5m, which is much more reasonable than the displacement needed with a spherical source. The associated RMSE is 15.83 cm, which is significantly better than our results using conduit flow sources. Before the 2006 eruption, no conduit, or fracture was present where the magma must have extrude and to form the dome. The opening of a pathway for magma flow may also be a realistic scenario for the observed deformation. Here, however, we did not take into account the impact of the summit complex rheology, which was proven to have a potentially huge influence on observed deformation. This makes it difficult to discriminate between the possible scenarios.

4.6.3 Quality of the data

Aside from the complexity of the summit geology and rheology, and that of flow conditions inside the conduit, constraining flow conditions evolution in the conduit from observed deformation is also complicated by the data quality and sparsity. The

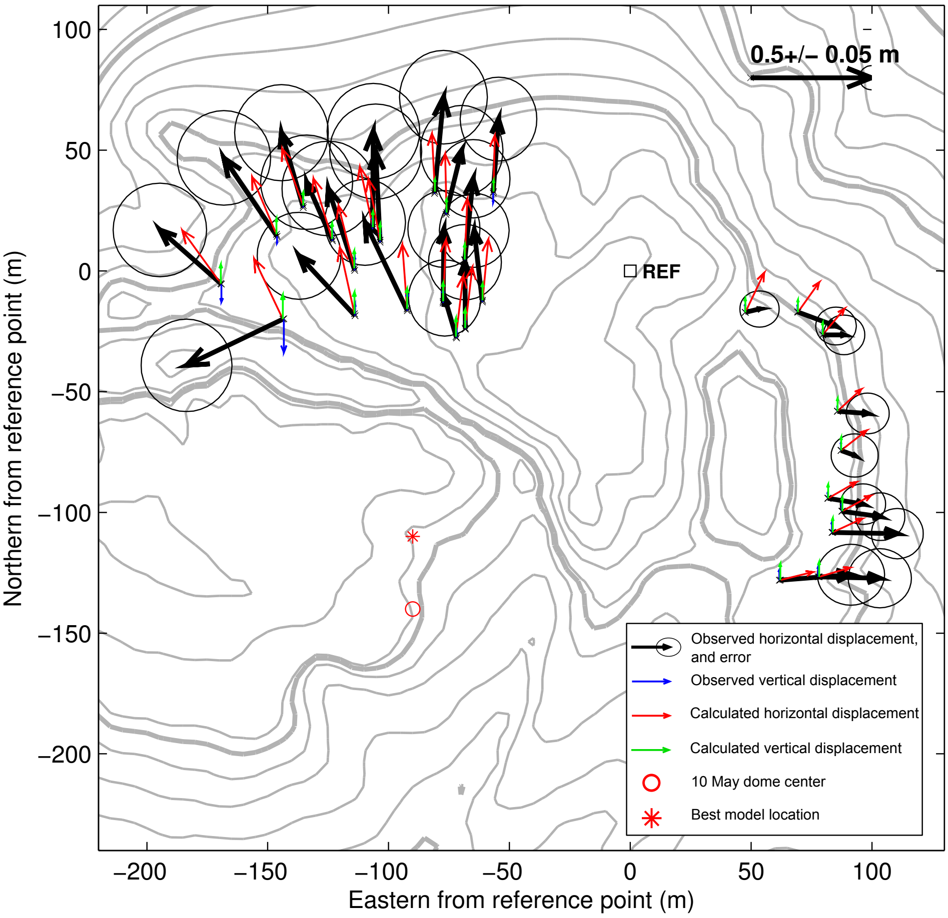

Figure 4.25: Ground deformation associated with the best pressurised conduit model. Conduit pressure: 8.2MPa, RMSE: 15.83 cm (no model RMSE: 26.62cm)

data we used here were recorded manually using a moving receiving GNSS antenna that had to be positioned vertically at each benchmark during 2mn (fig. 4.12). Meteorological conditions at the volcano summit can be very windy, and make it hard to keep this position. Besides, the good precision of the data is ensured with the fact that the loop described by the receiving antenna is closed and repeated, and by the three rapid–static measurements on a closed triangle that better constrain the data (section 4.3.1, fig. 4.11). Because of conditions at the summit (wind, rain, but also volcanic hazard), some measures could not be entirely completed, resulting in lower precision on the benchmarks positions.

Added with these field difficulties, the time period between two kinematic GNSS measurement campaigns can be very long. Moreover, no campaign can be done during eruption periods, for obvious reasons. It is therefore not possible to follow flow conditions evolution during an eruption. The recorded kinematic deformation therefore capture a long time period evolution, making it difficult to separate the possible different events that occurred.

Using permanent stations reduces the problem caused both by meteorological conditions and time sparsity of the data. However, these GNSS stations are much more expensive and having a dense network like the benchmark network used here is not possible. In addition, the deformation caused by conduit flow is very local, and stations have to be close to the volcanic vent to detect its variations. Moreover, although such a network may help forecasting transitions from effusive to explosive, stations close to the vent would be destroyed during explosive phases, limiting monitoring of conditions evolution along with the eruption.

4.7 Conclusion

In order to evaluate the potential for monitoring flow conditions evolution within the conduit from near field ground deformation, we interpreted ground deformation data recorded at Merapi a few days before the onset of the 2006 eruption using numerical modelling of the deformation associated with flow conditions. We provide evidence that conduit flow models give important clues for interpreting the observed deformation. Using realistic flow conditions, a major part of the observed deformation is retrieved, while Mogi source models fail in explaining the observations. This is in agreement with precedent observations from Beauducel et al. (2006), Albino et al. (2011) and others. It also confirms that ground deformation associated with magma flow in the conduit is visible in the near field.

However, our results also demonstrate the complexity and the limits of monitoring flow conditions from ground deformation at Merapi. The presence of several faults and fractured area, as well as the inhomogeneity of the summit rheology have an important impact on the observed deformation, and complexify its interpretation in terms of magmatic activity. Together with the complexity of physical processes that may happen in the conduit before and during an eruption, it makes it very difficult to determine conditions in the conduit, and then to forecast their possible evolution. Besides, having deformation data that are recorded close to the volcanic vent, in a dense network and frequently is a real challenge in terms of material and maintenance, for field conditions and safety reasons.

Ground deformation observations on itself may hardly be sufficient for monitoring flow conditions evolution within the conduit. However the observation of magma extrusion rate, remote gas measurements, as well as seismic observations may help discriminate between the different scenarios and constrain interpretations on the eruptive regime evolution.

Chapter 5

Coupling magma and gas flow in transient regimes

Contents

In the conduit, the magma experiences pressure variations. These modifications induce a disequilibrium between the gas pressure within bubbles and the magma ambient pressure. These changes can be due either to gas pressure evolution or to the magma experiencing global pressure variations. In the first case, gas loss to the country rock, for example, may cause the gas pressure to decrease down to a lower level than the ambient pressure. In the second case the ambient pressure evolves and is no more equal to the gas pressure.

Such a disequilibrium may trigger magma volume changes, associated with an evolution of the flow conditions. In the magma flow model described in chap. 1, we assume that gas pressure and magma pressure are equal for calculating magma flow conditions. The magma porosity only depends on the magma pressure and water mass fraction. This implies that if gas is lost at the conduit margins and top, the magma porosity will adapt instantaneously to the new gas mass fraction. It implies some instantaneous changes in the amount of magma present within the conduit. Provided the high viscosity values of the melt that will slow down balance processes, this is not sustainable for effusive silicic magma flow conditions. In order to solve transient regime problems, we need to clarify the response of magma flow by compaction/dilatation and flow conditions adaptation to changes in the gas pressure.

In this chapter we first review some models from the literature that describe the evolution of a small batch of magma experiencing such a pressure disequilibrium. We point out important parameters that control these volume changes, and highlight a few trends for the magma flow response. In a the second time, we consider the case of a volcanic conduit, in which the pressure disequilibrium may evolve both with space and time. At this point, we rely on a two-phase description of magma and gas flow. Eventually, we propose an adaptation of our magma and gas flow models to integrate the influence of the pressure disequilibrium between gas and ambient pressure on flow conditions.

5.1 Effects of gas pressure variations on magma flow

5.1.1 Dilatation and compaction of a small batch of magma

Magma rising towards the surface undergoes decompression that induces gas exsolution and bubble growth. These are key processes for magma flow dynamics and eruptive style determination (e.g. Sparks, 1997; Melnik and Sparks, 2005). Over the last decades, bubble growth in the magma has drawn a lot of attention, and has been extensively studied through analytical (Sparks, 1978; Prousevitch et al., 1993; Barclay et al., 1995; Navon and Lyakhovsky, 1998; Lensky et al., 2004), numerical

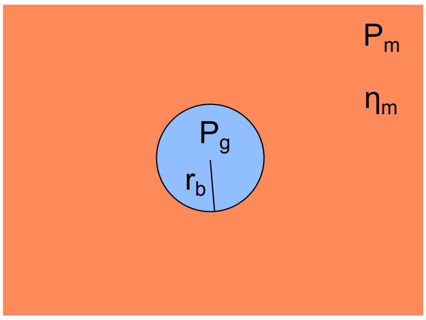

Figure 5.1: The infinite melt model consist in one gas bubble in an infinite space of melt. The bubble growth depends of the pressure difference between gas p_g and melt at infinite p_m, and on the melt viscosity η_m.

(Blower et al., 2001) and experimental studies (Navon and Lyakhovsky, 1998; Gardner et al., 2000; Lensky et al., 2004; Fiege and Cichy, 2015). These studies provided evidence for the controlling roles of volatile diffusion over the formation of bubbles, and of magma viscous reaction to bubble expansion on their growth (Navon and Lyakhovsky, 1998; Blower et al., 2001).

In particular, two end-member analytical models have extensively been used. The first one considers the growth of a single bubble within an infinite space of melt (Sparks, 1978; Barclay et al., 1995) (fig. 5.1). In this model, time–dependent growth of the bubble depends on the difference between the gas pressure p_g and the ambient pressure p_m (infinite condition) to which the system was decompressed. It also depends on the magma viscosity. The pressure applied by the gas at the magma–gas interface is responsible for the presence of a pressure gradient around the bubble. This triggers magma flow, thus allowing bubble growth.

The second model considers bubbles within a foam, which can be modelled as an assemblage of bubbles, each surrounded with a shell of melt (Prousevitch et al., 1993; Barclay et al., 1995; Navon and Lyakhovsky, 1998; Lensky et al., 2002) (fig. 5.2). In this model, the time dependent bubble growth depends on the difference between the pressure applied by the gas at the magma–gas interface p_g, and the ambient pressure, which acts as a boundary condition at the outer side of the melt shell. It also depends on the ratio between the initial size of the bubble R_0 and the thickness of the melt shell h_0, which is linked with porosity, and on melt viscosity. In this model, the pressure difference between gas and ambient pressure is also responsible for a pressure gradient within the melt shell, that causes the melt to flow and the bubble to expand. In this model, the limited size of the melt shell, which varies with time, is a way to account for bubble–bubble interactions. More recently, Mancini et al. (2016) proposed a similar bubble growth model, in which bubble sizes

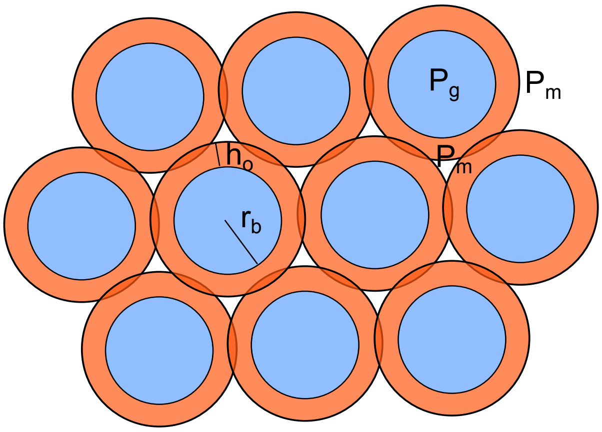

Figure 5.2: The foam model assumes that each bubble is surrounded with a shell of melt of finite volume. The bubble growth with time depends on the difference between the pressure applied by the gas at the inner boundary of the shell p_g, and the ambient pressure applied at its outer side p_m. It also depends on the ratio between bubble radius and shell thickness R_0/h_0, and on melt viscosity η_m.

were different. This complex bubble size distribution enables to link bubble growth processes with coalescence issues.

In these models, changes in the gas pressure (relative to the ambient pressure) act on melt flow by applying normal stress at the gas–magma interface, and therefore creating a local pressure gradient. The bubble growth kinetics also depends on the magma porosity. Similarly, a batch of magma that is compressed will evolve so that the size of the bubbles decreases, depending on the difference between gas and ambient pressure, and on the magma porosity.

These Lagrangian models are very helpful to understand the possible evolution of a small batch of magma within the conduit. They are based on a simple two–phase description of a small batch of magma, and suppose that the magma–gas interface location is known. Considering modelling of a larger volcanic system, such as a volcanic conduit, the position of the magma–gas interface cannot be known. Indeed, it it would require huge capacities in memory and high calculation cost. In such systems, an Eulerian description, using locally averaged values for magma and gas properties and flow conditions is generally preferred.

Besides, in such large systems, the melt pressure, and magma porosity vary with space and time. In addition, the magma is confined in a fixed area (e.g. the conduit) with the limits of which it may interact (e.g. no slip at the conduit walls). Changes of the magma volume in response to pressure changes are therefore associated to an adaptation of flow conditions that can be complex. Here, we consider the hypothetical example of a large batch of magma in a closed, non deformable box, with magma porosity and gas pressure being uniform with space. For the example

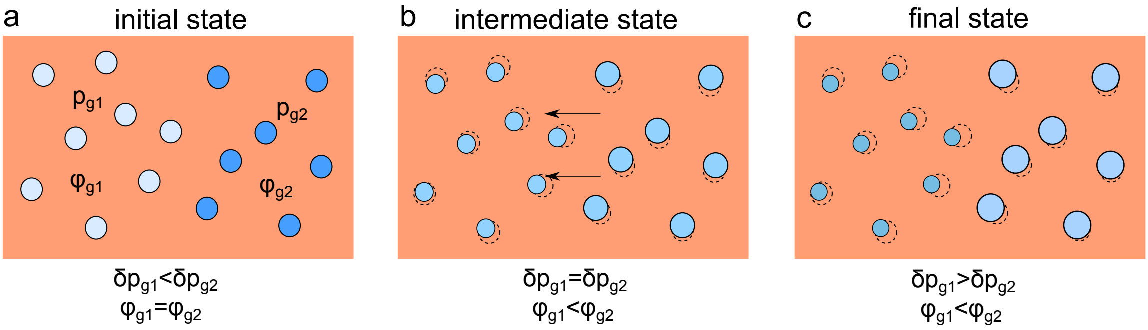

Figure 5.3: Sketch of the adaptation of magma in a closed box to a non-uniform increase in the gas pressure ($p_{g2} > p_{g1} > p_m$). (a) Initial state. p_{g2} is higher, relative to p_m, than p_{g1} ($\delta p_{g2} > \delta p_{g1}$, with $\delta_p = p_g - p_m$). Magma moves to compensate this discrepancy. (b) Intermediate step. $p_{g2} = p_{g1}$ ($\delta p_{g2} > \delta p_{g1}$), but the porosity is not homogeneous, and the magma is not in an equilibrium state yet (section 5.1.1 and 5.1.3). (c) Final, or equilibrium state.

simplicity, we also assume that the magma is composed of an incompressible liquid phase and a compressible gas phase, between which no material exchange occur. In this precise case, a uniform gas pressure increase inside the bubbles will cause no change in the magma total volume (the box is closed) and porosity. Besides, the magma local volume and local porosity will not change either, because the pressure disequilibrium and porosity are the same everywhere in the volume.

However, if the variations in gas pressure are not uniform (fig. 5.3a), the disequilibrium between ambient and gas pressure is not uniform anymore. It triggers changes in the magma porosity to compensate these differences. Magma porosity increases where the differences $p_g - p_m$ are the highest, and decreases where they are the lowest, causing bulk magma flow in response to compaction/dilatation gradients (fig. 5.3b). Since volume variations depend both on this pressure difference and on the porosity, the final state may correspond to an assembly of batches of magma with a higher porosity and lower pressure difference, and batches of magma with a reduced porosity and increased pressure difference (fig. 5.3c).

Such systems are well described by eulerian two-phase flow models, that take into account interactions between the two phases (gas and incompressible liquid phase) and spatial variations of the parameters we described here.

5.1.2 Magma and gas diphasic flow

Bercovici et al. (2001), developed a numerical model for a two-phase flow of two incompressible phases with similar properties. In the momentum conservation equations proposed for the matrix m and the fluid f phases, they indroduce the interfacial force term, that accounts for the forces applied at the interface between the two phases. This interfacial force term is decomposed as the assemblage of (1) surface tension forces, (2) drag forces and (3) pressure forces. The interfacial force applied to the matrix h_m is written as a body force, since it is averaged on a small volume, in which the interface between the two phases, whose orientation is assumed isotropic, is represented by the interface density number α.

The expressions of the interfacial force terms for the matrix h_m and fluid h_f are written as follows :

$$\begin{aligned} h_f &= c\Delta v + (\varphi p_f + (1-\varphi)p_m)\nabla\varphi + \varphi\nabla(\Gamma\alpha) \qquad (5.1) \\ h_m &= -c\Delta v - (\varphi p_f + (1-\varphi)p_m)\nabla\varphi + (1-\varphi)\nabla(\Gamma\alpha) \end{aligned}$$

where $\Delta v = v_m - v_f$, with v_m and v_f the matrix and fluid velocities. p_m and p_f are the matrix and fluid pressures, φ is the fluid volume fraction, Γ is the surface tension at the matrix–fluid interface, and c is the drag coefficient.

In this expression, the first term, $c\Delta v$, is the drag force. At the interface, magma and gas velocities have to be the same, to respect continuity conditions. This condition limits gas and magma flow the same way a no slip condition at the conduit walls limits bulk magma flow. The resulting force is called drag force, and its expression depends on the difference between the matrix and fluid velocities Δv (averaged locally). The third term, $\varphi\nabla(\Gamma\alpha)$, corresponds to the surface tension force. At the magma–gas interface, surface tension plays an important role during bubble nucleation. The bubble overpressure has to be high enough to overcome this surface tension and create the bubble (Navon and Lyakhovsky, 1998). Its influence is however negligible for bigger bubbles. Eventually, the second term, $(\varphi p_f + (1-\varphi)p_m)\nabla\varphi$ for the fluid phase, refers to pressure forces at the interface. In the case of a low gas pressure in a magma–gas flow, the pressure difference between gas and mush would apply a traction at the interface towards the gas phase. In the same way, the reaction force to this traction applied by the mush (melt+crystals) would prevent the bubble to collapse and cause the gas to stay at low pressure. This pressure force opposes to the pressure force term in the general momentum equation, for each phase.

The momentum equations defined by Bercovici et al. (2001), for a two-phase flow with incompressible phases, were adapted to magma and gas creeping flow (acceleration and inertia are negligible in the momentum equation) by Michaut and Bercovici (2009). For magma and gas two-phase flow , the effect of surface tension is neglected, as it is only significant for tiny bubbles during nucleation.

$$\begin{aligned} 0 &= -\varphi_g \left[\nabla p_g + \rho_g g z\right] + c\Delta v \qquad (5.2)\\ 0 &= -(1-\varphi_g)\left[\nabla p_{mc} + \rho_{mc} g z\right] + \nabla \cdot \left[(1-\varphi_g)\tau_m\right] - c\Delta v + \Delta p \nabla \varphi_g \end{aligned}$$

with $\Delta q = q_m - q_g$ for any quantity q. Neglecting the gravitational force for the gas, the first equation is equivalent to a Darcy equation, with $c = \mu_g \varphi_g^2 / K$ (where K is the viscous permeability) (Bercovici et al., 2001). Such two-phase flow models were applied for studying magma degassing in 1D conduit flow models (Michaut and Bercovici, 2009; Michaut et al., 2013). They however do not take into account degassing conditions evolution with depth.

5.1.3 Adaptation to 2D conduit flow modelling

In order to include the observations made in the precedent sections in the 2D degassing model, we need to adapt the conservation equations we presented in chap. 1. We still aim at working with two momentum equations: one for the gas (Darcy), and the other for bulk magma (gas+melt+crystals). Combining the two momentum equations from Michaut and Bercovici (2009) (φ (5.3)-1 + (1-φ) (5.3)-2), we end up with an average momentum equation for magma–gas flow (5.3). We can see that in this equation the interfacial forces applied to gas and to magma cancel each other. The difference in pressure between magma and gas should however still act on magma–gas flow. At the magma–gas interface, we saw that a decrease in gas pressure would apply a traction force to magma, and that the viscous reaction force from the magma would apply a traction to the gas phase, preventing bubble collapse. Although these forces evolve with time and bulk flow, they act as pressure forces that interact with pressure forces internal to each phase. In the average equation, although interfacial forces are no longer present, the pressure difference between magma and gas is taken into account within the bulk pressure term.

$$0 = \nabla \bar{p} - \bar{\rho} g z + \nabla \cdot \left[(1-\varphi_g)\bar{\tau}_m\right] \qquad (5.3)$$

with $\bar{q} = \varphi q_g + (1-\varphi) q_m$ for any quantity q. The equations we used for magma bulk flow in chap. 1 are slightly different from the average expression derived from the Michaut and Bercovici (2009) equations. We indeed used expressions for the bulk viscosity and volume viscosity that were derived from multiphase models and experiments, and represent the magma bulk properties. Besides, we did not assume a creeping flow and therefore did not neglect acceleration and inertia terms. One major default in these equations, however, is that we assumed that magma and gas pressures were equal. Using this assumption, our expression for the magma bulk pressure do not account for possible existing differences in magma and gas pressures. In the following paragraphs, we therefore decide to use the average pressure force expression defined by Bercovici et al. (2001) that appears in the average momentum equation 5.3:

$$\bar{P} = \varphi p_g + (1 - \varphi) p_m \tag{5.4}$$

5.2 General conservation equations

Using the mean pressure as defined by Bercovici et al. (2001), we write the mass and momentum conservations.

$$\nabla \cdot (\rho \mathbf{u}) = 0 \tag{5.5}$$

$$\rho(\mathbf{u} \cdot \nabla)\mathbf{u} = \nabla \cdot [-\bar{P}\bar{\mathbf{I}} + \eta(\nabla \mathbf{u} + (\nabla \mathbf{u}^T) + (\kappa - \frac{2}{3}\eta)(\nabla \cdot \mathbf{u})\bar{\mathbf{I}}] + \rho \mathbf{g} \tag{5.6}$$

Since

$$\bar{P} = p_m + \varphi_g \delta p \tag{5.7}$$

with $\delta p = (p_g - p_m)$. Equation (5.6) can also be arranged in

$$\rho(\mathbf{u} \cdot \nabla)\mathbf{u} = \nabla \cdot [-p_m\bar{\mathbf{I}} + \eta(\nabla \mathbf{u} + (\nabla \mathbf{u}^T) + (\kappa - \frac{2}{3}\eta)(\nabla \cdot \mathbf{u})\bar{\mathbf{I}}] + \rho \mathbf{g} - \nabla(\varphi_g \delta p) \tag{5.8}$$

In this model, changes in flow conditions also depend on the gradients of porosity and pressure disequilibrium. This matches with the Lagrangian models and general trends we described in section 5.1.

In the next sections, we propose an adaptation of the magma and gas flow models equations so that the bulk flow model can be solved with equation 5.8. Unlike our precedent model, gas and magma pressure are different. Consequently the porosity cannot be determined from the magma pressure. In the following equations, we assume that the magma is composed by an incompressible phase, that includes the melt and crystals phases, and by a compressible gas phase. We neglect the volume variations associated with material (water) exchange between the melt and gas phases.

5.3 Closed system, impermeable magma

In this section, we consider the case where magma is not permeable and gas stays within the magma during its ascent towards the surface. In this case, gas pressure does not vary due to degassing. However, the magma is submitted to decompression, triggering bubble growth and flow conditions evolution with depth. The steady state solution for this model should be very close to the magma bulk flow solution in closed system obtained in chap. 1, except for kinematic effects of bubble growth time scale that are taken into account in this case.

Because the magma is not permeable and gas does not separate from the magma, the volatile mass fraction remains constant with depth here.

5.3.1 Volume fractions

Melt and crystals phases are incompressible. The mass conservation for the incompressible phase (melt+crystals), hereafter called mush, can then be written:

$$\frac{\partial \rho_{mc}\varphi_{mc}}{\partial t} + \nabla \cdot (\rho_{mc}\varphi_{mc}\mathbf{u}) = 0 \tag{5.9}$$

with ρ_{mc} the density of the mush, φ_{mc} its volume fraction, and $\mathbf{u}$ its velocity. Since melt and crystals have constant relative mass fractions, the density of the incompressible phase remains constant, and (5.9) reduces to an incompressible phase volume fraction conservation equation:

$$\frac{\partial \varphi_{mc}}{\partial t} + \nabla \cdot (\varphi_{mc} u) = 0 \tag{5.10}$$

From this equation, knowing the proportions of melt and crystals, it is possible to get the volume fractions of melt and of crystals:

$$\begin{aligned} \varphi_m &= \varphi_{mc}(1 - \varphi_{c,0}) \qquad (5.11) \\ \varphi_c &= \varphi_{mc}\varphi_{c,0} \end{aligned}$$

where $\varphi_{c,0}$ is the volume fraction of crystals in the magma when no gas is present. Besides, since the magma is composed of the incompressible melt and crystal phases and of the gas phase, we have access to the volume fraction of gas:

$$\varphi_g = 1 - \varphi_{mc} \tag{5.12}$$

5.3.2 Gas pressure

The total mass fraction of water relative to melt C_{H2O} remains constant. We assume that the mass fraction of dissolved water relative to melt C_m only depends on the pressure within the melt (p_m) and is always at equilibrium with it (the melt is not oversaturated).

$$C_m = \min(C_{H2O,0}, K_h\sqrt{p_m}) \tag{5.13}$$

with $C_{H2O,0}$ the initial total mass fraction of water relative to melt, which here equals C_{H2O}, and K_h the Henry's constant for water. Knowing the volume fraction of melt and the mass fraction of dissolved water in melt, we can calculate the total mass of water vapor m_g in a unit of magma.

$$m_g = C_m \varphi_m \rho_m \tag{5.14}$$

with ρ_m the melt density. We assume here that the density of the water dissolved within the melt is also ρ_m. Knowing the volume fraction of gas, and assuming that the water vapor behaves as an ideal gas, we can calculate the gas pressure.

$$\rho_g = \frac{m_g}{\varphi_g} \tag{5.15}$$

$$p_g = \frac{RT\rho_g}{M} \tag{5.16}$$

with R the ideal gas constant, T the magma temperature, and M the water molar mass. Combining these equations results in:

$$p_g = \frac{RTC_m(1-\varphi_g)\rho_m}{M\varphi_g} \tag{5.17}$$

5.4 Permeable magma

In this section, we consider that the magma can be permeable, allowing gas flow and possible loss. Gas pressure can vary due to degassing. Therefore, the total mass fraction of volatiles in the conduit can vary with time and depth. We also need to take into account mass conservation for water.

5.4.1 Volume fractions

The volume fraction of melt and crystals, incompressible, is still calculated using (5.10), and the volume fraction of gas comes from (5.12).

5.4.2 Mass conservation for water

The mass of water, in a volume of magma, varies with (1) the flux of dissolved water, associated with magma flow and (2) the flux of water vapor that depends on both the magma flow (bubble advection) and the gas permeable flow. Here,w consider that gas flow is laminar and Darcian.

5.4.2.1 Permeable gas flow

The Darcian velocity for the gas is obtained from:

$$u_d = \frac{-k_1 \nabla p_g}{\mu_g} \tag{5.18}$$

5.4.2.2 Mass conservation for water

Knowing magma velocity and gas Darcian velocity, we write the mass conservation for water:

$$\frac{\partial m_{H2O}}{\partial t} = -\nabla \cdot (C_m \varphi_m \rho_m u + \rho_g (u_d + \varphi_g u)) \tag{5.19}$$

5.4.3 Water repartition between the melt (dissolved) and gas phases

5.4.3.1 Dissolved water

The mass of dissolved water depends on the pressure of the magma and on the total amount of water. If magma pressure is high, and the melt is undersaturated with water, the water tends to be completely dissolved within the melt. Conversely, if the magma pressure is lower and the melt is oversaturated with water, the amount of dissolved water is proportional to magma pressure and melt amount.

$$m_m = \min(m_{H2O}, K_h\sqrt{p}\varphi_l\rho_m) \tag{5.20}$$

C_m can be retrieved from m_m:

$$C_m = \frac{m_m}{\rho_m\varphi_l + m_m} \tag{5.21}$$

5.4.3.2 Gas

The excess water remains in the gas phase.

$$m_g = m_{H2O} - m_m \tag{5.22}$$

5.4.4 Gas pressure

Knowing the mass and volume fraction of gas, we get the gas density.

$$\rho_g = \frac{m_g}{\varphi_g} \tag{5.23}$$

Assuming that water vapor behaves as an ideal gas:

$$p_g = \frac{RT\rho_g}{M} \tag{5.24}$$

5.5 Conclusion and perspectives

We presented an adaptation of conduit flow numerical modelling that fully couples magma and gas flow in time for transient regime. This method should be used for future conduit flow modelling, in particular for studying the evolution of conduit flow conditions along with an eruption.

We are currently working on implementing this numerical model. The first step will be to solve simple problems with known solutions using this model. The model will then be applied for a closed system, and results should be compared to the solution described in chap. 1. Eventually, the evolution of the system in open conditions using this method may give new insights on transitions from effusive to explosive eruptive regime.

Conclusion

This work, based on numerical simulations, experimental samples analysis, and the interpretation of ground deformation observed in the near field at Merapi Volcano, aimed at improving our understanding of volcanic activity evolution at andesitic volcanoes. Numerical modelling (e.g. Jaupart and Allègre, 1991; Diller et al., 2006; Collombet, 2009), together with field observations (e.g. Edmonds et al., 2003; Druitt and Kokelaar, 2002) and experimental investigations (e.g. Spieler et al., 2004; Kueppers et al., 2006; Mueller et al., 2011) have provided evidence for the important role of degassing processes occurring in the conduit in the evolution of volcanic activity. Although several conduit flow models investigated the influence of gas loss to the country rock on flow conditions (e.g. Jaupart and Allègre, 1991; Diller et al., 2006), they are often limited to the introduction of a sink term that does not evolve with time. Collombet (2009) first designed a 2D conduit flow model that takes into account gas permeable flow in both horizontal and vertical directions within the conduit. Her study was however restricted to steady–state effusive flow conditions.

We here worked on better understanding the evolution of gas loss conditions along with an eruption from 2D numerical modelling in transient regimes. We identified parameters that control gas loss in the upper conduit, and their possible implication in terms of volcanic activity evolution. We also evaluated the usefulness of near field ground deformation for retrieving flow conditions in the conduit.

Advances in gas loss modelling

We propose a new 2D time–dependent numerical model for gas loss in the upper conduit at andesitic volcanoes. This model is one–way coupled with magma flow and uses magma flow conditions as entrance parameters. It accounts for gas flow in both horizontal and vertical directions, and its possible leakage at the rop of the conduit and to the country rock. It also allows for solving gas flow in the conduit with conditions that evolve with time, and can therefore be used to study the evolution of gas loss along with an eruption. Using this model, we studied the influence on gas loss of several parameters that may evolve during an eruption. We provide evidence that horizontal gas flux in the conduit is of primary importance, as gas is mainly lost at the conduit walls. These results highlight the importance of considering 2D modelling for understanding degassing in the conduit, since gas flux depends on the horizontal variations of permeability and pressure between the conduit center and edges.

We also propose an adaptation of magma flow modelling in the conduit so that it can be fully coupled, in time, with gas loss. This new coupling model, that still needs to be implemented, provides the advantage of keeping the one phase assumption for magma bulk flow in 2D. This indeed remains today a powerful tool for taking the magma complex rheology into account without generating too much numerical complexity. In addition, contrary to existing models, this coupling model allows for studying the evolution of magma flow and degassing during transient regimes in 2D. Although results are not available yet, they may provide important insights on flow conditions evolution during an eruption. In particular, the evolution of a plug at the top of the conduit, or that of the gas–depleted layers observed in steady–state effusive conditions by Collombet (2009) could be studied. The influence of external factors, such as dome emplacement or collapse, may also be investigated in greater details.

Parameters controlling gas loss

Using the time–dependent model we developed for gas loss, we investigated the influence on degassing of parameters that may evolve during a dome–forming event. Aside from providing evidence that hazard would increase with dome growth because of gas pressure increase in the shallow part of the conduit, our results give insights on the parameters that control gas loss in the conduit. We show that gas loss is extremely dependent on magma permeability and on pressure conditions in the rock surrounding the conduit, while the dome permeability has almost no influence, contrary to the common idea. The surrounding rock permeability has only a second–order influence that depends on its proximity with the magma permeability range of values (Chevalier et al., 2017).

We further investigated the influence of permeability development in the conduit on gas loss, that is poorly constrained today (Gonnermann and Manga, 2007; Rust and Cashman, 2011). We compared gas loss solutions obtained from different permeability laws, including one new permeability law that we designed from experimental samples analysis and that can be easily integrated into 2D gas flow modelling. Results provide evidence that the percolation threshold, which characterises the very moment when magma becomes permeable, as well as the way magma permeability evolves with porosity have a huge influence on gas loss. We show in particular the important influences of the bubble number density and of the bubble size distribution, that are controlling parameter for permeability development in the conduit. We provide evidence that the evolution of these parameters during an eruption, for example due to the occurrence in the conduit of an additional nucleation event, may have a huge impact on magma permeability, and consequently on the evolution of the eruptive regime.

All these results provide evidence that gas loss in the upper conduit mainly occurs at the conduit walls, and therefore depends on the ability for the gas to flow from the conduit center to the conduit margins. This confirms the importance of fully coupling magma with gas flow in time for studying gas loss evolution. The formation of gas–depleted layers at the conduit walls for example, as observed by Collombet (2009), might limit gas escape at the conduit margins. Gas loss may therefore decrease, and make flow conditions to evolve towards more explosive conditions.

Magma permeability development in the conduit

Although being a controlling parameter for gas flow within the conduit, permeability evolution in ascending magma is poorly constrained (Gonnermann and Manga, 2007; Mueller et al., 2005; Rust and Cashman, 2011). Working on experimental samples analysis, we aimed at better understanding the large variability of permeability–porosity relationships observed in silicic samples. We propose an expression for the percolation threshold that succeeds in classifying a large dataset of permeable and impermeable silicic samples (Burgisser et al., 2017). Using this percolation threshold, we also develop a new permeability law that unifies most of the permeability–porosity relationships observed in silicic samples (Burgisser et al., 2017). In particular, our observations of permeability development in silicic magma provide evidence for the essential roles of the bubble number density and of the bubble size distribution spread. We indeed observe that an increase in the bubble number density tends to decrease the bulk magma permeability, although it also decreases the percolation threshold, therefore leading to an earlier permeability development. An increase in the bubble size distribution spread, on another hand, tends to facilitate the permeability development.

We also adapted our permeability law so that it accounts for bubble deformation due to flow conditions in the conduit. Our work is however based on a small number of samples having experienced deformation. Moreover, this deformation is relatively small compared with the deformation that bubbles may experience in the conduit. In addition, it is limited to pure shear, while in the conduit bubble deformation is mainly caused by simple shear (e.g. Rust et al., 2003; Okumura et al., 2010). Further investigating the influence of bubble deformation on permeability would however be of great interest for conduit flow modelling. It is indeed associated with the development of a possibly important permeability anisotropy (Bouvet de Maisonneuve et al., 2009, e.g). This permeability anisotropy may significantly influence gas flux towards the conduit margins, therefore impacting on gas loss and on the eruptive regime evolution.

The permeability law we developed succeeded in reassembling a large range of permeability–porosity relationships. It is however restricted to the permeability developed from bubble coalescence. Recent studies on permeability in effusive conditions highlighted the controlling role of fractures in magma permeability at low porosities (Kushnir et al., 2016). Although magma fracturing is restricted to the conduit shallow part, this may significantly influence gas overpressure build up in the shallow conduit and dome. Besides, Rust and Cashman (2004) evidenced the hysteresis behaviour of magma permeability. This also is not taken into account in the permeability law we developed, although it might have a huge influence it the case of magmas that have already experienced degassing. In the case of the formation of gas–depleted layers in the conduit as observed by Collombet (2009), taking this hysteresis effect into account may be extremely important for studying gas loss evolution.

Ground deformation

We evaluate the feasibility of using ground deformation observation in the near field for monitoring magma flow evolution within the conduit. We interpret ground deformation observed at the Merapi volcano using simple conduit flow conditions as deformation sources. Conduit flow models provide important clues for interpreting the observed deformation, and we were able to retrieve part of the deformation observed in the near field, for which Mogi source models didn't produced satisfactory results. In the case of the Merapi volcano, the complexity of the summit rheology and geology, together with the sparsity of the data however make it very complex to constrain flow conditions from observed deformation. This may however be applicable to other volcanoes, and should be further investigated.

In addition, ground deformation is not the only observable geophysical signal that is linked with conduit flow conditions and degassing processes. Gas emissions variations correlated with volcanic activity have indeed been observed at many andesitic volcanoes (Edmonds et al., 2003; Johnson et al., 2008; Sheldrake et al., 2016). Besides, shallow seismicity is thought to be linked with degassing mechanisms, as well as with the magma rheology in the upper conduit (Voight et al., 2006; Neuberg, 2000). Magma extrusion rate can also be quantified using a diversity of observation techniques (Pallister et al., 2013). Further development of conduit flow modelling would help understanding these observations, and their link with magma flow conditions and gas loss. This may provide clues for better interpreting these data and, by corroborating interpretations, for getting information on the evolution of conditions in the conduit during an eruption.

In this thesis, we provided evidence that gas loss in the conduit mainly occurs at the conduit margins, were gas flows to the country rock. We demonstrated that gas loss is controlled by the magma permeability and by pressure conditions in the surrounding rock, because these two parameters are determinant for gas flux from inside the conduit to the conduit edges and then to the country rock. Further investigations on magma permeability evolution with flow conditions and degassing history, as well as on conditions in the rock surrounding the conduit are still needed. However, the results we presented here highlight the primary importance of coupling gas loss with magma flow conditions in a full way for studying transient regimes. Future results from the model adaptation we proposed in this way may give important clues for better understanding the evolution of flow conditions and of volcanic activity with time, as well as for interpreting geophysical signals observed at andesitic volcanoes.

List of Symbols

Constants

Symbol	Name	Unit	value
R	Ideal gas constant	J.mol^{-1}.K^{-1}	8.314
g	Gravity acceleration	m.s^{-2}	9.81
M	Water molar mass	g.mol^{-1}	0.018
P_a	Atmospheric pressure	Pa	10^5
ρ_{H_2O}	Water density	kg.m^{-3}	1000
μ_g	Gas viscosity	Pa.s	$1.5{\cdot}10^{-5}$
K_h	Water solubility coefficient		$4.11 \cdot 10^{-6}$
n	Water solubility pressure exponent		0.5
E	Edifice rocks Young's modulus	Pa	1
ν	Edifice rocks Poisson's ratio		0.25
ρ_{H_2O}	Water density	kg.m^{-}3	1000

Parameters and variables – magma and gas flow modelling

Symbol	Name	Unit
	Composition	
$C_{H_2O,0}$	Initial mass fraction of water relative to melt	wt%
C_{H_2O}	Total mass fraction of water relative to melt	wt%
C_s	Mass fraction of dissolved water in saturated melt	wt%
C_m	Mass fraction of dissolved water in the melt	wt%
C_l	Mass fraction of dissolved water in the melt at saturation	wt%
C_g	Mass fraction of water vapor relative to melt	wt%
φ_g	Gas volume fraction	
φ_c	Crystals volume fraction	
φ_m	Melt volume fraction	
$\varphi_{c,0}$	Initial crystals volume fraction	
$\varphi_{m,0}$	Initial melt volume fraction	
ϕ_g	Gas volume fraction	vol%
ϕ_{cr}	Porosity threshold for percolation	vol%
ϕ_t	Total porosity	vol%

Symbol	Name	Unit
ϕ_c	Connected porosity	vol%
S_0	Volume of groundmass attached to one bubble	m^3
S_b	Volume of gas corresponding to one bubble	m^3
r_b	Bubble radius	m
d_b	Bubble diameter	m
N_m	Bubbles number density relative to groundmass	m^{-3}
	Magma properties	
η	Magma bulk dynamical viscosity	Pa·s
η_m	Melt dynamical viscosity	Pa·s
η_{rc}	Crystals dynamical viscosity coefficient	Pa·s
η_{mc}	Groundmass dynamical viscosity	Pa·s
η_{rb}	Bubbles dynamical viscosity coefficient	Pa·s
η_1	Bubbles dynamical viscosity coefficient end-member 1	Pa·s
η_2	Bubbles dynamical viscosity coefficient end-member 1	Pa·s
μ_g	Gas dynamical viscosity	Pa·s
ρ	Magma bulk density	kg·m^{-3}
ρ_m	Melt density	kg·m^{-3}
ρ_g	Gas density	kg·m^{-3}
ρ_c	Crystals density	kg·m^{-3}
ρ_{H_2O}	Water density	kg·m^{-3}
κ	Magma bulk volume viscosity	Pa·s
T	Magma temperature	K
p	Magma pressure	Pa
p_g	Gas pressure	Pa
δp	Gas pressure variation (chap. 2 and 3)	Pa
δp	Pressure difference between magma and gas (chap. 5)	Pa
$\mathbf{u}$	Magma velocity	m·s^{-1}
$\mathbf{u_d}$	Darcian velocity for the gas	m·s^{-1}
$\mathbf{u_f}$	Forchheimer velocity for the gas	m·s^{-1}
$\mathbf{u_a}$	Gas advection velocity	m·s^{-1}
$Q_{melt \to gas}$	Gas exsolution rate	kg·s^{-1}
$\dot{\gamma}$	Shear strain rate	$^{-1}$
$\ddot{\gamma}$	Shear strain rate time derivative	$^{-1}$
Γ	Bubble/melt surface tension	N·m^{-1}
λ	Bubble relaxation time	s
α	Magma–gas interface density	m^{-1}
C_a	Capillary number	
C_d	Dynamic capillary number	
Z_g	Nucleation depth	m
Re	Reynolds number for the gas	
m_g	Mass of gas in a unit volume of magma	kg
m_m	Mass of dissolved water in a unit volume of magma	kg
m_{H_2O}	Total mass of water in a unit volume of magma	kg
K or k_1	Magma viscous permeability	m^2

Symbol	Name	Unit
K_V	Magma vertical viscous permeability	m^2
K_H	Magma horizontal viscous permeability	m^2
k_2	Magma inertial permeability	m
K_H	Rock viscous permeability	m^2
	Bubble network characteristics	
d_a	Bubble diameter	m
d_t	Throat diameter	m
z_m	Interbubble distance	m
N_m	Bubbles number density relative to groundmass	m^{-3}
σ_a/d_a	Bubble size distribution spread	
τ	Bubble network tortuosity	
θ	Bubble orientation angle relative to flow	°
l	Bubble semi-major axis	m
b	Bubble semi-minor axis	m
a	Bubble equivalent sphere radius	m
D	Bubble deformation parameter	
e_1	Bubble elongation direction	
e_2	Bubble elongation orthogonal direction	
ε	Bubble elongation coefficient	
χ	Bubble flattening coefficient	
	Geometry	
H	Conduit length	m
a_c	Conduit radius	m
r_{rock}	Surrounding rock shell radius	m
R_s	Deformable rock radius	m
H_s	Deformable rock depth	m
r	Radial spatial coordinate	m
z	Vertical spatial coordinate	m
	Boundary conditions	
P_{top}	Pressure at the conduit top	Pa
P_{bot}	Pressure at the conduit bottom	Pa
P_c	Overpressure in the magma chamber	Pa
P_{rock}	Pressure in the surrounding rock	Pa
$P_{rock,0}$	Pressure in the surrounding rock far from the conduit	Pa
dP	Pressure difference between $P_{rock,0}$ and conduit pressure	Pa
c	Conduit pressurising coefficient	
K_{rock}	Surrounding rock permeability	m^2
Z_{lith}	Brittle to ductile (Hydro- to lithostatic) transition depth	m

Parameters and variables – ground deformation

Symbol	Name	Unit
a_m	Mogi sphere radius	m
H_m	Mogi sphere depth	m
P_m	Pressure applied at the Mogi sphere edges	m
H	Conduit length	m
a_c	Conduit radius	m
H_p	Plug thickness	m
P_c	Overpressure pressure at the conduit bottom	Pa
P_p	Overpressure beneath the plug	Pa
μ_m	Magma viscosity	Pa·s^{-1}
μ_p	Plug viscosity	Pa·s^{-1}
Q	Extrusion rate at the conduit vent	m^3·s^{-1}
E	Edifice rocks' Young's Modulus	Pa
r	radial spatial coordinate	m
z	vertical spatial coordinate	m
δr	Radial displacement	m
δz	Radial displacement	m
R	Root Mean Square Error	m
f	Pressure fitting coefficient	
d_i	Recorded displacement at station i	m
m_i	Modeled displacement at station i	m
ε_i	Error on displacement at station i	m

Bibliography

Abdullah, N., Valette, B., Lesage, P., et al., 2017. Multi-scale seismic tomography of the Merapi-Merbabu volcanic complex, Indonesia. EGU General Assembly, 19423.

Albino, F., 2011. Modélisation des intéractions magma-encaissant : application aux zones de stockage et aux conduits de volcans andésitiques. Ph.D. thesis, Université de Grenoble.

Albino, F., Pinel, V., Massol, H., Collombet, M., 2011. Conditions for detection of ground deformation induced by conduit flow and evolution. Journal of Geophysical Research 116, B06201.

Alidibirov, M., Dingwell, D., 1996. Magma fragmentation by rapid decompression. Letters to Nature 380, 146–148.

Alidibirov, M., Dingwell, D., 2000. Three fragmentation mechanisms for highly viscous magma under rapid decompression. Journal of Volcanology and Geothermal Research 100, 413–421.

Allard, P., 1983. Forecasting Volcanic Events. Ch. The origin of hydrogen, carbon, sulphur, nitrogen and rare gases in volcanic exhalations; evidence from isotope geochemistry, pp. 337–386.

Allard, P., 2014. Magma degassing constraints on the budget and dynamics of background dome-forming eruptive activity at Merapi volcano. Cities on Volcanoes 8, Yogyakarta, September 2014, 1.V. 243.

Anderson, S., Fink, J., 1990. Lava flows and domes. Springer Berlin Heidelberg, Ch. The development and distribution of surface textures at the Mount St. Helens dome, pp. 25–46.

Andreastuti, S., Alloway, B., Smith, I., 2000. A detailed tephrostratigraphic framework at Merapi Volcano, Central Java, Indonesia: implications for eruption predictions and hazard assessment. Journal of Volcanology and Geothermal Research 100, 51–67.

Arámbula-Mendoza, R., Lesage, P., Valdés-Gonzàlez, C., Varley, N., Reyes-Dàvila, G., Navarro, C., 2011. Seismic activity that accompanied the effusive and explosive eruptions during the 2004-2005 period at Volcán de Colima, Mexico. Journal of Volcanology and Geothermal Research 205, 30–46.

Bagdassarov, N., Dingwell, D., 1992. A rheological investigation of vesicular rhyolite. Journal of Volcanology and Geothermal Research 50, 307–322.

Ball, J., Stauffer, P., Calder, E., Valentine, G., 2015. The hydrothermal alteration of cooling lava domes. Bulletin of Volcanology 77, 102.

Barclay, J., Herd, R., Edwards, B., Christopher, T., Kiddle, E., Plail, M., Donovan, A., 2010. Caught in the act: implications for the increasing abundance of mafic enclaves during the recent eruptive episodes of the Soufrière Hills Volcano, Montserrat. Geophysical Research Letters 137.

Barclay, J., Riley, D., Sparks, R., 1995. Analytical models for bubble growth during decompression of high viscosity magmas. Bulletin of Volcanology 57, 422–431.

Barclay, J., Rutherford, M., Carroll, M., Murphy, M., Devine, J., Gardner, J., Sparks, R., 1998. Experimental phase equilibria constraints on pre-eruptive storage conditions of the Soufriere Hills magma. Geophysical Research Letters 25, 3437–3440.

Beauducel, F., Carbone, D., 2015. A strategy to explore the topography-driven distortions in the tile field induced by a spherical pressure source: the case of mt Etna. Geophysical Journal International 201, 1471–1481.

Beauducel, F., Cornet, F., 1999. Collection and three-dimensional modeling of gps and tilt data at merapi volcano, java. Journal of Geophysical Research 104, 725–736.

Beauducel, F., Cornet, F.-H., 2000. Constraints on magma flux from displacement data at Merapi Volcano, Java, Indonesia. Journal of Geophysical Research 105, 8193–8203.

Beauducel, F., Nandaka, M., Cornet, F., Diament, M., 2006. Mechanical discontinuities monitoring at Merapi volcano using kinematic GPS. Journal of Volcanology and Geothermal Research 150, 300–312.

Bercovici, D., Ricard, Y., Schubert, G., 2001. A two-phase model for compaction and damage. 1. General Theory. Journal of Geophysical Research 106 no. B5, 8887–8906.

Berthommier, P., Camus, G., Condomines, M., Vincent, P.-M., 1990. Le Merapi (Centre Java): Eléments de chronologie d'un strato-volcan andésitiquue. Comptes Rendus de l'Académie des Sciences de Paris 311 no. 2, 213–218.

Blower, J., 2001. Factors controlling permeability-porosity relationships in magma. Bulletin of Volcanology 63, 497–504.

Blower, J., Mader, H., Wilson, S., 2001. Coupling of viscous and diffusive controls on bubble growth during explosive volcanic eruptions. Earth and Planetary Science Letters 193, 47–56.

Blundy, J., Cashman, K., 2005. Rapid decompression-driven crystallization recorded by melt inclusions from Mount St. Helens volcano. Geology 33 no.10, 793–796.

Blundy, J., Cashman, K., Berlo, K., 2008. A volcano rekindled: The renewed eruption of Mount St. Helens, 2004-2006. U.S. Geological Survey Professional Paper, Ch. Evolving magma storage conditions beneath the Mount St. Helens inferred from chemical variations in melt inclusions from the 1980-1986 and current (2004-2006) eruptions., pp. 755–790.

Bluth, G., Rose, W., 2004. Observations of eruptive activity at Santiaguito Volcano, Guatemala. Journal of Volcanology and Geothermal Research 136, 297–302.

Bonaccorso, A., Currenti, G., Del Negro, C., Boschi, E., 2010. Dike deflection modelling for inferring magma pressure and withdrawal, with application to Etna 2001 case. Earth and Planetary Science Letters 293, 121–129.

Borosiva, A., Martel, C., Gouy, S., Pratomo, I., Sumarti, S., Toutain, J., Bindeman, I., de Parseval, P., Metaxian, J.-P., Surono, 2013. Highly explosive 2010 Merapi eruption: Evidence for shallow-level crustal assimilation and hybrid fluid. Journal of Volcanology and Geothermal Research 261, 193–208.

Botton, S., Duquenne, F., Egels, Y., Even, M., Willis, P., 1997. Gps localisation et navigation. Ed. Paris Hermès.

Bouvet de Maisonneuve, C., Bachman, O., Burgisser, A., 2009. Characterization of juvenile pyroclasts from the Kos Plateau Tuff (Aegean Arc): Insights into the eruptive dynamics of a large rhyolitic eruption. Bulletin of Volcanology 71, 643–658.

Boué, A., Lesage, P., Cortés, G., Valette, B., Reyes-Dávila, G., 2015. Real-time eruption forecasting using the material Failure Forecast Method with Bayesian approach. Journal of Geophysical Research : Solid Earth 120.

Brugger, C., Hammer, J., 2010. Crystallization kinetics in continuous decompression experiments: Implications for interpreting natural magma ascent processes. Journal of Petrology 51 no. 9, 1941–1965.

Budi-Santoso, A., Lesage, P., Dwiyono, S., Sumarti, S., Subandriyo, Surono, Jousset, P., Metaxian, J., 2013. Analysis of the seismic activity associated with the 2010 eruption of Merapi Volcano, Java. Journal of Volcanology and Geothermal Research 261, 153–170.

Burgisser, A., Chevalier, L., Gardner, J., Castro, J., 2017. The percolation threshold and permeability evolution of ascending magmas. Earth and Planetary Science Letters.

Burgisser, A., Gardner, J., 2004. Experimental constraints on degassing and permeability in volcanic conduit flow. Bulletin of Volcanology 67, 42–56.

Burgisser, A., Poussineau, S., Arbaret, L., Druitt, T., Giachetti, T., Bourdier, J.-L., 2010. Pre-explosive conduit conditions of the 1997 Vulcanian explosions at Soufrière Hills Volcano, Montserrat: I. Pressure and vesiculatiry distributions. Journal of Volcanology and Geothermal Research 194, 27–41.

Byrdina, S., Friedel, S., Vandemeulebrouck, J., Budi-Santoso, A., Suhari, Suryanto, W., Rizal, M., Winata, E., Kusdaryanto, 2017. Geophysical image of the hydrothermal system of Merapi volcano. Journal of Volcanology and Geothermal Research 329, 30–40.

Camus, G., Gourgaud, A., Mossand-Berthommier, P.-C., Vincent, P.-M., 2000. Merapi (Central Java, Indonesia): An outline of the structural and magmatological evolution, with a special emphasis to the major pyroclastic events. Journal of Volcanology and Geothermal Research 100, 139–163.

Canedo, E., Favelukis, M., Tadmor, Z., Talmon, Y., 1993. An experimental study of bubble deformation in viscous liquids in simple shear flow. American Institute of Chemical Engineering Journal 39, 553–559.

Carn, S., Krueger, A., Krotkov, A., Arellano, N., Yang, S., 2008. Daily monitoring of Ecuadorian volcanic degassing from space. Journal of Volcanology and Geothermal Research 176, 141–150.

Carr, B., Clarke, A., Vanderkluysen, L., 2016. The 2006 lava dome eruption of Merapi Volcano (Indonesia): Detailed analysis using MODIS TIR. Journal of Volcanology and Geothermal Research 311, 60–71.

Cashman, K., Blundy, J., 2000. Degassing and crystallization of ascending andesite and dacite. Phylosophical Transactions of the Royal Society of London A 358, 1487–1513.

Castro, J., Burgisser, A., Schipper, C., Mancini, S., 2012. Mechanisms of buble coalescence in silicic magmas. Bulletin of Volcanology 74, 2339–2352.

Chadwick, J., Troll, V., Ginibre, C., Morgan, D., Gertisser, R., Waight, T., Davidson, J., 2007. Carbonate assimilation at Merapi Volcano, Java, Indonesia: Insights from crystal isotope stratigraphy. Journal of Petrology 48 no. 9, 1793–1812.

Chadwick, J., Troll, V., Waight, T., van der Zwan, F., Schwarzkopf, L., 2013. Petrology and geochemistry of igneous inclusions in recent Merapi deposits: a window into the sub-volcanic plumbing system. Contributions to Mineralogy and Petrology 165, 259–282.

Chevalier, L., Collombet, M., Pinel, V., 2017. Temporal evolution of magma flow and degassing conditions during dome growth, insights from 2d numerical modeling. Journal of Volcanology and Geothermal Research.

Christopher, T., Blundy, J., Cashman, K., Cole, P., Edmonds, M., Smith, P., Sparks, R., Stinton, A., 2015. Crustal-scale degassing due to magma system destabilization and magma-gas decoupling at Soufrière Hills Volcano, Montserrat. Geochemistry, Geophysics, Geosystems 16, 2797–2811.

Christopher, T., Edmonds, M., Humphreys, M., Herd, R., 2010. Volcanic gas emissions from Soufrière Hills Volcano, Montserrat 1995-2009, with implications for maphic magma supply and degassing. Geophysical Research Letters 37, L00E04.

Christopher, T., Humphreys, M., Barclay, J., Genareau, K., De Angelis, S., Plail, M., Donovan, A., 2014. Petrological and geochemical variation during the Soufrière Hills eruption, 1995 to 2010. Geological Society of London Memoirs 39, 317–342.

Cichy, S., Botcharnikov, R., Holtz, F., Behrens, H., 2011. Vesiculation and microlite crystallization induced by decompression: a case study of the 1991-1995 Mt Unzen eruption (Japan). Journal of Petrology 52 no. 7-8, 1469–1492.

Cimarelli, C., Costa, A., Mueller, S., Mader, H., 2011. Rheology of magmas with bimodal crystal size and shape distributions: Insights from analog experiments. Geochemistry, Geophysics, Geosystems 12 no.7, QO7O24.

Clarisse, L., Coheur, P., Prata, A., Hurtmans, D., Razavi, A., Phulpin, T., Hadji-Lazaro, J., Clerbaux, C., 2008. Tracking and quantifying volcanic SO_2 with IASI, the september 2007 eruption at Jebel at Tair. Atmospheric Chemistry and Physics 8, 7723–7734.

Clarke, A., Stephens, S., Teasdale, R., Sparks, R., Diller, K., 2007. Petrologic constraints on the decompression history of magma prior to Vulcanian explosions at the Soufrière Hills volcano, Montserrat. Journal of Volcanology and Geothermal Research 161, 261–274.

Collier, L., 2005. The interaction of gas-charged magma and seismic waves. Ph.D. thesis, University of Leeds.

Collier, L., Neuberg, J., 2006. Incorporating seismic observations into 2D conduit flow modeling. Journal of Volcanology and Geothermal Research 152, 331–346.

Collombet, M., 2009. Two-dimensional gas loss for silicic magma flows: toward more realistic numerical models. Geophysical Journal International 177, 309–318.

Commer, M., Helwig, S., Hördt, A., Scholl, C., 2006. New results on the resistivity structure of Merapi Volcano of long-offset transient electromagnetic data. Geophysical Journal International 167, 1172–1187.

Coombs, M., Sisson, T., Bleick, H., Menton, S., Nye, C., Payne, A., Cameron, C., Larsen, J., Wallace, K., Bull, K., 2013. Andesites of the 2009 eruption of Redoubt Volcano, Alaska. Journal of Volcanology and Geothermal Research 259, 349–372.

Costa, A., Caricchi, L., Bagdassarov, N., 2009a. A model for the rheology of particle-bearing suspensions and partially molten rocks. Geochemistry, Geophysics, Geosystems 10, Q03010.

Costa, A., Sparks, R., Macedonio, G., Melnik, O., 2009b. Effects of wall-rock elasticity on magma flow in dykes during explosive eruptions. Earth and Planetary Science Letters 288, 455–462.

Costa, A., Wadge, G., Melnik, O., 2012. Cyclic extrusion of a lava dome based on a stick-slip mechanism. Earth and Planetary Science Letters 337-338, 39–46.

Costa, F., Andreastuti, S., Bouvet de Maisnonneuve, C., Pallister, J., 2013. Petrological insights into the storage conditions, and magmatic processes that yielded the centennial 2010 Merapi explosive eruption. Journal of Volcanology and Geothermal Research 261, 209 –235.

De Mets, C., Gordon, R., Argus, D., Stein, 1990. Current plate motion. Geophysical Journal International 101, 425–478.

De' Michieli Vitturi, M., Clarke, A., Neri, A., Voight, B., 2008. Effects of conduit geometry on magma ascent dynamics in dome-forming eruptions. Earth and Planetary Science Letters 272, 567–578.

De' Michieli Vitturi, M., Clarke, A., Neri, A., Voight, B., 2010. Transient effects of magma ascent dynamics along a geometrically variable dome-feeding conduit. Earth and Planetary Science Letters 295, 541–553.

De' Michieli Vitturi, M., Clarke, A., Neri, A., Voight, B., 2013. Extrusion cycles during dome-building eruptions. Earth and Planetary Science Letters 371-372, 37–48.

Deegan, F., Troll, V., Freda, C., Misiti, V., Chadwick, J., 2011. Fast and furious: crustal CO_2 release at Merapi volcano, Indonesia. Geology Today 27 no. 2, 63–64.

Deegan, F., Troll, V., Freda, C., Misiti, V., Chadwick, J., McLeod, C., Davidson, J., 2010. Magma-carbonate interaction processes and associated CO_2 release at Merapi volcano, Indonesia: Insights from experimental petrology. Journal of Petrology 51 no. 5, 1027–1051.

Degruyter, W., Bachman, ., Burgisser, A., Manga, M., 2012. The effects of outgassing on the transition between effusive and explosive silicic eruptions. Earth and Planetary Science Letters 349-350, 161–170.

Degruyter, W., Bachman, O., Burgisser, A., 2009. Controls on magma permeability in the volcanic conduit during the climactic phase of the Kos Plateau Tuff eruption (Aegean Arc). Bulletin of Volcanology 72, 63.

Del Gaudio, P., 2014. Rheology of bimodal crystals suspensions: Results from analogue experiments and implications for magma ascent. Geochemistry, Geophysics, Geosystems 15 no. 1, 284–291.

Diller, K., Clarke, A., Voight, B., Neri, A., 2006. Mechanisms of conduit plug formation: Implications for vulcanian explosions. Geophysical Research Letters 33, L20302.

Dingwell, D., Bagdassarov, N., Bussod, G., Webb, S., 1993. Magma rheology. experiments at high pressures and application to the earth's mantle. Mineralogy Association of Canada Short Course Handbook 21, 233–333.

Drignon, M., Bechon, T., Arbaret, L., Burgisser, A., Komorowski, J.-C., Martel, C., Miller, H., Yaputra, R., 2016. Pre-explosive conduit conditions during the 2010 eruption of Merapi volcano (Java, Indonesia). Geophysical Research Letters 43.

Druitt, T., Kokelaar, B. (Eds.), 2002. The eruption of Soufrière Hills Volcano, Montserrat, from 1995 to 1999. Vol. 21. The Geological Society of London, Memoirs.

Druitt, T., Young, S., Baptie, B., Bonadonna, C., Calder, E., Clarke, A., Cole, P., Harford, C., Herd, R., Luckett, R., Ryan, G., Voight, B., 2002. The eruption of Soufrière Hills Volcano, Montserrat, from 1995 to 1999. Vol. 21. The Geological Society of London, Memoirs, Ch. Episodes of cyclic Vulcanian explosive activity with fountain collapse at Soufrière Hills Volcano, Montserrat, pp. 281–306.

Edmonds, M., Oppenheimer, C., Pyle, D., Herd, R., Thompson, G., 2003. SO_2 emissions from Soufrière Hills Volcano and their relationship to conduit permeability, hydrothermal interaction and degassing regime. Journal of Volcanology and Geothermal Research 124, 23–43.

Eichelberger, J., Carrigan, C., Westrich, H., Price, R., 1986. Non-explosive silicic volcanism. Nature 323, 16.

Eilers, H., 1943. Die viskositäts konzentrationsabhängigkeit kolloider systeme in organischen lösungsmitteln. Kolloid Zeitschrift 102, 154–169.

Einstein, A., 1911. Berichtigung zu meiner Arbeit: Eine neue Bestimmung der Moleküldimensionen. Annals of Physics 34, 591–592.

Erdmann, S., Martel, C., Pichavant, M., Bourdier, J.-L., Champallier, R., Komorowski, J.-C., Cholik, N., 2016. Constraints from phase equilibrium experiments on pre-eruptive storage conditions in mixed magma systems: A case study on crystal-rich basaltic andesites from Mount Merapi, Indonesia. Journal of Petrolgy 57 no. 3, 535–560.

Erdmann, S., Martel, C., Pichavant, M., Kushnir, A., 2014. Amphibole as an archivist of magmatic crystallization conditions: problems, potential, and implications for inferring magma storage prior to the paroxysmal 2010 eruption of Mount Merapi, Indonesia. Contributions to Mineralogy and Petrology 167, 1016.

Farquharson, J., Heap, M., Varley, N., Baud, P., Reuschlé, T., 2015. Permeability and porosity relationships of edifice-forming andesites: A combined field and laboratory study. Journal of Volcanology and Geothermal Research 297, 52–68.

Fiege, A., Cichy, S., 2015. Experimental constraints on bubble formation and growth during ascent: A review. American Mineralogist 100, 2426–2442.

Galle, B., Oppenheimer, C., Geyer, A., McGonigle, A., Edmonds, M., Horrocks, L., 2003. A miniaturised ultraviolet spectrometer for remote sensing of SO_2 fluxes: a new tool for volcano surveillance. Journal of Volcanology and Geothermal Research 119, 241–254.

Gardner, J., 2007. Bubble coalescence in rhyolitic melts during decompression from high pressure. Journal of Volcanology and Geothermal Research 166, 161–176.

Gardner, J., Hilton, M., Carroll, M., 2000. Bubble growth in highly viscous silicate melts during continuous decompression from high pressure. Geochimica et Cosmochimica Acta 64 no.8, 1473–1483.

Gaunt, H., Sammonds, P., Meredith, P., Smith, R., Pallister, J., 2014. Pathways for degassing during the lava dome eruption of Mount St. Helens 2004-2008. Geology 42, 947–950.

Gertisser, R., Charbonnier, S., Keller, J., Quidelleur, X., 2012. The geological evolution of Merapi volcano, Central Java, Indonesia. Bulletin of Volcanology 74, 1213–1233.

Gertisser, R., Keller, J., 2003. Temporal variations in magma composition at Merapi Volcano (Central Java, Indonesia): magmatic cycles during the past 2000 of explosive activity. Journal of Volcanology and Geothermal Research 123, 1–23.

Giachetti, T., Druitt, T., Burgisser, A., Arbaret, L., Calven, C., 2010. Bubble nucleation, growth and coalescence during the 1997 Vulcanian explosions of Soufrière Hills Volcano, Montserrat. Journal of Volcanology and Geothermal Research 193, 215–231.

Giordano, D., Russell, J., Dingwell, D., 2008. Viscosity of magmatic liquids: A model. Earth and Planetary Science Letters 271, 123–134.

Gonnermann, H., Manga, M., 2007. The fluid mechanics inside a volcano. Annual Review of Fluid Mechanics 39, 321–356.

Green, D., Neuberg, J., Cayol, V., 2006. Shear stress along the conduit walls as a plausible source of tilt at Soufrière Hills Volcano, Montserrat. Geophysical Research Letters 33, L10306.

Guido, S., Greco, F., 2001. Drop shape under slow steady shear flow and during relaxation. Experimental results and comparison with theory. Rheologica Acta 40, 176–184.

Guth, E., Gold, O., 1938. On the hydridynamical theory of the viscosity of suspensions. Physical Review 53, 322.

Hamilton, W., 1979. Tectonics of the Indonesian region. U.S. Geological Survey Professional Paper 1078, 1–345.

Harris, A., Allen III, J., 2008. One-, two- and three-phase viscosity treatments for basaltic lava flows. Journal of Geophysical Research 113.

Hautmann, S., Hidayat, D., Fournier, N., Linde, A., Sacks, I., Williams, C., 2013. Pressure changes in the magmatic system during the Decemeber 2008/January 2009 extrusion at Soufrière Hills Volcano, Montserrat (W.I.), derived from strain data analysis. Journal of Volcanology and Geothermal Research 250, 34–41.

Hess, K.-U., Dingwell, D., 1996. Viscosities of hydrous leucogranitic melts: A non-Arrhenian model. American Mineralogist 81, 1297–1300.

Hinch, E., Acrivos, A., 1980. Long slender drops in a simple shear flow. Journal of Fluid Mechanics 98, 305–328.

Holland, A., Watson, I., Phillips, J., Caricchi, L., Dalton, M., 2011. Degassing processes during lava dome growth : Insights from Santiaguito lava dome, Guatemala. Journal of Volcanology and Geothermal Research 202, 153–166.

Hui, H., Zhang, Y., 2007. Toward a general viscosity equation for natural anhydrous and hydrous silicate melts. Geochimica et Cosmochimica Acta 71, 403–416.

Huppert, H., Woods, A., 2002. The role of volatiles in magma chamber dynamics. Nature 420, 493–495.

Hurwitz, S., Kipp, K., Ingebritsen, S., Ried, M., 2003. Groundwater flow, heat transport, and water table position within volcanic edifices. Journal of Geophysical Research 108.

Ikeda, R., Kajiwara, T., Omura, K., Hickman, S., 2008. Physical rock properties in and around a conduit zone by well-logging in the Unzen Scientific Drilling Project, Japan. Journal of Volcanology and Geothermal Research 175, 13–19.

Innocenti, S., Andreastuti, S., Furman, T., del Marmol, M.-A., Voight, B., 2013a. The pre-eruption conditions for explosive eruptions at Merapi volcano as revealed by crustal texture and mineralogy. Journal of Volcanology and Geothermal Research 261, 69–86.

Innocenti, S., del Marmol, M.-A., Voight, B., Andreastuti, S., Furman, T., 2013b. Textural and mineral chemistry constraints on evolution of Merapi Volcano, Indonesia. Journal of Volcanology and Geothermal Researcj 261, 20–37.

Jarrard, R., 1986. Relations among subduction parameters. Reviews of Geophysics 24, 217–284.

Jaupart, C., Allègre, C., 1991. Gas content, eruption rate and instabilities of eruption regime in silicic volcanoes. Earth and Planetary Science Letters 102, 413–429.

Johnson, J., Lees, J., Gerst, A., Sahagian, D., Varley, N., 2008. Long-period earthquakes and co-eruptive dome inflation seen with particle image velocimetry. Nature 456, 377–381.

Kameda, M., Katsumata, T., Ichihara, M., 2008. Deformation of bubbles in a highly viscous pipe flow. Fluid Dynamics Research 40, 576–584.

Kedrinskiy, V., 2009. Explosive eruptions of volcanoes: simulation, shock tube methods and multi-phase mathematical models. Shock Waves, 19–26.

Kendrick, J., Lavallée, Y., Hess, K.-U., Heap, M., Gaunt, H., Meredith, P., Dingwell, D., 2013. Tracking the permeable porous network during strain-dependent magmatic flow. Journal of Volcanology and Geothermal Research 260, 117–126.

Kendrick, J., Lavallée, Y., Varley, N., Wadsworth, F., Lamb, O., Vasseur, J., 2016. Blowing off steam: Tuffisite formation as a regulator for lava dome eruptions. Frontiers in Earth Sciences 4, 41.

Kilburn, C., 2003. Multiscale fracturing as a key to eruption forecasting. Journal of Volcanology and Geothermal Research 125, 271–289.

Klug, C., Cashman, C., Bacon, C., 2002. Structure and physical characteristics of pumice from the climatic eruption of Mount Mazama (Crater Lake), Oregon. Bulletin of Volcanology 64, 486–501.

Klug, C., Cashman, K., 1994. Vesiculation of May 18, 1980, Mount St. Helens magma. Geology 22, 468–472.

Klug, C., Cashman, K., 1996. Permeability development in vesiculating magmas: Implication for fragmentation. Bulletin of Volcanology 58, 87–100.

Koulakov, I., Bohm, M., Asch, G., Lühr, B.-G., Manzanares, A., Brotopuspito, K., Fauzi, P., Purbawinata, M., Puspito, N., Ratdomopurbo, A., Kopp, H., Rabbel, W., Shevkunova, E., 2007. P and S velocity structure of the crust and the upper mantle beneath central Java from local tomography inversion. Journal of Geophysical Research 112, B08310.

Koulakov, I., Maksotova, G., Jaxybulatov, K., Kasatkina, E., Shapiro, N., Luehr, B.-G., El Khrepy, S., 2016. Structure of the magma reservoirs beneath Merapi and surrounding volcano centers of Central Java modeled from ambient noise tomography. Geochemistry, Geophysics, Geosystems 17.

Kozono, T., Koyaguchi, T., 2009. Effects of relative motion between gas and liquid on 1-dimensional steady flow in silicic volcanic conduits: 1. An analytical method. Journal of Volcanology and Geothermal Research 180, 21–36.

Krieger, I., Dougherty, T., 1959. A mechanism for non-Newtonian flow in suspensions of rigid spheres. Transactions. Society of Rheology 3, 137–152.

Kueppers, U., Perugini, D., Dingwell, D., 2006. “Explosive energy ” during volcanic eruptions from fractal analysis of pyroclasts. Earth and Planetary Science Letters 248, 800–807.

Kushnir, A., Martel, C., Bourdier, J.-L., Heap, M., Reuschlé, T., Erdmann, S., Komorowski, J.-C., Cholik, C., 2016. Probing permeability and microstructure: Unravelling the role of a low-permeability dome on the explosivity of Merapi (Indonesia. Journal of Volcanology and Geothermal Research 316, 56–71.

Lavallée, Y., Benson, P., Heap, M., Hess, K., Flaws, A., Schillinger, B., Meredith, P., Dingwell, D., 2013. Reconstructing magma failure and the degassing network of dome-building eruptions. Geology 41, 515–518.

Lavallée, Y., Varley, N., Alatorre-Ibargüengoita, M., Hess, K.-U., Kueppers, U., Mueller, S., Richard, D., Scheu, B., Spieler, O., Dingwelle, D., 2012. Magmatic architecture of dome-building eruptions at Volcán de Colima, Mexico. Bulletin of Volcanology 74, 249–260.

Lee, S., 1990. Universality of continuum percolation. Physical Review 42, 4877–4880.

Lensky, N., Lyakhovsky, V., Navon, O., 2002. Expansion dynamics of volatile-supersaturated fluid and bulk viscosity of bubbly magma. Journal of Fluid Mechanics 460, 39–56.

Lensky, N., Navon, O., Lyakhovsky, V., 2004. Bubble growth during decompression of magma: experimental and theoretical investigation. Journal of Volcanology and Geothermal Research 129, 7–22.

Lindoo, A., Larsen, J., Cashman, K., Dunn, A., Neill, O., 2016. An experimental study of permeability development as a function of crystal-free melt viscosity. Earth and Planetary Science Letters 435, 45–54.

Llewellin, E., Mader, H., Wilson, S., 2002a. The rheology of a bubbly liquid. Proceedings of the Royal Society A 458, 987–1016.

Llewellin, E., Manga, M., 2005. Bubble suspension rheology and implications for conduit flow. Journal of Volcanology and Geothermal Research 143, 205–217.

Llewelling, E., Mader, H., Wilson, S., 2002b. The constitutive equation and flow dynamics of bubbly magmas. Geophysical Research Letters 29, 2170.

Luehr, B.-G., Koulakov, I., Rabbel, W., Zschau, J., Ratdomopurbo, A., Brotopuspito, K., Fauzi, P., Sahara, D., 2013. Fluid ascent and magma storage beneath Gunung Merapi revealed by multi-scale seismic imaging. Journal of Volcanology and Geothermal Research 261, 7–19.

Maccaferri, F., Bonafede, M., Rivalta, E., 2010. A numerical model of dyke propagation in layered elastic media. Geophysical Journal International 180, 1107–1123.

Maccaferri, F., Bonafede, M., Rivalta, E., 2011. A quantitative study of the mechanisms governing dike propagation, dike arrest and sill formation. Journal of Volcanology and Geothermal Research 208, 39–50.

Maccaferri, F., Rivalta, E., Keir, D., Acocella, V., 2014. Unloading-driven off-axis volcanism in rift zones. Nature Geoscience 7, 297–300.

Mackenzie, J., 1950. Elastic constants of a solid containing spherical holes. Proceedings of the Royal Society B 63, 2–11.

Mader, H., Llewellin, E., Mueller, S., 2013. The rheology of two-phase magmas: A review and analysis. Journal of Volcanology and Geothermal Research 257, 135–158.

Mancini, S., Forestier-Coste, L., Burgisser, A., James, F., Castro, J., 2016. An expansion-coalescence model to track gas bubble populations. Journal of Volcanology and Geothermal Research 313, 44–58.

Manga, M., Castro, J., Cashman, K., Loewenberg, M., 1998. Rheology of bubble-bearing magmas. Journal of Volcanology and Geothermal Research 87, 15–28.

Martel, C., 1996. Conditions pré-éruptives et dégazage des magmas andésitiques de la Montagne Pelée (Martinique: étude pétrologique et expérimentale. Ph.D. thesis, Université d'Orléans.

Martel, C., Bourdier, J., Pichavant, M., Traineau, H., 2000. Textures, water content and degassing of silicic andesites from recent plinian and dome-forming eruptions at Mount Pelée Volcano (Martinique, Lesser Antilles arc). Journal of Volcanology and Geothermal Research 96, 191–206.

Martel, C., Poussineau, S., 2007. Diversity of eruptive styles inferred from the microlites of Mt Pelée andesite (Martinique, Lesser Antilles). Journal of Volcanology and Geothermal Research 166, 233–254.

Massol, H., 2001. Ascent and decompression of viscous vesicular magma in a volcanic conduit. Journal of Geophysical Research 106, 16233–16240.

Massol, H., Jaupart, C., 1999. The generation of gas overpressure in volcanic eruptions. Earth and Planetary Science Letters 166, 57–70.

Massol, H., Jaupart, C., 2009. Dynamics of magma flow near the vent: Implications for dome eruptions. Earth and Planetary Science Letters 279, 185–196.

Massol, H., Koyaguchi, T., 2005. The effect of magma flow on nucleation of gas bubbles in a volcanic conduit. Journal of Volcanology and Geothermal Research 143, 69–88.

Mastin, L., Lisowski, M., Roeloffs, E., Beeler, N., 2009. Improved constraints on the estimated size and volatile content of the Mount St. Helens magma system from the 2004-2008 history of the dome growth and deformation. Geophysical Research Letters 36, L20304.

Matthews, S., Gardeweg, M., Sparks, R., 1997. The 1984 to 1996 cyclic activity of Lascar Volcano, northern Chile: Cycles of dome growth, dome subsidence, degassing and explosive eruptions. Bulletin of Volcanology 59, 72–82.

Matthews, S., Jones, A., Gardeweg, M., 1994. Lascar Volcano; northern Chile: evidence for steady-state disequilibrium. Journal of Petrology 35, 401–432.

Matthews, S., Sparks, R., Gardeweg, M., 1999. The Piedras Grandes-Soncor eruptions, Lascar volcano, Chile: evolution of a zoned magma chamber in the central Andean upper crust. Journal of Petrology 40, 1891–1919.

Mei, E., Lavigne, F., Picquout, A., de Bélizal, E., Brunstein, D., Grancher, D., Sartohadi, J., Cholik, N., Vidal, C., 2013. Lessons learned from the 2010 evacuations at Merapi Volcano. Journal of Volcanology and Geothermal Research 261, 348–365.

Melnik, O., Barmin, A., Sparks, R., 2005. Dynamics of magma flow inside volcanic conduits with bubble overpressure buildup and gas loss through permeable magma. Journal of Volcanology and Geothermal Research 143, 53–68.

Melnik, O., Costa, A., 2014. Dual chamber-conduit models of non-linear dynamics behaviour at Soufrière Hills Volcano, Montserrat. Vol. 39. The Geological Society of London, Memoirs, pp. 61–69.

Melnik, O., Sparks, R., 1999. Nonlinear dynamics of lava dome extrusion. Nature 402, 37–41.

Melnik, O., Sparks, R., 2002. The eruption of Soufrière Hills Volcano, Montserrat, from 1995 to 1999. Vol. 21. The Geological Society of London, Memoirs, Ch. Dynamics of magma ascent and lava extrusion at Soufrière Hills Volcano, Montserrat, pp. 153–171.

Melnik, O., Sparks, R., 2005. Controls on conduit magma flow dynamics during lava dome building eruptions. Journal of Geophysical Research 110, B02209.

Menand, T., Daniels, K., Benghiat, P., 2010. Dyke propagation and sill formation in a compressive tectonic environment. Journal of Geophysical Research 115, BO8201.

Michaut, C., Bercovici, D., 2009. A model for the spreading and compaction of two-phase viscous gravity currents. Journal of Fluid Mechanics 630, 299–329.

Michaut, C., Ricard, Y., Bercovici, D., Sparks, R., 2013. Eruption cyclicity at silicic volcanoes potentially caused by magmatic gas waves. Nature Geoscience 6, 850–860.

Mogi, K., 1958. Relations between the eruptions of various volcanoes and the deformations of the ground surfaces around them. Bulletin of the Earthquake Research Institute 36, 99–134.

Moitra, P., Gonnermann, H., 2015. Effects of crystal shape- and size-modality on magma rheology. Geochemistry, Geophysics, Geosystems 16, 1–26.

Mueller, S., Melnik, O., Spieler, O., Sheu, B., Dingwell, D., 2005. Permeability and degassing of dome lavas undergoing rapid decompression: An experimental determination. Bulletin of Volcanology 67, 526–238.

Mueller, S., Scheu, B., Kueppers, U., Spieler, O., Richard, D., Dingwell, D., 2011. The porosity of pyroclasts as an indicator of volcanic explosivity. Journal of Volcanology and Geothermal Research 203, 168–174.

Mueller, S., Scheu, B., Spieler, O., Dingwell, D., 2008. Permeability control on magma fragmentation. The Geological Society of America 36, 399–402.

Müller, M., Hördt, A., Neubauer, F., 2002. Internal structure of Mount Merapi, Indonesia, derived from log-offset transent electromagnetic data. Journal of Geophysical Research 107 no. B9, 2187.

Murphy, M., Sparks, R., Barclay, J., Carroll, M., Brewer, T., 2000. Remobilization of andesite magma by intrusion of mafic magma at the Soufrière Hills Volcano, Montserrat, West Indies. Journal of Petrology 41, 21–42.

Nadeau, O., William-Jones, A., Stix, J., 2013. Magmatic-hydrothermal evolution and devolatilization beneath Merapi volcano, Indonesia. Journal of Volcanology and Geothermal Research 261, 50–68.

Nakada, S., Motomura, Y., 1999. Petrology of the 1991-1995 eruption at Unzen: effusion pulsation and groundmass crystallization. Journal of Volcanology and Geothermal Research 89, 173–196.

Navon, ., Lyakhovsky, V., 1998. The physics of explosive volcanic eruptions. Vol. 145. The Geological Society of London, Special Publications, Ch. Vesiculation processes in silicic magmas, pp. 27–50.

Navon, O., Chekhmir, A., Lyakhovsky, V., 1998. Bubble growth in highly viscous melts : theory, experiments, and autoexplosivity of dome lavas. Earth and Planetary Science Letters 160, 763–776.

Neuberg, J., 2000. Characteristics and causes of shallow seismicity in andesite volcanoes. Philosophical Transactions of the Royal Society Series A 358, 1533–1546.

Newhall, C., Bronto, S., Alloway, B., Banks, N., Bahar, I., del Marmol, M., Hadisantono, R., Holcomb, R., McGeehin, J., Micsic, J., Rubin, M., Sayudi, S., Sukhyar, R., Andreastuti, S., Tilling, R., Torley, R., Trimble, D., Wirakusumah, A., 2000. 10,000 years of explosive eruptions of Merapi Volcano, Central Java: Archeological and modern implications. Journal of Volcanology and Geothermal Research 100, 9–50.

Newhall, C., Melson, W., 1983. Explosive activity associated with the growth of volcanic domes. Journal of Volcanology and Geothermal Research 17, 111–131.

Nishimura, T., 2006. Ground deformation due to magma ascent with and without degassing. Geophysical Research Letters 33, L23309.

Nishimura, T., 2009. Ground deformation caused by magma ascent in an open conduit. Journal of Volcanology and Geothermal Research 187, 178–192.

Ogburn, S., Loughlin, S., Calder, E., 2015. The association of lava dome growth with major explosive activity (VEI ≥ 4): Domehaz, a global dataset. Bulletin of Volcanology 77, 40.

Okumura, S., Nakamura, M., Nakano, T., Uesugi, K., Tsuchiyama, A., 2010. Shear deformation experiments on vesicular rhyolite: Implications for brittle fracturing, degassing, and compaction of magmas in volcanic conduits. Journal of Geophysical Research 115, B06201.

Pallister, J., Scneider, D., Griswold, J., Keeler, R., William, C., Noyles, C., Newhall, C., Ratdomopurbo, A., 2013. Merapi 2010 eruption - Chronology and extrusion rates monitored with satellite radar and used in eruption forecasting. Journal of Volcanology and Geothermal Research 261, 144–152.

Papale, P., Polacci, M., 1999. Role of carbon dioxide in the dynamics of magma ascent in explosive eruptions. Bulletin of Volcanology 60 no. 8, 583–594.

Pistone, M., Cordonnier, B., Ulmer, P., Caricchi, L., 2016. Rheological flow laws for multiphase magmas: An empirical approach. Journal of Volcanology and Geothermal Research 321, 158–170.

Prata, A., Bernardo, C., 2007. Retrieval of volcanic $S0_2$ column abundance from Atmospheric Infrared Sounder data. Journal of Geophysical Research 146, 60–76.

Preece, K., Barclay, J., Gertisser, R., Herd, R., 2013. Textural and micro-petrological variations in the eruptive products of the 2006 dome-forming eruption of Merapi volcano, Indonesia: Implications for sub-surface processes. Journal of Volcanology and Geothermal Research 261, 98–120.

Preece, K., Gertisser, R., Barclay, J., Berlo, K., Herd, R., 2014. Pre- and syn-eruptive degassing and crystallisation processes of the 2010 and 2006 eruptions of Merapi volcano, Indonesia. Contributions to Mineralogy and Petrology 168, 1061.

Prousevitch, A., Sahagian, D., Anderson, A., 1993. Dynamics of diffusive bubble growth in magmas: isothermal case. Journal of Geophysical Research 98, 22283–22307.

Prud'Homme, R., Bird, R., 1978. The dilatational properties of suspensions of gas bubbles in incompressible newtonian and non-newtonian fluids. Journal of Non-Newtonian Fluid Mechanics 3, 261–279.

Rallison, J., 1980. Note on the time-dependent deformation of a viscous drop which is almost spherical. Journal of Fluid Mechanics 98, 625–633.

Ratdomopurbo, A., Beauducel, F., Subandriyo, J., Agung Nandaka, I., Newhall, C., Suharna, Sri Sayudi, D., Suparwaka, H., Sunarta, 2013. Overview of the 2006 eruption of Mt. Merapi. Journal of Volcanology and Geothermal Research 261, 87–97.

Ratdomopurbo, A., Poupinet, G., 1995. Monitoring a temporal change of seismic velocity in a volcano: application to the 1992 eruption of Mt. Merapi (Indonesia. Geophysical Research Letters 22 no. 7, 775–778.

Ratdomopurbo, A., Poupinet, G., 2000. An overview of the seismicity of Merapi volcano (Java, Indonesia), 1983-1994. Journal of Volcanology and Geothermal Research 100, 193–214.

Rebscher, D., Westerhaus, M., Welle, W., Nandaka, I., 2000. Monitoring ground deformation at the Decade Volcano Gunung Merapi, Indonesia. Physics and Chemistry of the Earth 25, 9–11.

Richet, P., Bottinga, Y., 1995. Structure, dynamics and properties of silicate melts. Ch. Rheology and configurational entropy of silicate melts.

Ritchie, L., Cole, P., Sparks, R., 2002. The eruption of Soufrière Hills Volcano, Montserrat, from 1995 to 1999. No. 21. The Geological Society of London, Memoirs, Ch. Sedimentology of deposits from the pyroclastic density current of 26 December 1997 at Soufrière Hills Volcano, Montserrat, pp. 435–456.

Rivalta, E., Taisne, B., Bunger, A., Katz, R., 2015. A review of mechanical models of dike propagation: Schools of thought, results and future directions. Tectonophysics 638, 1–42.

Rivers, M., Carmichael, I., 1987. Ultrasonic studies of silicate melts. Journal of Geophysical Research 92, 9247–9270.

Robertson, R., 1998. The explosive eruption of Soufrière Hills Volcano, Montserrat, West Indies, 17 September, 1996. Geophysical Research Letters 25, 3429–3432.

Roscoe, R., 1952. The viscosity of suspensions of rigid spheres. Journal of Applied Physics 2, 267–269.

Rust, A., Cashman, K., 2004. Permeability of vesicular silicic magma: Inertial and hysteresis effects. Earth and Planetary Science Letters 228, 93–107.

Rust, A., Cashman, K., 2011. Permeability controls on expansion and size distributions of pyroclasts. Journal of Geophysical Research 116, B11202.

Rust, A., Manga, M., 2002a. Bubble shapes and orientations in low re simple shear flow. Journal of Colloid and Interface Science 249, 476–480.

Rust, A., Manga, M., 2002b. Effects of bubble deformation on the viscosity of dilute suspensions. Journal of Non-Newtonian Fluid Mechanics 104, 53–63.

Rust, A., Manga, M., Cashman, K., 2003. Determining flow type, shear rate and shear stress in magmas from bubble shapes and orientations. Journal of Volcanology and Geothermal Research 122, 111–132.

Saar, M., Manga, M., 1999. Permeability-porosity relationship in vesicular basalts. Geophysical Research Letters 26, 111–114.

Sahimi, M., 1994. Applications of Percolation Theory. Taylor & Francis Ltd., London.

Sanderson, R., Johnson, J., Lees, J., 2010. Ultra-long period seismic signals and cyclc deflation coincident with eruptions at Santiaguito volcano, Guatemala. Journal of Volcanology and Geothermal Research 198, 35–44.

Sato, H., Fujii, T., Nakada, S., 1992. Crumbling of dacite dome lava and generation of pyroclastic flows at Unzen Volcano. Letters to Nature 360, 664–666.

Savov, I., Luhr, J., Navarro-Ochoa, C., 2008. Petrology and geochemistry of lava and ash erupted from Volcán de Colima, Mexico, during 1998-2005. Journal of Volcanology and Geothermal Research 174, 241–256.

Scott, J., Mather, T., Pyle, D., Rose, W., Chigna, G., 2012. The magmatic plumbing system beneath Santiaguito Volcano, Guatemala. Journal of Volcanology and Geothermal Research 237-238, 54–68.

Shaw, H., 1972. Viscosities of magmatic silicate liquids; and empirical method of prediction. American Journal of Science 272, 870–889.

Shaw, H., 1974. Diffusion of water in granitic liquids: Part I. Exerimental data; Part II. Mass transfer in magma chambers. Carnegis Institute Washington Publications 634, 139–172.

Sheldrake, T., Sparks, R., Cashman, K., Wadge, G., Aspinall, W., 2016. Similarities and differences in the hitorical records of lava dome-building volcanoes: Implications for understanding magmatic processes and eruption forecasting. Earth-Science Reviews 160, 240–263.

Shields, J., Mader, H., Pistone, M., Caricchi, L., Floess, D., Putlitz, B., 2014. Strain-induced degassing of three-phase magmas during simple shear. Journal of Geophysical Research: Earth Sciences 119, 6936–6957.

Sibree, J., 1934. The viscosity of froth. Transactions of the Faraday Society 28, 325–331.

Siswowidjoyo, S., Tulus, Djumarma, A., Matahelumual, J., Tjetjep, W., Pratomo, I., Bahar, I., 1985. Kegiatan G. Merapi, Jawa Tengah, tahun 1984. Proc. PIT XIV Ikatan Ahli Geologi Indonesia, 181–192.

Solikhin, A., Pinel, V., Vandemeulebrouck, J., Thouret, J.-C., Hendrasto, M., 2015. Mapping the 2010 Merapi pyroclastic deposits using dual-polarization Synthetic Aperture Radar (SAR) data. Remote Sensing of Environment 158, 180–192.

Sparks, R.S.J. Barclay, J., Calder, E., Herd, R., Komorowski, J.-C., Luckett, R., Norton, G., Ritchie, L., Voight, B., Woods, A., 2002. The eruption of Soufrière Hills Volcano, Montserrat, from 1995 to 1999. No. 21. The Geological Society of London, Memoirs, Ch. Generation of a debris avalanche and violent pyroclastic density current on 26 December (Boxing Day) 1997 at Soufrière Hills Volcano, Montserrat, pp. 409–434.

Sparks, R., 1978. The dynamics of bubble formation and growth in magmas: a review and analysis. Journal of Volcanology and Geothermal Research 3, 1–37.

Sparks, R., 1997. Causes and consequences of pressurisation in lava dome eruptions. Earth and Planetary Science Letters 150, 177–189.

Sparks, R., Murphy, M., Lejeune, A., Watts, R., Barclay, J., Young, S., 2000. Control on the emplacement of the andesite lava dome of the Soufrière Hills Volcano, Montserrat by degassing-induced crystallization. Terra Nova 12, 14–20.

Sparks, R., Young, S., 2002. The eruption of Soufrière Hills Volcano, Montserrat, from 1995 to 1999. No. 21. The Geological Society of London, Memoirs, Ch. The eruption of Soufrière Hills Volcano, Montserrat (1995-1998): overview of scientific results, pp. 45–70.

Sparks, R., Young, S., Barclay, J., Calder, E., Cole, P., Darroux, B., Davies, M., Druitt, T., Harford, C., Herd, R., James, M., Lejeune, A., Loughlin, S., Norton, G., Skerrit, G., Staviusk, M., Stevens, N., Toothill, J., Wadge, G., Watts, R., 1998. Magma production and growth of the lava dome of the Soufrière Hills Volcano, Montserrat, West Indies: November 1995 to December 1997. Geophysical Research Letters 25, 3421–3424.

Spieler, O., Kennedy, B., Kueppers, U., Dingwell, D., Scheu, B., Taddeucci, J., 2004. The fragmentation threshold of pyroclastic rocks. Earth and Planetary Science Letters 226, 139–148.

Stix, J., 1993. A model of degassing at Galeras Volcano, Colombia, 1988-1993. Geology 21, 963–967.

Surono, Philippe, J., Pallister, J., Boichu, M., Buongiorno, M., Budi-Santoso, A., Costa, F., Andreastuti, S., Prata, F., Scheinder, D., Clarisse, L., Humaida, H., Sumarti, S., Bignami, C., Griswold, J., Carn, S., Oppenheimer, C., Lavigne, F., 2012. The 2010 explosive eruption of Java's Merapi Volcano - a '100-year' event. Journal of Volcanology and Geothermal Research 241-242, 121–135.

Szramek, L., Gardner, J., Larsen, J., 2006. Degassing and microlite crystallization of basaltic andesite magma erupting at Arenal Volcano, Costa Rica. Journal of Volcanology and Geothermal Research 157, 182–201.

Taisne, B., Jaupart, C., 2008. Magma degassing and intermittent lava dome growth. Geophysical Research Letters 35.

Takeuchi, S., Nakashima, S., Tomiya, A., Shinohara, H., 2005. Experimental constraints on the low gas permeability of vesicular magma during decompression. Geophysical Research Letters 32, L10312.

Takeuchi, S., Tomiya, A., Shinohara, H., 2009. Degassing conditions for permeable silicic magmas: Implications from decompression experiments with constant rates. Earth and Planetary Science Letters 283, 101–110.

Taylor, G., 1932. The viscosity of a fluid containing small drops of another fluid. Proceedings of the Royal Society of London A 138, 41–48.

Taylor, G., 1934. The formation of emulsion in definable fields of flow. Proceedings of the Royal Society of London A 146, 501–523.

Tiede, C., Fernandez, J., Gerstenecker, C., Tiampo, K., 2007. A hybrid model for the summit region of Merapi Volcano, Java, Indonesia, derived from gravity changes and deformation measured between 2000 and 2002. Pure and Applied Geophysics 164, 837–850.

Troll, V., Chadwick, J., Jolis, E., Deegan, F., Hilton, D., Schwarzkopf, L., Blythe, L., Zimmer, M., 2013a. Crustal volatile release at Merapi volcano; the 2006 earthquakes and eruption events. Geology Today 29 no. 3, 96–101.

Troll, V., Deegan, F., Jolis, E., Harris, C., Cahdwick, J., Gertisser, R., Schwarskopf, L., Borisova, A., Bindeman, I., Sumarti, S., Preece, K., 2013b. Magmatic differentiation processes at merapi volcano: inclusion petrology and oxygen isotopes. Journal of Volcanology and Geothermal Research 261, 38–49.

Troll, V., Hilton, D., Jolis, E., Chadwick, J., Lythe, L., Deegan, F., Schwarzkopf, L., Zimmer, M., 2012. Crustal CO_2 liberation during the 2006 eruption and earthquake events at Merapi volcano, Indonesia. Geophysical Research Letters 39, L11302.

Truby, J., 2016. Rheology, eruption, and flow of three-phase magma. Ph.D. thesis, Durham University.

Truby, J., Mueller, S., Llewellin, E., Mader, H., 2015. The rheology of three-phase suspensions at low bubble capillary number. Proceedings of the Royal Society A 471.

Tuffen, H., Dingwell, D., Pinkerton, H., 2003. Repeated fracture and healing of silicic magma generate flow banding and earthquakes ? Geology 31, 1089–1092.

van Bemmelen, R., 1949. The geology of Indonesia. General Geology 1A.

van der Zwan, F., Chadwick, J., Troll, V., 2013. Textural history of recent basaltic-andesites and plutonic inclusions deom Merapi volcano. Contributions of Mineralogy and Petrology 166, 43–63.

Van Padang, N., 1933. Die uitbarsting van den Merapi (Midden Java) in de jaren 1930-1931. Vulcanologi en Seismologi Med. 12, 1–117.

Vetere, F., Behrens, H., Holtz, F., Neuville, D., 2006. Viscosity of andesitic melts – new experimental data and a revised calculation model. Chemical Geology 228, 233–245.

Vetere, F., Behrens, H., Schuelessler, J., Holtz, F., Misiti, V., Borchers, L., 2008. Viscosity of andesite melts and its implication for magma mixing prior to Unzen 1991-1995 eruption. Journal of Volcanology and Geothermal Research 175, 208–217.

Voight, B., 1988. Development of geodetic monitoring program at Merapi volcano, Java. United States Geological Survey unpublished report.

Voight, B., Casadevall, T., Cornelius, R., 1989. Development of geodetic monitoring program at Merapi volcano, Indonesia. International Association of Volcanology and Chemistry of the Earth's Interior General Assembly, Santa Fe.

Voight, B., Constantine, E., Siswowidjoyo, S., Torley, R., 2000. Historical eruptions of Merapi Volcano, Central Java, Indonesia, 1768–1998. Journal of Volcanology and Geothermal Research 100, 69–138.

Voight, B., Elsworth, D., 2000. Instability and collapse of hazardous gas-pressurized lava-domes. Geophysical Research Letters 27, 1–4.

Voight, B., Hoblitt, R., Clarke, A., Miller, A., Lynch, L., McMahon, J., 1998. Remarkable cyclic ground deformation monitored in real-time on Montserrat, and its use in eruption forecasting. Geophysical Research Letters 25 no. 18, 3405–3408.

Voight, B., Sparks, R., Miller, A.D. ans Stewart, R., Hoblitt, R., Clarke, A., Ewart, J., Aspinall, W., Baptie, B., Calder, E., Cole, P., Druitt, T., Hartford, C., Herd, R., Jackson, P., Lejeune, A., Lockhart, A., Loughlin, S., Luckett, R., Lynch, L., Norton, G., Robertson, R., Watson, I., Watts, R. ans Young, S., 2006. Magma flow instability and cyclic activity at Soufrière Hills Volcano, Montserrat, British West Indies. Science 283, 1138–1139.

Wagner, D., Koulakov, I., Rabbel, W., Luehr, B.-G., Wittwer, A., Kopp, H., Bohm, M., Asch, G., the MERAMEX Scientists, 2007. Joint inversion of active and passive seismic data in Central Java. Geophysical Journal International.

Walker, G., Wilson, L., Bowell, E., 1971. Explosive volcanic eruptions - I. The rate of fall of pyroclasts. Geophysical Journal of the Royal Astronomical Society 22, 377–383.

Wallace, P., Anderson, A., 1999. Volatiles in magmas. Encyclopedia of volcanoes.

Wallace, P., Anderson, A., Davis, A., 1995. Quantification of pre-eruptive exsolved gas contents in silicic magmas. Letters to Nature 377, 612–616.

Walter, T., Ratdomopurbo, A., Subandriyo, Aisyah, N., Sri Brotopuspito, K., Salzer, J., Lühr, B., 2013. Dome growth and coulée spreading controlled by the surface morphology, as determined by piwel offsets in photographs of the 2006 Merapi eruption. Journal of Volcanology and Geothermal Research 261, 121–129.

Watanabe, T., Shimizu, Y., Noguchi, S., Nakada, S., 2008. Permeability measurements on rock samples from Unzen Scientific Drilling Project Drill Hole 4 (USDP-4). Journal of Volcanology and Geothermal Research 175, 82–90.

Watson, I., Oppenheimer, C., Voight, B., Francis, P., Clarke, A., Stix, J., Miller, A., Pyle, D., Burton, M., Young, S., Norton, G., Loughlin, S., Darroux, B., Staff, M., 2000. The relationship between degassing and ground deformation at Soufrière Hills Volcano, Montserrat. Journal of Volcanology and Geothermal Research 98, 117–126.

Widiwijayanti, C., Clarke, A., Elsworth, D., Voight, B. ., 2005. Geodetic constraints on the shallow magma system at Soufrière Hills Volcano, Montserrat. Geophysical Research Letters 32, L11309.

William, C., Wadge, G., 1998. The effects of topography on magma chamber deformation models: application to Mt. Etna and radar interferometry. Geophysical Research Letters 25 no. 10, 1549–1552.

William, C., Wadge, G., 2000. An accurate and efficient method for including the effects of topography in three-dimensional elastic models of ground deformation with applications to radar interferometry. Journal of Geophysical Research 105 no. B4, 8103–8120.

Wilson, L., 1976. Explosive volcanic eruptions - III. Plinian eruption columns. Geophysical Journal of the Royal Astronomical Society 45, 543–556.

Wilson, L., Sparks, R., Huang, T., Watkins, N., 1978. The control of eruption column heights by eruption energetics and dynamics. Journal of Geophysical Research 83, 1829–1836.

Wilson, L., Sparks, R., Walker, G., 1980. Explosive volcanic eruptions - IV. The control of magma properties and conduit geometry on eruption column behaviour. Geophysical Journal of the Royal Astronomical Society 63, 117–148.

Witham, C., 2005. Volcanic disasters and incidents: A new database. Journal of Volcanology and Geothermal Research 148, 191–233.

Woods, A., Koyaguchi, T., 1994. Transitions between explosive and effusive eruptions of silicic magmas. Nature 370, 641–644.

Woods, A., Sparks, R., Ritchie, L., Batey, J., Gladstone, C., Bursik, M., 2002. The eruption of Soufrière Hills Volcano, Montserrat, from 1995 to 1999. No. 21. The Geological Society of London, Memoirs, Ch. The explosive decompression of a pressurized volcanic dome: the 26 December 1997 collapse and explosion of Soufrière Hills Volcano, Montserrat, pp. 457–466.

Wright, H., Roberts, J., Cashman, K., 2006. Permeability of anisotropic tube pumice: Model calculations and measurements. Geophysical Research Letters 33, L17316.

Young, K., Voight, B., Subandriyo, Sajiman, Miswanto, casadevall, T., 2000. Ground deformation at Merapi Volcano, Java, Indonesia: distance changes, June 1988-October 1995. Journal of Volcanology and Geothermal Research 100, 233 –259.